

TOPICAL REPORT

**BRAYTON CYCLE HEAT EXCHANGER
AND DUCT ASSEMBLY (HXDA),
PRELIMINARY DESIGN
AND TECHNOLOGY TESTS****CASE FILE
COPY**

prepared for
NATIONAL AERONAUTICS AND SPACE ADMINISTRATION

October 15, 1972

CONTRACT NO. NAS3-15347

NASA Lewis Research Center
Cleveland, Ohio 44135
P. T. Kerwin, Project Manager
Space Power Systems Division

NOTICE

This report was prepared as an account of Government-sponsored work. Neither the United States, nor the National Aeronautics and Space Administration (NASA), nor any person acting on behalf of NASA:

- A.) Makes any warranty or representation, expressed or implied, with respect to the accuracy, completeness, or usefulness of the information contained in this report, or that the use of any information, apparatus, method, or process disclosed in this report may not infringe privately-owned rights; or
- B.) Assumes any liabilities with respect to the use of, or for damages resulting from the use of; any information, apparatus, method or process disclosed in this report.

As used above, "person acting on behalf of NASA" includes any employee or contractor of NASA, or employee of such contractor, to the extent that such employee or contractor of NASA or employee of such contractor prepares, disseminates, or provides access to any information pursuant to his employment or contract with NASA, or his employment with such contractor.

Requests for copies of this report should be referred to

National Aeronautics and Space Administration
Scientific and Technical Information Facility
P. O. Box 33
College Park, Md. 20740

TOPICAL REPORT

BRAYTON CYCLE HEAT EXCHANGER
AND DUCT ASSEMBLY (HXDA),
PRELIMINARY DESIGN
AND TECHNOLOGY TESTS

by

M. G. Coombs, C. J. Morse, R. F. Graves,
J. J. Killackey, and J. C. Gibson

AIRESEARCH MANUFACTURING COMPANY
Los Angeles, California

prepared for

NATIONAL AERONAUTICS AND SPACE ADMINISTRATION

October 15, 1972

CONTRACT NO. NAS3-15347

NASA Lewis Research Center
Cleveland, Ohio 44135

P. T. Kerwin, Project Manager
Space Power Systems Division

FOREWORD

The studies described herein, which were performed by the AiResearch Manufacturing Company, a division of The Garrett Corporation were performed under NASA Contract NAS3-15347. The work was done under the direction of the NASA Project Manager, Mr. P. T. Kerwin, Space Power Systems Division, NASA-Lewis Research Center.

CONTENTS

<u>Section</u>		<u>Page</u>
1	INTRODUCTION AND SUMMARY	1
	Introduction	1
	Summary	3
	Reference Preliminary Design	3
	Brazing Development Tests	8
	Recuperator Structural Tests	8
	Heat Source Heat Exchanger Structure Tests	9
	Alternate Low Temperature Braze Alloy Tests	10
2	SYSTEM PRELIMINARY DESIGN	11
	Introduction	11
	Component Thermal Analysis and Design	11
	Recuperator	11
	Heat Source Heat Exchanger	18
	Waste Heat Exchanger	36
	System Design	53
	Close-Coupled Heat Source Heat Exchanger System	53
	Duct and Manifold Sizes	53
	Remote Heat Source Heat Exchanger System	63
	Structural Analysis and Design	69
	Structural Design Considerations	69
	HXDA Structural Design	83
3	BRAZING DEVELOPMENT TESTS	115
	Introduction	115
	Test Specimen Design	115
	Test Specimen Fabrication	115
	Test Procedure	119

CONTENTS (Continued)

<u>Section</u>	<u>Page</u>
Data Reduction	119
Results and Discussion	120
Conclusions	123
4 RECUPERATOR STRUCTURAL TESTS	124
Introduction	124
Test Specimen Design	126
Test Specimen Fabrication	133
Test Procedure	134
Data Reduction	137
Plastic Strain Range	137
Cycles to Failure	139
Results and Discussion	141
Conclusions	
5 HEAT SOURCE HEAT EXCHANGER STRUCTURE TESTS	147
Introduction	147
Test Specimen Design	147
Test Specimen Fabrication	147
Test Procedure	155
Data Reduction	158
Plastic Strain Range	158
Cycles to Failure	161
Results and Discussion	162
Conclusions	170
6 ALTERNATE LOW TEMPERATURE BRAZE ALLOY TESTS	173
Introduction	173
Test Specimen Design	174
Test Specimen Fabrication	174

CONTENTS (Continued)

<u>Section</u>	<u>Page</u>
Test Procedure	182
Plate Fin Burst Testing	182
Low Cycle Fatigue Testing	182
Data Reduction	186
Plastic Strain Range	186
Cycles to Failure	189
Results and Discussion	191
Conclusion	193

ILLUSTRATIONS

<u>Figure</u>		<u>Page</u>
1-1	Brayton Cycle Heat Exchanger Technology Program Schedule	2
1-2	HXDA Reference Design Heat Exchangers	5
1-3	HXDA System	6
2-1	HXDA Design Point Conditions	12
2-2	Variation of Mass with Pressure Drop for Recuperator Counterflow Section	13
2-3	Variation of Total Recuperator Mass with Total Recuperator Pressure Drop, Fin Set 1	15
2-4	Variation of Total Recuperator Mass with Total Recuperator Pressure Drop, Fin Set 2	16
2-5	Variation of Total Recuperator Mass with Total Recuperator Pressure Drop, Fin Set 3	17
2-6	Triangular-End Recuperator Geometry	19
2-7	Variation of Total Recuperator Mass with Total Recuperator Pressure Drop for Optimized Designs	20
2-8	Variation of Frontal Area with Gas Pressure Drop and Fin Diameter for Heat Source Heat Exchanger	23
2-9	Variation of Mass with Gas Pressure Drop and Fin Diameter for Heat Source Heat Exchanger	24
2-10	Recuperator and Heat Source Heat Exchanger Frontal Areas for Several Fin Diameters	25
2-11	Variation of Recuperator and Heat Source Heat Exchanger Mass with Fin Diameter for Matched Gas Face Areas	26
2-12	Variation of Frontal Area with Gas Pressure Drop and Tube Spacing for Heat Source Heat Exchanger	27

ILLUSTRATIONS (Continued)

<u>Figure</u>		<u>Page</u>
2-13	Variation of Mass with Gas Pressure Drop and Tube Spacing for Heat Source Heat Exchanger	28
2-14	Recuperator and Heat Source Heat Exchanger Frontal Areas for Several Tube Spacings	30
2-15	Variation of Recuperator and Heat Source Heat Exchanger Mass with Tube Spacing for Matched Gas Face Areas	31
2-16	Variation of Frontal Area with Gas Pressure Drop and Fins per Cm for Heat Source Heat Exchanger	32
2-17	Variation of Mass with Gas Pressure Drop and Fins per Cm for Heat Source Heat Exchanger	33
2-18	Recuperator and Heat Source Heat Exchanger Frontal Areas for Several Fin Diameters	34
2-19	Variation of Recuperator and Heat Source Heat Exchanger Mass with Number of Fins per Cm for Matched Gas Face Areas	35
2-20	Waste Heat Exchanger Mass Using MIPB Coolant	39
2-21	Waste Heat Exchanger Face Area Using MIPB Coolant	40
2-22	Waste Heat Exchanger Liquid Pressure Drop Using MIPB Coolant	41
2-23	Waste Heat Exchanger Mass Using DC-200 (2.0 CS) Coolant	43
2-24	Waste Heat Exchanger Face Area Using DC-200 (2.0 CS) Coolant	44
2-25	Waste Heat Exchanger Liquid Pressure Drop Using DC-200 (2.0 CS) Coolant	45
2-26	Waste Heat Exchanger Mass Using DC-200 (1.0 CS) Coolant	46
2-27	Waste Heat Exchanger Face Area Using DC-200 (1.0 CS) Coolant	47

ILLUSTRATIONS (Continued)

<u>Figure</u>		<u>Page</u>
2-28	Waste Heat Exchanger Liquid Pressure Drop Using DC-200 (1.0 CS) Coolant	48
2-29	Waste Heat Exchanger Characteristics Using MIPB at 0.935 Effectiveness	50
2-30	Waste Heat Exchanger Characteristics Using NAK-78 Coolant	52
2-31	HSHX-NAK Buffer Zone Concept	65
2-32	Remote Heat Source Heat Exchanger Characteristics in Parallel Flow System (Dimensions for Core only)	66
2-33	Remote Heat Source Heat Exchanger Characteristics in Series Flow System (Dimensions for Core only)	67
2-34	Design Curve Format for Pressure and Inertia Load Allowable Stress	77
2-35	Typical Stress-Strain Cycles Illustrating Two Creep Damage Cases	80
2-36	Allowable Thermal Strain Design Curve Format	81
2-37	Low-Carbon Nickel (Nickel 201) Direct Stress (Strain) Allowable vs Operating Temperature	86
2-38	347 Steel Direct Stress (Strain) Allowable vs Operating Temperature	87
2-39	Hastelloy X Direct Stress (Strain) Allowable vs Operating Temperature	88
2-40	Haynes 25 Direct Stress (Strain) Allowable vs Operating Temperature	89
2-41	Nuclear Brayton-Cycle HXDA Arrangement	90
2-42	Interface Loads	91
2-43	HSHX Transition Piece Detail	93
2-44	Tieplate Thermal Analysis Schematic	95

ILLUSTRATIONS (Continued)

<u>Figure</u>		<u>Page</u>
2-45	Heat Source Heat Exchanger (HSHX)	98
2-46	HSHX Cross Section Through No-Flow Pan	99
2-47	HSHX Cross Section Through Liquid Pan	100
2-48	Plate Temperature Gradient Analysis	103
2-49	Recuperator	105
2-50	Typical Component Temperature and Stress-Strain Behavior	106
2-51	Preliminary Heat Exchanger Mounting System	109
2-52	Comparison of Thermal Provisions and Directions for Load Capability of Planar and Box Type Mounting Bracket Arrays	110
2-53	Bellows Design	112
3-1	Brazing Development Test Module	116
3-2a	Fillet Formation of 0.008 mm Thick Palniro 1 Braze Alloy (Micro 24834)	121
3-2b	Fillet Formation of 0.013 mm Thick Palniro 1 Braze Alloy (Micro 24837)	121
3-2c	Sample Showing Filler Formation of 0.019 mm Thick Palniro 1 Braze Alloy (Micro 24838)	122
3-2d	Sample Showing Braze Joint Configuration of 0.025 mm Thick Palniro 1 Braze	122
4-1	Plate-Fin Core Thermal Loads	126
4-2	Recuperator Test Specimens	128
4-3	Weld-Over-Braze Low Cycle Fatigue Specimen Design	133
4-4	Fatigue Test Apparatus (Page 1 of 2)	136
	Fatigue Test Apparatus (Page 2 of 2)	137

ILLUSTRATIONS (Continued)

<u>Figure</u>		<u>Page</u>
4-5	Assumed True Stress-Strain Cyclic Behavior, Lengthwise Component	139
4-6	Comparison of Recuperator and Hastelloy X Parent Metal Specimens at Room Temperature	144
4-7	Comparison of Recuperator and Hastelloy X Parent Metal Specimens at 1000 K	145
5-1	Heat Source Heat Exchanger Test Specimens	148
5-2	Fatigue Test Apparatus (Page 1 of 2)	156
	Fatigue Test Apparatus (Page 2 of 2)	157
5-3.	Assumed True Stress-Strain Cyclic Behavior, Lengthwise Component	159
5-4	HSHX Parent Metal Cycle Life Summary	164
5-5	Comparison of Parent Metal and Welded Specimens at Room Temperature	165
5-6	Comparison of Parent Metal and Welded Specimens at 1030 K (Continuous 0.33 Hz Cycle Rate)	167
5-7	Grain Structure of Haynes 25 Parent Metal Tested at 1030 K on the 13 cm Mandrel	168
5-8	Comparison of Hastelloy X, Inconel 625, Haynes 25 (L-605), and Haynes 188 at Elevated Temperature	169
6-1	Alternate Low Temperature Braze Alloy Test Specimens	175
6-2	Weld-Over-Braze Low Cycle Fatigue Specimen Design	181
6-3	Plate Fin Test Specimen	183
6-4	Fatigue Test Apparatus (Page 1 of 2)	184
	Fatigue Test Apparatus (Page 2 of 2)	185

ILLUSTRATIONS (Continued)

<u>Figure</u>		<u>Page</u>
6-5	Assumed True Stress-Strain Cyclic Behavior Lengthwise Component	187
6-6	Cycles to Failure vs Plastic Strain Range for 347 Stainless Steel Braze with Palniri and Nicuman 23 (Pan to Header Bar Type)	192

TABLES

<u>Table</u>		<u>Page</u>
2-1	Recuperator Counterflow Section Fin Sets	14
2-2	Comparison of End Section Ratios	18
2-3	Heat Source Heat Exchanger Core Matrix	36
2-4	Waste Heat Exchanger Fin Sets	38
2-5	Comparison of Waste Heat Exchanger Coolants	42
2-6	Performance of MIPB Waste Heat Exchanger at E = 0.95	49
2-7	Waste Heat Exchanger Designs at E = 0.935	49
2-8	Performance of MIPB Waste Heat Exchanger at E = 0.935	51
2-9	HXDA Reference Design Heat Exchangers	54
2-10	Duct Sizes and Pressure Losses	63
2-11	Remote Heat Source Heat Exchanger Design Conditions	64
2-12	Comparison of Parallel Flow and Series Flow Heat Source Heat Exchangers	68
2-13	Fluid Conditions for Mechanical Design	75
2-14	HXDA Material Selection Summary	82
2-15	Material Properties	84
2-16	HSHX Allowable ΔT 's	101
2-17	Typical High Temperature Bellows Design	113
3-1	Burst Pressure, Test Results for Recuperator Test Modules	120
4-1	Test Conditions, Recuperator Structural Evaluation	125
4-2	Plastic Strain Ranges and Material Properties for Recuperator Test Results	141

TABLES (Continued)

<u>Table</u>		<u>Page</u>
4-3	Recuperator Cycle Life Results	143
5-1	Plastic Strain Range and Material Properties	160
5-2	HSHX Cycle Life Results	163
6-1	Test Conditions, Alternate Braze Alloy Structural Evaluation	174
6-2	Plastic Strain Range and Material Properties for Alternate Braze Alloy Test Results	188
6-3	Waste Heat Exchanger Alternate Braze Alloy Evaluation Cycle Life Results	190
6-4	Plate Fin, Alternate Braze Alloy, Burst Test Results	191

ABSTRACT

A preliminary design of the heat exchanger and duct assembly (HXDA) for a 60 kwe, closed loop, Brayton cycle space power system is presented. This system is weight optimized within the constraints imposed by the defined structural and operational requirements. Also presented are the results of several small scale tests, directed to obtaining specific design data and/or the resolution of a design approach for long life Brayton cycle heat exchanger systems.

SECTION I

INTRODUCTION AND SUMMARY

INTRODUCTION

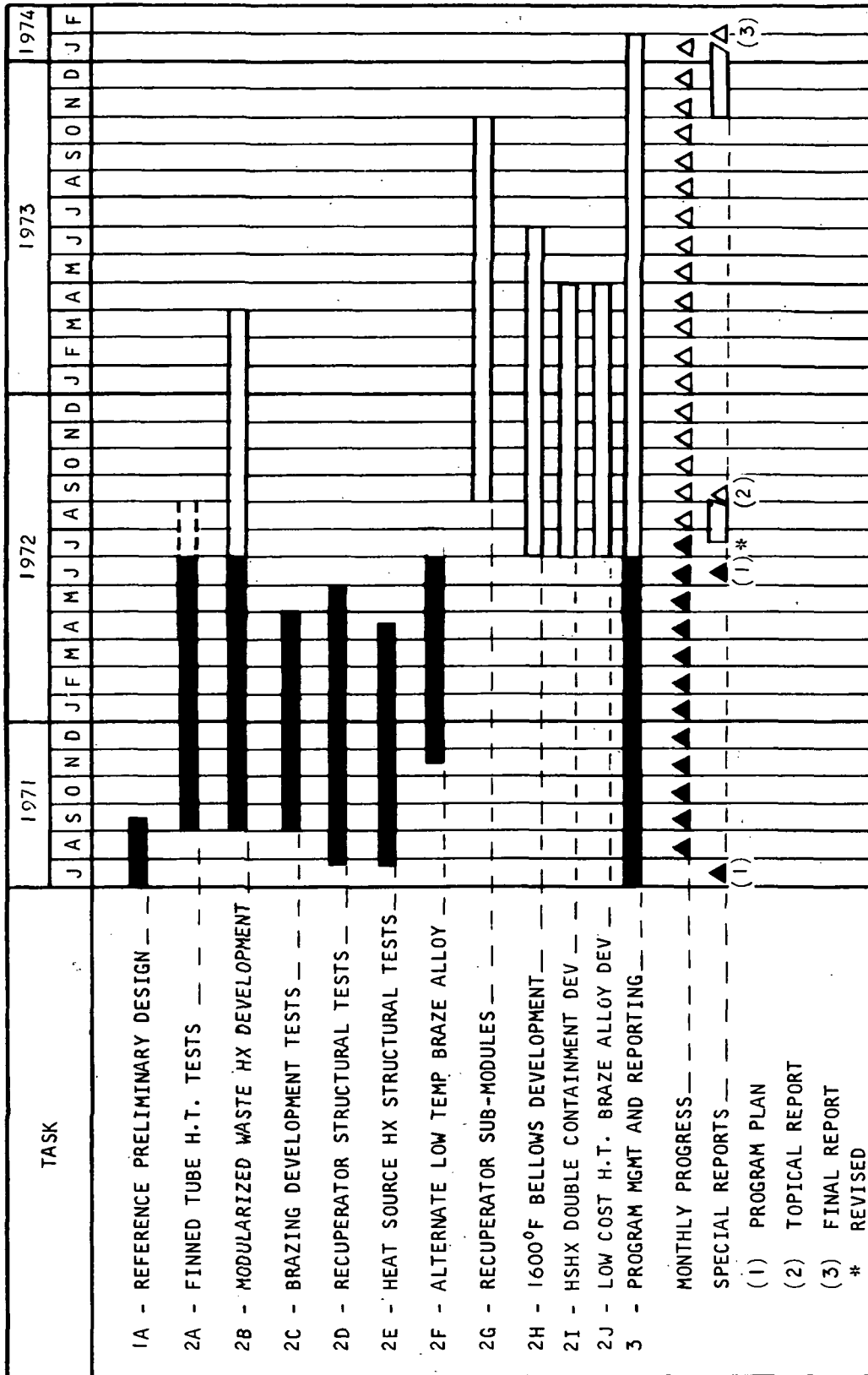
This report presents a summary of a major portion of the work performed by AiResearch for the Lewis Research Center under Contract Number NAS3-15347 from June 1971 through June 1972. This program is a follow-on to the NASA study reported in NASA CR-72783 entitled "Conceptual Design Study of a Nuclear Brayton Cycle Heat Exchanger and Duct Assembly (HXDA)" and NASA CR-72816 entitled "Preliminary Design Study of a Nuclear Brayton Cycle Heat Exchanger and Duct Assembly (HXDA)". In June of 1971, work was initiated on this program which was directed to the design, fabrication, and testing of a heat exchanger and duct assembly suitable for a closed Brayton cycle space power system in the 60 kwe class. The initial phase of this program was the preliminary system design and a series of small scale tests directed to obtaining data and the demonstration of certain design techniques.

In January 1972 the HXDA program was reoriented from the development of a specific power system to a technology program for advanced Brayton-cycle heat exchangers and associated equipment. The detailed design and full-size heat exchanger fabrication efforts were terminated. However, the small scale tests and several fabrication technology tasks were retained. This resulted in the formulation of some twelve work tasks and covers a period of about 2-1/2 years of effort. The program schedule is shown in Figure I-1 in terms of the defined work tasks. The fabrication technology tasks include high temperature bellows studies, heat exchanger double containment techniques, and braze alloy evaluations. Each work task has as its objective the development of design data and/or the resolution of some critical design feature for heat exchanger systems suitable for advanced closed-loop Brayton-cycle power systems.

The work summarized in this topical report consists of the work tasks that have been completed as of June 30, 1972. These work tasks are as follows:

<u>Task No.</u>	<u>Title</u>
1A	Reference Preliminary Design
2C	Brazing Development Tests
2D	Recuperator Structural Tests
2E	Heat Source HX Structural Tests
2F	Alternate Low Temperature Braze Alloy

The remaining tasks will be documented in a final report that will be prepared at the end of the contract period (see Figure I-1).



■ COMPLETED □ SCHEDULED □ RESCHEDULED

S-58828-2

Figure 1-1. Brayton Cycle Heat Exchanger Technology Program Schedule

SUMMARY

Reference Preliminary Design

The design point for the preliminary design of the HXDA was selected by NASA as a result of their studies reported in NASA TMX-67811, by P.T. Kerwin.

The HXDA system was weight optimized within the operational and structural constraints imposed. This required a careful parametric study of the major system components and the selection of component designs to yield a minimum overall system weight.

1. Component Thermal Analysis and Design

The HXDA consists of three heat exchanger components plus interconnecting ducting. The heat exchangers are:

- (1) A gas-to-gas recuperator that transfers waste heat from the turbine exhaust stream to the high pressure gas leaving the compressor
- (2) A liquid-to-gas heat source heat exchanger that transfers heat from either the primary reactor NaK or a secondary NaK loop to the high-pressure Brayton cycle gas
- (3) A gas-to-liquid waste heat exchanger that transfers waste heat from the low-pressure recuperator outlet stream to a suitable liquid in the heat rejection loop

The component thermal design and analysis effort was concerned with the optimization of each of the three heat exchangers to obtain minimum overall size and weight of a system in which the heat exchangers are close-coupled to form a single assembly (HXDA). Secondary consideration was given to decoupling the heat source heat exchanger and locating it in a remote bay area where it could accept heat directly from the primary NaK rather than a secondary NaK loop. The results of the previous preliminary design study, summarized in NASA CR-72816, formed the basis for the starting point of this study by establishing the basic heat exchanger configurational types that are optimum for this system.

The recuperator is a counterflow, plate-fin unit with crossflow triangular end sections, constructed of Hastelloy X. Three separate optimization procedures were utilized in the design of this unit. First, the counterflow section core matrix (fin height, fin thickness, and fin spacing) was optimized to obtain the minimum-weight recuperator design as a function of total counterflow section gas fractional pressure drop. Second, the triangular end section geometry (triangle height and shape) was analyzed to obtain the relationship between weight and pressure drop for minimum-weight end section designs. All end section geometries considered were designed to yield uniform distribution of gas to the counterflow core. Third, the pressure drop split between counterflow section and end sections was selected to give minimum heat exchanger weight

for any given total gas fractional pressure drop. The end result of the recuperator analysis was, thus, a curve of heat exchanger weight as a function of pressure drop based on optimized core geometry, end section geometry, and pressure drop split.

The heat source heat exchanger is a two-pass, cross-counterflow, finned-tubular unit of Haynes tubes and copper-stainless laminate fins. The fins are spiral wound on the tubes to form, in effect, a disc-finned tubular matrix. The core matrix geometry (fin diameter, fins/cm, and tube spacing) was optimized to obtain minimum combined weight of recuperator and heat source heat exchanger. The optimization procedure was based on a gas pressure drop split between recuperator and heat source heat exchanger for each different core matrix that yielded equal areas of the matching faces of these two units. Thus, the end result of this analysis was a definition of both the optimum core geometry for the heat source heat exchanger and the optimum pressure drop split between recuperator and heat source heat exchanger.

The waste heat exchanger is a seven-pass cross-counterflow, plate-fin unit of stainless steel construction and nickel fins. The core matrix geometry (fin height and fins/cm) was weight optimized, subject to the constraint of a 103 kN/sq m maximum liquid pressure drop. A comparison of heat exchanger designs based on the use of MIPB, DC-200 (1.0 cs), and DC-200 (2.0 cs) as the heat rejection fluids indicated that the unit with MIPB was 38 percent larger than either DC-200 unit, the primary reason being the relatively rapid increase of specific heat with temperature for MIPB, an effect detrimental to heat transfer performance. To reduce waste heat exchanger size, the initial design goal thermodynamic effectiveness of 0.95 was reduced to 0.935. The resultant heat exchanger design, sized for use with MIPB, yields effectivenesses of 0.947 and 0.948 with DC-200 (1.0 cs) and DC-200 (2.0 cs), respectively. A finned-tubular heat exchanger using NaK as the heat rejection fluid was also sized for this application, but the resultant design was not competitive on the basis of size or weight with the organic unit.

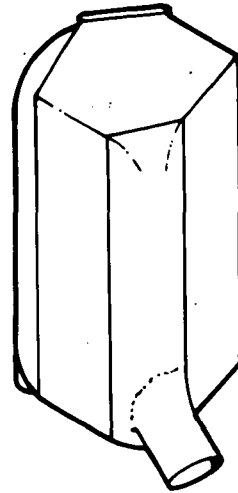
2. System Design

The heat exchanger designs are summarized in Figure 1-2 and the HXDA is shown in Figure 1-3. These two figures define the HXDA design in which the heat source heat exchanger is close-coupled to the recuperator. Gas ducting and manifold sizes are based on a ducting and manifold pressure loss of 0.5 percent. Total HXDA pressure loss is 3.0 percent including the ducts.

A preliminary analysis was made of a system in which the heat source heat exchanger is located remotely and accepts heat directly from the primary NaK circuit. To ensure separation of the radioactive primary NaK from the gas system, the heat source heat exchanger design in this system incorporates double tubes and headers with an interior buffer zone and provision for sensing leakage from either the gas or NaK circuit into this zone.

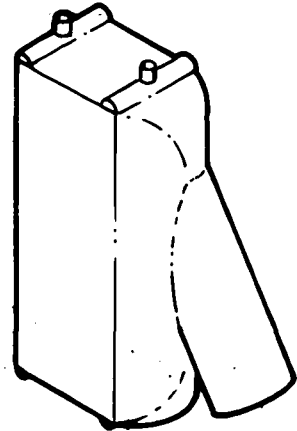
RECUPERATOR

Gas pressure drop	1.15 percent
Mass	382 kg
Core length	0.295 m
End section height, hot end	0.164 m
cold end	0.0876 m
End section ratio, hot end	0.65
cold end	0.573
Width	0.524 m
Stack height	1.05 m



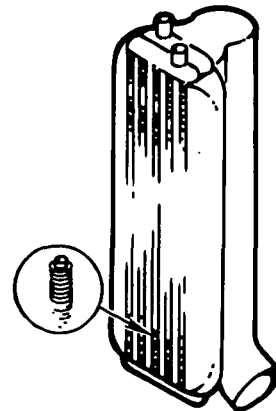
WASTE HEAT EXCHANGER

Gas pressure drop	0.90 percent
Mass (wet)	260 kg
Liquid pressure drop	103 kN/sq m
Gas-flow length	0.403 m
Liquid-flow length	1.06 m
Stack height	0.320 m



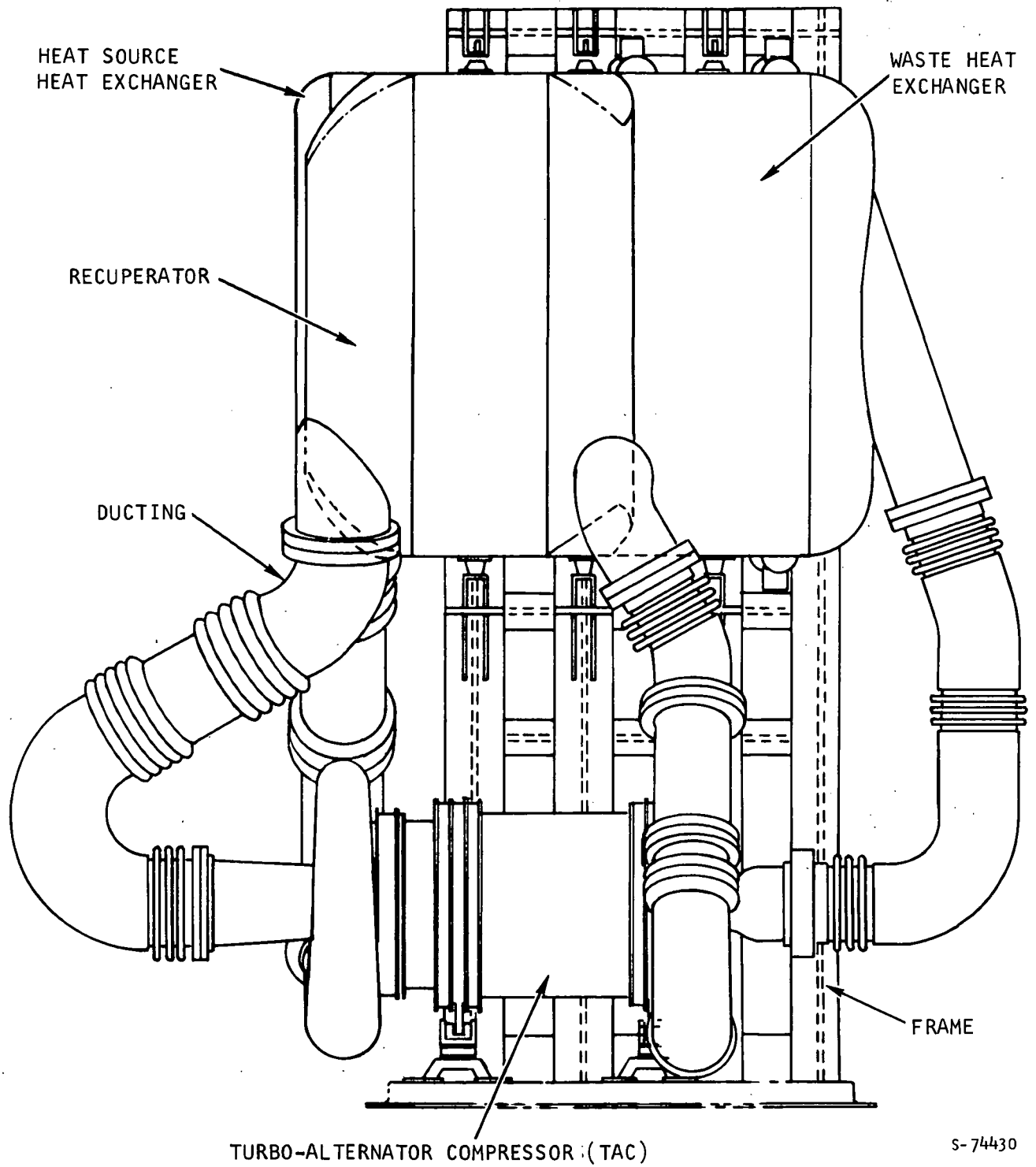
HEAT SOURCE HEAT EXCHANGER

Gas pressure drop	0.45 percent
Mass (wet)	73 kg
Liquid pressure drop	5.1 kN/sq m
Gas-flow length	0.143 m
Tube length (core)	1.06 m
No-flow length (core)	0.243 m
Number of tubes	92
Number of tube rows	8
Number of passes	2



S-74438

Figure 1-2. HXDA Reference Design Heat Exchangers



S-74430

Figure 1-3. HXDA System

3. Structural Considerations

Major considerations in the reference preliminary design have been given to achieve the following structural capabilities:

- (1) 100,000 hr life at sustained maximum fluid conditions with a 50 K overtemperature capability.
- (2) 24g longitudinal and 20g transverse loading capability with no excessive deformations or premature fatigue failures.
- (3) Pressure containment at sustained maximum fluid conditions with a 1.5 proof and a 2.5 burst pressure capability.
- (4) 1000 thermal cycles of operation insured by limiting the analytical thermal strains to a corresponding 4000 cycle life requirement.

The above capabilities are insured by formulating two composite design curves which display (1) allowable stress vs operating temperature, and (2) allowable thermal strain vs operating temperature for the selected materials. The material yield strength, ultimate strength, and ductility govern the low temperature region and material creep dominates the elevated temperature portion of the composite design curves. Following this approach, design curves are presented for Nickel 201, 347 steel, Hastelloy X, and Haynes 25. Based upon the allowable stresses and strains found in the design curves, structural members are sized and temperature differences established which will provide the structural capabilities outlined above.

The heat source heat exchanger design analysis is performed with emphasis on the recuperator interface area since this is considered the most critical area where structural considerations would impair the recuperator operating capability. Interface loading is considered and the severe temperature difference between the HSHX core and the recuperator high pressure outlet leads to the requirement for a transition piece design to control thermal loading. Allowable temperature differences are established within the HSHX and the recuperator structures. A survey of the allowable temperature differences required within the heat exchanger design shows that this constraint is realistic and the cyclic life objective is attainable. However, the limited scope of the reference preliminary design does not provide sufficient definition of the temperature distribution to determine specific component cyclic-life capabilities. Results of the preliminary design analysis indicate that the most critical areas for consideration of structural integrity are: (1) the transition piece between the HSHX core and the recuperator high-pressure outlet, (2) tierod-to-plate joints between the HSHX and the recuperator, (3) recuperator pan-to-heat exchanger core joint, and (4) the recuperator sheet-to-header bar interface.

A preliminary heat exchanger mount system was selected with the planar type structure being preferable to the box type. The ducting system was selected with link-type convolute bellows in each section to control flange loading. A typical high temperature bellows design is presented to show appropriate convolute shape and duct length requirements.

Brazing Development Tests

The recuperator and waste heat exchanger of the HXDA are brazed with the gold base braze alloy, Palniro-1. This braze alloy is very expensive and it is highly desirable to minimize the foil thickness to reduce the cost and weight of the heat exchangers. To this end, plate-fin test modules were brazed in a vacuum furnace with Palniro 1 braze foil thicknesses from 0.008 mm to 0.019 mm and tested to compare braze flow characteristics, braze alloy filleting characteristics, and room temperature short term burst capabilities. Photomicrographics of the completed test modules show a significant improvement in filleting characteristics as braze alloy thickness was increased and adequate braze flow characteristics were evident for all test modules.

Test results from the 0.019 and 0.013 mm braze foil test modules show that a 25 percent reduction of braze alloy only reduces the short term pressure containment capabilities by 10 percent with reasonable filleting characteristics. Further reduction of braze foil thickness to 0.008 mm did not show a drastic reduction of short term pressure containment capability but braze filleting was almost nonexistent. Therefore, the brazing development tests show potential for the use of braze foil thicknesses in the range of 0.013 to 0.025 mm as a cost and weight savings measure. Future testing should be performed on test modules fabricated from 0.013 mm braze foil to obtain creep rupture and low-cycle fatigue design data.

Recuperator Structural Tests

Small scale tests were undertaken to establish the cyclic thermal strain capability of two critical recuperator fabrication areas: (1) the pan-to-heat exchanger core joint, and (2) the sheet-to-header bar interface. These areas typically experience severe thermal strains due to temperature differences developed during transient heating conditions associated with each duty cycle.

Test specimens simulating the joints were fabricated from Hastelloy X and subjected to strain-controlled cyclic testing. Fatigue failures were initially produced at room temperature to obtain basic low-cycle fatigue data which could be compared with parent metal and plate-fin testing performed under NASA Contract NAS 1-5002. Specimen fatigue failures were repeated at 1000 K to obtain cyclic life where creep damage is sustained during each load cycle because the recuperator is required to operate at 955 K.

Results of the room temperature tests show that the sheet-to-header bar specimens will provide approximately 70 percent of the parent metal cyclic strain capability obtained in previous tests. This reduction in cyclic strain capability is attributed to the presence of braze alloy. The room temperature pan-to-header bar specimens showed a further 15 percent reduction in cyclic strain capability. The comparable plate-fin data from previous testing shows the lower cyclic strain capability. This further reduction in fatigue strength was primarily attributed to the offset-fin geometry which is unique to the plate-fin test specimens.

The elevated temperature test results compare similarly; however, the slope of the life cycle curve is different for each specimen pointing to the need for further evaluation of cyclic creep damage accumulated at the required operating temperature.

Heat Source Heat Exchanger Structure Tests

Small scale tests were undertaken to verify the low-cycle fatigue properties of the candidate materials selected in the preliminary design of the heat source heat exchanger (HSHX). Test specimens were designed and fabricated to simulate the use of Haynes 188 or Haynes 25 in the following metallurgical conditions as required in HSHX fabrication:

Simple parent metal bars with no welds

Parent metal bars with a weld joint

Parent metal/Hastelloy X bimetallic welded bars

All test specimens were subjected to a pre-test accelerated life vacuum exposure for 100 hr at 1140 K. This thermal aging cycle is intended to simulate operating exposure in a vacuum at a temperature of 977 K for times up to the 100,000 hr design life. Under strain-controlled cyclic load conditions, fatigue failures were initially produced in each of the specimen types at room temperature to obtain basic low-cycle fatigue data. Fatigue failures were repeated at 1030 K to obtain comparative cyclic fatigue data with imposed overtemperature conditions because the heat source heat exchanger is required to operate at 977 K. In addition to these tests, separate specimens consisting of simple parent metal bars were subjected to an elevated temperature cyclic load profile which included a 5 min hold time. The addition of a sustained load duration within each test cycle is intended to provide a qualitative measure of fatigue strength degradation associated with combined load conditions.

Results of the parent metal testing shows that Haynes 188 provides superior room temperature cyclic fatigue capability. The elevated temperature test results, however, show that Haynes 188 and Haynes 25 will provide similar low-cycle fatigue capabilities. Test results from the welded specimens show that the welding process significantly reduces low-cycle fatigue capability. The percentage degradation of parent metal cyclic strain capability for Haynes 188 was found to be 32 percent in the standard weld specimens and 52 percent in the bimetallic weld specimen as a result of the elevated temperature testing. Identical testing of the Haynes 25 weld specimens showed a comparatively smaller 14 percent degradation of cyclic strain capability due to the standard weld and a comparatively similar 45 percent degradation due to the bimetallic weld.

As a result of the HSHX structure tests, it was concluded that either Haynes 188 or Haynes 25 will provide acceptable material for use in fabricating the heat source heat exchanger. Results of the testing clearly indicate that the weld process significantly impairs low-cycle fatigue properties and the parent metal allowable cyclic strain should be reduced by approximately 50 percent for use in establishing the 1000 cycle life objective in the fabricated heat source heat exchanger.

Alternate Low Temperature Braze Alloy Tests

The objective of these tests was to select a low cost, ductile braze alloy suitable for use in fabrication of the waste heat exchanger as an alternate to the costly Palniro 1 braze alloy. Alternate ductile braze alloys were suggested based on the results of a company sponsored IR&D evaluation. Several alloys, such as Nicuman 23 and AMI-176HP-C, have similar properties and brazing characteristics. Nicuman 23 was selected for use in the cyclic life and rupture test specimen because of its acceptable performance and its availability in foil form.

Small specimen sections of the waste heat exchanger plate fin core were fabricated using the alternate braze alloy and short term burst tests were performed on these specimens. Results of the burst testing at the waste heat exchanger temperature level (640 K) shows acceptable pressure containment capability. Furthermore, the reduction in room temperature burst strength at temperature correlates with the reduction of parent metal tensile strength thus eliminating the need for creep rupture testing.

Low-cycle fatigue test specimens were fabricated to simulate the waste heat exchanger pan-to-header bar joint with and without a weld pass over the Nicuman 23 braze joint. Test results from the brazed specimens indicate adequate cyclic life is attainable and no significant degradation need be associated with elevated temperatures less than 640 K. Fabrication of the brazed and welded test specimens gave indications of weld bead cracking. Metallographic examination of various weld specimens indicated that a better weld resulted from the pulse-arc welding procedure than the normal TIG welding procedure. However, random failures exhibited by the test specimens regardless of the weld procedure indicated that the problem was associated with the test specimen design. A revised test specimen design was accomplished to eliminate the cracking problem but fabrication and testing of the revised design were not included in the scope of this task.

Nicuman 23 is structurally adequate as an alternate braze alloy for use in the waste heat exchanger environment, however, acceptability of the weld-over-braze joint design was not determined and testing of the redesigned test specimen is required to verify the use of the superimposed weld.

Experience gained on welding the low-cycle fatigue bars indicates that additional handling procedures would be required in welding a large core that was brazed with the Nicuman 23 braze alloy. In addition to using the nickel weld filler wire to weld over the Nicuman 23 braze alloy, the welding must be accomplished in an inert (argon) atmosphere to minimize the oxidation associated with using a high manganese containing braze alloy.

SECTION 2

SYSTEM PRELIMINARY DESIGN

INTRODUCTION

In this section, the work performed for the preliminary design of the HXDA and HXDA components is summarized. The effort is described under three major subheadings entitled Component Thermal Analysis and Design, System Design, and Structural Design and Analysis. The design point conditions for the HXDA system are summarized in Figure 2-1. The preliminary design was concerned with the weight optimization of the HXDA system within the constraints imposed by the defined structural and operational requirements. The optimization was based on a close-coupled HXDA with matched heat exchanger faces, i.e., the waste heat exchanger and the heat source heat exchanger were constrained to closely match the respective recuperator face areas to allow the construction of a close coupled heat exchanger package. In addition, as the program progressed, several variations of the system were investigated, such as several organic coolants for the waste heat exchanger loop, NaK heat exchangers for the heat source heat exchanger, etc. These items, integrated into the text where they fit most logically, represent variations to the baseline HXDA system defined in Figure 2-1.

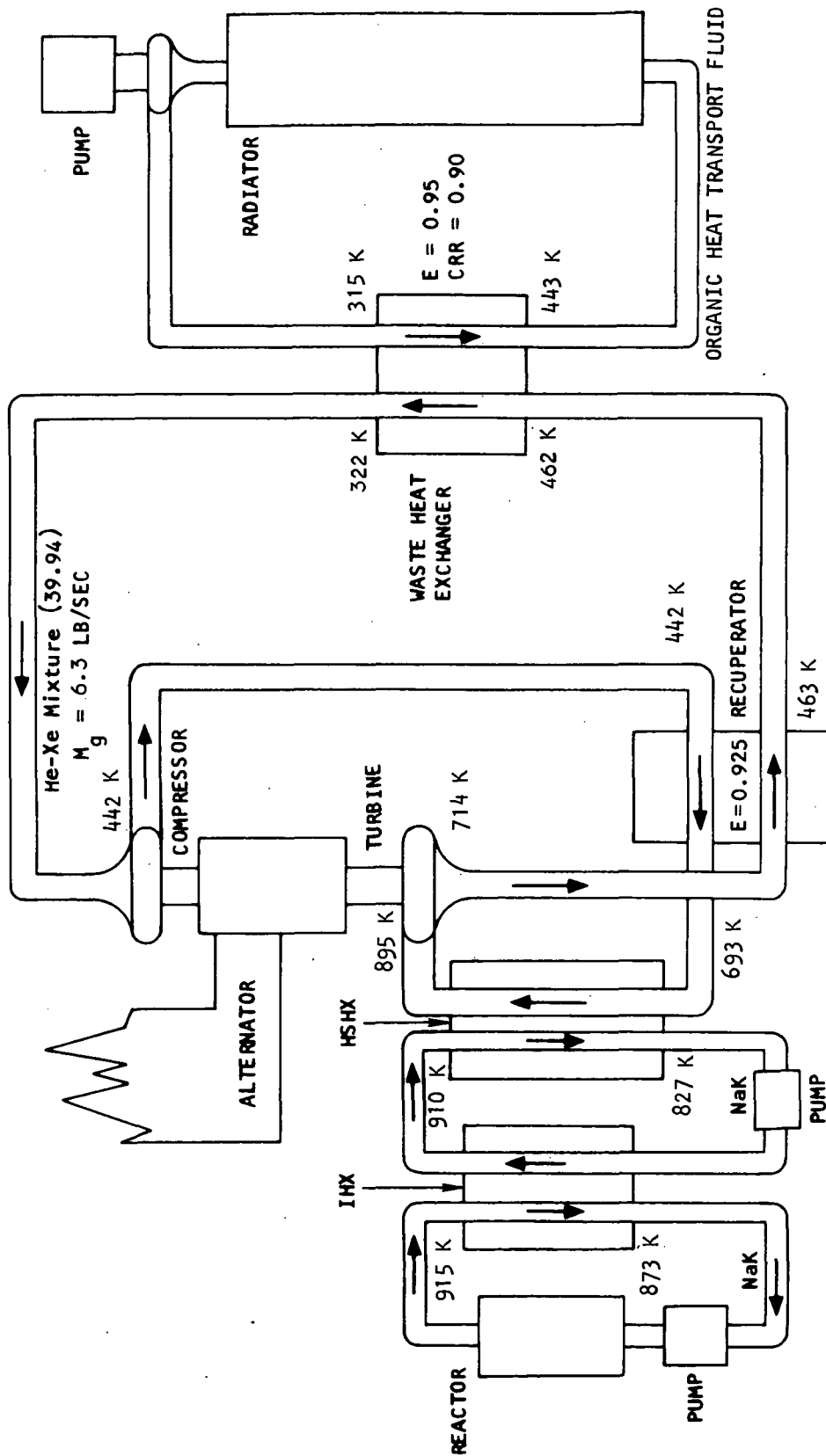
COMPONENT THERMAL ANALYSIS AND DESIGN

Recuperator

1. Counterflow Section

To determine the optimum recuperator core matrix for the new set of HXDA design conditions, a series of plate-fin counterflow cores was sized as a function of gas fractional pressure drop using three different fin sandwich geometries. The fin combinations analyzed were those found to yield the lowest recuperator weights during the previous HXDA design study. Because of the decrease in gas pressure level for the current design, it was expected that the optimum core matrix would shift toward a less compact fin configuration for the new HXDA and a new optimization study was required to establish the optimum fin set.

The fin sets analyzed are listed in Table 2-1 and the corresponding counterflow section weights are shown as a function of gas fractional pressure drop in Figure 2-2. The weights were calculated using (1) the minimum standard-gauge fin thicknesses required for pressure containment on both the high pressure and low pressure sides, and (2) the minimum standard-gauge fin thickness on the high pressure side and a fin thickness 0.00508 cm thicker than minimum gauge on the low pressure side. The fin thickness was increased on the low pressure side only because, in all cases, the low pressure side is both the minimum conductance side and the side with the lower fin efficiency. A comparison of counterflow section weights resulting from the two different fin thickness assumptions indicates that the minimum fin thickness required for structure is, in all cases, the optimum thickness on a weight basis. Further analyses, therefore, were based on the use of minimum-thickness fins.



COMPRESSOR INLET PRESSURE - 35.8 KN/SQ M
 COMPRESSOR OUTLET PRESSURE - 696 KN/SQ M
 TURBINE OUTLET PRESSURE - APPROXIMATELY 367 KN/SQ M

MECHANICAL DESIGN PRESSURES

- 1380/827 KN/SQ M AT 1145 K CONDITIONS

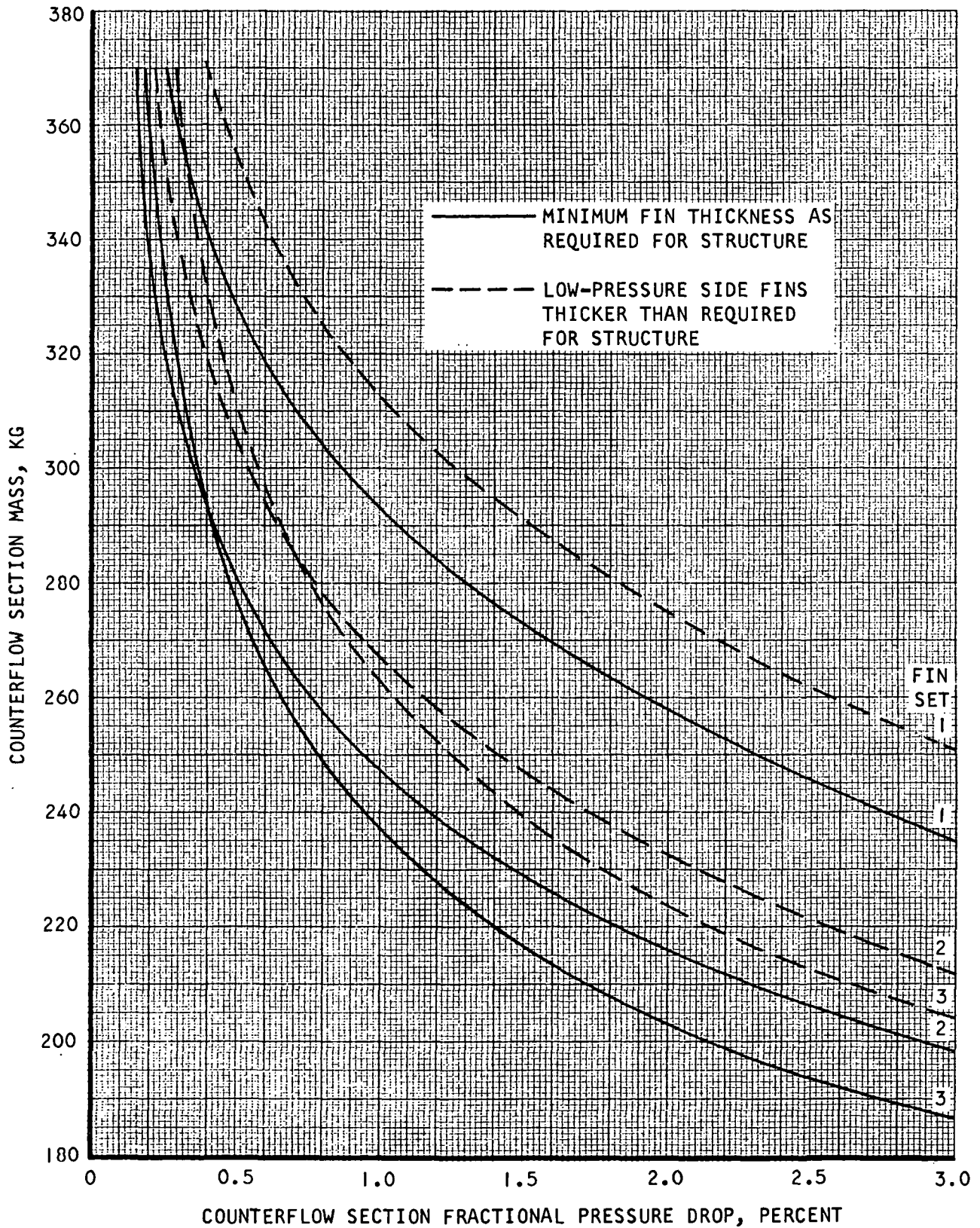
HSX DESIGN TEMPERATURE

- 980K

$\left(\frac{\Delta P}{P}\right)_{HXDA} = 0.03 \text{ (HEAT EXCHANGER AND DUCTS)}$

S-64174 -A

Figure 2-1. HXDA Design Point Conditions



S-64993

Figure 2-2. Variation of Mass with Pressure Drop for Recuperator Counterflow Section

The recuperator material is Hastelloy X for all cases. The weight calculations are based on a tube plate thickness of 0.0203 cm, a side bar/side plate thickness of 0.254 cm, and top and bottom plates of 0.152 cm. The cores were sized using AiResearch computer program H1010A, which accounts for the effect of axial conduction of heat in the heat exchanger matrix. For fin set 2 at a pressure drop of 0.5 percent, the UA increase required to compensate for axial conduction was 4.2 percent, which may be compared with a value of 2.6 percent for the same fin set at the previous design study cycle conditions.

TABLE 2-1
RECUPERATOR COUNTERFLOW SECTION FIN SETS

Fin Set	Low-Pressure Side			High-Pressure Side		
	Fins/cm	Fin Ht (cm)	Min Gauge Fin Thick (cm)	Fins/cm	Fin Ht (cm)	Min Gauge Fin Thick (cm)
1	6.30	0.389	0.0102	6.30	0.318	0.0203
2	6.30	0.318	0.0102	7.88	0.254	0.0152
3	7.88	0.254	0.0102	7.88	0.190	0.0152

2. End Sections

During the HXDA design study previously completed, the use of triangular end sections for fluid manifolding was found to yield lower weight systems than could be obtained with the use of rectangular end sections for this purpose. This was due both to the lower recuperator weights associated with triangular ends and to better face area matches obtained with the triangular geometry. Based on those results, the triangular end section geometry was selected for the current HXDA design effort.

To obtain an optimum pressure drop split between the recuperator counterflow core and the triangular end sections, a series of end section designs was calculated as a function of pressure drop for each counterflow section fin set of Table 2-1 at each of several counterflow section pressure drops. The calculations were performed using AiResearch computer program H1440, which computes end section geometries yielding uniform core flow distribution. The end sections utilize plain rectangular-fin sandwiches with 3.94 fins/cm of minimum standard gauge consistent with the strength required for pressure containment.

Results of the end section optimization study are shown in Figures 2-3 through 2-5. In each of these figures the total of recuperator counterflow section and end section weights is plotted as a function of total pressure

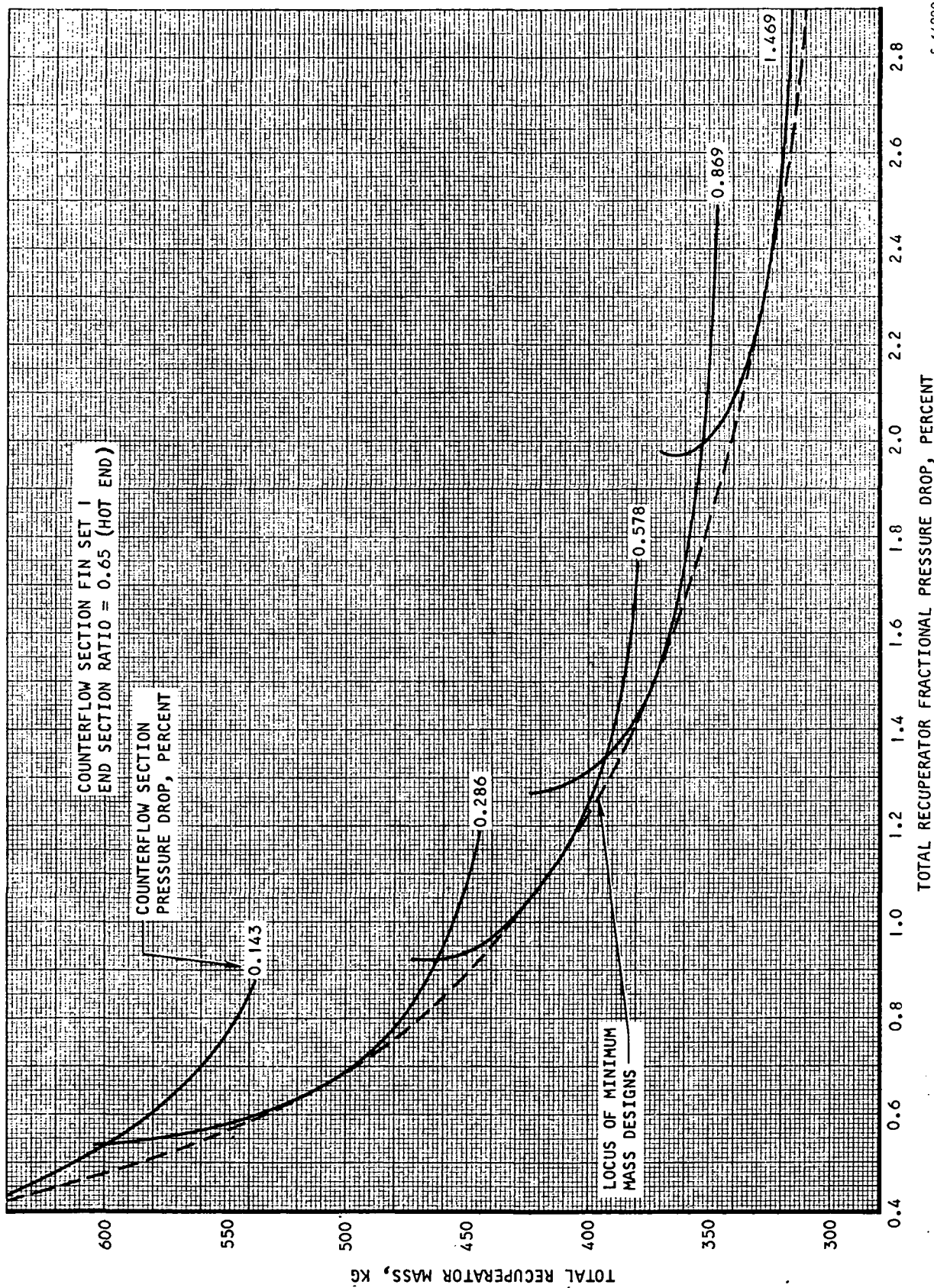


Figure 2-3. Variation of Total Recuperator Mass with Total
Recuperator Pressure Drop, Fin Set I

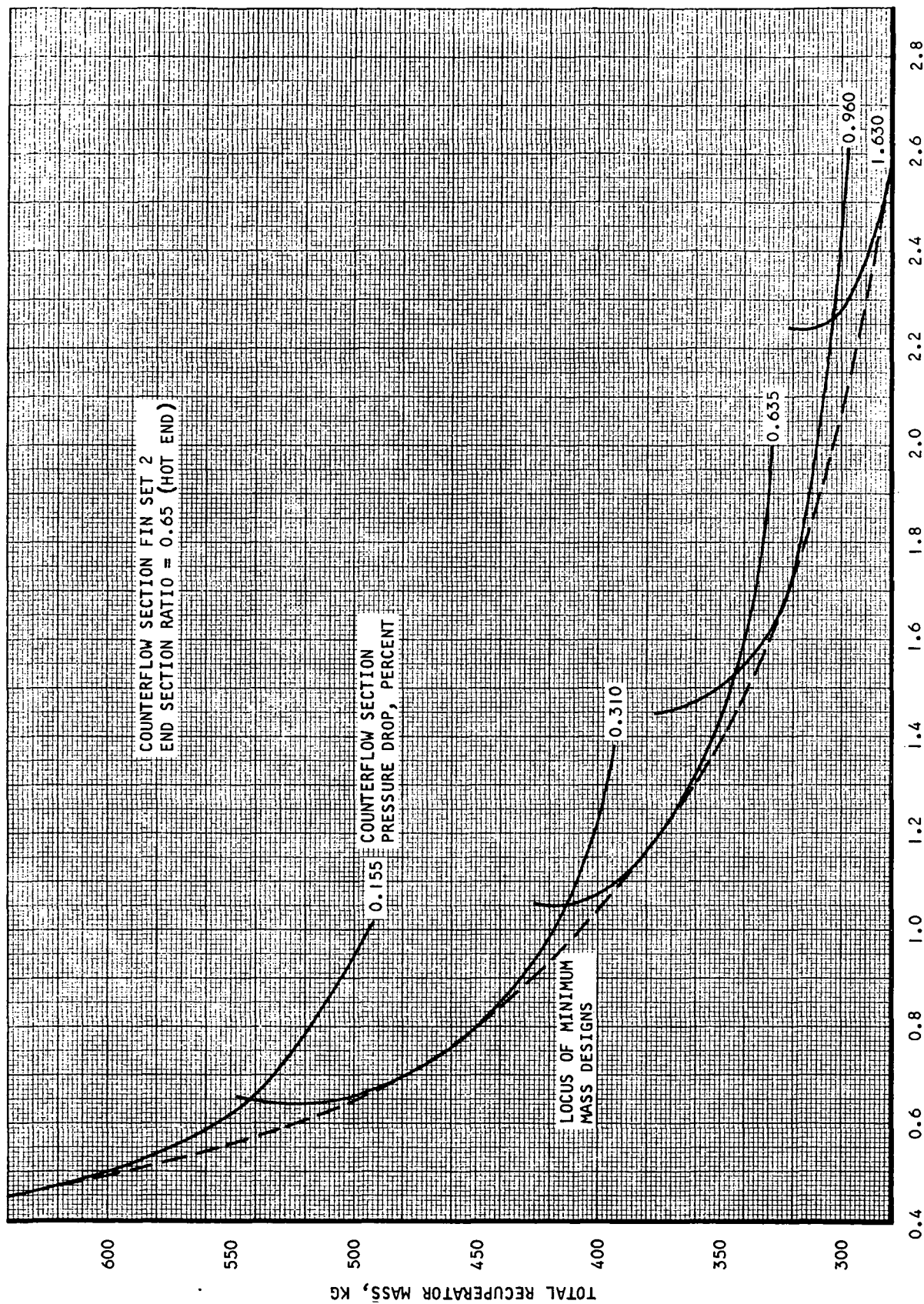
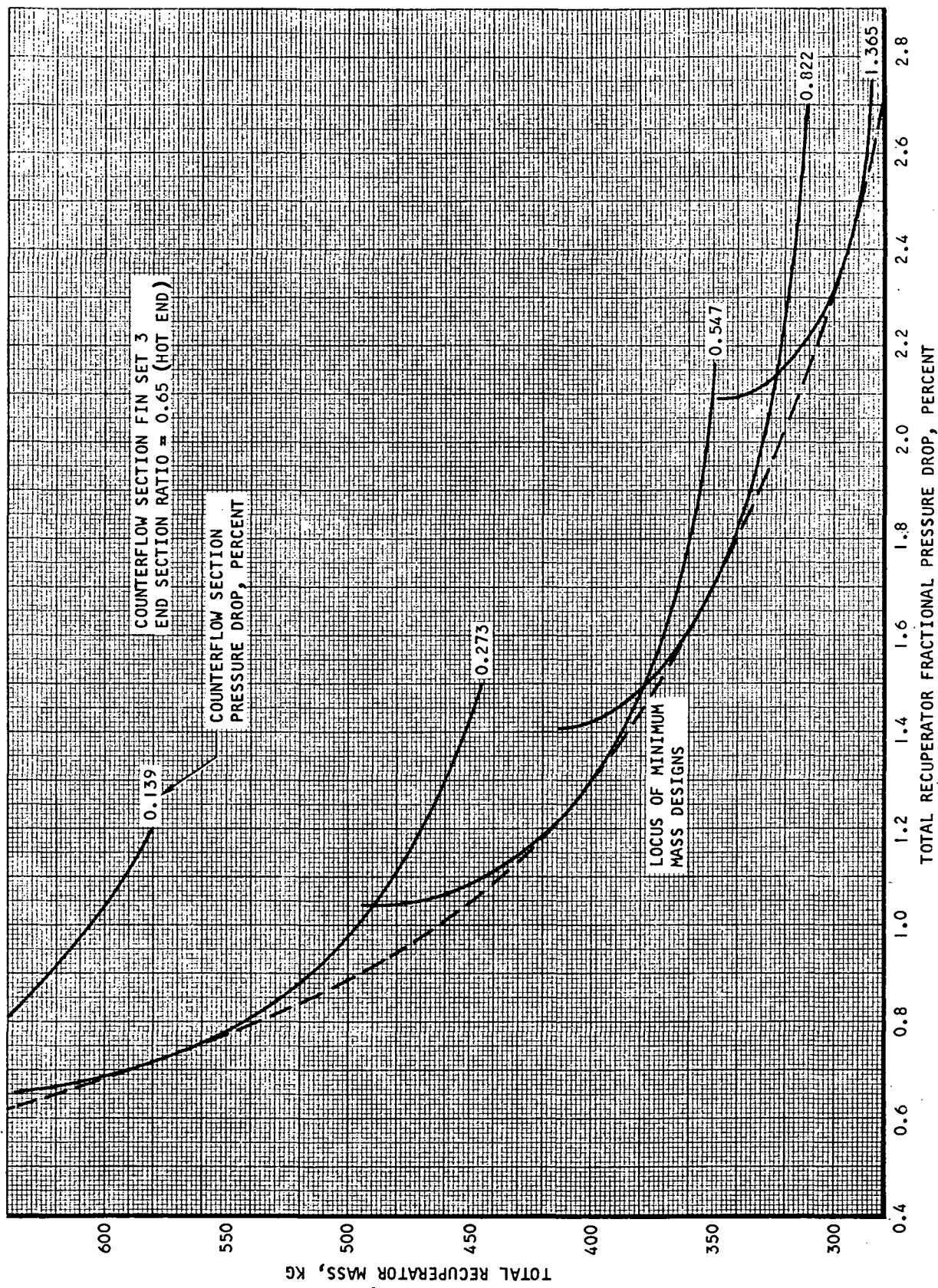


Figure 2-4. Variation of Total Recuperator Mass with Total
Recuperator Pressure Drop, Fin Set 2

S-64991



S-64992

Figure 2-5. Variation of Total Recuperator Mass with Total Recuperator Pressure Drop, Fin Set 3

drop for fixed values of the counterflow section pressure drop. The dashed line drawn tangent to the curves represents the locus of minimum-weight recuperator designs (i.e., each point on the dashed line corresponds to an optimum pressure drop split between recuperator counterflow core and end sections). The analysis was based on a hot-end end section $RATIO$ (ratio of projected end section low-pressure side width to counterflow section width, as shown in Figure 2-6) of 0.65 but would be essentially the same for any value of $RATIO$ from 0.60 to 0.75. This is illustrated in Table 2-2, where end section pressure loss and weight are compared for four values of hot-end $RATIO$. The comparison is based on fin set 2 in the counterflow section, a counterflow section pressure drop of 0.635 percent, and a hot-end end section height of 15.2 cm. The cold-end end section height and $RATIO$ are required values for uniform core flow distribution.

TABLE 2-2
COMPARISON OF END SECTION RATIOS*

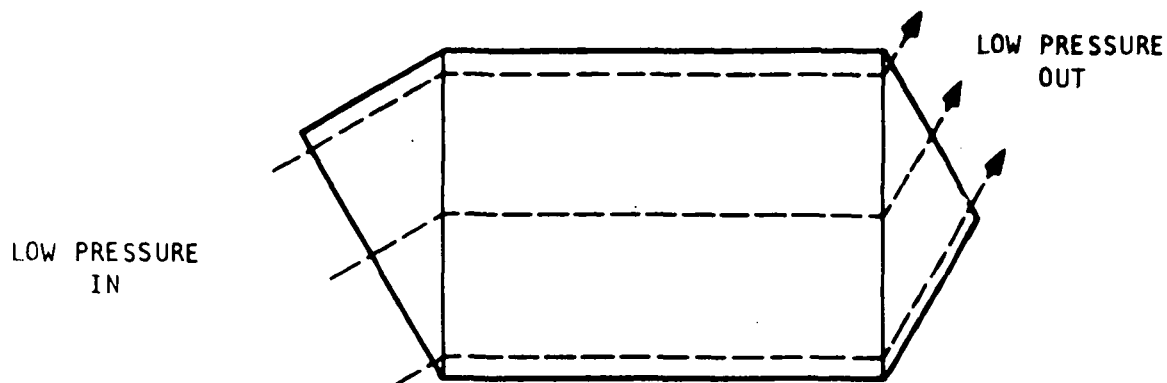
Hot-End End Section		Cold-End End Section		Total End Section	
Height, cm	Ratio	Height, cm	Ratio	$\Delta P/P$, percent	Mass, kg
15.2	0.60	8.60	0.550	0.562	107
15.2	0.65	8.55	0.575	0.563	106
15.2	0.70	8.96	0.612	0.538	108
15.2	0.75	8.88	0.650	0.558	108

*Counterflow section fin set 2
Counterflow section pressure loss = 0.635 percent

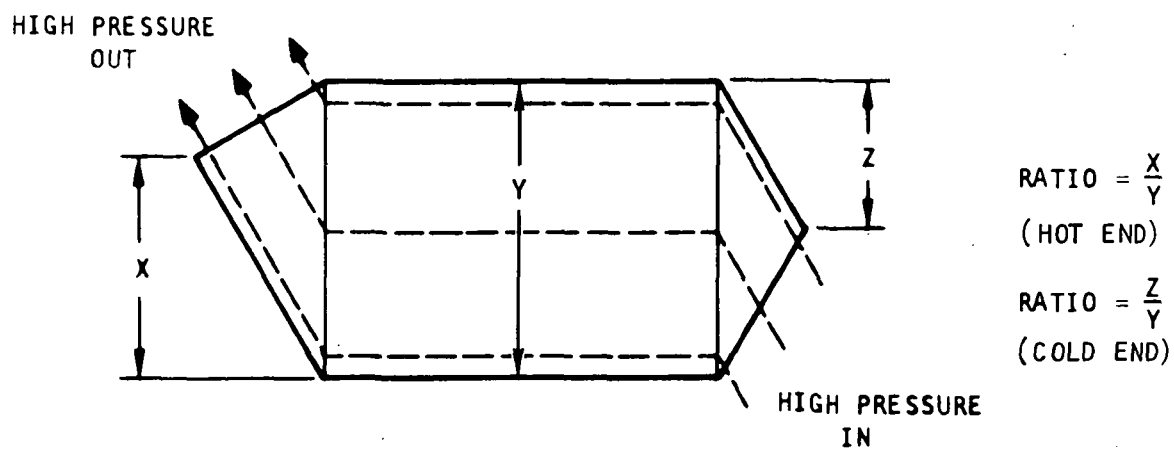
Total recuperator weights, including counterflow and end sections, are summarized in Figure 2-7. Fin set 2 yields the minimum-weight recuperator over the total pressure drop range of interest. Further studies were, therefore, limited to the use of this core matrix in the recuperator.

Heat Source Heat Exchanger

An initial study was conducted to optimize the heat source heat exchanger core matrix. The optimum matrix obtained from this study is the matrix to be used for the small-scale finned-tube heat transfer test. Further refinement of the core geometry will then be possible, based on the results of the small scale tests.



a. Low-Pressure Side Fin Sandwich



b. High-Pressure Side Fin Sandwich

S-62855 -A

Figure 2-6. Triangular-End Recuperator Geometry

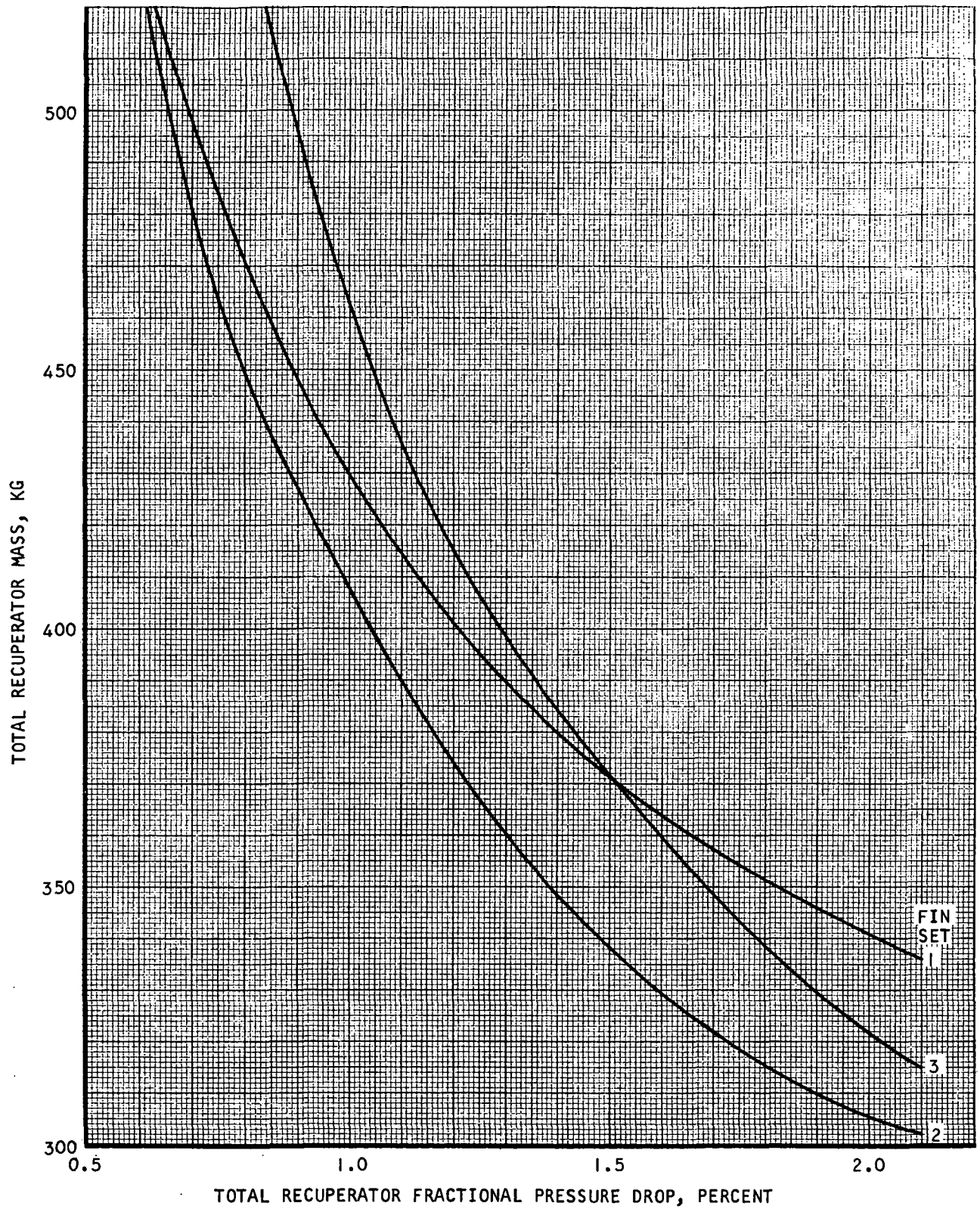


Figure 2-7. Variation of Total Recuperator Mass with Total Recuperator Pressure Drop for Optimized Designs

S-64994

During the HXDA study program, the finned-tubular unit was identified as optimum for the heat source heat exchanger. This configuration yields a highly efficient and compact heat transfer matrix while satisfying the structural and materials problems associated with high-temperature containment of the liquid metal coolant. The fins for this matrix consist of strips of a copper-stainless laminate helically wound on the tubes to form, in effect, a disc-finned tubular geometry. The copper-stainless laminate (0.00762 cm copper, 0.00508 cm stainless) provides both the high conductivity required for efficient heat transfer and the necessary strength at the heat source operating temperature. A final selection of the tube material was not made at this time, but the choice of tube material does not significantly affect the heat transfer design of the core. For present purposes, Haynes 25 or 188 is assumed as the material of construction throughout the heat exchanger. Other core parameters established during the HXDA study program and used here include a tube OD of 1.27 cm and a tube wall thickness of 0.508 cm.

To determine the optimum heat source heat exchanger matrix with respect to the overall system, consideration must be given not only to the weight of the heat source heat exchanger, but also to the effect that face area matching of the heat source unit to the recuperator has on system pressure drop allocations and thus on the weights of other system components.* To facilitate this analysis, it was assumed that the total pressure drop required for the ducting system and waste heat exchanger is 1.40 percent (1.44 percent was the allocation to these components as determined in the previous study program), leaving 1.60 percent for the total of recuperator and heat source heat exchanger pressure drops. Since the previous studies on this system indicated that the pressure drop required in the heat source unit for face area matching with the recuperator was considerably greater than the pressure drop for minimum system weight, the optimum matrix represents a compromise between minimum unit weight and minimum unit frontal area.

Three core parameters were varied to obtain the optimum heat exchanger matrix. These are fin diameter, transverse tube spacing, and number of fins per cm.

1. Fin Diameter

The ratio of fin diameter to tube diameter was varied between 1.3 and 1.7. The variations of frontal area and wet weight with gas fractional pressure drop for several fin diameters in this range are shown in Figures 2-8 and 2-9. The tube arrangement used during this analysis was an equilateral triangular array with a minimum clearance of 0.127 cm between fin tips on adjacent tubes. The use of minimum clearance between finned tubes results in a minimum-volume heat exchanger, which minimizes exchanger wrap-up weight.

*This study was based exclusively on the use of a heat source heat exchanger that could be close-coupled to the recuperator; thus, matching of the heat source heat exchanger gas face to the recuperator high-pressure outlet face was required.

Two-pass and four-pass units were calculated and the two-pass units were chosen on the basis of heat exchanger aspect ratio. The required aspect ratio of the gas face (tube length \div no-flow length) for mating with the recuperator high-pressure outlet face is approximately 4:1 (corresponding to a recuperator counterflow section aspect ratio of 2:1); and this could not be obtained with a four-pass unit within the allowable NaK pressure drop of 34.4 kN/sq m. With the two-pass unit, a NaK pressure drop of 6.89 kN/sq m gave approximately the required aspect ratios and was therefore used for all of the curves of Figures 2-8 and 2-9. The variation of weight with NaK pressure drop was insignificant.

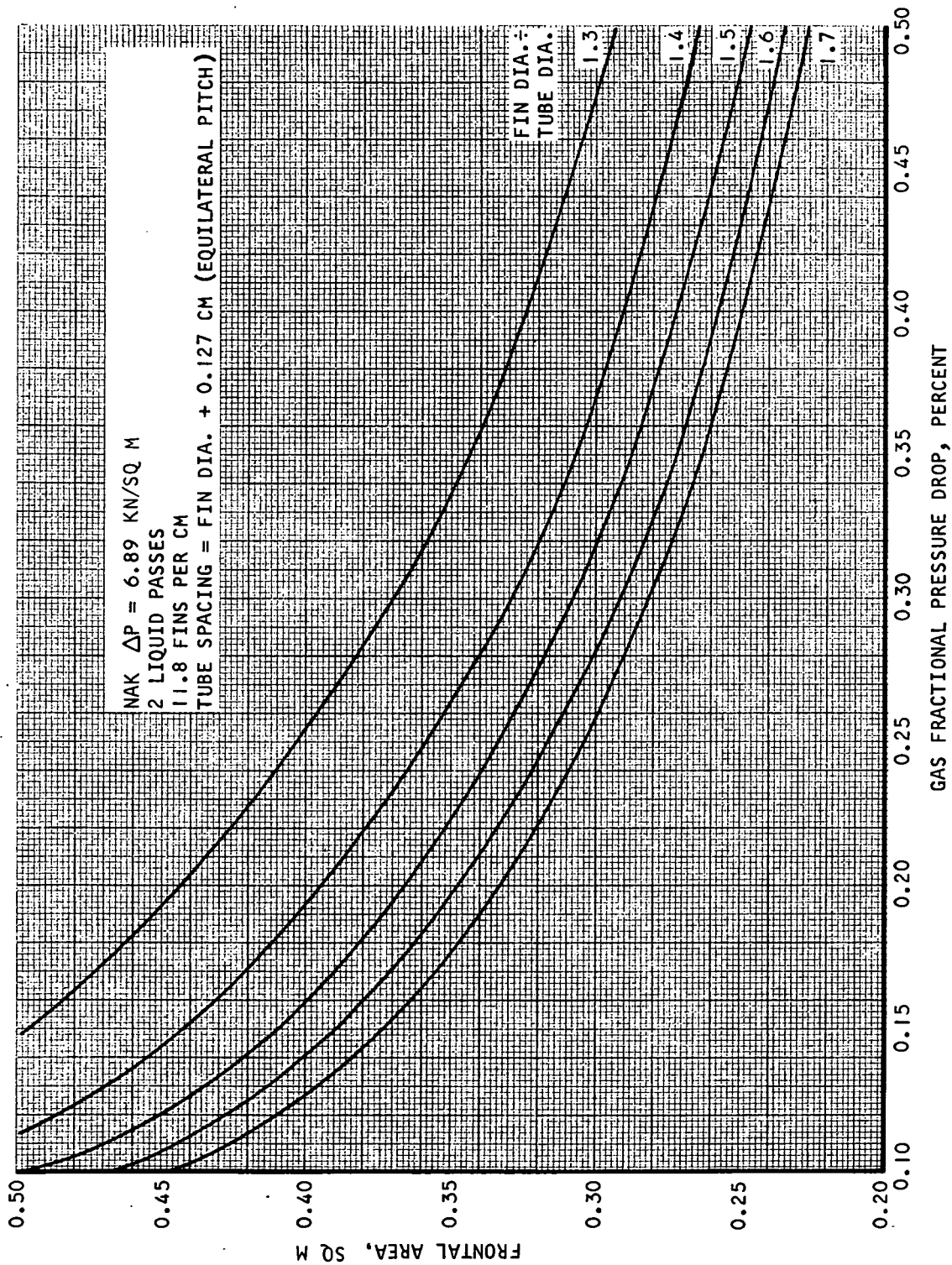
Heat exchanger core matrix sizes were calculated by AiResearch computer program H0424 and wrap-up weights were calculated with X0600. The X0600 program estimates the weight of the heat exchanger sides, headers, and internal tube supports required for gas containment and exchanger structural integrity. The addition of these wrap-up weights to the core matrix weight results in total heat exchanger weights that are appropriate for use in system optimization studies.

Using the frontal areas of Figure 2-8 and the areas calculated for the recuperator high-pressure outlet, the matched-area pressure drop split between heat source unit and recuperator was determined for each ratio of fin diameter to tube diameter. The face area curves are shown in Figure 2-10. Each intersection between a heat source heat exchanger curve and the recuperator curve represents a matched-face pressure drop of 1.60 percent for the two heat exchangers.

Total weight of the two heat exchangers, based on the matched-face pressure drop splits, is shown as a function of fin diameter in Figure 2-11. Minimum weight occurs at a ratio of fin diameter to tube OD of approximately 1.5. Referring to Figure 2-10, this corresponds to an optimum heat source heat exchanger pressure drop of 0.45 percent and a recuperator pressure drop of 1.15 percent. Minimum weight for the heat source unit alone corresponds to a ratio of fin diameter to tube diameter of 1.3, but the reduction in face area with increasing fin diameter increases the optimum fin diameter on a total system weight basis to approximately 1.5.

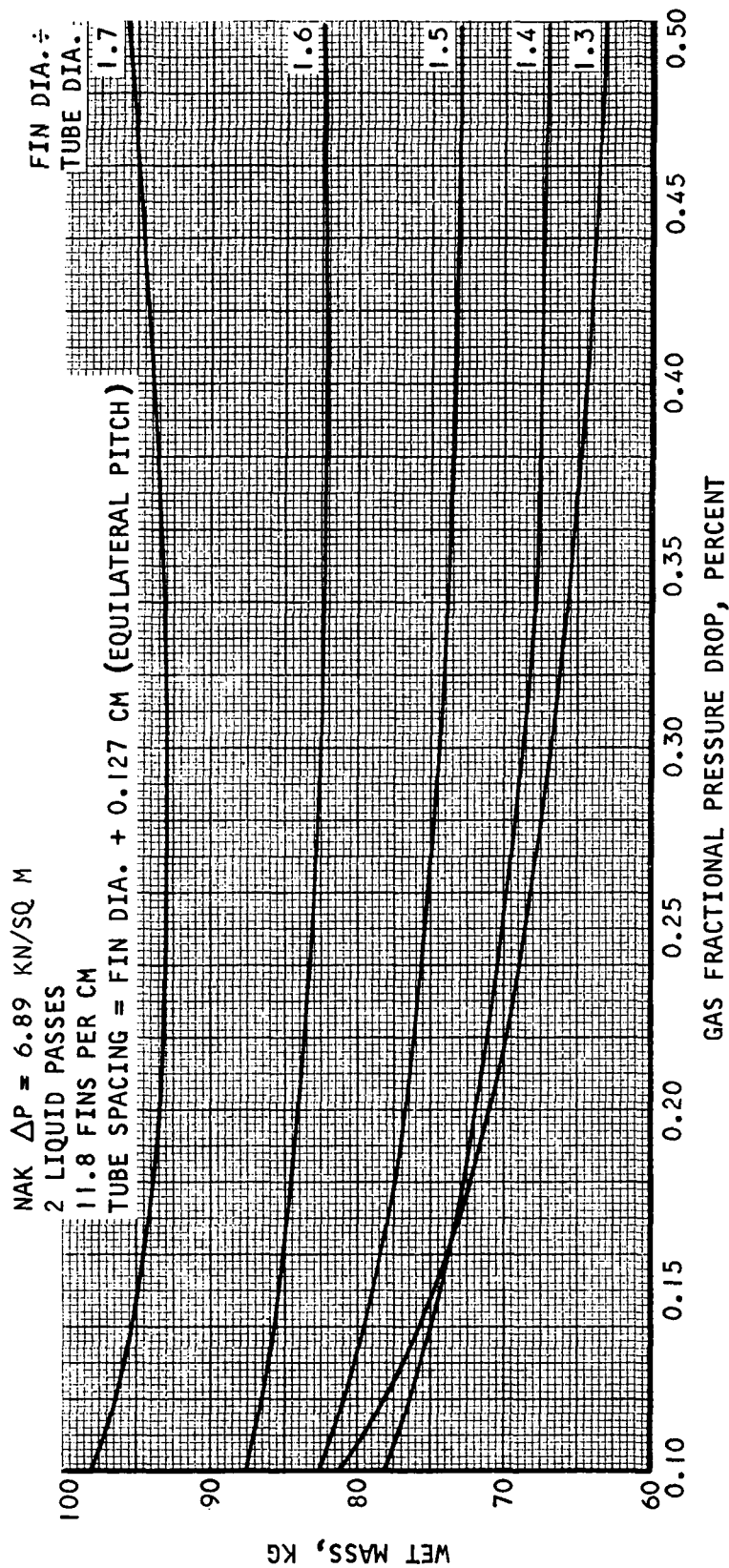
2. Transverse Tube Spacing

The ratio of transverse tube spacing (spacing perpendicular to the gas flow) to tube diameter was varied from 1.5 to 2.3. The ratio of fin diameter to tube diameter for this study was 1.4, so the closest spacing value considered corresponds to a minimum clearance between fins on adjacent tubes. The tube row spacing was kept constant at 1.30 times the tube diameter, corresponding to an equilateral triangular array for the minimum transverse spacing case but not for the wider spacings. Based on heat exchanger aspect ratio considerations, the two-pass unit was selected in preference to the four-pass unit and a NaK pressure drop of 3.45 kN/sq m was used. Heat exchanger frontal area and weight, including structural wrap-up, are shown as functions of pressure drop and transverse spacing in Figures 2-12 and 2-13. It can be seen that minimum weight occurs at minimum transverse tube spacing, whereas



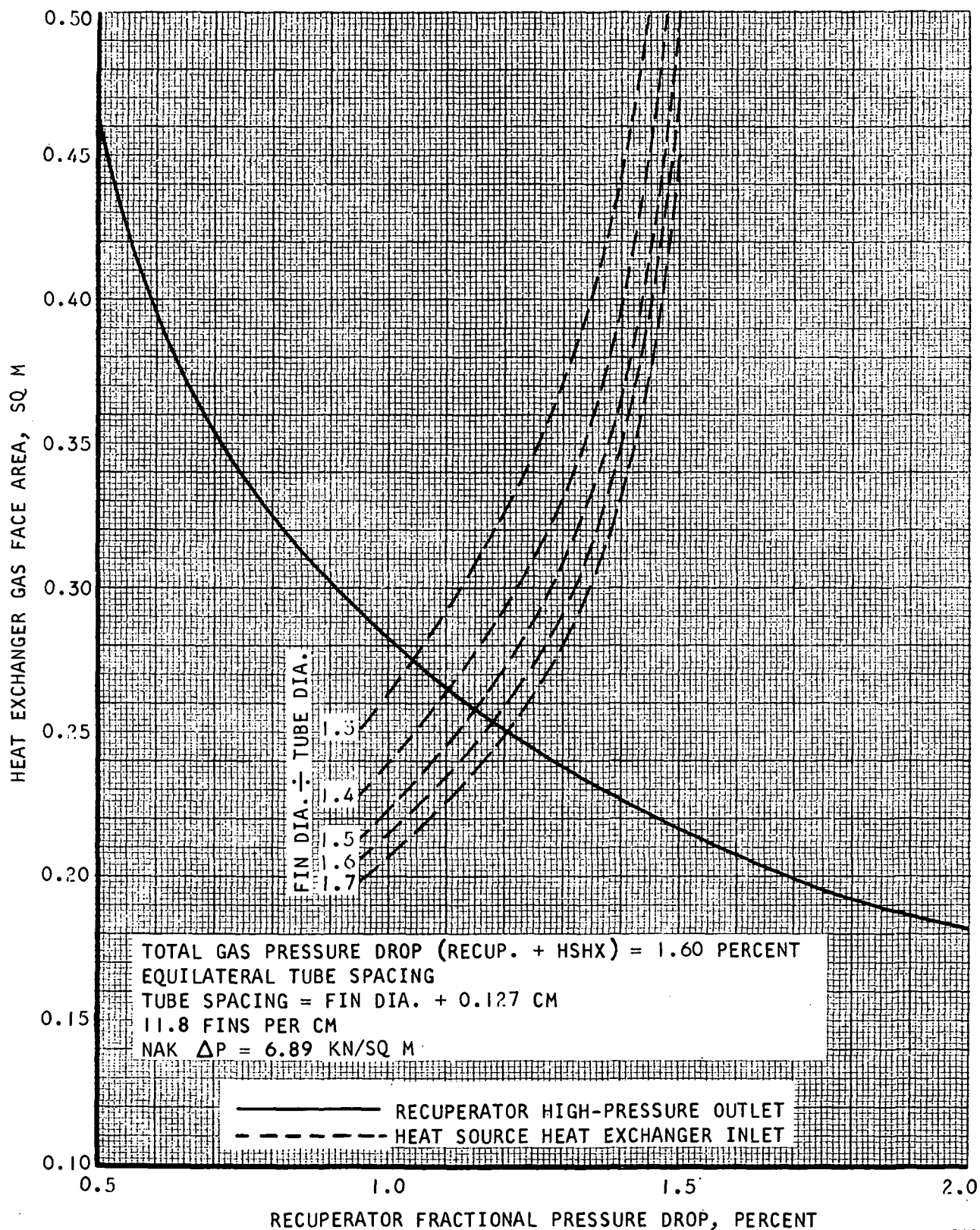
S-64995

Figure 2-8. Variation of Frontal Area with Gas Pressure Drop and Fin Diameter for Heat Source Heat Exchanger



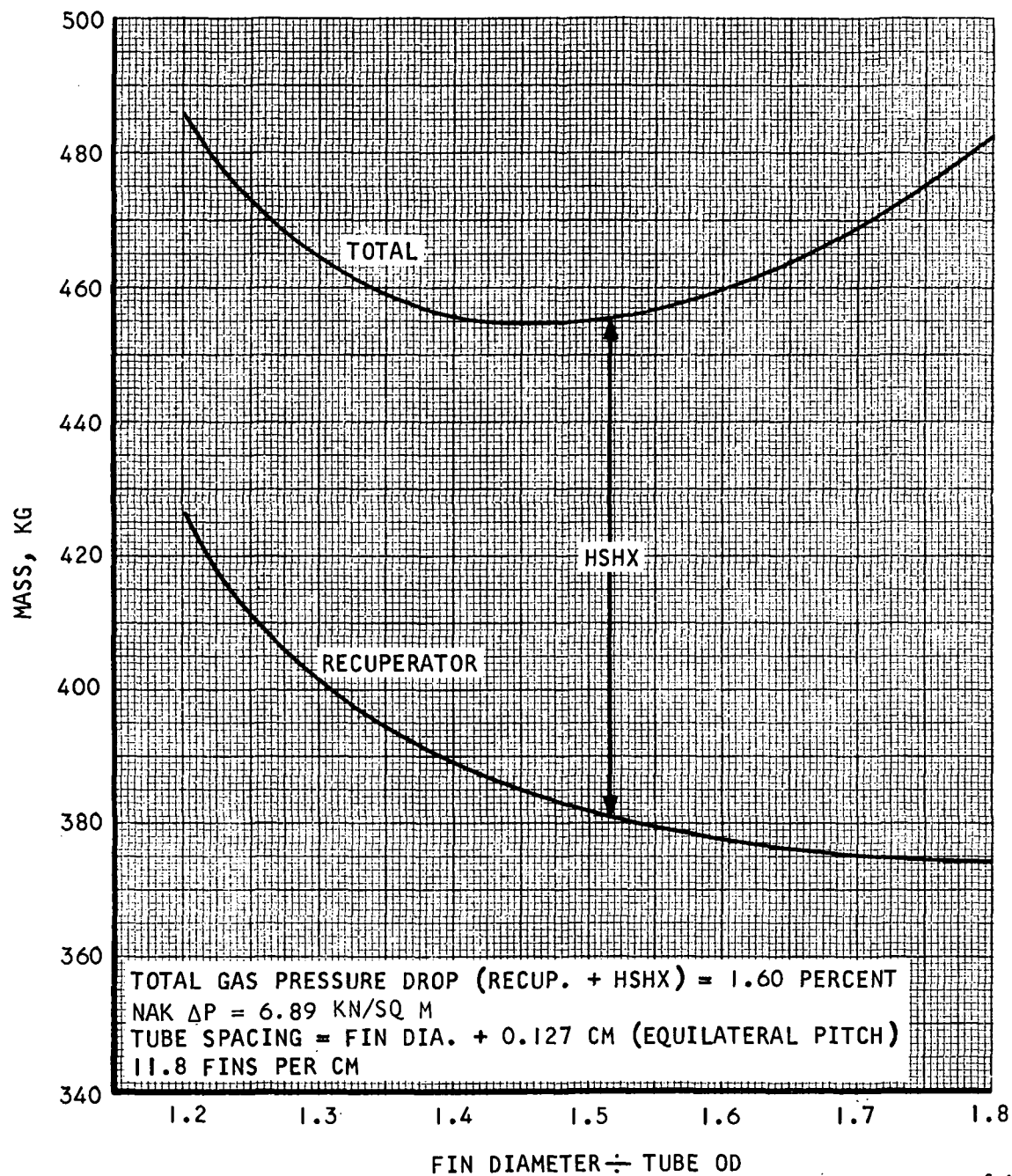
S-65003

Figure 2-9. Variation of Mass with Gas Pressure Drop and Fin Diameter for Heat Source Heat Exchanger



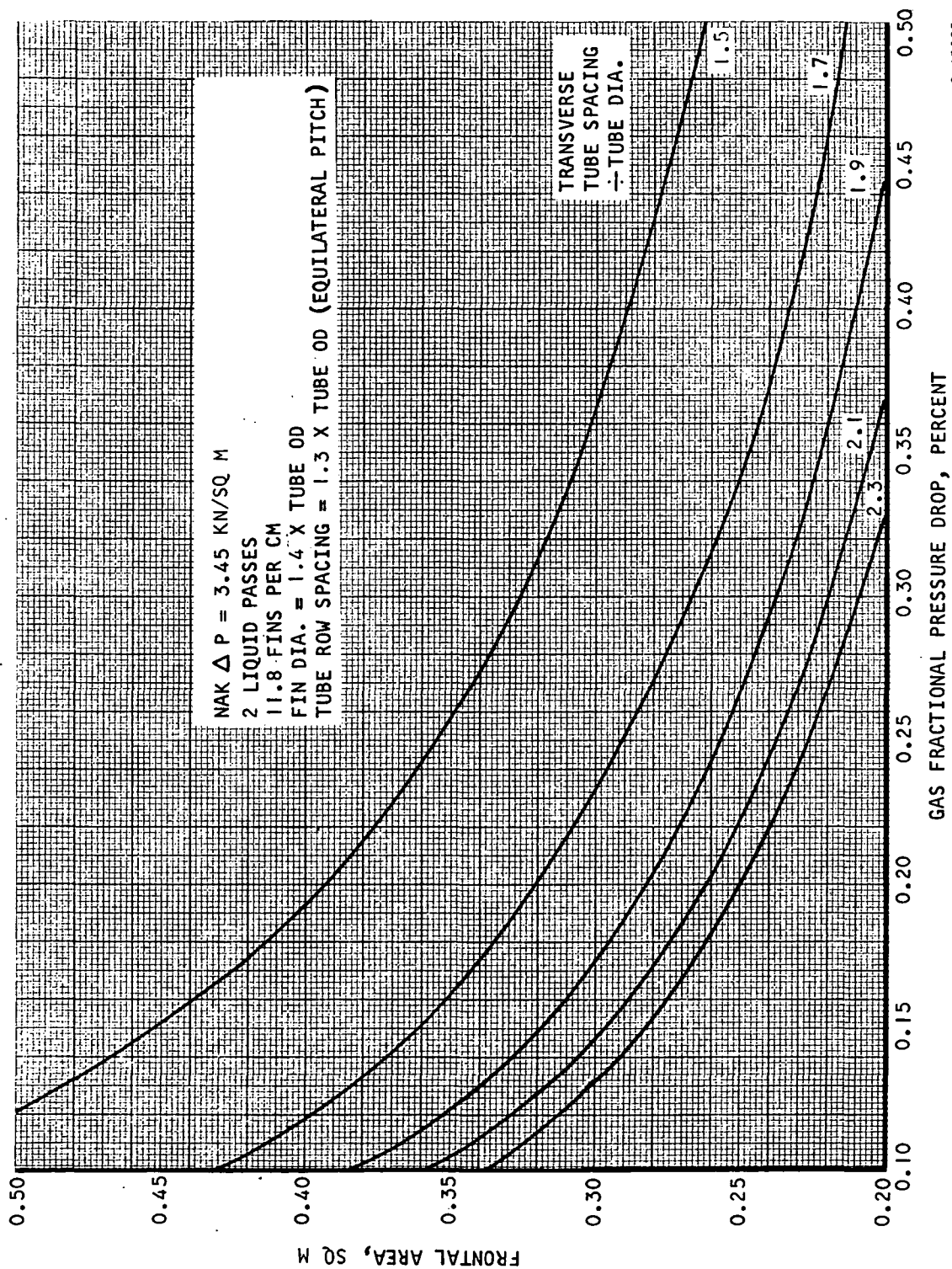
S-65005

Figure 2-10. Recuperator and Heat Source Heat Exchanger Frontal Areas for Several Fin Diameters



S-64996

Figure 2-11. Variation of Recuperator and Heat Source Heat Exchanger Mass with Fin Diameter for Matched Gas Face Areas



S-65002

Figure 2-12. Variation of Frontal Area with Gas Pressure Drop and Tube Spacing for Heat Source Heat Exchanger

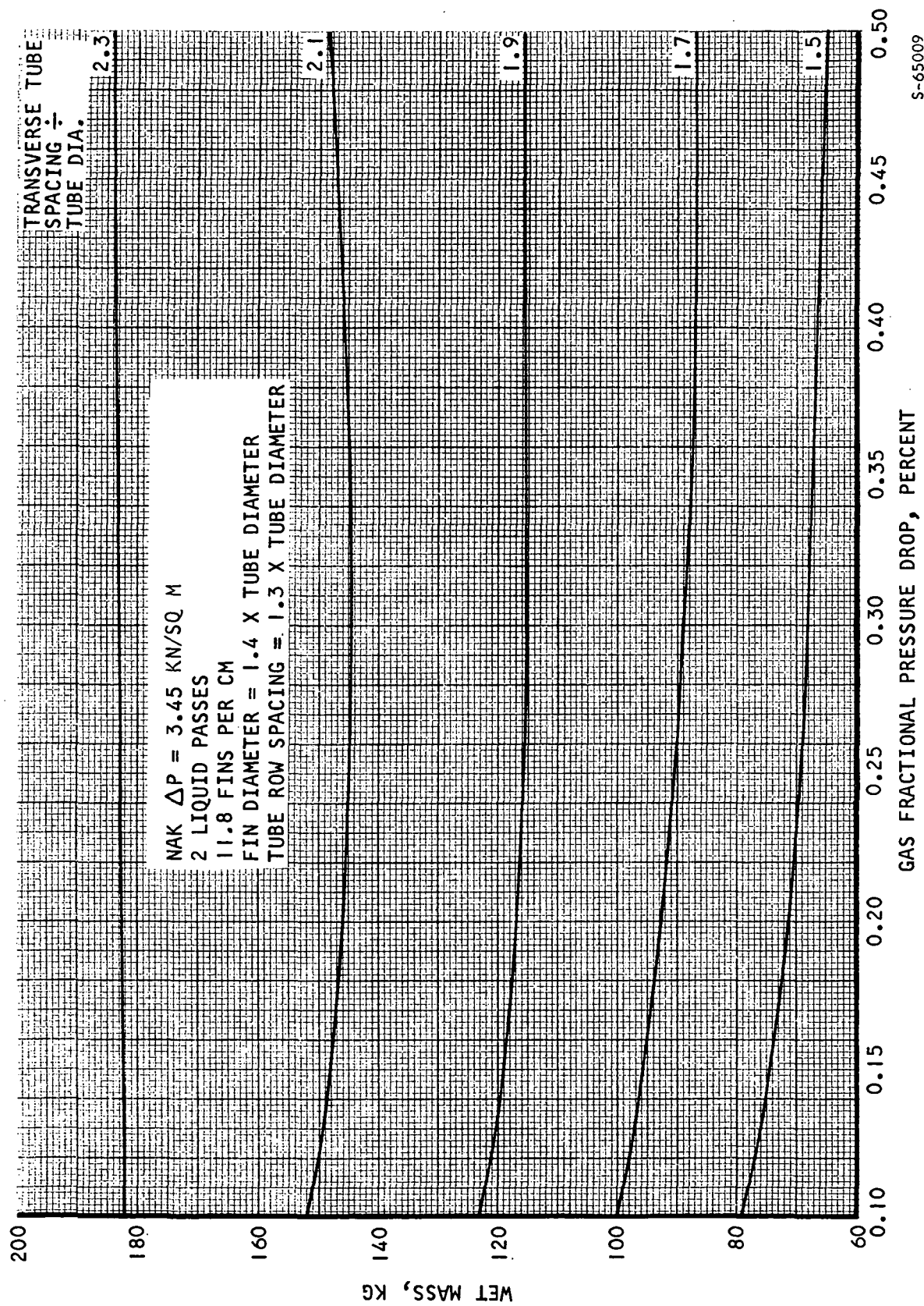


Figure 2-13. Variation of Mass with Gas Pressure Drop and Tube Spacing for Heat Source Heat Exchanger

frontal area decreases with increasing spacing. The increase in weight with tube spacing is primarily due to increased structural wrap-up as heat exchanger volume increases.

The pressure drop splits required to match recuperator and heat source heat exchanger face areas, based on a total pressure drop of 1.60 percent, are obtained from Figure 2-14. Using these pressure drops, total weight for the two components is shown as a function of tube spacing in Figure 2-15. It can be seen that minimum weight occurs at essentially minimum spacing, or a ratio of transverse spacing to tube diameter of 1.5. As spacing increases, the decrease in recuperator weight (due to increasing recuperator pressure drop) is more than offset by the rapid increase in weight of the heat source heat exchanger.

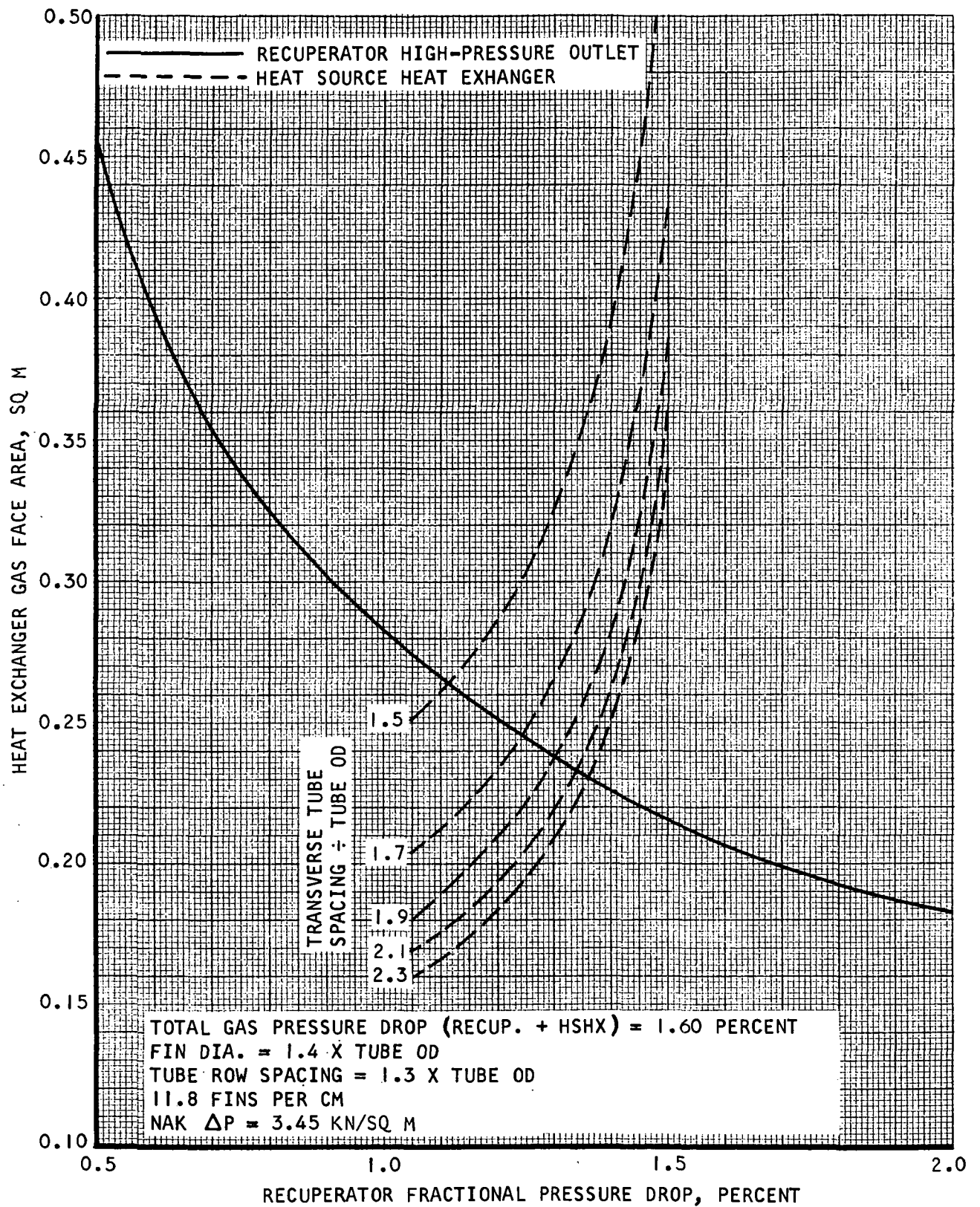
3. Fin Spacing

The effect of fin spacing was investigated by varying the number of fins/cm from 5.91 to 13.8. The matrix parameters kept constant for this analysis were a ratio of fin diameter to tube diameter of 1.5 and a ratio of tube spacing (equilateral pitch) to tube diameter of 1.6. To obtain a favorable aspect ratio for mating with the recuperator, the use of two liquid passes and a NaK pressure drop of 3.45 kN/sq m were selected. Based on these conditions, the variations of heat exchanger frontal area and weight (including structural wrap-up) with pressure drop and fins per cm are shown in Figures 2-16 and 2-17. It can be seen that weight decreases quite rapidly while frontal area increases only slightly with increasing fins/cm. The weight variation is due primarily to the change in structural wrap-up weight as core volume varies.

Based on a total pressure drop of 1.60 percent, the heat source heat exchanger and recuperator (high pressure outlet) face areas are plotted as functions of recuperator pressure drop in Figure 2-18. Using the intersection points to define the matched-area pressure drop splits, total weight of the recuperator and heat source unit is plotted as a function of fins/cm in Figure 2-19. Total weight decreases with increasing fins/cm over the total range studied. It is likely that the maximum number of fins/cm that can be fabricated is about 11.8. This limitation does not represent a serious weight penalty however, since only a minor weight saving is obtained by increasing fins/cm above 11.8.

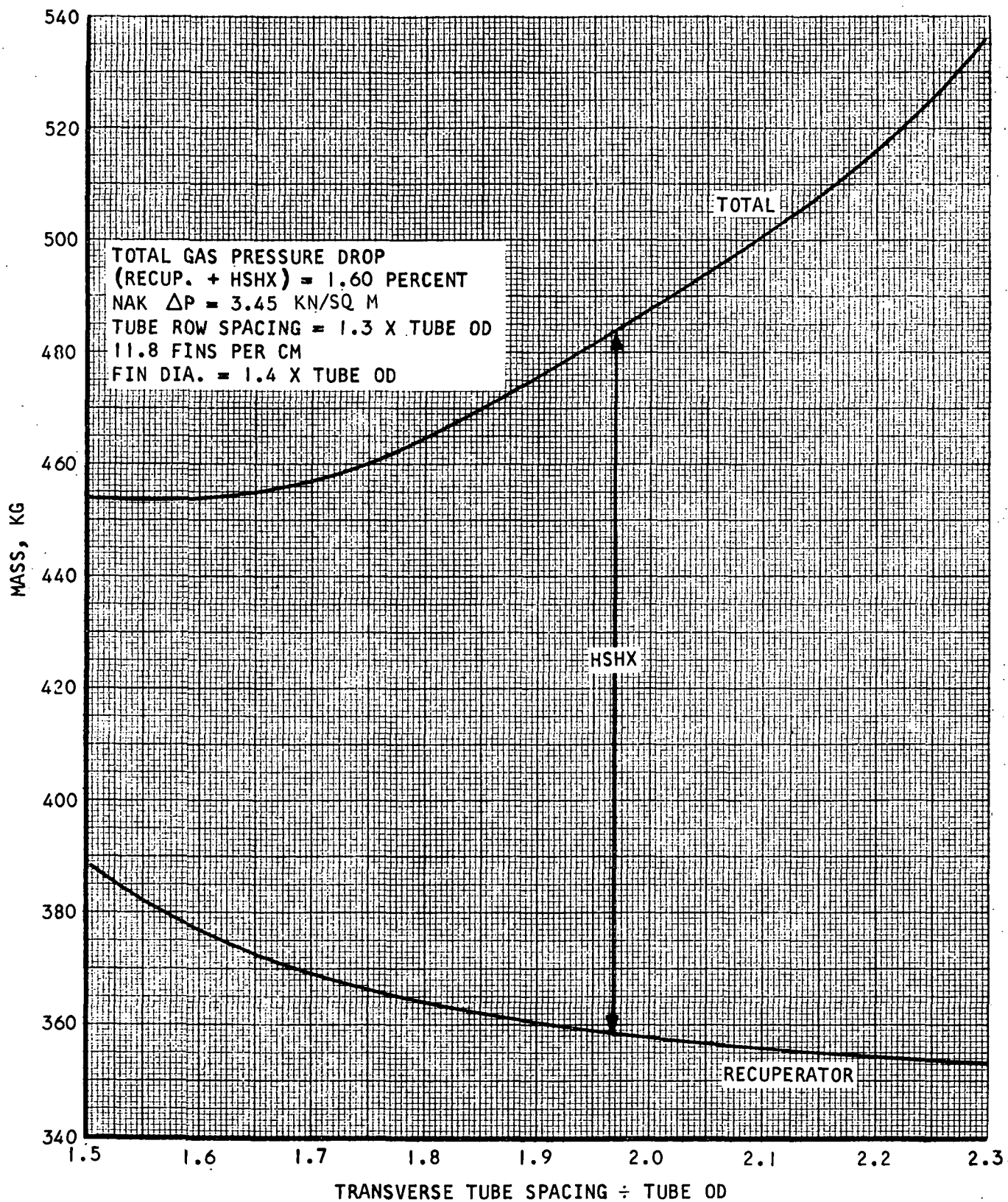
4. Conclusion

Based on the preceding studies, an optimum core matrix was selected for the heat source heat exchanger. This matrix is summarized in Table 2-3.



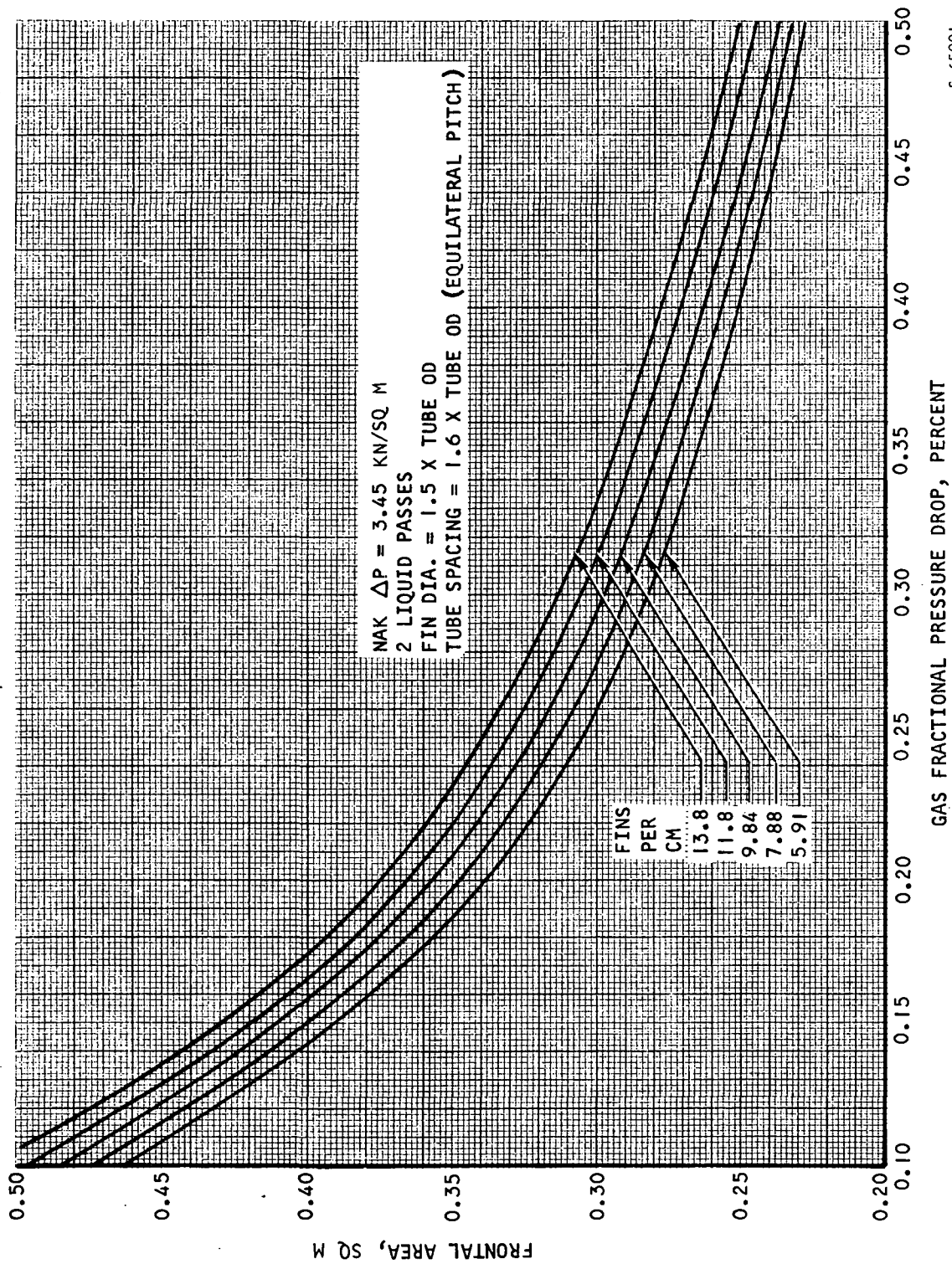
S-65007

Figure 2-14. Recuperator and Heat Source Heat Exchanger Frontal Areas for Several Tube Spacings



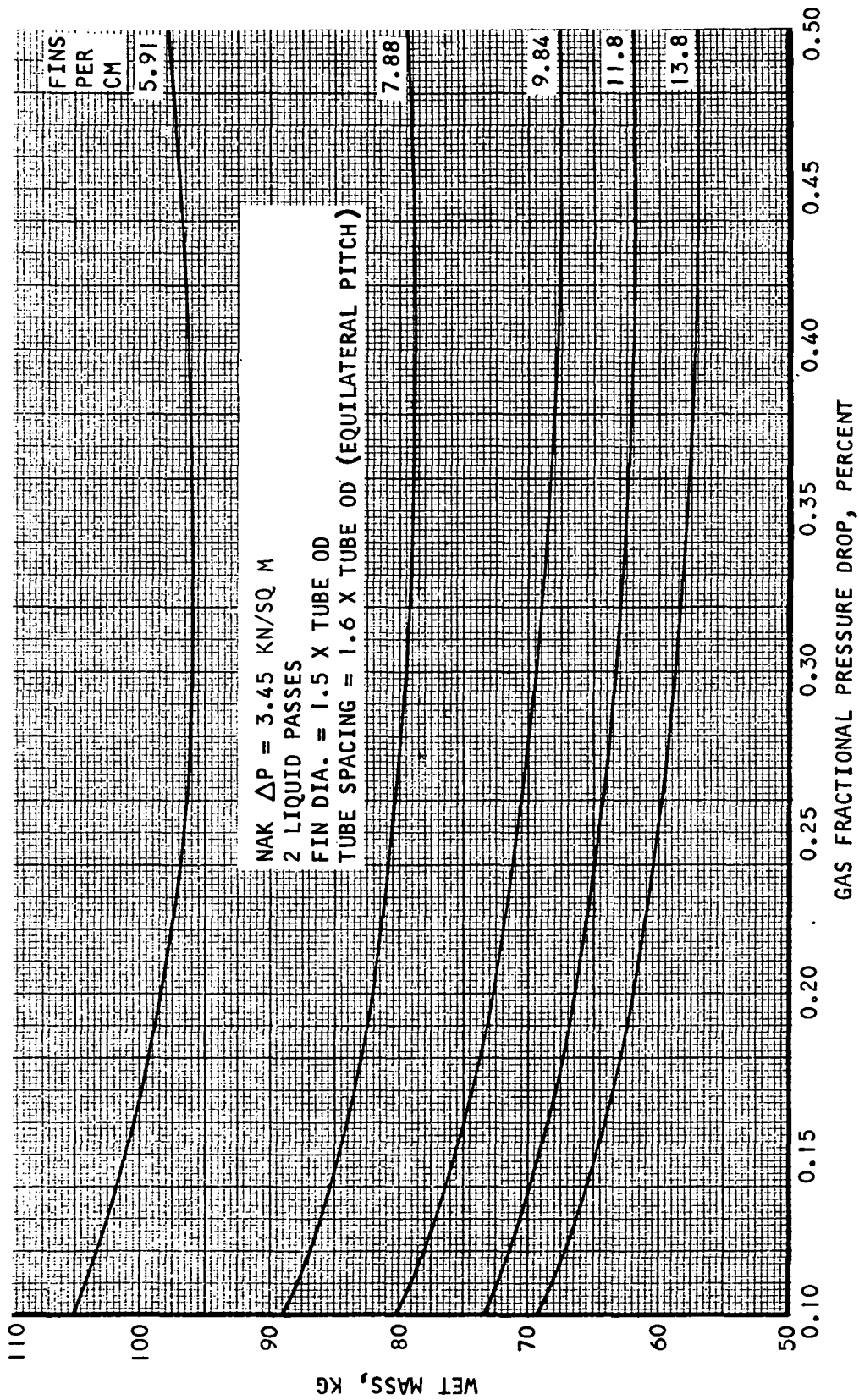
S-65006

Figure 2-15. Variation of Recuperator and Heat Source Heat Exchanger Mass with Tube Spacing for Matched Gas Face Areas



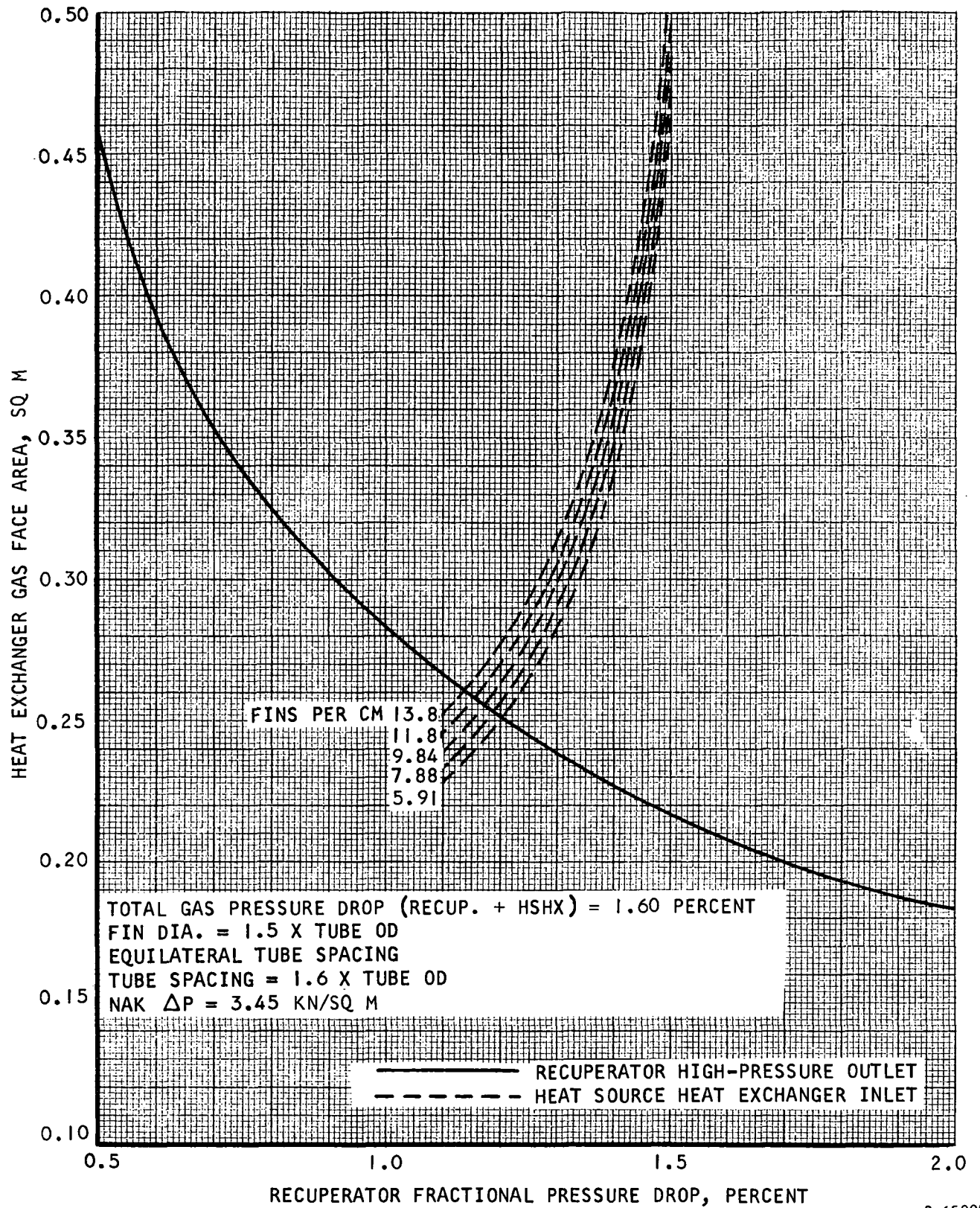
S-65001

Figure 2-16. Variation of Frontal Area with Gas Pressure Drop and Fins per Cm for Heat Source Heat Exchanger



S-65004

Figure 2-17. Variation of Mass with Gas Pressure Drop and Fins per Cm for Heat Source Heat Exchanger



S-65008

Figure 2-18. Recuperator and Heat Source Heat Exchanger Frontal Areas for Several Fin Diameters

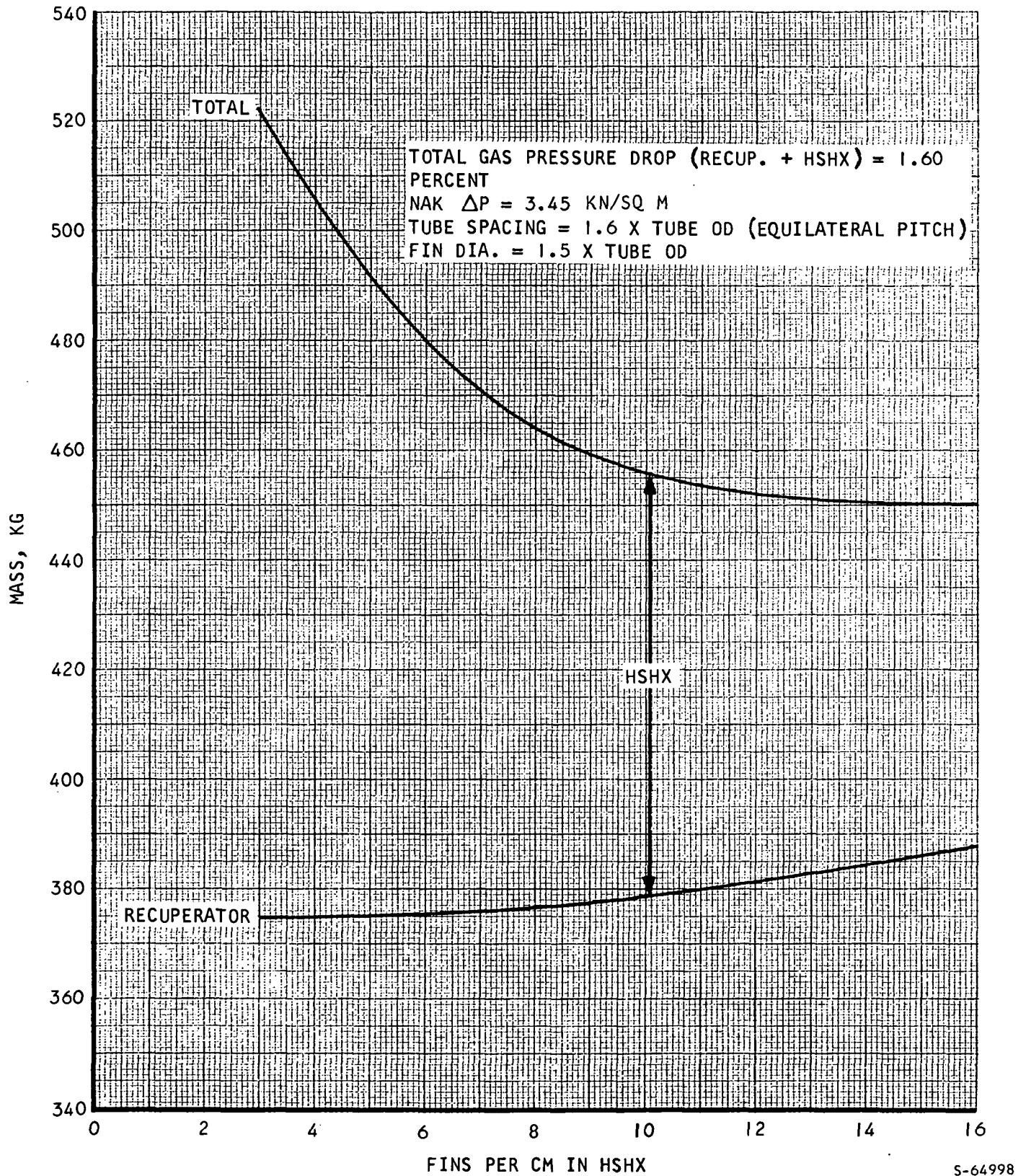
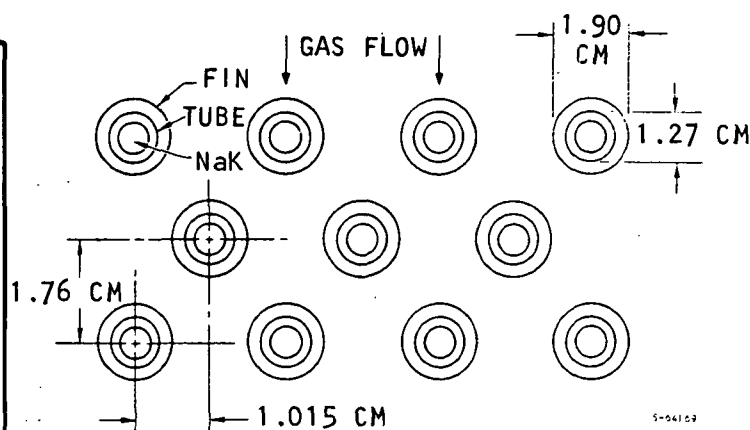


Figure 2-19. Variation of Recuperator and Heat Source Heat Exchanger Mass with Number of Fins per Cm for Matched Gas Face Areas

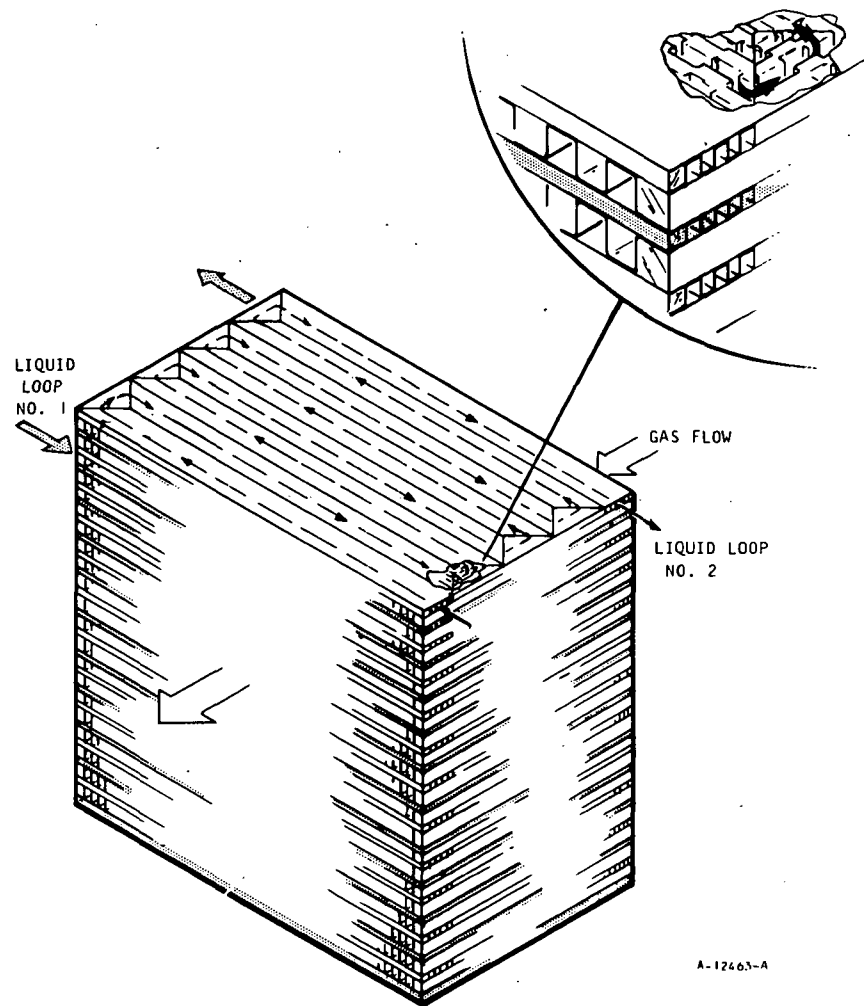
TABLE 2-3

HEAT SOURCE HEAT EXCHANGER CORE MATRIX

Tube OD	1.27 cm
Fin dia	1.90 cm
Fin thickness, copper	0.00762 cm
Fin thickness, stainless	0.00508 cm
Fins/cm	11.8
Transverse tube spacing	2.03 cm
Tube row spacing	1.76 cm

Waste Heat Exchanger1. Effectiveness = 0.950

The waste heat exchanger was designed to the original problem statement effectiveness of 0.95 for each of the three candidate radiator fluids. The sizing was performed for each of several fin sets over a gas fractional pressure drop range of 0.2 to 1.2 percent. The heat exchanger flow configuration in all cases was cross-counterflow, with the liquid multipassed eight times and the gas making a single crossflow pass. Liquid side redundancy is obtained in this design by integrating both liquid circuits into a single waste heat exchanger core. The two independent liquid flows enter at opposite sides of the heat exchanger and use alternate liquid passages. The order of passages in the core stack-up is, therefore, liquid 1, gas, liquid 2, gas, liquid 1, etc. Since only one of the liquid circuits is active at any given time, the ratio of the number of gas passages to the number of active liquid passages in this arrangement is two to one, providing a relatively high ratio of gas-side heat transfer area to liquid-side heat transfer area. To maintain separation of the two liquid circuits at the interpass turns, mitered-fin turning sections are utilized in place of the usual interpass pans. This design approach is illustrated in the following sketch.



A-12463-A

Eight-Pass Cross-Counterflow Plate-Fin
Heat Exchanger with Two Liquid Loops

The fin sets used in the analysis are shown in Table 2-4; they range in compactness from 14.7 sq cm/cu cm (total active heat transfer area per unit volume) for fin set 1, to 18.6 sq cm/cu cm for fin set 5. In all cases, the fin material is nickel whereas the remainder of the unit is stainless steel.

TABLE 2-4

WASTE HEAT EXCHANGER FIN SETS

Fin Set	Gas Side			Liquid Side		
	Fins/cm	Fin Ht, cm	Fin Thickness, cm	Fins/cm	Fin Ht, cm	Fin Thickness, cm
1	6.30	0.389	0.00762	7.88	0.190	0.00508
2	6.30	0.318	0.00762	7.88	0.190	0.00508
3	7.88	0.254	0.00762	7.88	0.190	0.00508
4	7.88	0.254	0.00762	7.88	0.127	0.00508
5	7.88	0.190	0.00762	7.88	0.127	0.00508

Although heat exchanger weight generally decreases with increasing compactness in this range, two factors reduce the advantage of the more compact surfaces: (1) gas face area increases with increasing compactness on the gas side, resulting in a requirement for a higher gas pressure drop allotment to the waste heat exchanger to match recuperator and waste heat exchanger face areas, and (2) liquid pressure drop increases with increasing compactness due primarily to the shorter heat exchanger dimension in the gas-flow (liquid flow width) direction. Results of the previous HXDA design study indicated that minimum weight solutions correspond to less gas pressure drop in the waste heat exchanger than is required for matched faces, so that the decreased weight associated with use of the more compact surfaces would be at least partially offset by increased weight in the recuperator and heat source heat exchanger due to a less favorable pressure drop split. The penalty associated with increased liquid pressure drop has not been ascertained at this time, but the design objective is a pressure drop in the range of 69 to 103 kN/sq m.

Weight, gas face area, and liquid pressure drop for the waste heat exchanger with MIPB as the liquid coolant are shown in Figures 2-20 through 2-22. These curves are based on a constant value of 0.3 for the ratio of heat exchanger stack height to liquid flow length. This aspect ratio is approximately equal to the ratio of recuperator low-pressure outlet face width to recuperator stack height and thus provides a match between gas faces if the waste heat exchanger liquid flow direction is aligned parallel to the recuperator stack height dimension. This orientation is preferable to aligning the stack heights of the two heat exchangers because it results in fewer fin sandwiches and a higher liquid mass velocity in the waste heat exchanger.

The effect of variable liquid specific heat C_p on heat exchanger performance was estimated to be equivalent to a 38 percent change in UA. The effect of the increase in liquid C_p with temperature is to decrease the mean temperature difference between fluid streams and thus increase heat exchanger required UA. This effect is more severe with MIPB as the coolant than with either of the other two candidate fluids because of the more rapid increase of C_p with temperature for MIPB. For DC-200 (1.0 cs) and DC-200 (2.0 cs), the estimated UA effects due to variable C_p are 24 percent and 20 percent, respectively.

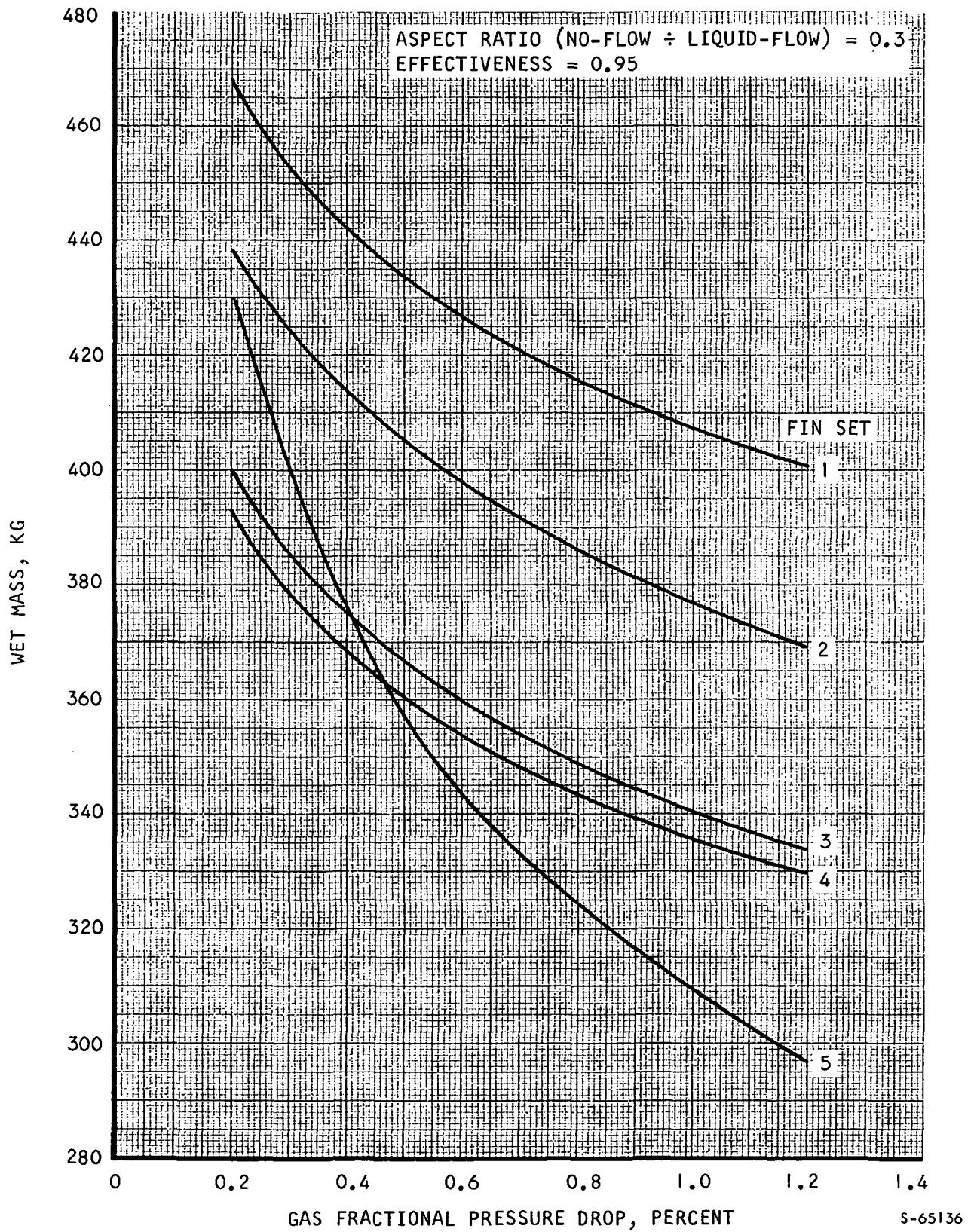


Figure 2-20. Waste Heat Exchanger Mass Using MIPB Coolant

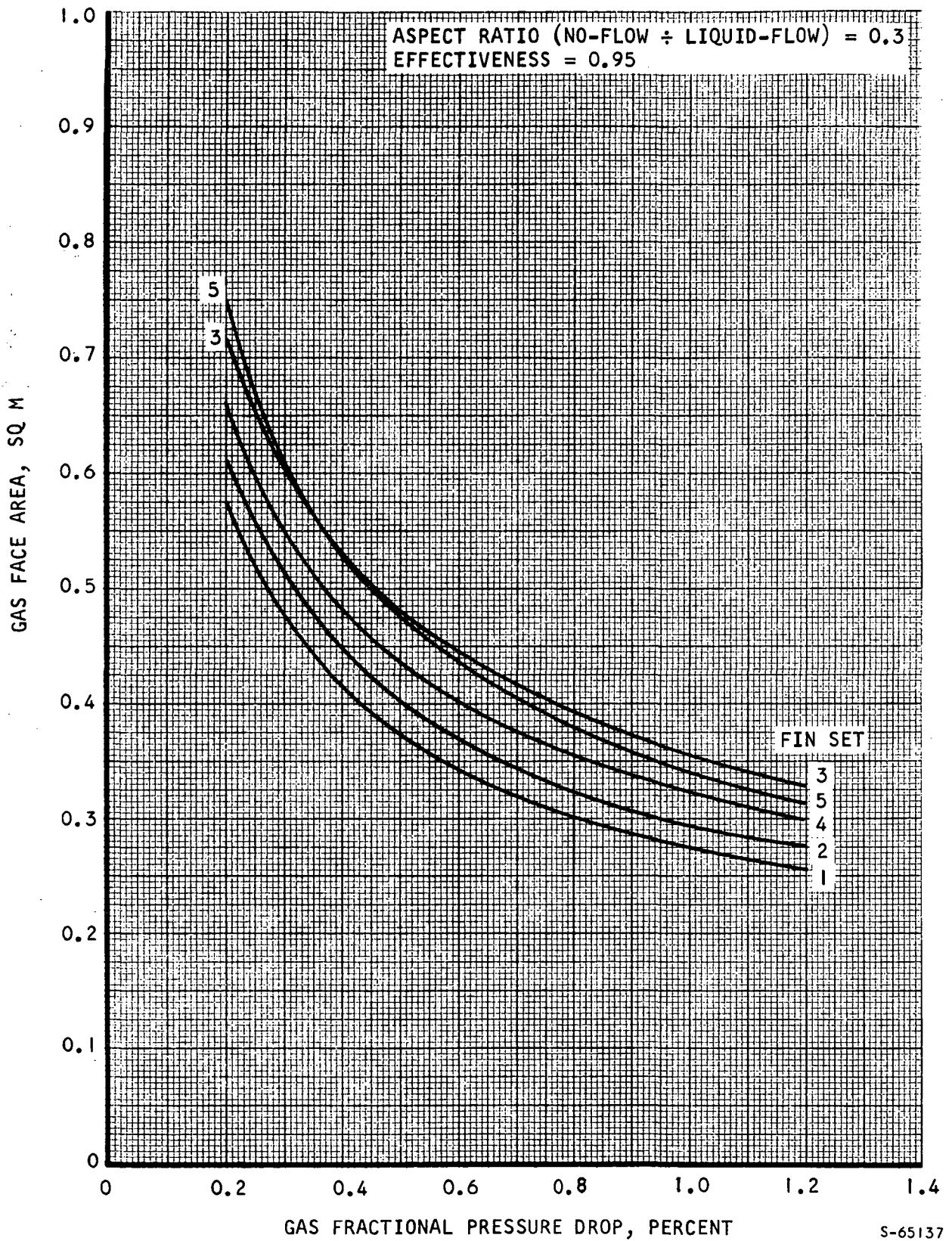
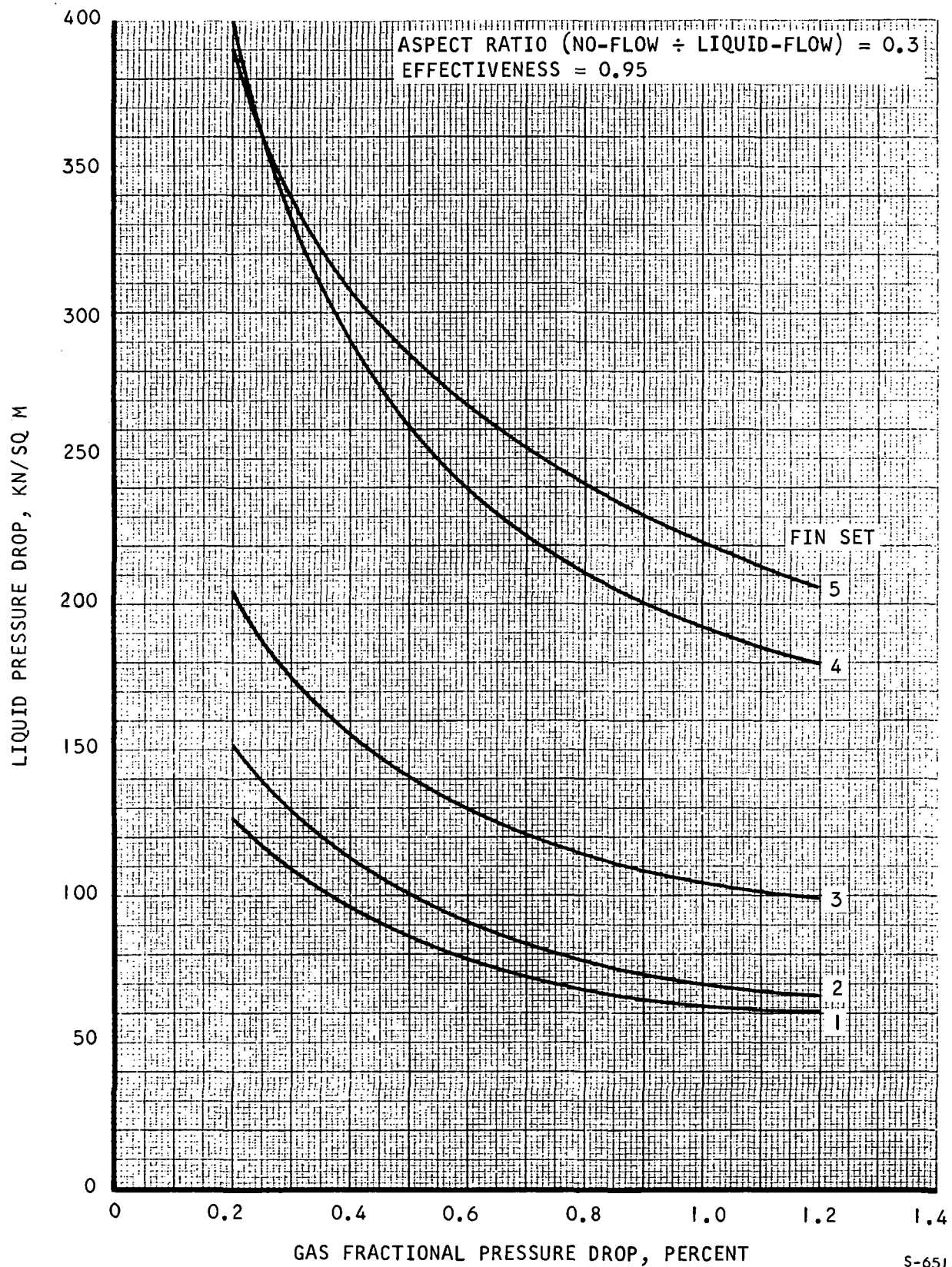


Figure 2-21. Waste Heat Exchanger Face Area Using MIPB Coolant



S-65138

Figure 2-22. Waste Heat Exchanger Liquid Pressure Drop Using MIPB Coolant

Based on Figure 2-22, only fin sets 1, 2, and 3 yield liquid pressure drops in the allowable design range. Of these, fin set 3 yields the lowest heat exchanger weight, but also has the largest gas face area. Therefore, complete system designs for each fin set based on matched heat exchanger faces would be required to identify the fin set yielding the minimum overall system weight.

Curves of waste heat exchanger weight, gas face area, and liquid pressure drop for the other two candidate coolants, DC-200 (2.0 cs) and DC-200 (1.0 cs), are shown in Figures 2-23 through 2-28. As with MIPB as the coolant, fin set 3 yields both the lightest heat exchanger and the largest gas face area. A comparison of waste heat exchanger characteristics using the three different radiator fluids is shown in Table 2-5, based on a gas fractional pressure drop of 0.9 percent.

TABLE 2-5

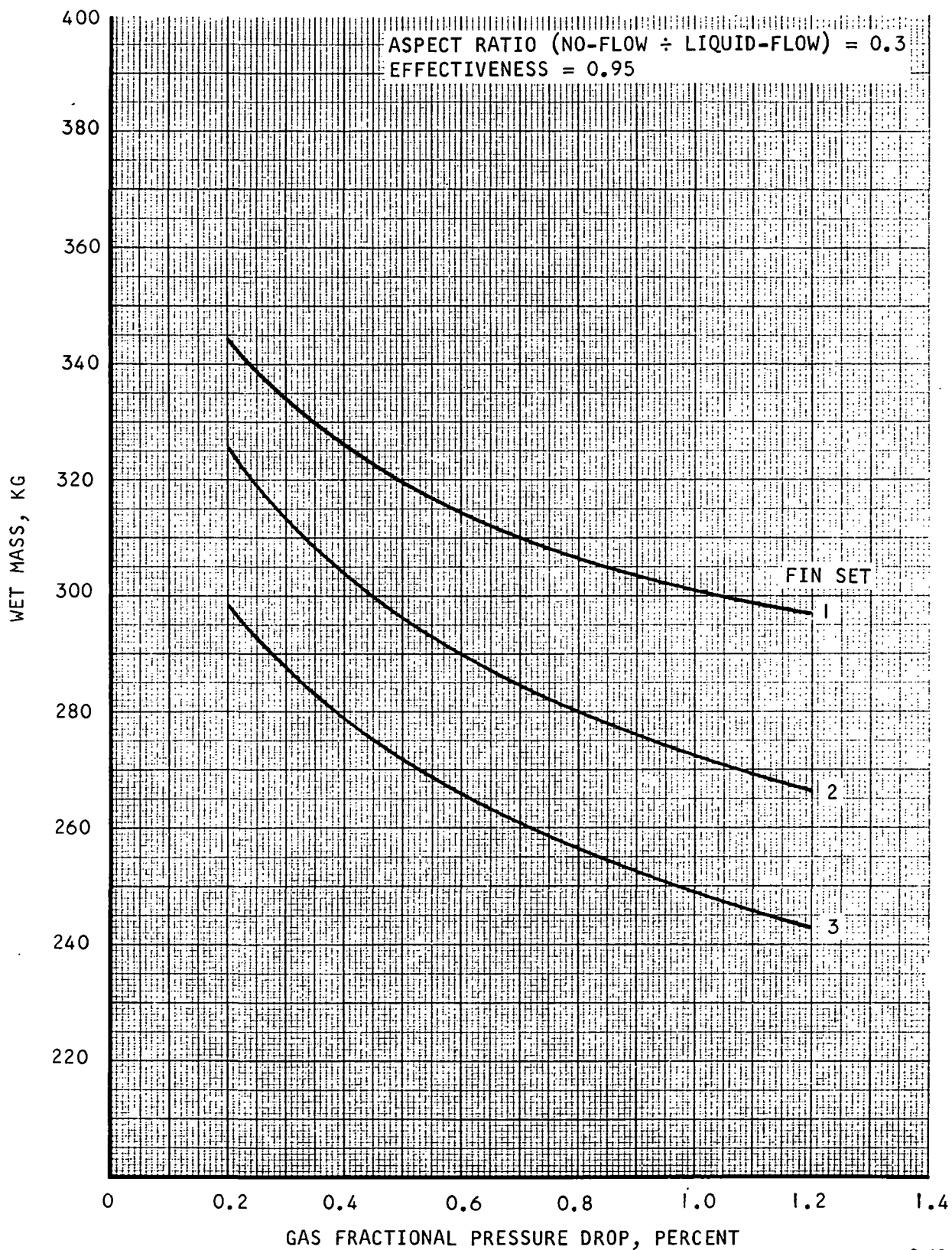
COMPARISON OF WASTE HEAT EXCHANGER COOLANTS*

Coolant	Heat Exchanger Wet Mass, kg	Gas Face Area, sq m	Liquid Pressure Drop, kN/sq m
DC-200 (1.0 cs)	248	0.330	94
DC-200 (2.0 cs)	253	0.330	130
MIPB	345	0.376	110

*Effectiveness = 0.95, $\Delta P/P$ gas = 0.009

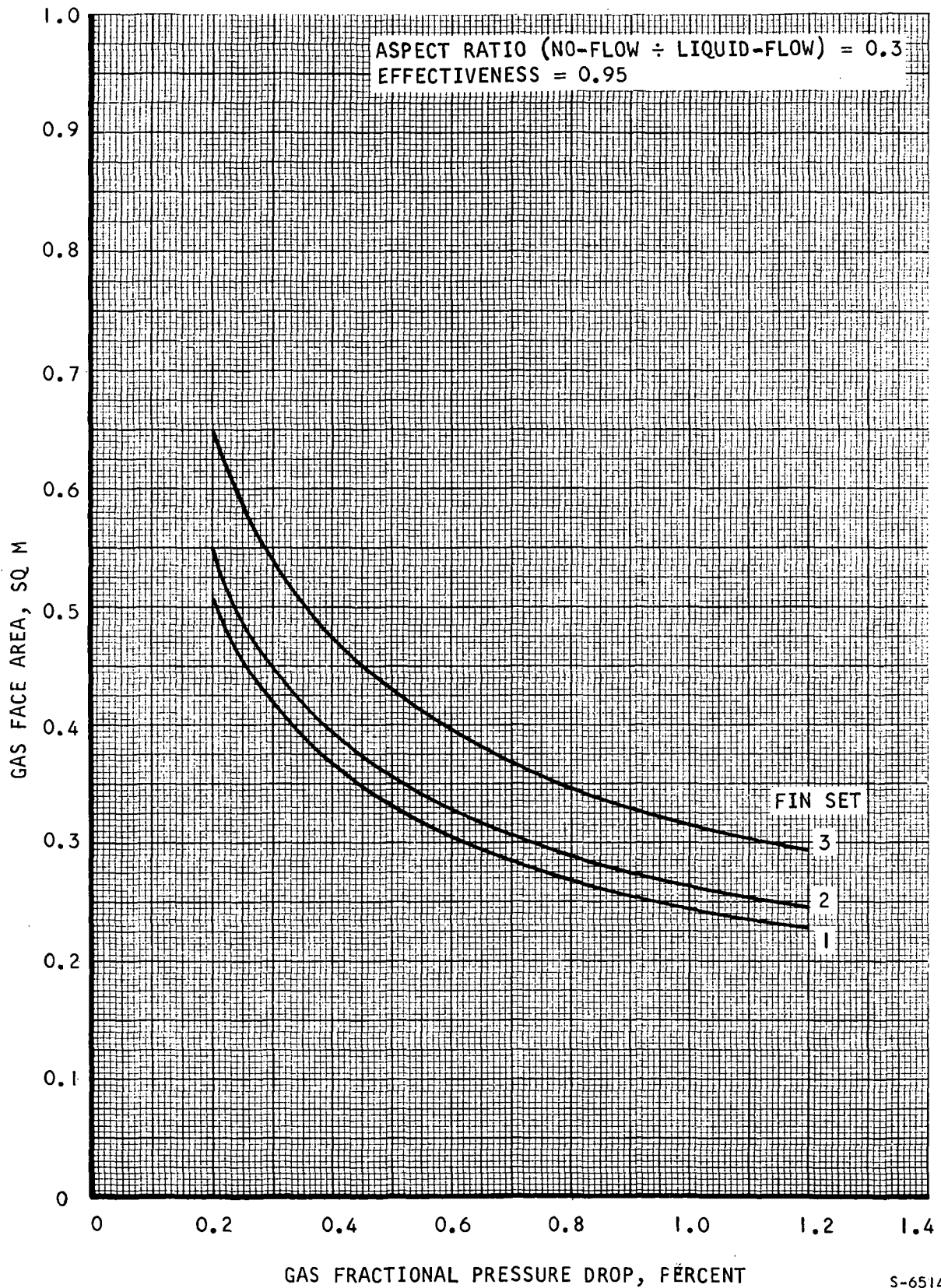
A pressure drop of approximately 0.9 percent for the waste heat exchanger was obtained from the system design procedures followed during the previous HXDA study program. From the recuperator and heat source heat exchanger studies, the recuperator low-pressure outlet face area corresponding to a waste heat exchanger pressure drop of 0.9 percent (based on a total system loss of 3.0 percent and allowing 0.5 percent for the ducts) is 0.328 sq m. Thus, it can be seen that the assumed gas pressure drop split is approximately correct if either DC-200 fluid is used, whereas a somewhat higher waste heat exchanger pressure loss allocation would be required in a system utilizing MIPB.

From Table 2-5 it can be seen that the use of MIPB at a waste heat exchanger effectiveness of 0.95 involves a penalty of about 95 kg, or 38 percent in waste heat exchanger weight. Total system weight penalty with the use of MIPB would be slightly greater due to the larger face area of the MIPB heat exchanger.



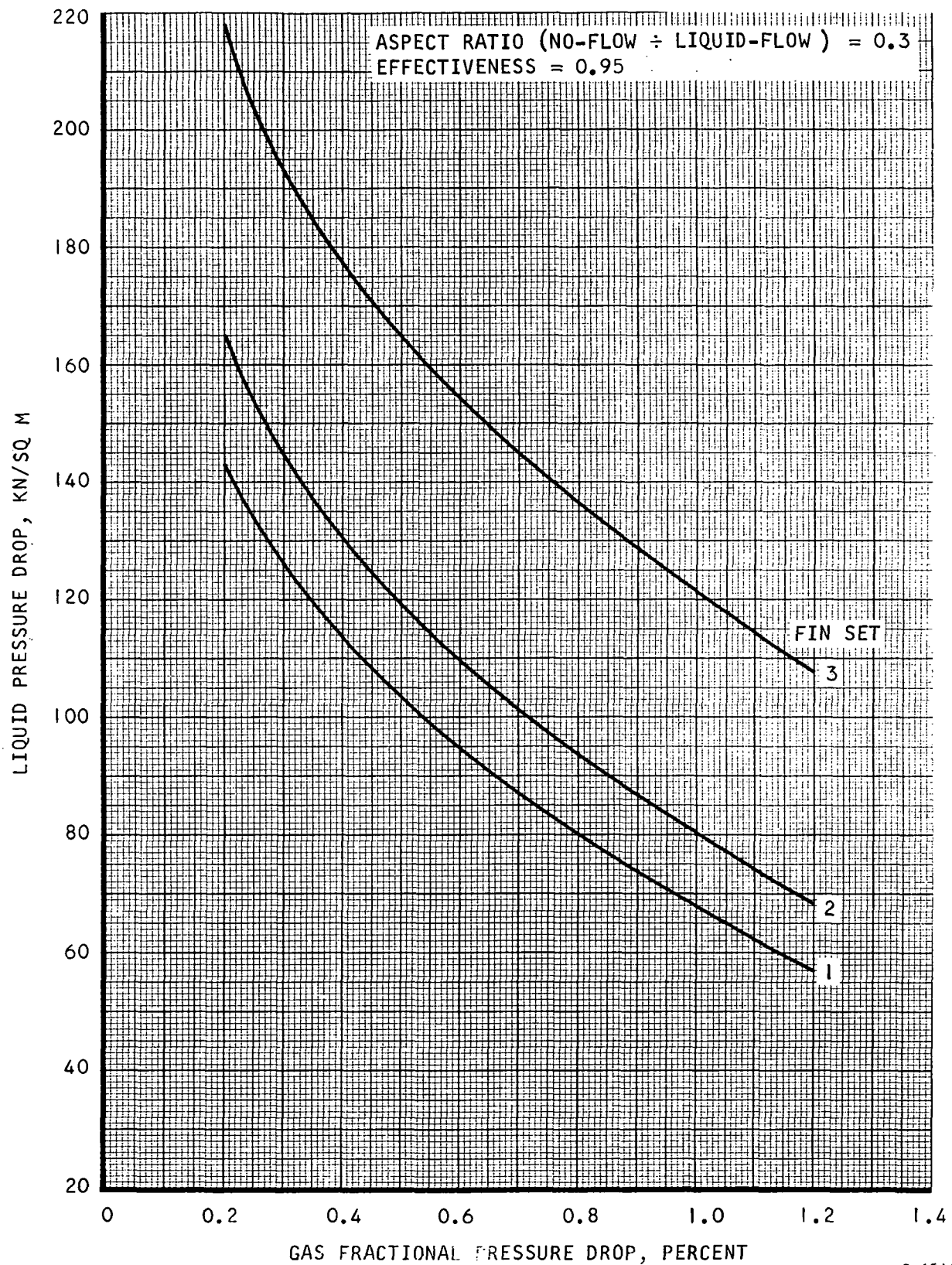
S-65139

Figure 2-23. Waste Heat Exchanger Mass Using
DC-200 (2.0 CS) Coolant



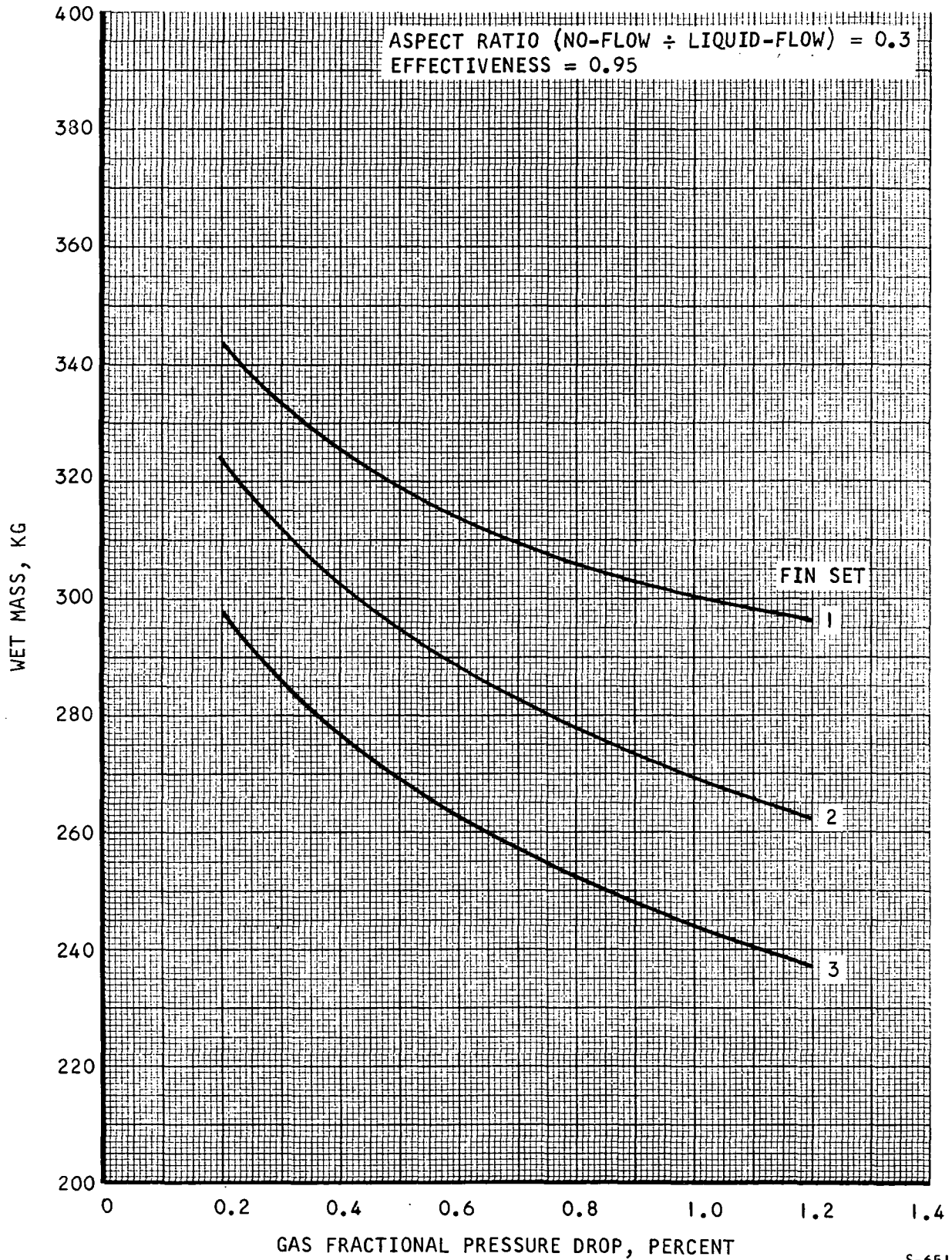
S-65140

Figure 2-24. Waste Heat Exchanger Face Area Using
DC-200 (2.0 CS) Coolant



S-65143

Figure 2-25. Waste Heat Exchanger Liquid Pressure Drop
Using DC-200 (2.0 °C) Coolant



S-65142

Figure 2-26. Waste Heat Exchanger Mass Using
DC-200 (1.0 CS) Coolant

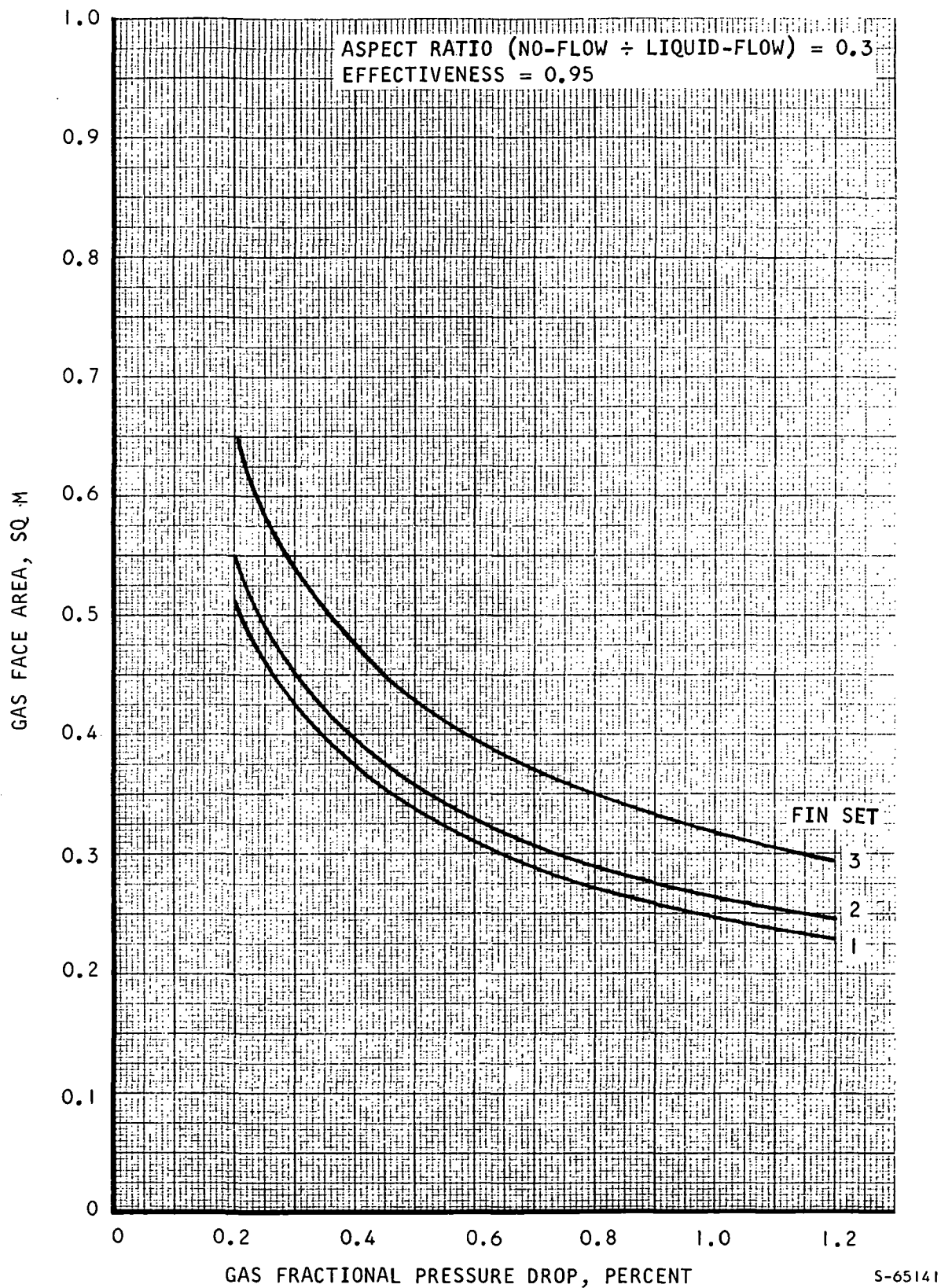
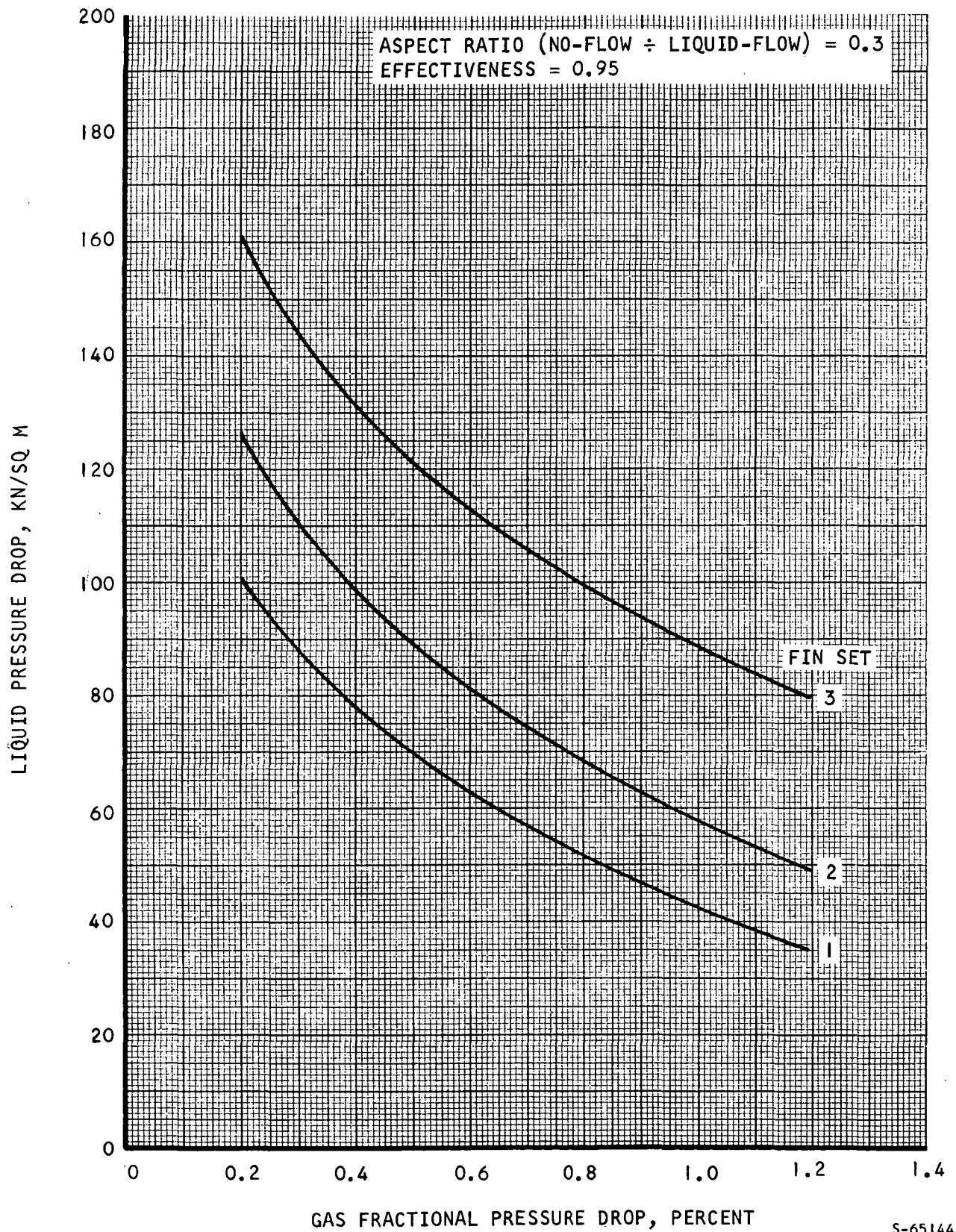


Figure 2-27. Waste Heat Exchanger Face Area
Using DC-200 (1.0 CS) Coolant



S-65144

Figure 2-28. Waste Heat Exchanger Liquid Pressure Drop
Using DC-200 (1.0 CS) Coolant

Performance of the waste heat exchanger designed for use with MIPB is shown in Table 2-6 for all three fluids.

TABLE 2-6
PERFORMANCE OF MIPB WASTE HEAT EXCHANGER AT $E = 0.95$

Coolant	Effectiveness	Gas Pressure Drop, percent	Liquid Pressure Drop, kN/sq m
MIPB	0.95	0.900	110
DC-200 (2.0 cs)	0.963	0.896	13.4
DC-200 (1.0 cs)	0.962	0.896	9.0

Due to the large size of this heat exchanger, the effectiveness with either DC-200 fluid is increased substantially from the system design point. Liquid pressure drops with DC-200 in the MIPB heat exchanger are less than those obtained in the smaller heat exchangers designed for use with DC-200.

2. Effectiveness = 0.935

To reduce the size of the waste heat exchanger while using MIPB as the liquid coolant, designs were obtained for a heat exchanger effectiveness of 0.935. The capacity-rate ratio remained at 0.90. To obtain liquid pressure drops in the desired range, the number of liquid passes was varied between six and eight. With the exception of the variation in the number of passes, the construction of this heat exchanger is identical to the design for 0.95 effectiveness.

Weight, face area, and liquid pressure drop for these designs are shown in Figure 2-29 as functions of gas fractional pressure drop. The fin configuration used in all cases corresponds to fin set 3 of Table 2-4, and the heat exchanger aspect ratio (stack height divided by liquid flow length) was kept constant throughout the analysis at 0.3. Table 2-7 summarizes the results at a gas fractional pressure drop of 0.9 percent.

TABLE 2-7
WASTE HEAT EXCHANGER DESIGNS AT $E=0.935^*$

Number of Liquid Passes	Heat Exchanger Wet Mass, kg	Gas Face Area, sq m	Liquid Pressure Drop, kN/sq m
6	280	0.342	66
7	260	0.335	103
8	252	0.323	145

*Coolant = MIPB, $\Delta P/P$ gas = 0.009

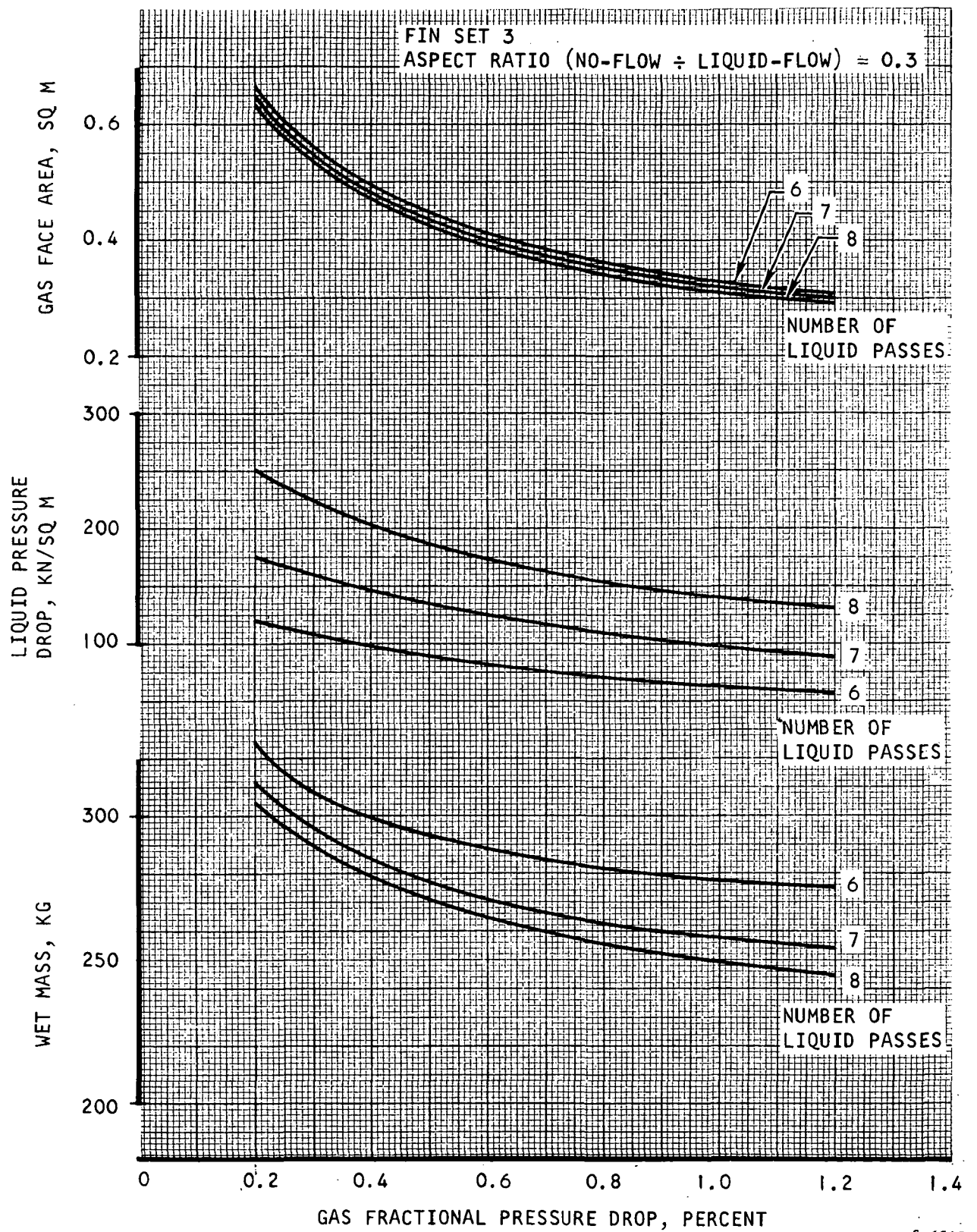


Figure 2-29. Waste Heat Exchanger Characteristics
Using MIPB at 0.935 Effectiveness

At seven liquid passes, the pressure drop limit of 103 kN/sq m is just met with a heat exchanger mass of 260 kg. The face area of 0.335 sq m approximately matches the recuperator low-pressure outlet face for this assumed gas pressure drop split.

Performance of the waste heat exchanger, as designed for use with MIPB at an effectiveness of 0.935, is summarized for each of the three candidate coolants in Table 2-8. Use of either of the Dow-Corning fluids would give a higher effectiveness at a lower liquid pressure drop than is obtained using MIPB.

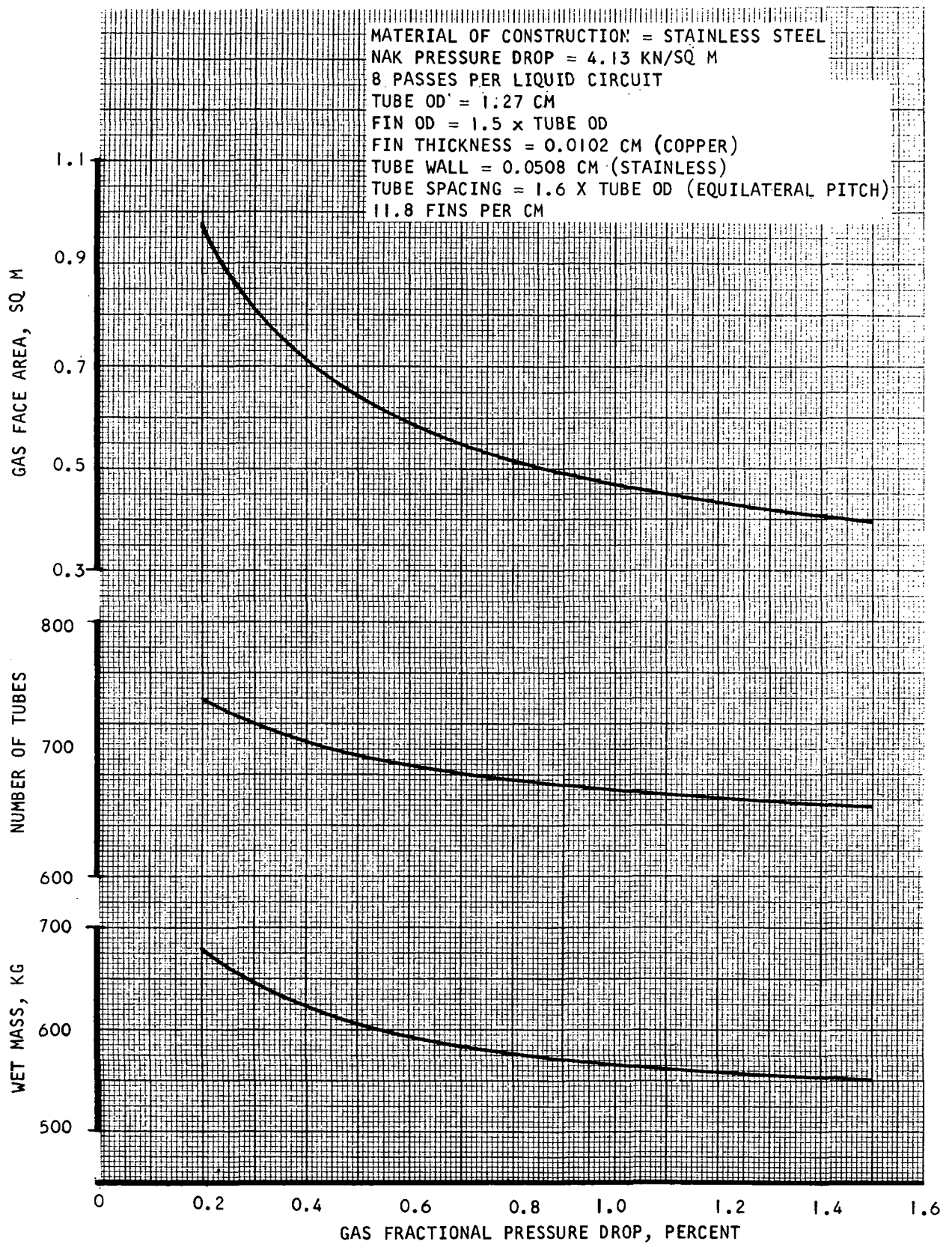
TABLE 2-8
PERFORMANCE OF MIPB WASTE HEAT EXCHANGER AT E=0.935

Coolant	Effectiveness	Gas Pressure Drop, percent	Liquid Pressure Drop, kN/sq m
MIPB	0.935	0.900	103
DC-200 (2.0 cs)	0.948	0.898	90
DC-200 (1.0 cs)	0.947	0.898	62

The effect of axial conduction of heat on heat exchanger performance was calculated for the seven-pass design. The calculation was performed for an equivalent pure counterflow heat exchanger with the same metal area, gas flow length, and effectiveness as the actual cross-counterflow unit. This method of analysis has been found to be satisfactory for cases in which the axial conduction effect is relatively small. The analysis showed a 3.75 percent reduction in equivalent UA due to axial conduction. Since this amount of UA margin was included in the original design to account for axial conduction, no adjustment to the design was necessary.

3. NaK Waste Heat Exchanger

A finned-tubular unit using NaK-78 as the coolant was designed. The effectiveness of this unit was 0.95. Weight, gas face area, and number of coolant tubes are shown in Figure 2-30 as functions of the gas fractional pressure drop. Due primarily to the relatively large structural wrap-up for this unit, which weighs from 50 percent to 100 percent of the tube-fin core, this unit is not competitive with the plate-fin units. Figure 2-30 is based on the use of two independent cores in series to provide a redundant liquid circuit. The gas fractional pressure drop corresponds to the case in which the downstream core is active and the upstream core is on standby, this being the worst of the two possible cases due to the higher average gas temperature in this case. The NaK pressure drop of 4.13 kN/sq m was selected to give approximately the correct heat exchanger aspect ratio for matching with the recuperator.



S-65145

Figure 2-30. Waste Heat Exchanger Characteristics Using NAK-78 Coolant

SYSTEM DESIGN

Close-Coupled Heat Source Heat Exchanger System

Since the seven-pass design was selected for the waste heat exchanger, resulting in a close match of the recuperator and waste heat exchanger face areas at the assumed pressure drop allocation of 0.9 percent for the waste heat exchanger, a reoptimization of the system pressure drop split was not necessary. The pressure loss distribution for the reference design HXDA, therefore, consists of 0.9 percent in the waste heat exchanger and (from the studies matching recuperator and heat source heat exchanger) 1.15 percent in the recuperator and 0.45 percent in the heat source heat exchanger. This distribution assumes an allowance of 0.5 percent pressure drop for the ducts and manifolds.

The heat exchanger designs for the reference design HXDA are summarized in Table 2-9. Total heat exchanger mass in this HXDA design, including liquid inventories in the waste and heat source heat exchangers, is 715 kg.

Based on these core designs, layout drawings were prepared for the three system heat exchangers and are presented in the following drawings:

SK 51891 Recuperator

SK 51892 Heat Source Heat Exchanger

SK 51893 Waste Heat Exchanger

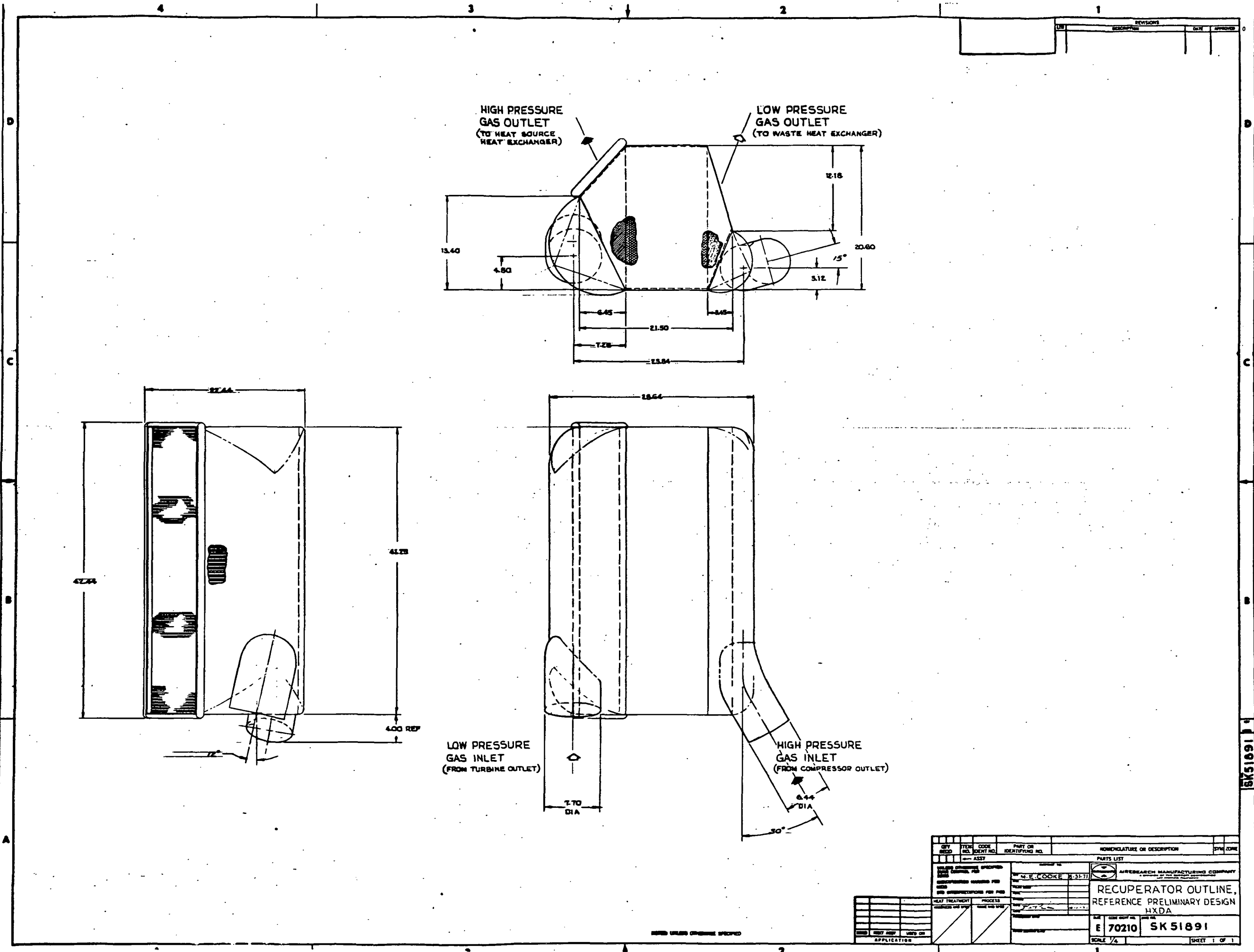
A layout drawing of the complete HXDA with the close-coupled heat source heat exchanger, and including the latest version of the TAC, is presented in SK 51879.

Duct and Manifold Sizes

An analysis was made of the pressure losses in the HXDA ducts and manifolds. The losses calculated include friction and turn losses in the ducts, losses associated with area change at duct/manifold interfaces, friction losses in the manifolds, and turning and area change losses involved in the transitions between manifolds and heat exchanger cores. The total pressure drop allotted to manifolds and ducts in the HXDA reference preliminary design is 0.5 percent.

The analysis of pressure losses is based on the reference system configuration shown in SK 51879, with ducts sized for constant gas velocity head throughout the ducting system. As an initial estimate of duct and manifold sizes, the duct diameters established during the HXDA preliminary design study (NASA CR-72816) were increased by 10 percent for the present system and the manifolds were made full-radius (i.e., manifold diameter set equal to the mating core dimension). Resulting duct and manifold diameters are listed in the second column of Table 2-10. These sizes correspond to the diameters shown on the reference system layout drawing SK 51879 with the exception of the turbine outlet duct, which is incorrectly sized on that drawing. Total calculated pressure loss for this ducting configuration is 0.707 percent, exceeding the 0.5 percent allotted for ducts and manifolds.

<u>Recuperator</u>	
Gas pressure drop	1.15 percent
Mass	382 kg
Core length	0.295 m
End section height, hot end	0.164 m
cold end	0.0876 m
End section ratio, hot end	0.65
cold end	0.573
Width	0.524 m
Stack height	1.05 m
<u>Waste Heat Exchanger</u>	
Gas pressure drop	0.90 percent
Mass (wet)	260 kg
Liquid pressure drop	103 kN/sq m
Gas-flow length	0.403 m
Liquid-flow length	1.06 m
Stack height	0.320 m
<u>Heat Source Heat Exchanger</u>	
Gas pressure drop	0.45 percent
Mass (wet)	73 kg
Liquid pressure drop	5.1 kN/sq m
Gas-flow length	0.143 m
Tube length (core)	1.06 m
No-flow length (core)	0.243 m
Number of tubes	92
Number of tube rows	8
Number of passes	2



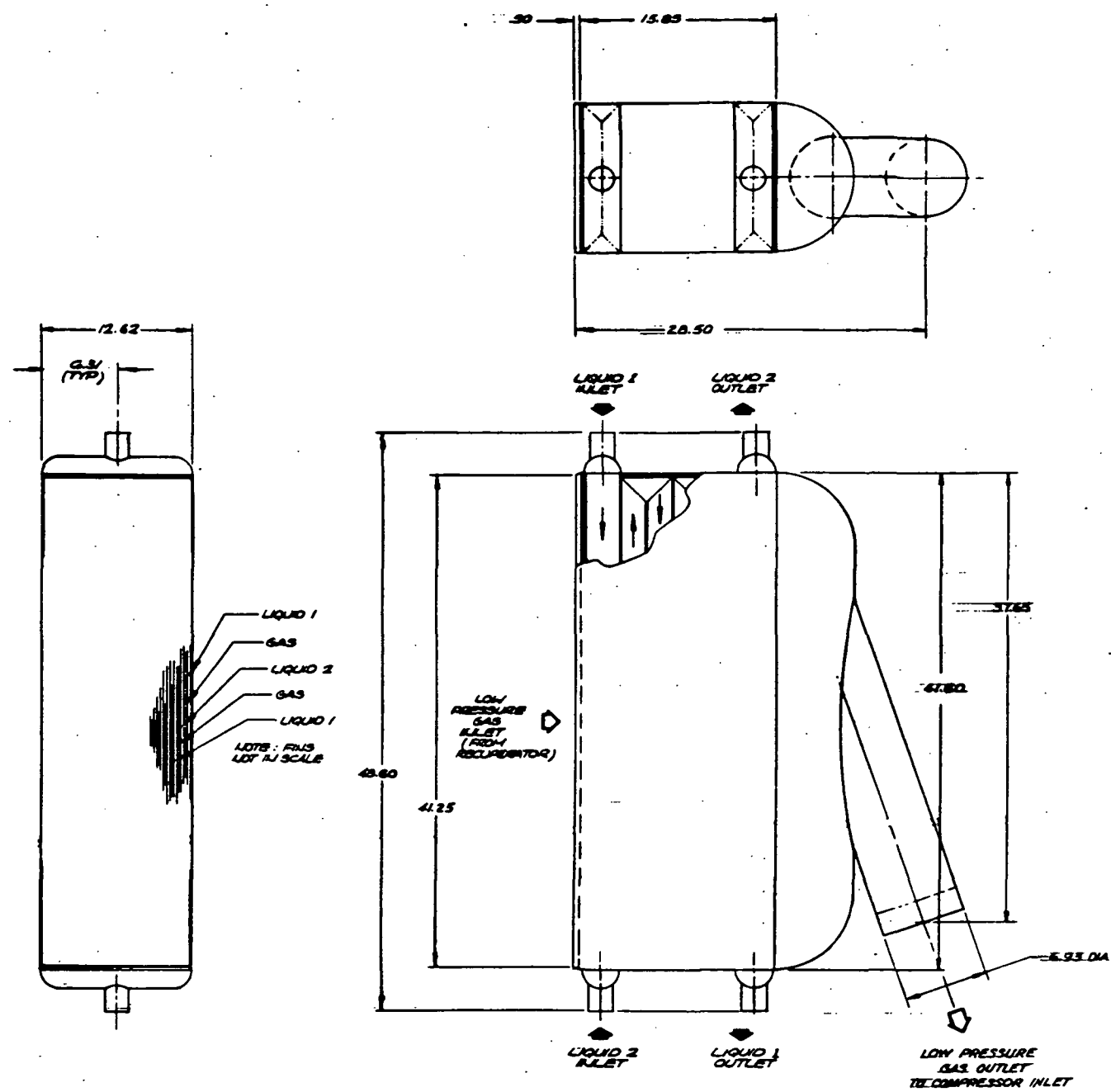
REV	DESCRIPTION	DATE	APPROVED
1			

QTY	ITEM	CODE	PART OR	DESCRIPTION OR DESCRIPTION	SYMBOL
REQD	NO.	IDENT NO.	IDENTIFYING NO.		
			ASSY		

MATERIAL SPECIFICATIONS		PROCESS	
ITEM	DESCRIPTION	ITEM	DESCRIPTION
1	STEEL	1	HEAT TREATMENT
2	BRASS	2	FINISH
3	COPPER	3	PAINT
4	ALUMINUM	4	ANODIZING
5	TITANIUM	5	WELDING
6	INCONEL	6	DRILLING
7	STAINLESS STEEL	7	MACHINING
8	MONEL	8	GRINDING
9	NICKEL	9	TURNING
10	PHOSPHOR BRONZE	10	THREADING
11	SILVER	11	REWORK
12	GOLD	12	SCRAP
13	PLATINUM	13	REWORK
14	IRIDIUM	14	SCRAP
15	OSMIUM	15	REWORK
16	ROSE GOLD	16	SCRAP
17	COBALT	17	REWORK
18	NIOBIUM	18	SCRAP
19	MOLYBDENUM	19	REWORK
20	ANTIMONY	20	SCRAP
21	BISMUTH	21	REWORK
22	GERMANIUM	22	SCRAP
23	ARSENIC	23	REWORK
24	SELENIUM	24	SCRAP
25	TELLUR	25	REWORK
26	POLYMER	26	SCRAP
27	GLASS	27	REWORK
28	CERAMIC	28	SCRAP
29	COMPOSITE	29	REWORK
30	OTHER	30	SCRAP

PARTS LIST	
ITEM NO.	DESCRIPTION
1	RECUPERATOR OUTLINE, REFERENCE PRELIMINARY DESIGN HXDA

SCALE	SHEET
1/4"	1 OF 1



QTY	ITEM	CODE	PART OR IDENTIFYING NO.	DESCRIPTION OR DESCRIPTION	QTY
1	WASTE HEAT EXCHANGER				1
PARTS LIST					
WASTE HEAT EXCHANGER OUTLINE - REF PRELIMINARY DESIGN HYDA					
E 70210		SK 5/893		SCALE 1/2"	
SHEET 1 OF 1					

NOTES: UNLESS OTHERWISE SPECIFIED

To reduce the ducting losses, all duct diameters were increased by 20 percent resulting in the sizes shown in the fourth column of Table 2-10. In addition, the heat source heat exchanger outlet manifold was sized larger than full-radius to obtain a manifold flow area equal to the area of the turbine inlet duct. With these changes, total calculated pressure loss in the ducting system is 0.447 percent, which meets the design value with a margin of 12 percent:

TABLE 2-10
DUCT SIZES AND PRESSURE LOSSES

	Initial Layout		Resized	
	Dia (cm)	Pressure Loss (percent)	Dia (cm)	Pressure Loss (percent)
Turbine inlet duct	19.5	0.078	23.5	0.045
Turbine outlet duct	21.5	0.181	25.8	0.108
Compressor inlet duct	17.6	0.124	21.1	0.068
Compressor outlet duct	16.4	0.098	19.6	0.056
Recup. L.P. inlet manifold	36.1	0.096	36.1	0.062
WHX outlet manifold	30.7	0.013	30.7	0.013
Recup. H.P. inlet manifold	24.0	0.092	24.0	0.092
HSX outlet manifold	24.4	0.025	25.9	0.003
Total	--	0.707	--	0.447

Remote Heat Source Heat Exchanger System

The design of a remote heat source heat exchanger was studied parametrically. The design requirements for this heat exchanger are given in Table 2-11. Because of its assumed location in a bay area between segments of the reactor shield, the intermediate NaK loop is eliminated from the system and the heat source heat exchanger transfers heat directly from the reactor loop to the working gas. As a result, the inlet NaK temperature is increased slightly and the required heat exchanger effectiveness is reduced a small amount as compared with the design conditions for the close-coupled heat source heat exchangers.

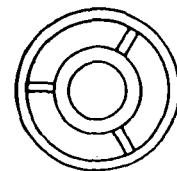
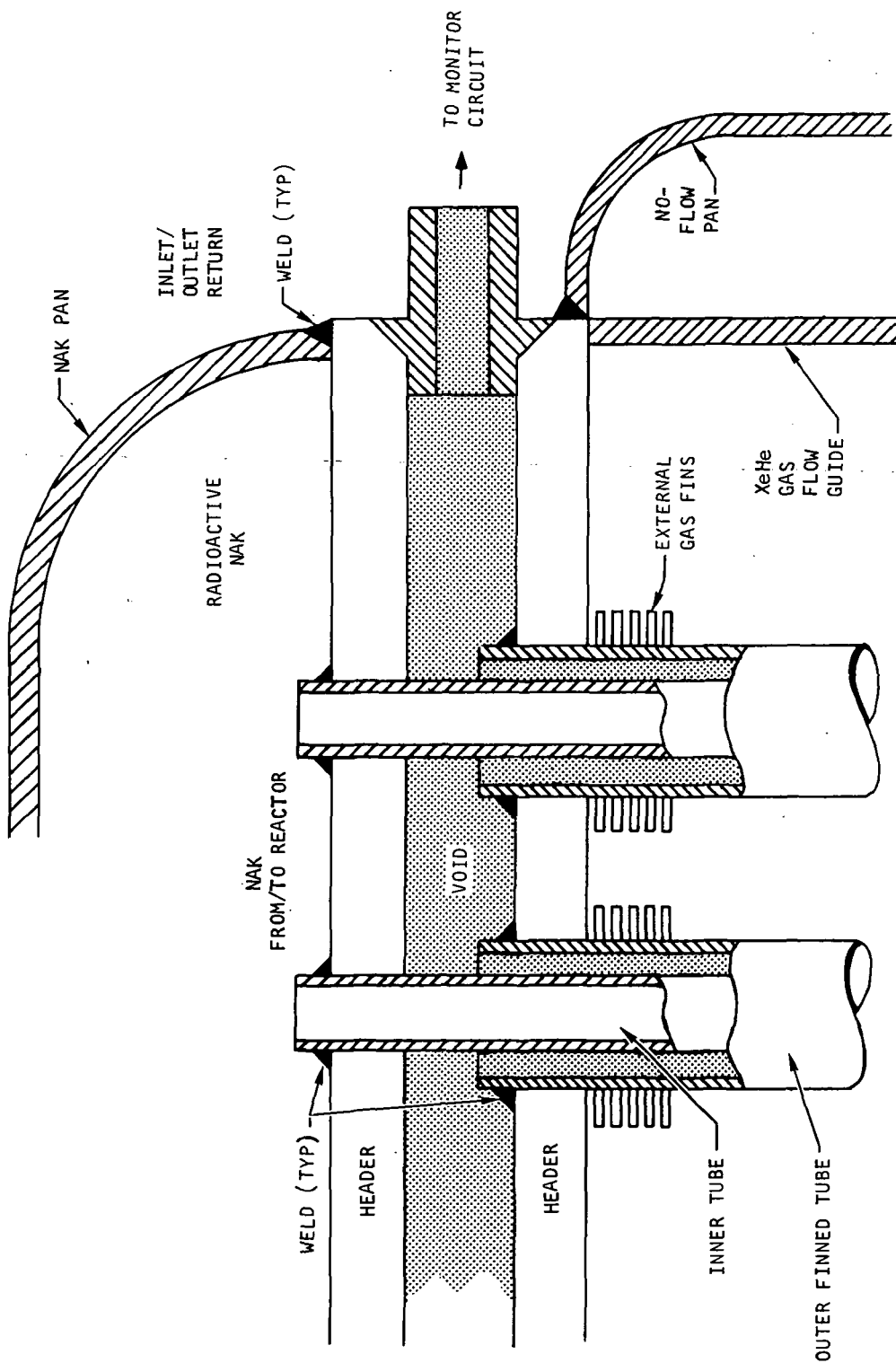
Two system flow configurations were considered, as indicated in Table 2-11, providing for two different ways of integrating a second heat exchanger into the reactor loop. In the parallel flow system, the second heat exchanger is placed in parallel with the heat source heat exchanger, resulting in a 50 percent bypass of the NaK flow and a NaK temperature drop equal to twice the NaK temperature rise in the reactor. In the series flow system, the second heat exchanger is placed either upstream or downstream of the heat source heat exchanger and thus does not affect the heat source heat exchanger design conditions.

TABLE 2-11
REMOTE HEAT SOURCE HEAT EXCHANGER DESIGN CONDITIONS

	Parallel Flow System	Series Flow System
NaK flow rate, kg/sec	4.08	8.16
NaK inlet temperature, K	914	914
NaK outlet temperature, K	831	872
XeHe flow rate, kg/sec	2.86	2.86
XeHe inlet temperature, K	694	694
XeHe outlet temperature, K	894	894
XeHe inlet pressure, kN/sq m abs	689	689

To ensure separation of the reactor loop NaK from the gas system, the heat exchanger design includes double tubes and headers with an interior void zone. This concept is shown in Figure 2-31. The outer finned tubes are 1.27 cm OD with a 0.0508 cm wall. The concentric inner tubes are 1.14 cm OD with a 0.0508 cm wall, leaving a 0.0127 cm gap between tubes. The void zone extends into the areas between the two header plates at both ends of the exchanger and is pressurized from an external source.

Weights and core dimensions of the remote heat source heat exchanger are shown as a function of gas fractional pressure drop and liquid pressure drop in Figure 2-32 for the parallel flow system and Figure 2-33 for the series flow system. The curves of heat exchanger mass include an estimate of structural wrap-up (no-flow pans, headers, etc.), but the dimensions plotted are for the core only. Overall heat exchanger dimensions would be increased by the size of the no-flow pans, gas inlet and outlet manifolds, and liquid manifolds and return pan.



HEAT SOURCE HEAT EXCHANGER
MATERIAL: HAYNES 25 OR 188

S-65806 -C

Figure 2-31. HS-HX-NAK Buffer Zone Concept

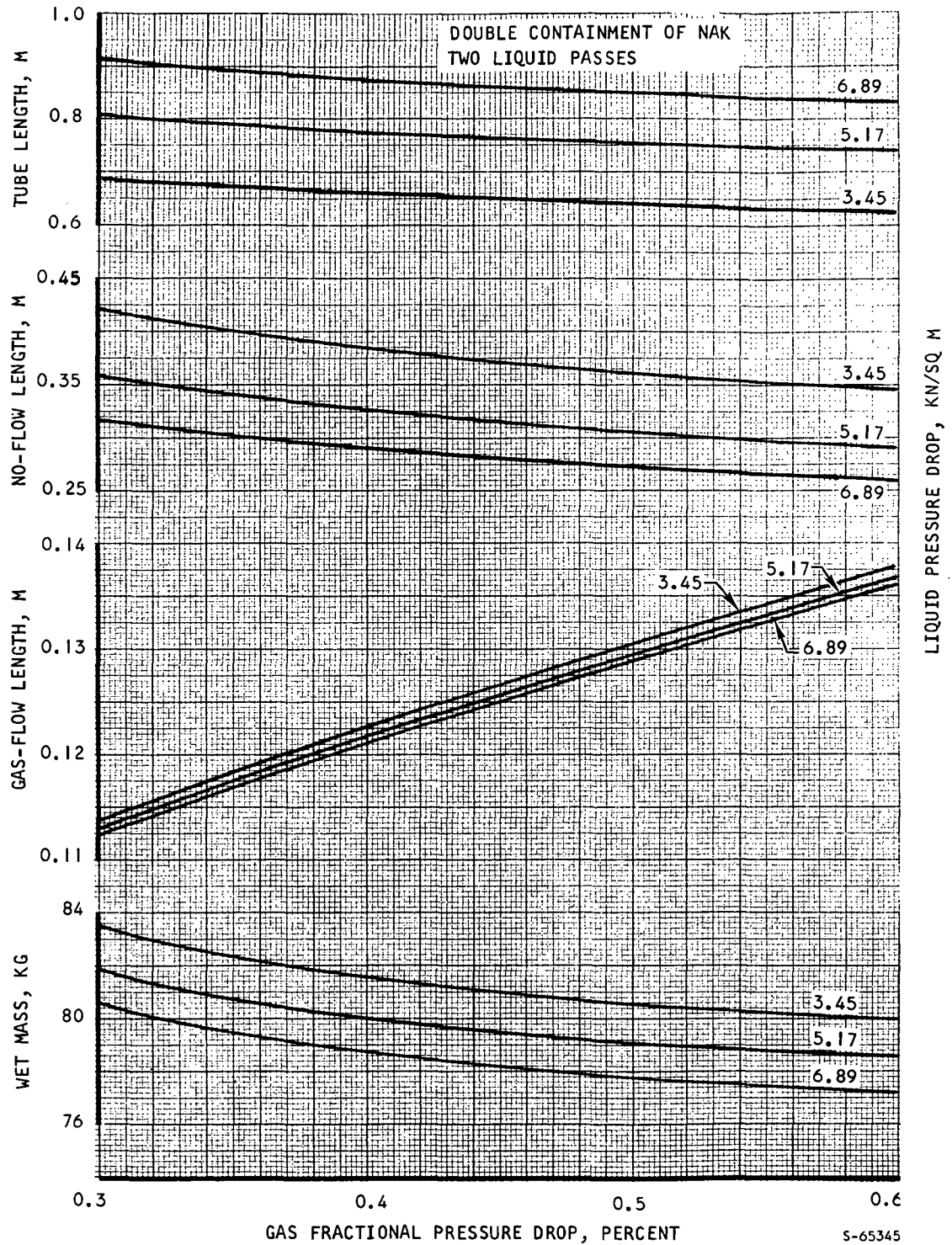


Figure 2-32. Remote Heat Source Heat Exchanger Characteristics in Parallel Flow System (Dimensions for Core Only)

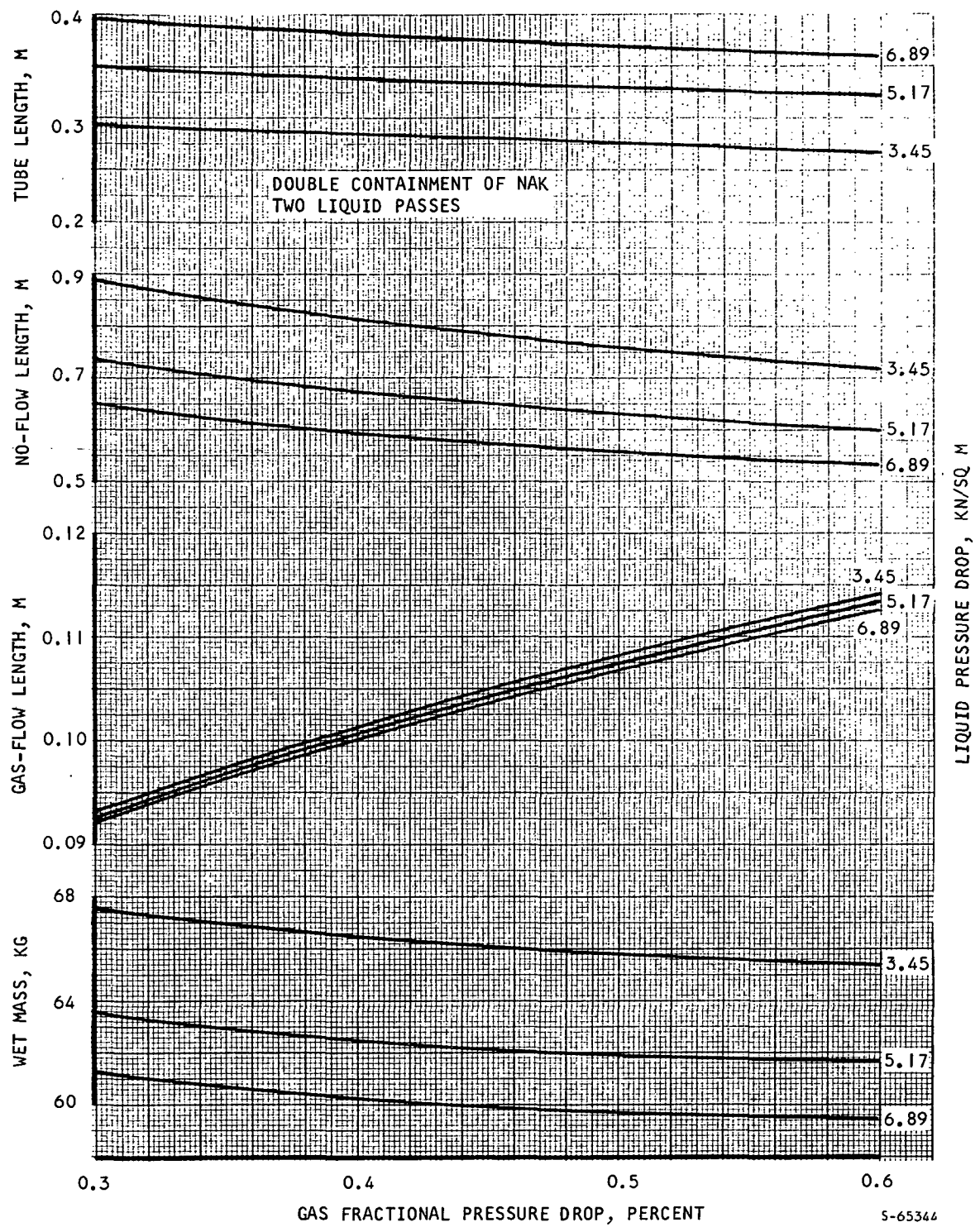


Figure 2-33. Remote Heat Source Heat Exchanger Characteristics in Series Flow System (Dimensions for Core Only)

In the parallel flow system, assuming that both the no-flow pans and gas manifolds are of the full radius type, overall heat exchanger dimensions in the no-flow and gas-flow directions would be approximately the same and equal to the sum of the no-flow and gas-flow core directions. At a gas fractional pressure drop of 0.45 percent and liquid pressure drop of 6.89 kN/sq m, for example, total exchanger dimensions would be approximately 41 cm by 41 cm by 100 cm (allowing 14 cm for liquid manifolds and return pan). Allowing additional space for thermal insulation, the required separation between shield segments for this design point would be approximately 50 cm. A slight reduction in pan size is possible through the use of elliptical, rather than circular, pans. In addition as seen in Figure 2-32, increasing the liquid pressure drop will result in a reduction in both the gas-flow and no-flow lengths.

In the series flow system, again assuming full radius pans and manifolds, the minimum overall heat exchanger dimension is the tube length dimension. At a gas fractional pressure drop of 0.45 percent and a liquid pressure drop of 3.45 kN/sq m, the total tube length dimension would be approximately 36 cm (allowing eight cm for liquid manifolds and return pan). Allowing additional space for thermal insulation, the required separation between shield segments for this design point would be approximately 45 cm. This could be reduced, at the expense of heat exchanger weight and number of tubes, through a further reduction in liquid pressure drop.

A comparison of the heat source heat exchanger designs for the two system flow configurations, based on the design points quoted above, is given in Table 2-12. The overall dimensions in this table are approximate and would be defined more exactly from detailed packaging and layout studies.

TABLE 2-12
COMPARISON OF PARALLEL FLOW AND SERIES FLOW
HEAT SOURCE HEAT EXCHANGERS

	Parallel Flow System	Series Flow System
Gas pressure drop, percent	0.45	0.45
Liquid pressure drop, kN/sq m	6.89	3.45
No-flow dimension, cm	41	89
Gas-flow dimension, cm	41	39
Tube length dimension, cm	100	36
Heat exchanger wet mass, kg	78	66
Number of coolant tubes	94	222

An outline drawing of the remotely located heat source heat exchanger is shown in SK 51930. The design shown in this sketch is based on a gas fractional pressure drop of 0.3 percent rather than the reference design value of 0.45 percent. The former value is more in line with a minimum-weight pressure drop split and also provides some additional pressure drop allowance for the increased ducting length of the remote HSHX system.

Drawing SK 51950 presents a preliminary layout of the HXDA showing the remotely located heat source heat exchanger. This heat exchanger is located in a shielded gallery along with other liquid metal components. The HXDA package is mounted on top of the outer surface of the shadow shield and there is sufficient room available so that two complete HXDA units could be supported from the single support frame.

STRUCTURAL ANALYSIS AND DESIGN

Structural Design Considerations

1. Operating Conditions

The specified operating requirements for the HXDA are

100,000 hr service life

1000 operating cycles

In addition, the system will be designed for inertia loads as specified in NASA Environmental Specification No. P2241-1 dated March 1, 1969. The design loads assume the HXDA to be shock mounted with a 15 Hz isolation system so that HXDA resonant amplifications above 50 Hz will be highly attenuated. The specified vibratory input at 15 Hz is 0.14 in. double amplitude displacement, giving 1.6 g in all directions. A damping coefficient equal to 10 percent of critical damping will limit the amplification factor to 5.0 at resonance, producing 8 g vibratory loading at the mount points. This mounting system would also provide shock isolation from the 20 g, half-sine-pulse of 10 millisecond time duration. Assuming a shock isolation factor of 0.5, the load at the mount brackets would be approximately 10 g. These loads combine with the 6 g constant longitudinal and 2 g constant lateral accelerations to produce the following design factors:

Longitudinal = 8 vibration + 10 shock + 6 acceleration = 24 g total

Lateral = 8 vibration + 10 shock + 2 acceleration = 20 g total

It is assumed that internal resonances will be sufficiently damped by the isolation system so that the 8 g vibration incurred at the 15 Hz mount system resonance is the maximum experienced by the HXDA. The longitudinal direction is assumed to be parallel to the TAC axis of rotation.

The mechanical design is based on the specified fluid conditions shown in Table 2-13. The heat exchanger conditions are presented in Table 2-13a and the duct conditions are summarized in Table 2-13b.

2. Structural Design Criteria

A variety of load conditions, stress conditions, and failure mode possibilities will be experienced by the unit during its ten-year service life. The detailed set of design criteria discussed below are used to design the various components.

a. Allowable Stresses for Internal Pressure and Inertia Load Design

A distinction will be made between direct stress causing uniform stress across a section, and bending which leads to maximum stresses only at the extreme fibers. This is a natural separation since structural deformations due to the two types are significantly different. The format for design curves of allowable stress vs operating temperature is also outlined.

(1) Direct Stresses

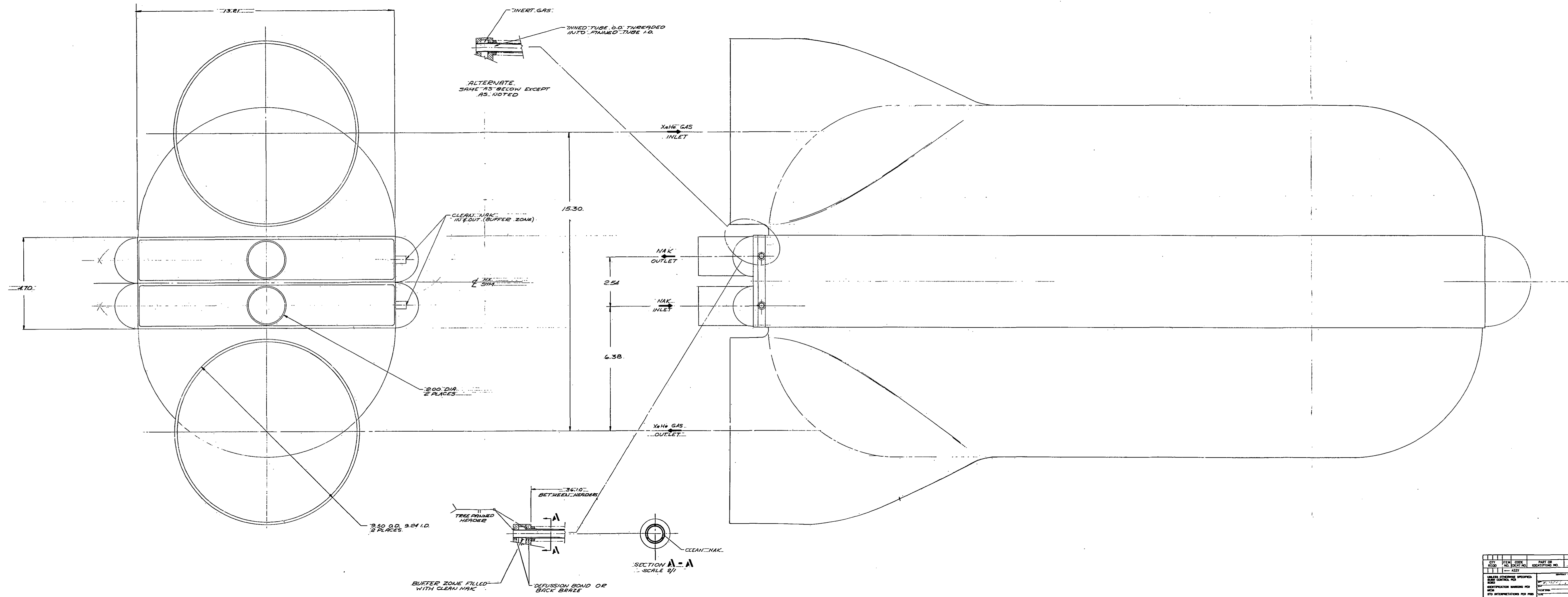
The standard design practice employed by AiResearch is to design the pressure carrying structure for proof pressures of 1.5 times the working pressures and for burst pressures of 2.5 times the working pressures. The structure must not yield at proof pressure or rupture at burst pressure. This implies that the proof pressure is the governing design condition if the ratio of yield stress to ultimate stress is less than 0.6 and that the burst pressure will govern if the ratio is greater than 0.6. The allowable stress at working pressure is, therefore, the lesser of the following:

$$\sigma_{all} = (\sigma_{ult})/2.5 \quad (2-1a)$$

$$\sigma_{all} = (\sigma_y)/1.5 \quad (2-1b)$$

Stresses due to the 20 or 24 g design inertia loads discussed above will also be governed by these criteria. This will ensure that excessive deformations do not occur at design loads and that vibratory load components, which are less than half of the total, do not cause fatigue failure. With these criteria, infinite structural life will be achieved since stresses will be below the material endurance life.

At elevated temperature for extended operating times, the above conditions must be satisfied and, in addition, the component must be satisfactory for creep effects. The criteria for creep, comparable to those for the short time loading, will be based upon stress-to-rupture and stress-to-one percent creep. Sustained pressure and inertia load operation is assumed at maximum operating temperature throughout the entire ten-year life. This is realistic for fluid pressure containment, however, it is a conservative approach for inertia loads which may be of short duration compared to the service life. However, this approach appears to be warranted due to the unknown duration



QTY	ITEM	CODE	PART OR IDENTIFYING NO.	NOMENCLATURE OR DESCRIPTION	SYM ZONE										
1	ASSEMBLY			HEAT EXCHANGER, HEAT SOURCE											
<table border="1"> <tr> <td>UNLESS OTHERWISE SPECIFIED:</td> <td>STANDARD</td> </tr> <tr> <td>IDENTIFICATION MARKING PER MIL-STD-1312</td> <td>PER MIL-STD-1312</td> </tr> <tr> <td>HEAT TREATMENT</td> <td>PROCESS</td> </tr> <tr> <td>FINISH</td> <td>FINISH</td> </tr> <tr> <td>WARRANTY</td> <td>WARRANTY</td> </tr> </table>						UNLESS OTHERWISE SPECIFIED:	STANDARD	IDENTIFICATION MARKING PER MIL-STD-1312	PER MIL-STD-1312	HEAT TREATMENT	PROCESS	FINISH	FINISH	WARRANTY	WARRANTY
UNLESS OTHERWISE SPECIFIED:	STANDARD														
IDENTIFICATION MARKING PER MIL-STD-1312	PER MIL-STD-1312														
HEAT TREATMENT	PROCESS														
FINISH	FINISH														
WARRANTY	WARRANTY														
70210 SK 51930				HEAT EXCHANGER, HEAT SOURCE											
SCALE 1/1				SHEET 1 OF 1											

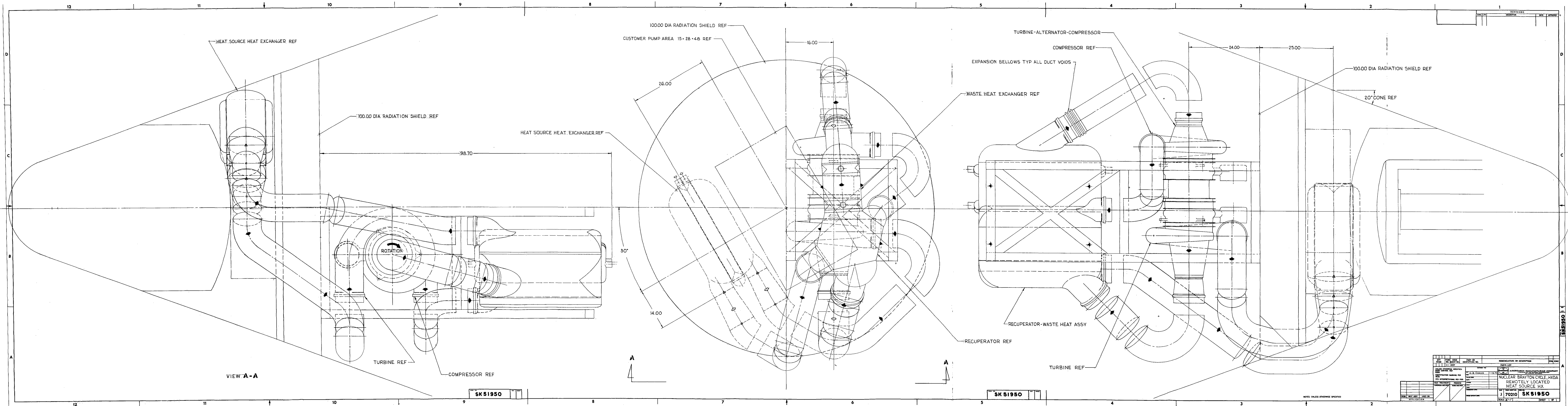


TABLE 2-13

FLUID CONDITIONS FOR MECHANICAL DESIGN

a. Heat Exchangers

Unit	Condition	Fluid	Maximum Fluid Conditions		
			Pressure, (1) kN/sq m	Temperature, K	
				Inlet	Outlet
Heat Source Hx	100,000 Hr Operation	NaK	340	980	
		He-Xe	1380		
	Shutdown	He-Xe	1100		
Recuperator	100,000 Hr Operation	He-Xe	830		590
		He-Xe	1380		590
	Shutdown	He-Xe (Both Circuits)	1100	960	590
Waste Hx	100,000 Hr Operation	DC100	520 ⁽²⁾	420	590
		He-Xe	830	590	420
	Shutdown	He-Xe	1100	590	420

NOTE: (1) Pressure difference between passes will be the maximum on either side.

(2) Tentative, not specified as the maximum

b. He-Xe Ducts

Duct	Condition	Maximum Fluid Conditions	
		Pressure, kN/sq m	Temperature, K
HSHX to TAC turbine	100,000 Hr	1380	1140
	Shutdown	1100	1140
TAC turbine to recuperator	100,000 Hr	830	960
	Shutdown	1100	960
TAC compressor to recuperator	100,000 Hr	1380	590
	Shutdown	1100	590
WHX to TAC compressor	100,000	830	420
	Shutdown	1100	420

of inertia loads and the simplification of the design criteria. Allowable stresses at working pressure will be the lesser of the following.

$$\sigma_{all} = [(1\text{-percent creep stress})_{100,000 \text{ hr}}]^{1/1.2} \quad (2-2a)$$

$$\sigma_{all} = [(\text{creep-rupture stress})_{100,000 \text{ hr}}]^{1/1.5} \quad (2-2b)$$

Material properties at elevated temperatures are very sensitive to temperature. For the candidate materials, an increase in temperature of 56 K typically leads to a decrease of approximately 33 percent in creep and stress rupture strengths. Therefore, an allowance must be made to account for the possibility of overtemperature. The design temperature used to establish allowable stresses is taken to be the maximum operating temperature plus 56 K. This overtemperature criterion results in an effective safety factor greater than those shown in Equation 2-2.

(2) Bending Stresses

When yield or ultimate strength governs the design and the limiting stress is due to bending, a small amount of yielding can be allowed in the outermost fibers. This yielding leads to a modified stress distribution through the thickness and the ideal plastic bending moment is 1.5 times the computed elastic bending moment for the same peak stress. Accordingly, the allowable indicated elastic stress due to bending loads will be 1.5 times the allowable values in Equation 2-1.

For bending load designs which will be governed by the material creep properties, the steady creep stresses are substantially lower than those indicated by an elastic analysis. By using the plastic hinge moment analogy, the allowable creep bending stress is also 1.5 times the values for direct stresses. Stated slightly differently, the actual sustained creep stress due to bending is taken to be 0.667 times the indicated elastic stress.

(3) Composite Design Curve Format

The above criteria can be efficiently summarized by plotting the allowable stress vs operating temperature for each material. The schematic curve in Figure 2-34 illustrates the low temperature region governed by yield or ultimate strength and an elevated temperature portion where creep is the dominating factor. Separate curves are required for direct and bending stresses, although, in practice, the constant ratio of 1.5 between the two allowable stress lines makes it unnecessary to construct both curves.

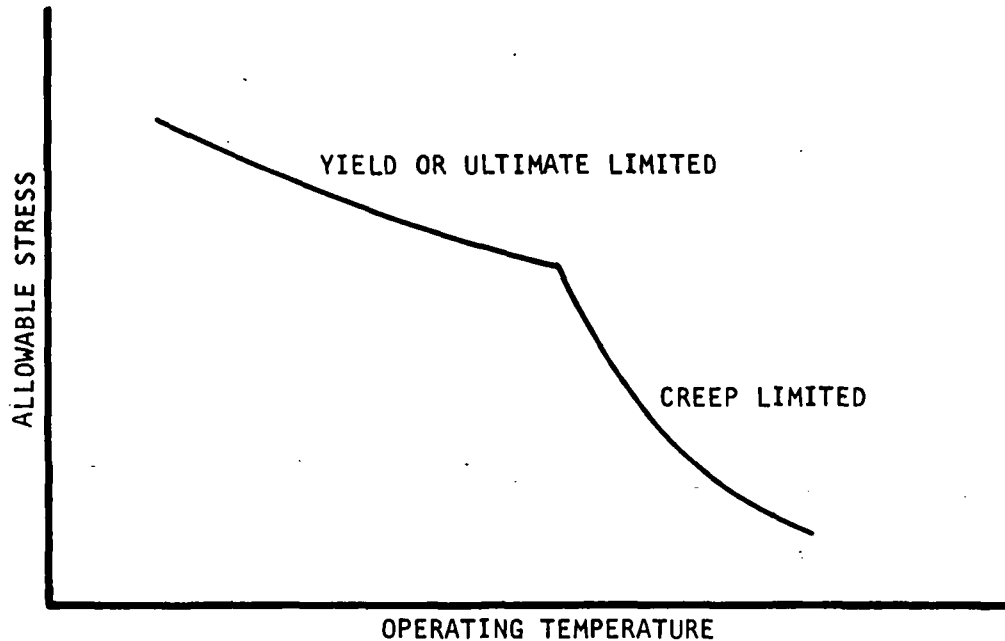


Figure 2-34. Design Curve Format for Pressure and Inertia Load Allowable Stress

b. Allowable Thermal Strains

The magnitude of thermal strains due to temperature differences developed during system operations will generally lead to a finite structure life (i.e., associated stresses will be above the material endurance limit). The specified minimum operating life requirement of the unit is 1000 thermal cycles so the acceptable thermal strain level must be established. A cycle will be defined as the sequence consisting of system startup, steady state operation for extended period and shutdown. A minimum design life of 4000 cycles will be used to provide a safety factor of about 2 on the thermal strain associated with the 1000 cycle design life. Design curves of allowable strain vs operating temperature will be computed for each material considering cycle life where fatigue dominates and or where creep is the prime factor.

Cumulative effects arising from varying load cycles or combinations of fatigue and creep damage will be based on the Robinson-Tiara approach recommended by Spera (Reference 1). The general expression for combined fatigue and creep damage for a variety of load cycles is the summation of cycle and time increments divided by the life for each load level, j:

$$\Delta\Phi = \Delta\Phi_F + \Delta\Phi_c = \sum_0^j \left(\frac{\Delta N_k}{N_{F,k}} + \frac{\Delta t_k}{t_{r,k}} \right) \quad (2-3)$$

where $\Delta\Phi$ = damage/cycle

$\Delta\Phi_F$ = fatigue damage/cycle

$\Delta\Phi_C$ = creep damage/cycle

ΔN_k = cycles at load level k

$N_{F,k}$ = cycle life at load level k

Δt_k = time at load level k

$t_{r,k}$ = time to creep rupture at load level k

Failure is assumed when

$$\sum \Delta\Phi = 1$$

Life estimates based on this approach are accurate for the fatigue fraction, however, at the present time considerable uncertainty exists in computing creep damage. Since creep damage can be an important factor, the best estimates are preferred to ignoring the phenomenon.

(1) Low-Cycle Fatigue with No Creep Interaction

At temperatures where creep is not a factor, the allowable strain will be based on the Manson method (Reference 2) for computing fatigue life based on the accumulated plastic strain. The cycle life, N , is related to the plastic strain range, ϵ_p , by

$$N = (C/\epsilon_p)^{1.67} \quad (2-4)$$

where C , the ductility constant, is based on material reduction-in-area properties, RA , by the relation

$$C = \{\ln [100/(100 - RA)]\}^{0.6}$$

The fatigue damage per cycle for a single strain level is therefore

$$\Delta\Phi_F = (\epsilon_p/C)^{1.67} \quad (2-5)$$

The allowable strain for a given cycle life can be obtained directly from this equation when C is known.

(2) Low-Cycle Fatigue with Creep Interaction

At elevated temperatures, creep damage during each operating cycle adds to the fatigue damage and cycle life can be greatly reduced. For the creep

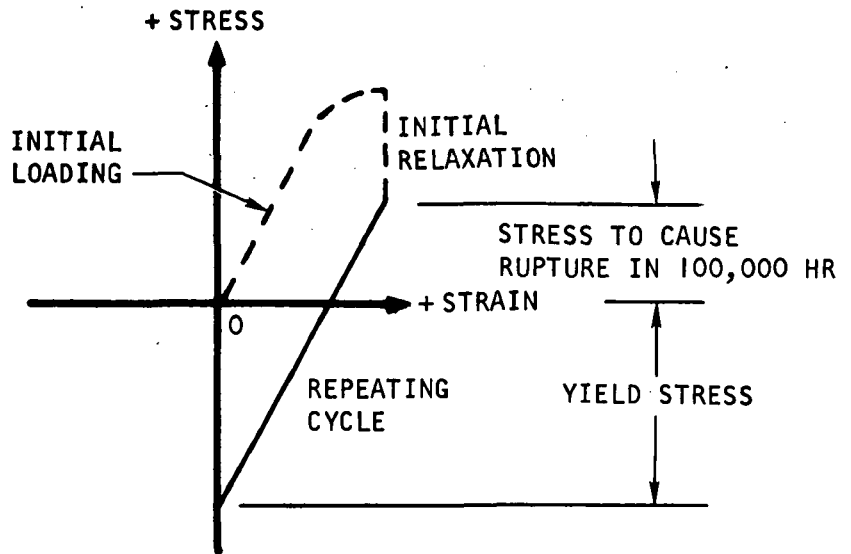
case the time history as well as the load cycle and associated stress-strain history must be defined. Accumulated creep damage can be divided into two types: (1) creep during a cycle characterized by continuously varying stresses and strains and (2) repetitive creep relaxation during extended times at constant applied strain. Of the two types, the accumulated damage due to repetitive creep relaxation is the most serious since the accumulated time under the applied constant strain may be nearly equal to the service life of the unit. Therefore, even though the stress steadily decreases during each interval of relaxation, the integrated damage cannot exceed that due to the acceptable constant stress applied for the 100,000 hr service life. Since the amount of relaxation becomes relatively small as the acceptable steady stress is reached, the allowable maximum repeating stress is approximately equal to this acceptable steady stress level. A repeating cycle which avoids this repetitive relaxation damage can be achieved by limiting the applied total strain, or applied apparent elastic stress, to the sum of the yield stress (strain) and the acceptable stress (strain) for 1 percent elongation in 100,000 hr. The allowable total strain is then

$$\epsilon_{all} = (\sigma_y + \sigma_{1\% \text{ in } 100,000 \text{ hr}})/E \quad (2-6)$$

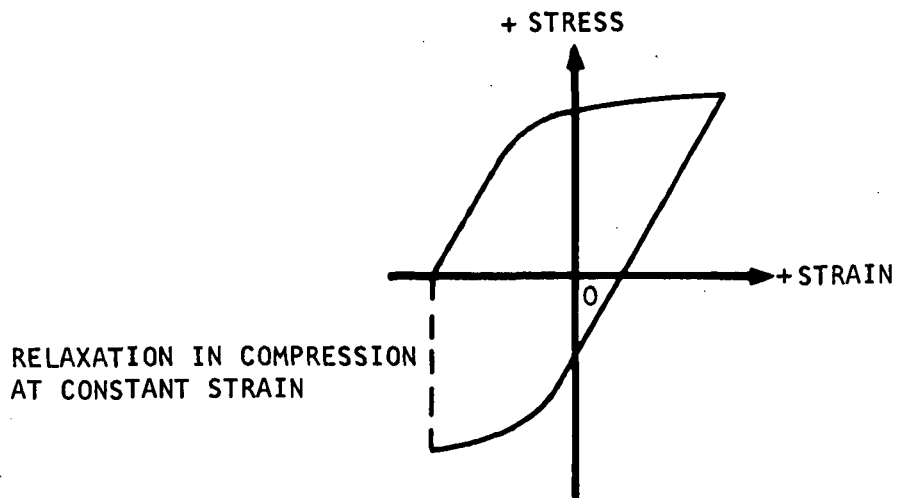
where E is the material elastic modulus. The acceptable cycle, shown in Figure 2-35, is preceded by an initial loading and stress relaxation at constant (maximum) strain. In subsequent cycles the material stress-strain history follows the elastic line from the yield stress at shutdown (cold) to the stress for 1 percent creep deformation (hot). The safety factor achieved by using this criteria will generally not be calculated; however, use of minimum yield values, stress to 1 percent elongation rather than rupture (also including overtemperature capability), and ignoring the small tolerable amount of relaxation at stresses above the acceptable steady-state level represent at least a factor of 1.25.

The above approach applies for either tensile or compressive sustained loads at elevated temperatures. However, recent work by Cooper (Reference 3) and Halford (Reference 4) indicates that compressive stresses are not damaging during constant strain or constant stress applications. This suggests that a second criterion be used when sustained tensile stresses are not present (bending loads are therefore excluded). The allowable repetitive strain can then be considerably greater than that given by Equation 2-6, but noticeably lower than the fatigue estimate due to the presence of accumulated creep damage. The damage can be estimated from Equation 2-1 for a stress-strain cycle such as shown in Figure 2-35b where no damage is attributed to a compressive relaxation if it exists. Good agreement of tests and estimates based on available engineering creep data have been obtained by Spera (References 1 and 5) and also from recent work at AiResearch for NASA Langley (Reference 6). For a single stress-strain loop the following expression will be evaluated to analytically determine the cycle damage fraction (overtemperature capability will again be included)

$$\Delta\phi_c = \int_0^t \frac{dt}{t_r} \quad (2-7)$$



- a. REPEATING CYCLE (SOLID LINE) TO AVOID REPETITIVE RELAXATION DAMAGE IN TENSION



- b. STABILIZED STRAIN LOOP WITH RELAXATION IN COMPRESSION (DAMAGE CALCULATED DURING CYCLE SHOWN BY SOLID LINE)

S-65000

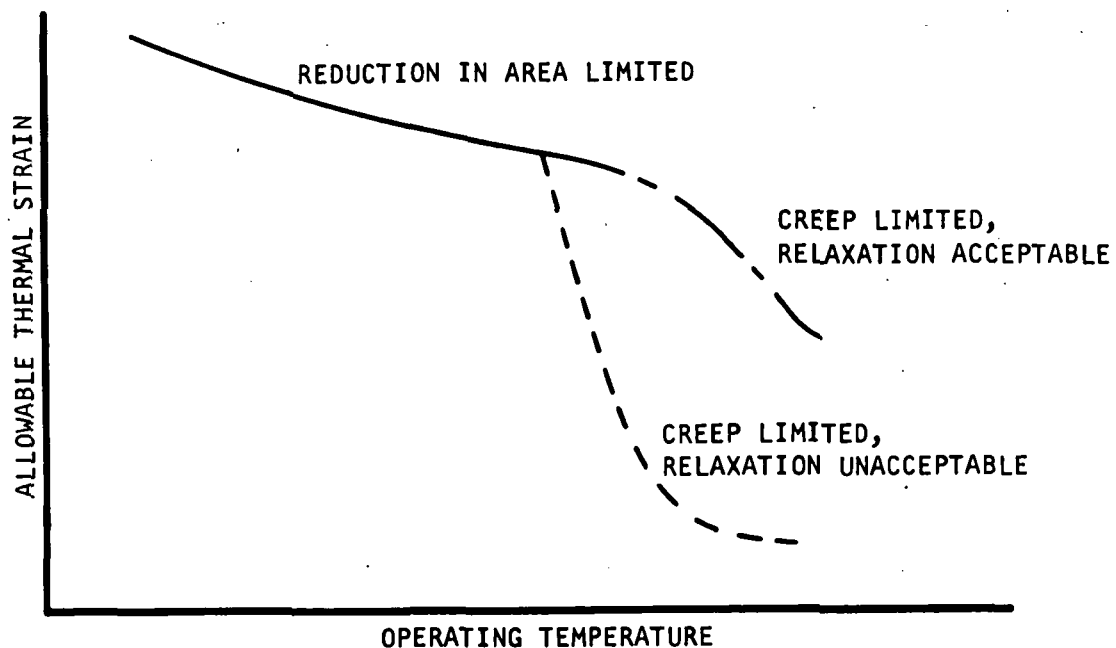
Figure 2-35. Typical Stress-Strain Cycles Illustrating Two Creep Damage Cases

Further discussion of the calculation of allowable strain for Hastelloy X given below illustrates the technique that will be used. It is also expected that supporting small scale tests to be performed on this program will provide improvements in the allowable thermal strain levels.

(3) Low-Cycle Fatigue Design Curve

With the above criteria, curves of allowable thermal strain vs operating temperature can be constructed for each material. An example schematic curve is shown in Figure 2-36. These curves are therefore analogous to the allowable stress vs temperature in Figure 2-34. It should be noted that the allowable total strain rather than the plastic strain component will be used in these design curves since total thermal strain is normally the output of an analysis of strains developed due to temperature differences in a structure. The total strain, plastic strain, and elastic strain in a repeating loop are related by

$$\epsilon_{\text{tot}} = 2 \epsilon_{\text{elastic}} + \epsilon_{\text{plastic}} \quad (2-8)$$



S-64997

Figure 2-36. Allowable Thermal Strain Design Curve Format

3. Material Properties

The maximum operating temperatures and the materials selected for various HXDA system components are summarized in Table 2-14.

TABLE 2-14

HXDA MATERIAL SELECTION SUMMARY

Component Type	Unit	Maximum Operating Temperature, K	Parent Materials	Weld Alloys	Braze Alloys
Heat Exchanger	Heat Source (HSHX)	980	Haynes 25	U	None
			Haynes 188 (alternate)		
	Recuperator	960	Hastelloy X	U	Palniro I Palniro Re Palniro 7
	Waste (WHX)	590	347 steel	U	Palniro I
Ducting	HSHX to TAC turbine	1140	321 steel (alternate)	U	None
			Nickel (fins)	U	Palniro I
			U	U	U
	TAC turbine to recuperator	960	Hastelloy X	U	U
Support Structure	TAC compressor to recuperator	590	347 steel 321 steel (alternate)	U	U
	WHX to TAC compressor	420	347 steel 321 steel (alternate)	U	U
	Frame	U	Inconel 718	U	U
			Alternates unspecified	U	U

U ~ Unspecified

Design values of parent metal material properties have been compiled for Nickel 201, 347 steel, Hastelloy X, and Haynes 25 following the approach outlined in the design criteria. This completes the parent metal properties for the waste heat exchanger (347 steel and Nickel 201), the recuperator (Hastelloy X) and the prime heat source heat exchanger material candidate (Haynes 25). The parent metal properties are summarized in Table 2-15 and allowable pressure and inertia stress and thermal strains are shown in Figures 2-37 through 2-40, for Nickel 201, 347 steel, Hastelloy X and Haynes 25, respectively.

The minimum yield strength and 1 percent creep stress values govern the allowable pressure and inertial load stresses as specified in equations 2-1 and 2-2 in the design criteria. Material creep properties will govern the design for Hastelloy X and Haynes 25 material at temperatures above approximately 800 K. The shaded creep limited region shown in Figures 2-40 and 2-41 (compressive relaxation permitted) was determined from stress-strain cycles at 1 cpm (lower limit) and 20 cpm (upper limit). The shaded band can also be considered to represent the uncertainty associated with the material behavior. The creep fraction of the total damage per cycle was estimated by equating the material creep rupture life to the stress level by the power law relation.

$$t_r = A\sigma^{-\ell} \quad (2-9)$$

where A and ℓ are a function of temperature. This relation combined with a linear relation between incremental total strain and time (linear strain rate) was used to compute creep damage.

The allowable stresses and strains apply to direct stresses on the parent material. Bending stresses are accommodated by modifications to the criteria discussed above. Also, the presence of weld or braze alloys will lead to modifications which are primarily obtained from small-scale tests.

HXDA Structural Design

The components of the nuclear brayton-cycle heat exchanger and duct assembly (HXDA) are shown in Figure 2-41. In the close-coupled arrangement shown in this figure, the HSHX is attached to, and supported by, the recuperator. In an optional system, the HSHX is remotely mounted with gas ducting leading to the recuperator high-pressure outlet. In this system, a pan forms the interface with the recuperator.

1. Heat Source Heat Exchanger (HSHX)

Preliminary design of the Heat Source Heat Exchanger (HSHX) has been performed with emphasis on the recuperator interface area. This is considered to be a critical area, since the HSHX design must not impair recuperator operating capability under any operating conditions.

TABLE 2-15
MATERIAL PROPERTIES

a. Low Carbon Nickel (Nickel 201)

Temperature K	(1) E, MN/sq m	(1) α , cm/cm K	RA Percent	Yield Stress, MN/sq m		Ultimate Stress, MN/sq m	Stress for 1 percent Creep in 100,000 Hr, MN/sq m
				Minimum ⁽²⁾	Typical ⁽³⁾		
290	193x10 ³		73	72	103	410	
370		13x10 ⁻⁶	74	72	102	390	
420			73	70	99	370	
480		14	72	70	99	370	
530			73	70	99	370	
590		14	72	70	99	370	
640			76	68	97	320	88 ⁽⁴⁾
700		15	80	65	93	280	56
760			80	62	89	260	36
810		15	84	59	83	230	23

- NOTES: (1) Nickel 200 values.
 (2) 70 percent of typical values to estimate the minimum.
 (3) Increase in strength between 420 and 640 K ignored.
 (4) Extrapolated
 (5) Density, 8.89 gm/cu cm
 (6) Data taken from Reference 7.

b. 347 Steel

Temperature, K	E, MN/sq m (Ref. 8)	α , cm/cm- K (Ref. 8)	RA Percent (Ref. 8)	Yield Stress, MN/sq m		Ultimate Stress MN/sq m (Ref. 8)
				A Basis (Ref. 9)	Typical (Ref. 8)	
290	190x10 ³	16x10 ⁻⁶	69	200	230	620
370	190	16	73	190		560
420				170	210	
480	180	17	75	160		490
530				160	190	
590	170	18	73	160		470
640				150	170	
700	160	18	69			

- NOTE: (1) Density, 8.26 gm/cu cm

TABLE 2-15 (Continued)

c. Hastelloy X

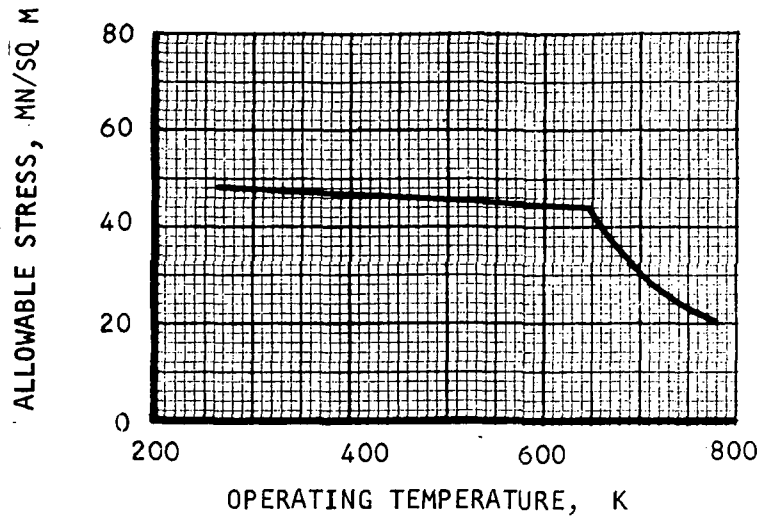
Temperature K	E, MN/sq m (Ref. 10)	α , cm/cm-K (Ref. 10)	(1) RA Percent (Ref. 6)	Yield Stress, MN/sq m		Ultimate Stress, MN/sq m (Ref. 11)	Stress for 1 Percent Creep in 100,000 Hr, (2) MN/sq m (Ref. 11)
				S Basis (Ref. 10)	Typical (Ref. 11)		
290	200×10^3		34	310	360	790	
370	200			290			
480	190	14.0×10^{-6}		260	340	710	
590	180	14.4		250	300	690	
700	170	14.7		240	300	690	
810	170	15.1		220	290	650	230
870							150
920	150	15.5		210	280	570	93
980			32(3)				59
1030		15.9		180	260	430	37
1090			40(4)				

- NOTES: (1) Minimum tested value, obtained for 0.025 cm sheet.
 (2) Values are lower than typical values quoted in the reference.
 (3) Tested at 1000 K
 (4) Tested at 1100 K
 (5) Density, 8.2 g/cu cm

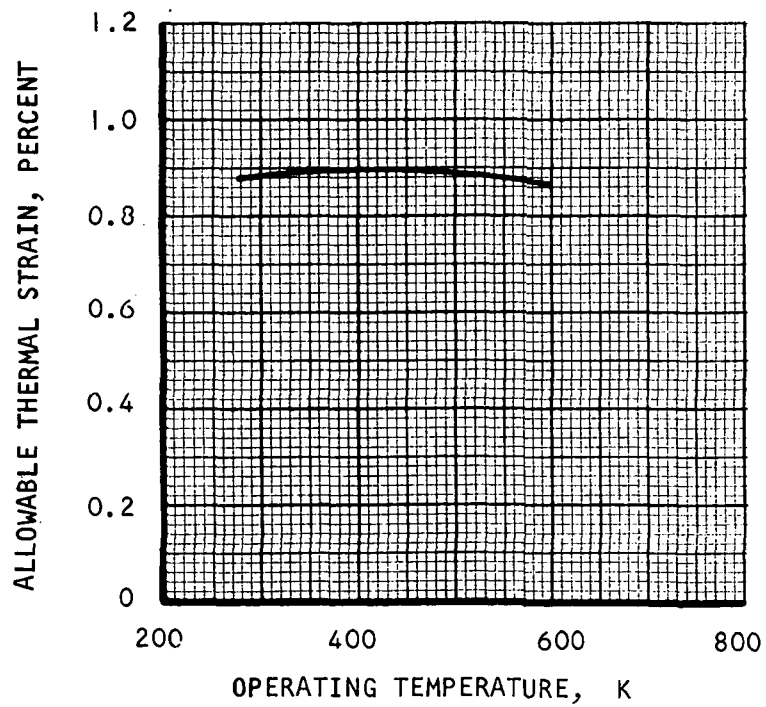
d. Haynes 25

Temperature K	E, MN/sq m (Ref. 10)	α , cm/cm-K (Ref. 10)	RA Percent (Ref. 12)	Yield Stress, MN/sq m		Ultimate Stress, MN/sq m (Ref. 13)	Stress for 1 Percent Creep in 100,000 Hr, MN/sq m (3) (Ref. 13)
				A. Basis (Ref. 10)	Typical (Ref. 13)		
290	240×10^3		59	370	460	1000	
370	220			320			
480	200	13.0×10^{-6}		260	320	880	
590	180	13.5		210	280	880	
700	180	14.2		190	270	860	
810	180	14.8	48	190	250	800	250
870							170
920	170	15.5	47	190	240	710	120
980							84
1033	160	16.2	24	190	260	460	59
1090							

- NOTES: (1) Reference 13 values are for 0.28 cm sheet
 (2) Density, 9.1 g/cu cm
 (3) 90 percent of Reference 14 values which are average properties, this provides creep strengths comparable to the less than average values used for Hastelloy X.



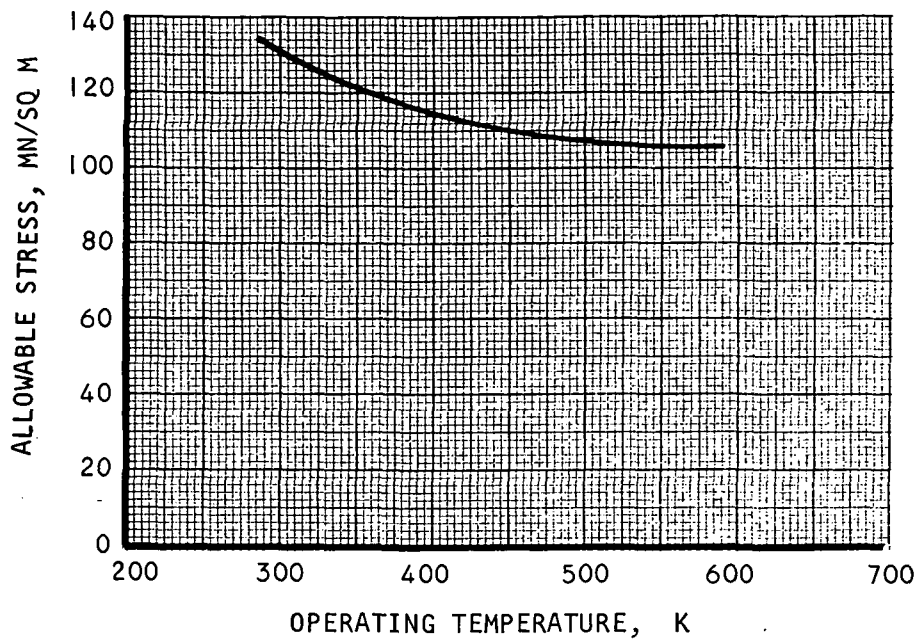
a. Direct Pressure and Inertia Load Allowable Stress



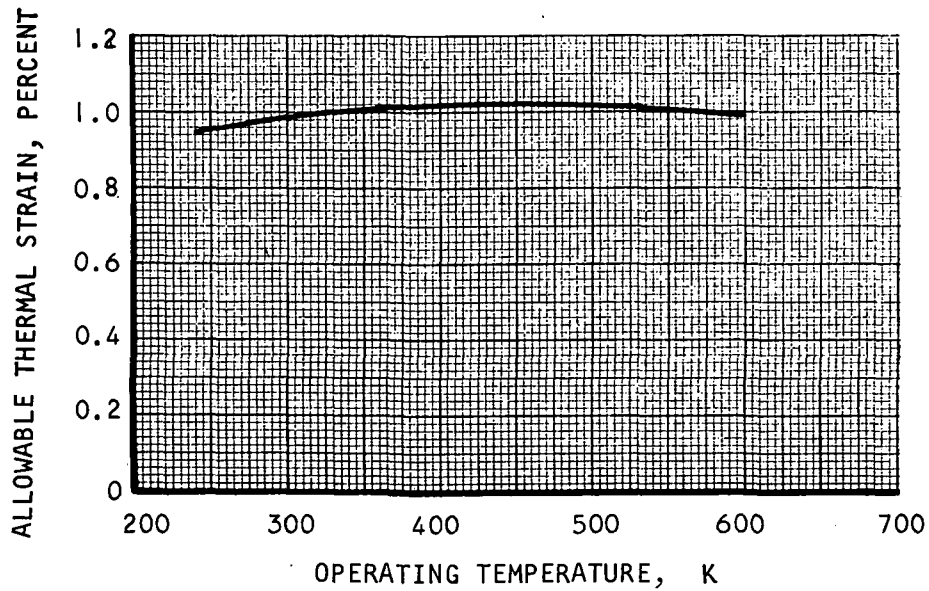
b. Allowable Thermal Strain for 4000 Cycles

S-65342

Figure 2-37. Low-Carbon Nickel (Nickel 201) Direct Stress (Strain) Allowable vs Operating Temperature



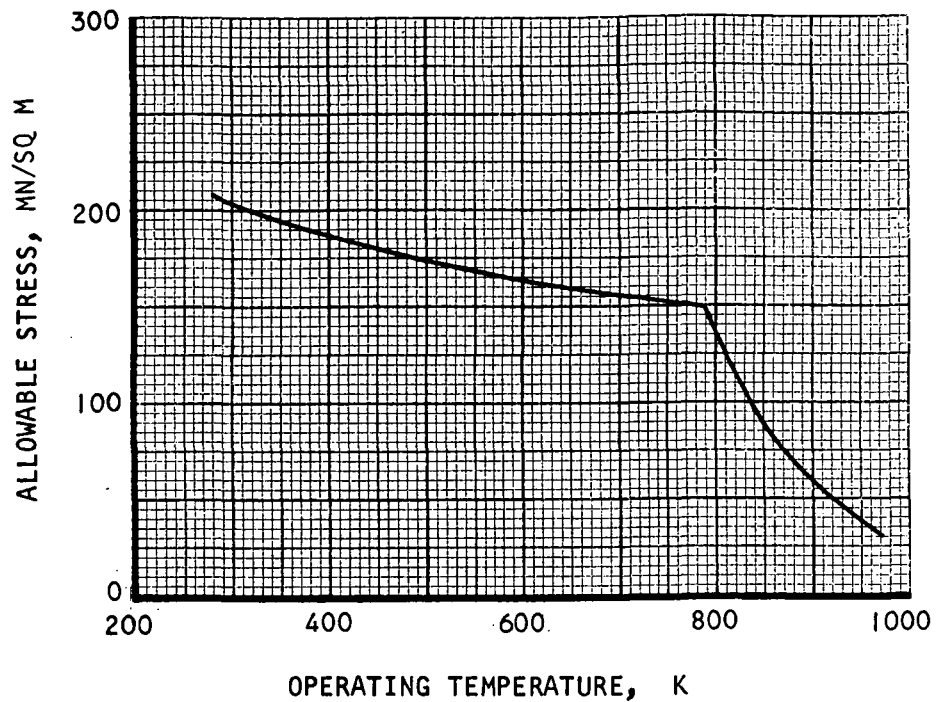
a. Pressure and Inertia Load Allowable Stress



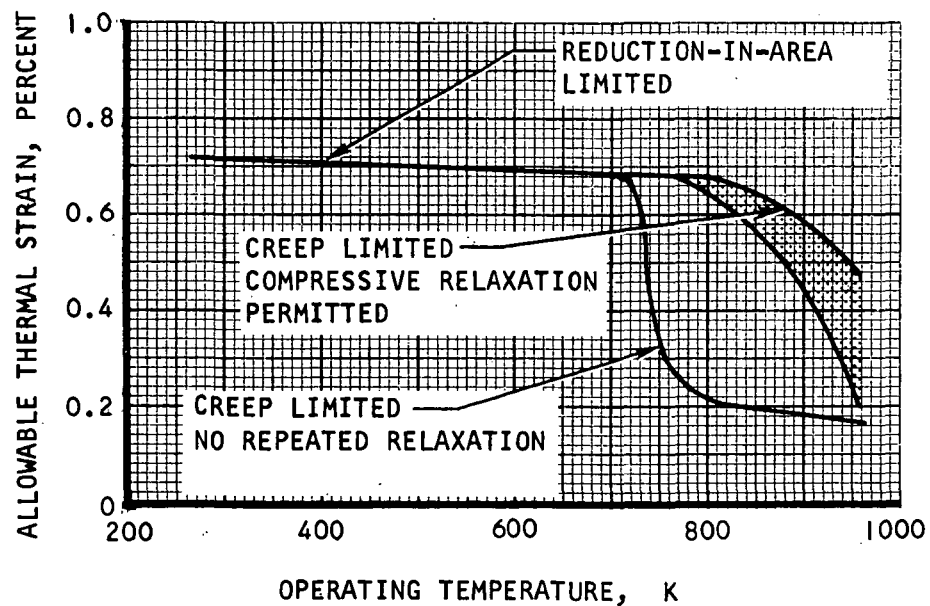
b. Allowable Thermal Strain for 4000 Cycles

S-65343

Figure 2-38. 347 Steel Direct Stress (Strain) Allowable vs Operating Temperature



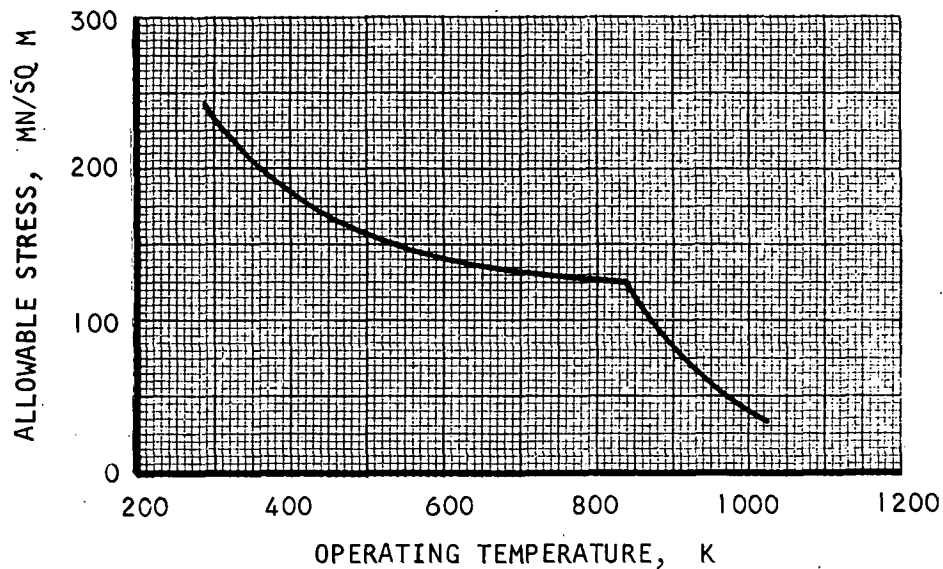
a. PRESSURE AND INERTIA LOAD ALLOWABLE STRESSES



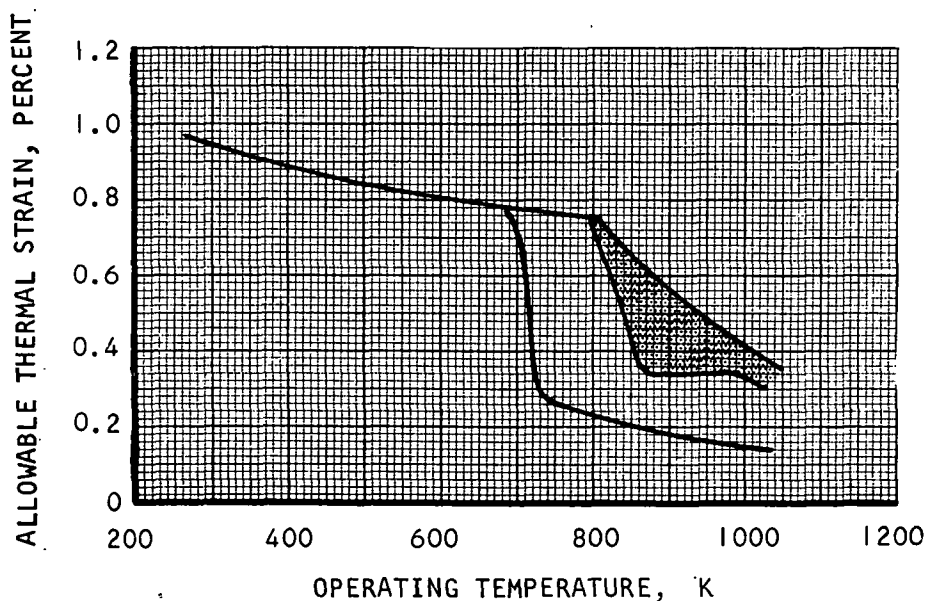
b. ALLOWABLE THERMAL STRAIN FOR 4000 CYCLES

S-64999

Figure 2-39. Hastelloy X Direct Stress (Strain) Allowable vs. Operating Temperature



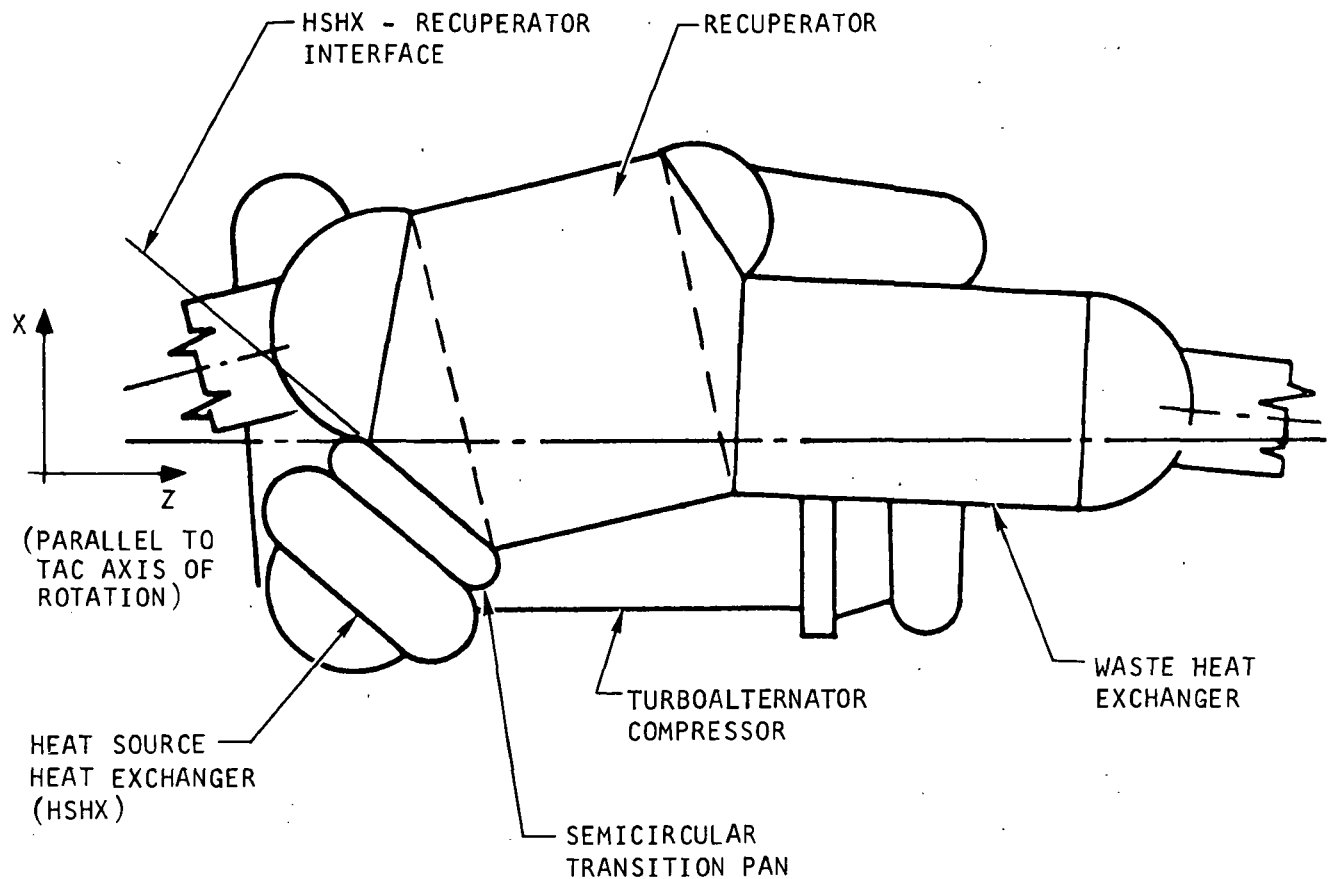
a. Pressure and Inertia Load Allowable Stress



b. Allowable Thermal Strain for 4000 Cycles
(See Figure for Curve Description)

S-65341

Figure 2-40. Haynes 25 Direct Stress (Strain) Allowable vs Operating Temperature



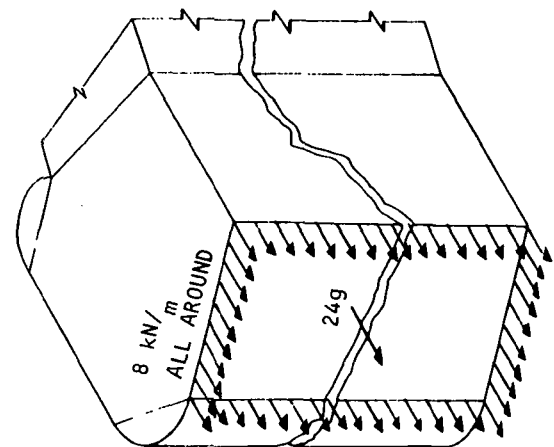
S-65185

Figure 2-41. Nuclear Brayton-Cycle HXDA Arrangement

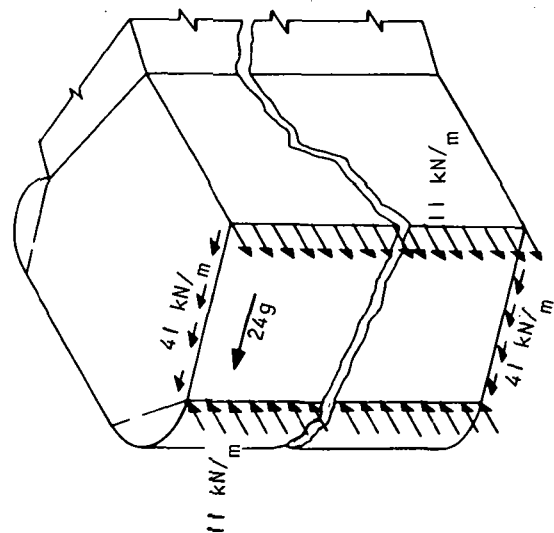
a. Interface Loads

Interface loads were determined for inertia loading previously specified and fluid pressure operating conditions specified in Figure 2-13. In addition, an arbitrary temperature difference across the transition piece was selected to illustrate thermal load at the interface.

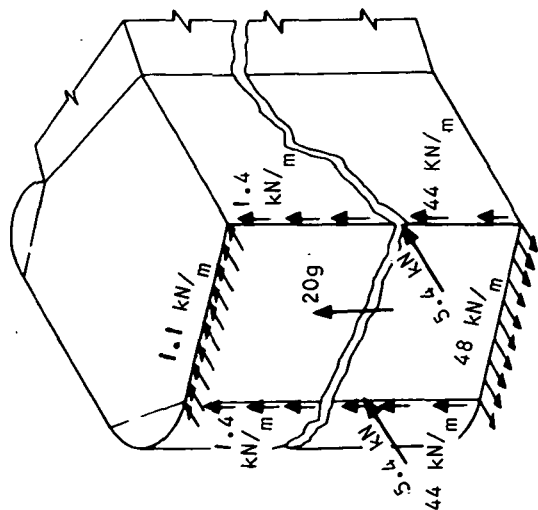
The effect of inertial loading in three different directions is shown in Figure 2-42. A calculated mass of 79 kg was used for the HSHX with an estimated center of gravity 13 cm from the interface. In the optional system with a pan attached to the recuperator, the interface inertial loads are low since pan weight will only be about 7 kg.



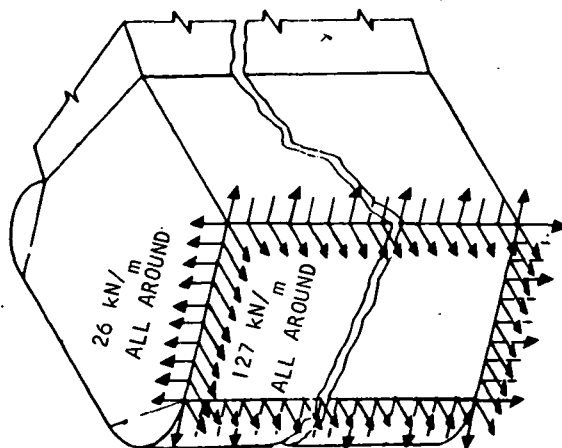
c. INERTIA LOADING
PERPENDICULAR TO INTERFACE -
24g



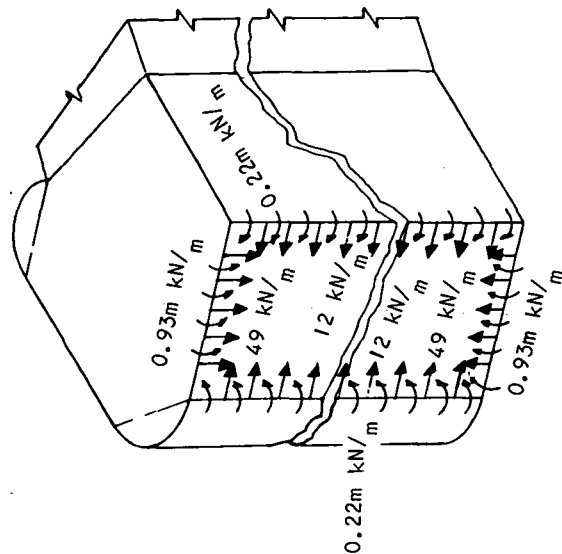
b. INERTIA LOADING
PARALLEL TO INTERFACE AND
PERPENDICULAR TO Y DIRECTION -
24g



a. INERTIA LOADING
Y-DIRECTION - 20g



d. PRESSURE LOADING
1380 kN/SQ M



e. THERMAL LOADING
ARBITRARY $\Delta T = 110$ K
SELECTION

Figure 2-42. Interface Loads

Interface inertial loads in the Y-axis (parallel to the interface and perpendicular to TAC axis of rotation) are shown in Figure 2-42a. The major portion of the HSHX weight is contributed by the tubes, which are supported in this direction by a single header plate. The header plate transmits the shear portion of the load to the interface where it is distributed along approximately one quarter of two opposite edges. The moment due to the 13-cm offset is resisted by a uniformly distributed tensile load on one interface edge and concentrated loads on the adjacent edges. The loads due to the remainder of the HSHX weight are also shown in the figure. Inertial loads, shown in Figure 2-42b (parallel to the interface and perpendicular to the Y-direction), produce a moment which is resisted by equally distributed tension and compression along two edges. The shear force causes equally distributed loads along the other two edges. Inertial forces in the direction of gas flow are balanced by equally distributed tensile loads along all four edges as shown in Figure 2-42c.

Gas pressure produces the interface loads shown in Figure 2-42d. In addition to the equally distributed tensile load along the four edges (blow-off load), there is an equally distributed shear load due to membrane forces from within the semicircular transition pans. In the optional system which has a semicircular outlet pan mounted on the recuperator, shear loads will be negligible.

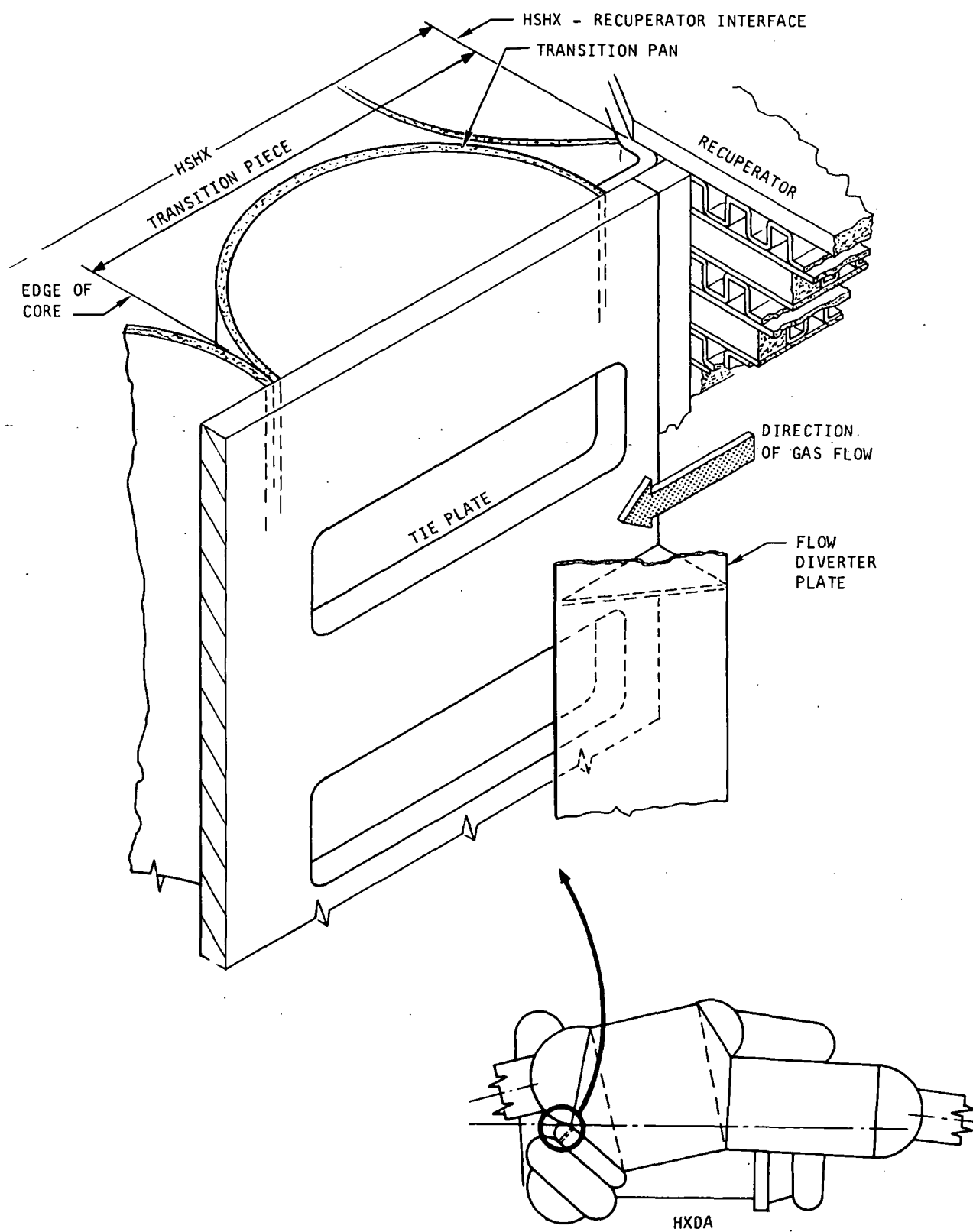
A 110°K temperature difference, ΔT , between the HSHX and recuperator was selected. The thermal loads caused by this ΔT generate the interface loads shown in Figure 2-42e. The ΔT value was arbitrarily selected to illustrate the thermal loads discussed below.

The individual interface loads shown in Figure 2-42 will be combined during operation. One of the inertial loads of the three shown in Figure 2-42a, b, and c will act simultaneously with pressure loading. The thermal loading of Figure 2-42d, however, will be considered separately.

b. Transition Piece Description

There will be a temperature difference, ΔT , between the recuperator high-pressure outlet (labeled HSHX-RECUPERATOR INTERFACE in Figure 2-43) and the edge of the HSHX core, particularly during transient heating conditions. If the heat exchanger core is mounted directly on the recuperator, an unsatisfactory structure will result primarily due to the effect of this ΔT across the HSHX header plate and recuperator side plates. The relatively thick header plate will have a much slower thermal response time than the thinner side plates and an unacceptable thermal strain will result. The magnitude of the ΔT is not known; however, previous experience precluded using this approach.

The approach selected utilizes a transition piece to separate the HSHX header plate and the recuperator side plate as shown in Figure 2-43. It consists of semicircular pans and tie plates around the periphery of the interface. The primary function of the pan is pressure containment with the additional purpose of supporting the shear forces caused by inertial loading.



S-65184

Figure 2-43. HSHX Transition Piece Detail

To minimize thermal loads, a portion of the hot gas may be directed by diverter plates to heat the pan at approximately the same rate as the recuperator components. The tie plates will primarily support tensile forces in the direction of gas flow (blow-off loads). This transition section will support pressure and inertial loads; however, thermal strains remain to be investigated to fully determine feasibility of the design.

c. Thermal Design

Thermal design of the HXDA is a primary consideration since potential temperature gradients may result in finite heat exchanger life (design life is 4000 cycles to achieve 1000 cycle life). These temperature gradients are the greatest in high-temperature regions, such as in the HSHX. In addition, the allowable gradients are severely limited at temperatures where material creep damage is a factor. For example, Figure 2-40 shows that the allowable strain for Haynes 25 decreases from about 0.8 percent to 0.25 percent between 700 and 755 K. A sample calculation for an allowable temperature differential across the transition section is illustrated in the following paragraphs.

Two-directional thermal loading occurs in the tie plates connecting the HSHX and recuperator due to the difference in size of the opposing heat exchanger faces. This causes guided cantilever bending of the tieplates as shown for one of the directions in Figure 2-44. The effect is most severe in the corners where the imposed deflections are largest. The deflection, Δ , imposed in one direction is $\Delta = L\alpha\Delta T/2$, where L is the length of one side and α is the thermal coefficient of expansion. The relation between load and deflection for a guided cantilever is

$$\Delta = \frac{Pl^3}{12EI}$$

where l is the length of the tieplate, E is the elastic modulus of the material, and I is the sectional moment of inertia. Equating the above equations and solving for P gives

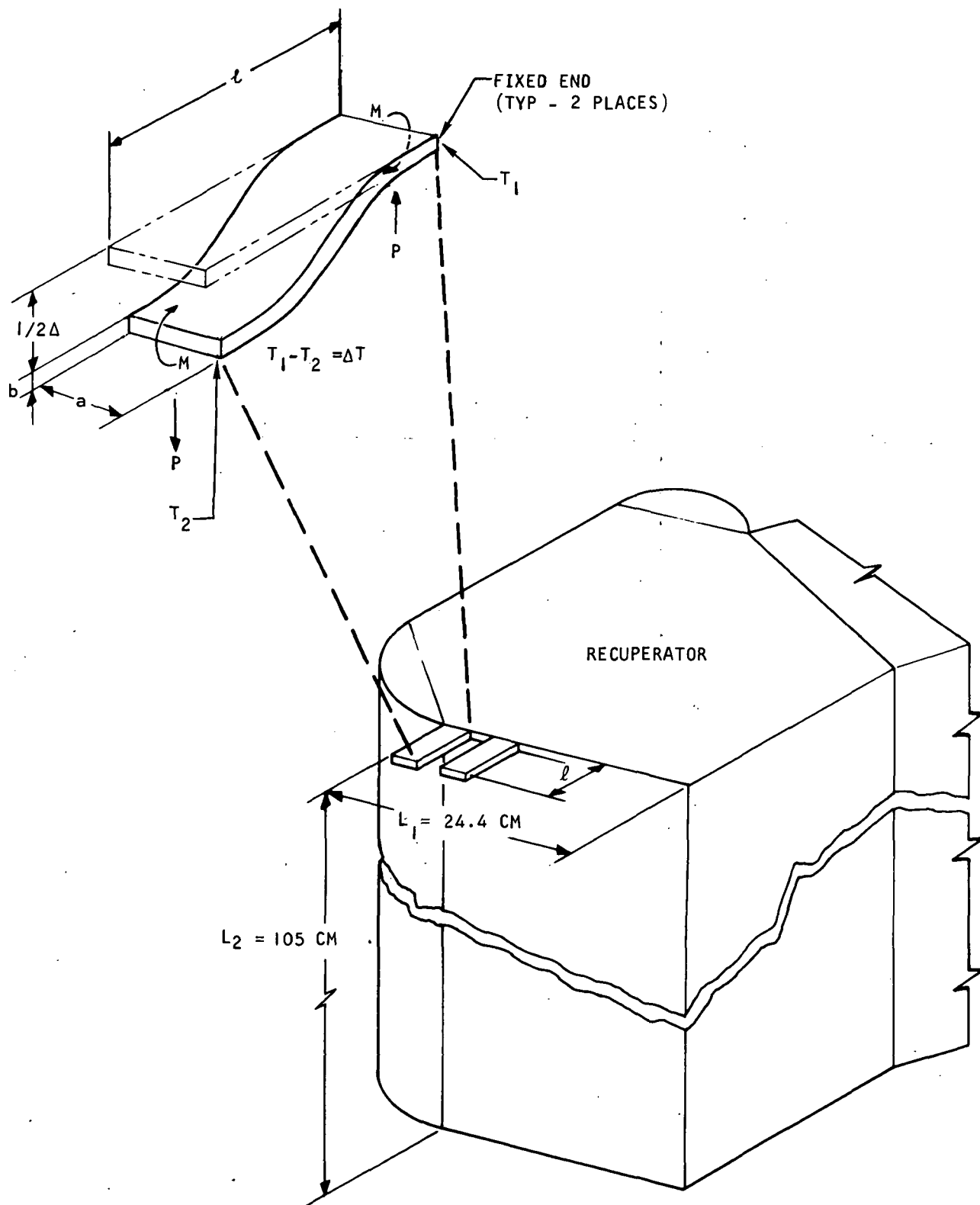
$$P = \frac{6EIL\alpha\Delta T}{l^3}$$

From this, the moment, M , is

$$M = \frac{Pl}{2} = \frac{3EIL\alpha\Delta T}{l^2}$$

and the maximum strain, ϵ , for a tieplate thickness, t , is

$$\epsilon = \frac{\sigma}{E} = \frac{M}{ZE} = \frac{3L\alpha\Delta Tt}{2l^2}$$



S-65186

Figure 2-44. Tieplate Thermal Analysis Schematic

using the relations

$$I = \frac{t^3}{12} \text{ and}$$

$$Z = \frac{t^2}{6}$$

The ΔT is therefore

$$\Delta T = \frac{2\ell^2 \epsilon}{3L\alpha t}$$

Since there is an allowable strain associated with the tieplate material there is a related allowable ΔT for one-dimensional loading,

$$(\Delta T)_{all} = \frac{2}{3} \frac{\ell^2 \epsilon_{all}}{L\alpha t} \quad (2-10)$$

For two-dimensional loading, consider a tieplate with cross-sectional dimensions a and b (Figure 2-44). The ΔT values for the two directions are

$$\Delta T = \frac{2\ell^2 \epsilon_1}{3L_1 \alpha a}, \text{ and}$$

$$\Delta T = \frac{2\ell^2 \epsilon_2}{3L_2 \alpha b}$$

However, ΔT and α are the same for both cases, so these equations can be combined, giving

$$\frac{\epsilon_1}{L_1 a} = \frac{\epsilon_2}{L_2 b} \quad (2-11)$$

Selection of ϵ_1 equal to ϵ_2 gives the maximum ΔT capability for the tieplate.

In addition, the tieplate cross-sectional area can be established from the requirement to support axial pressure forces (Figure 2-42d). The required area is

$$A = PL_3 / \sigma_{all} \quad (2-12)$$

where P is the loading (kN/m), L_3 is the tieplate segment spacing (cm), and σ_{all} is the material allowable pressure stress (MN/sq m). Since

$$A = ab,$$

Equations 2-2 and 2-3 may be combined to obtain

$$a = (L_2 L_3 P / L_1 \sigma_{all})^{1/2} \quad (2-13)$$

$$b = (L_1 L_3 P / L_2 \sigma_{all})^{1/2}$$

The allowable tensile stress for Haynes 25 was determined to be 69 MN/sq m based on the design criteria. The blow-off load (from Figure 2-42d) was 127 kN/meter of interface perimeter. The allowable strain based on the design criteria is 0.3 percent; this includes a factor of 1.5 to allow for bending. Finally, for a tieplate spacing of 2.5 cm, the allowable ΔT is 64 K. If the spacing is reduced to 0.8 cm the allowable ΔT will increase to 110 K. These results show that allowable temperature differences can be a small fraction of the operating temperature and transient heat transfer analysis will be required to estimate expected operating temperatures. The expected operating temperature difference must be less than the allowable difference for the component design to be acceptable.

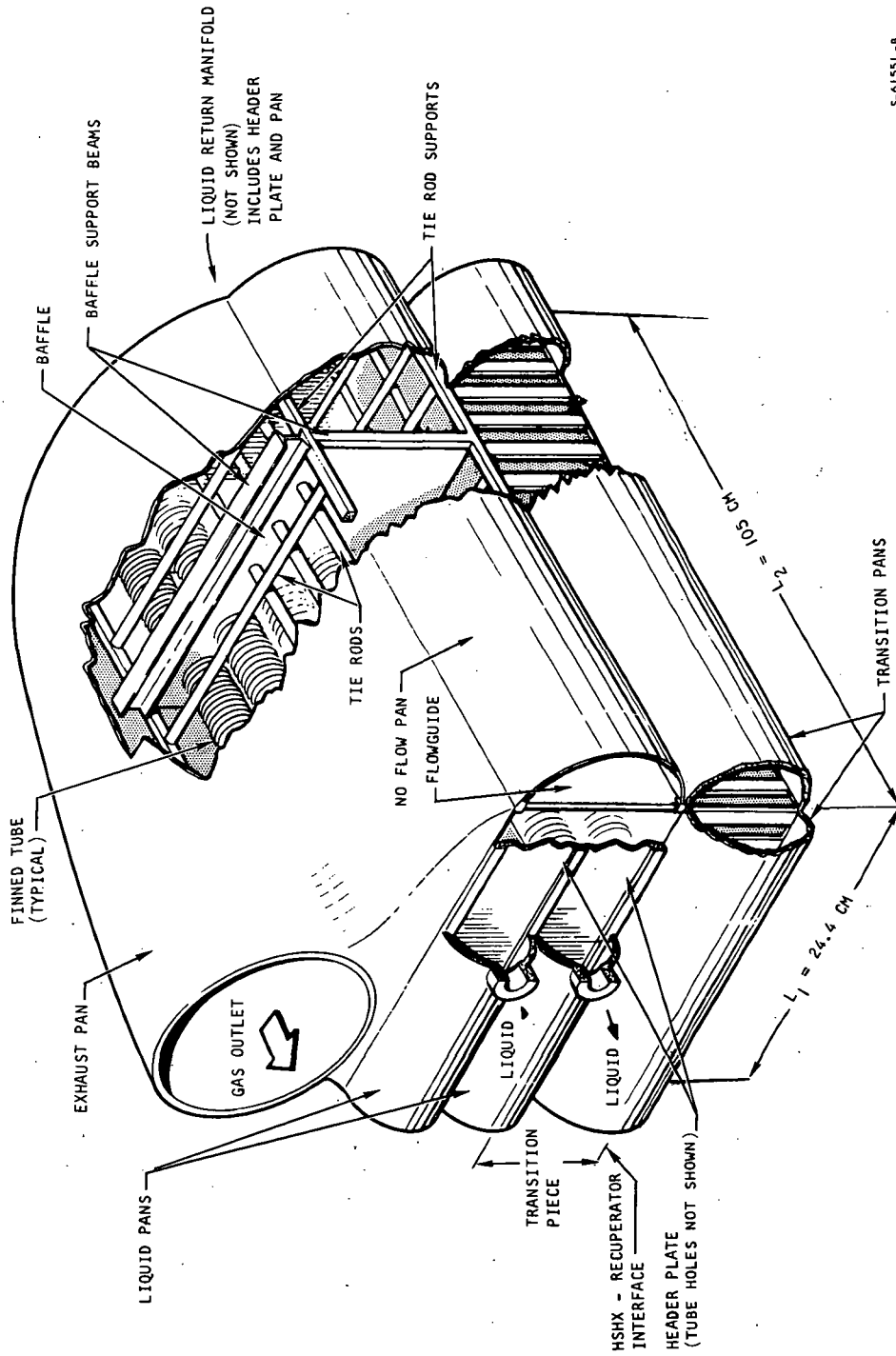
(1) Allowable Thermal Gradients

A survey of the allowable temperature differences between HSHX components was performed. The HSHX is shown in Figure 2-45 and the various interfaces at which temperature differences, ΔT , are developed and shown in the expanded views of the components in Figures 2-46 and 2-47. Table 2-16 summarizes the results of the analysis using component sizes based on pressure and inertia load considerations. The computed allowable temperature differences must be compared to predicted ΔT 's to determine whether or not the preliminary geometry for the HSHX is satisfactory. If the predicted ΔT values from heat transfer analysis exceed the computed allowable ΔT , the design is not satisfactory.

(2) Plate Restraint

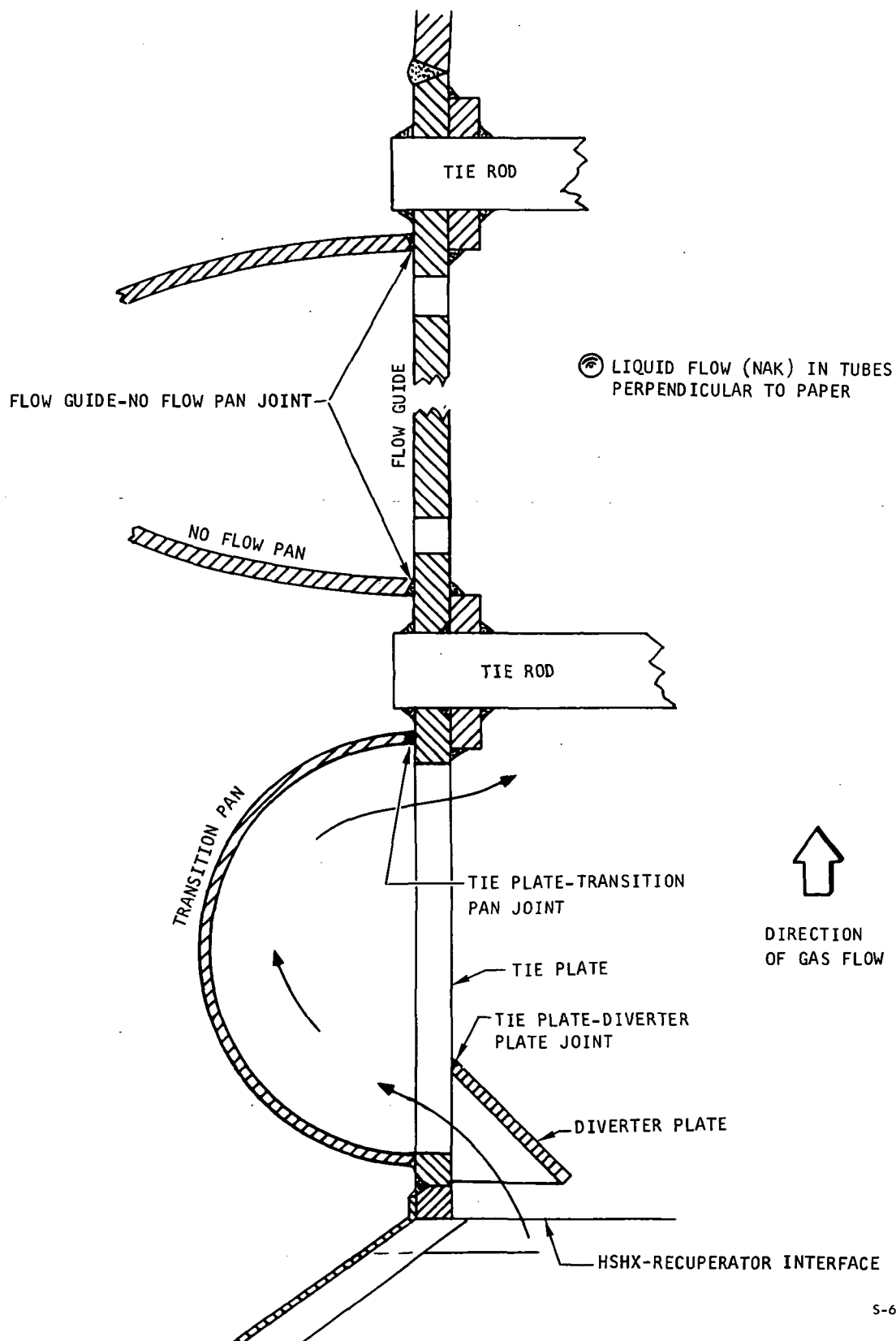
Shear loads occur at plate interfaces where there is a temperature difference between adjacent components. The various plate joints in the HSHX and the reasons for the ΔT 's are discussed below. The locations of these joints are shown in Figures 2-46 and 2-47.

When two different thickness plates are exposed to the same gas, the different response times lead to a ΔT between them. This is the case for the tieplate-transition pan joint with a thickness ratio, t_2/t_1 , of 6.25 and the tieplate-diverter plate joint with a t_2/t_1 of 3.12.



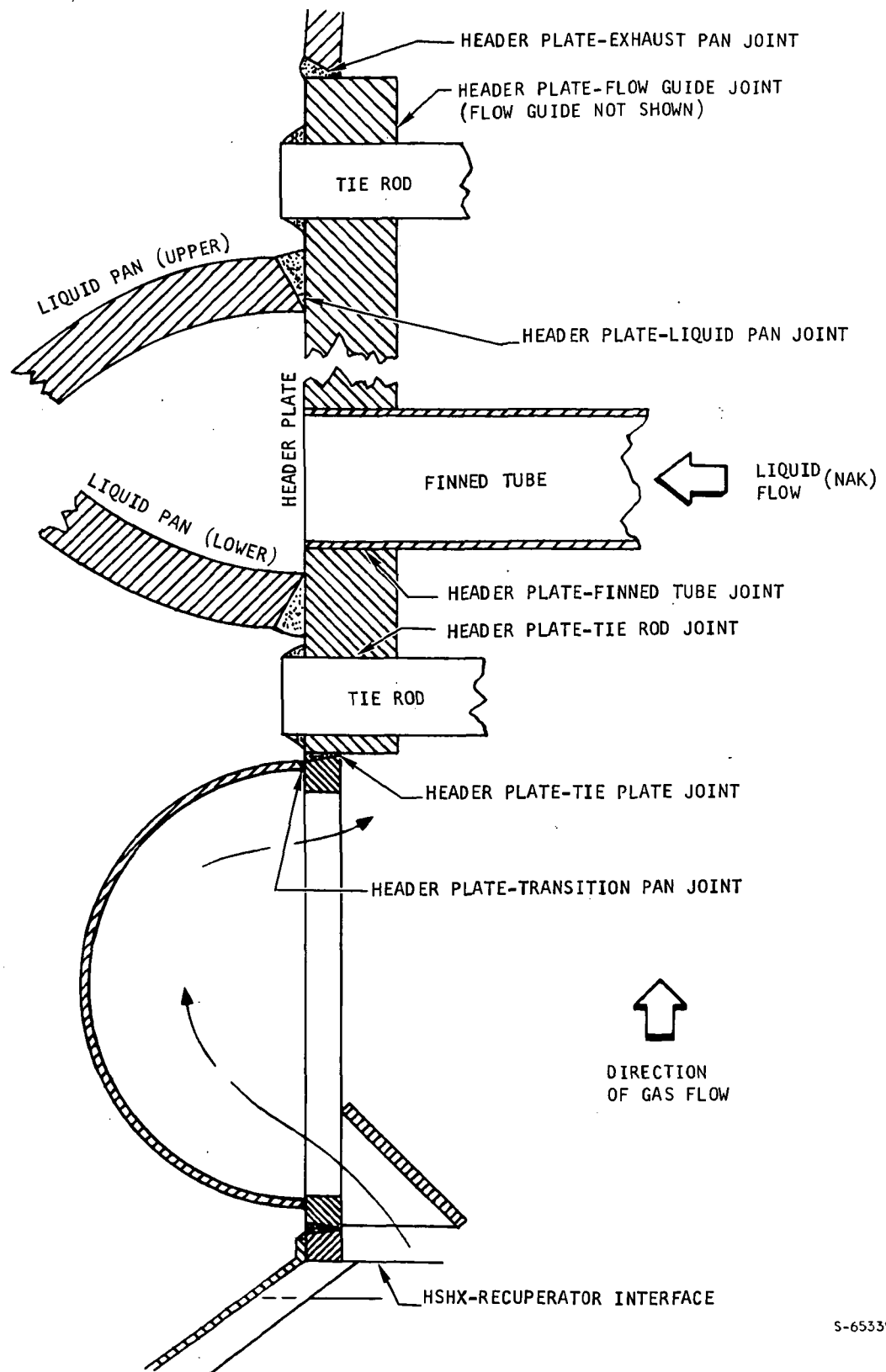
S-61551-B

Figure 2-45. Heat Source Heat Exchanger (HSHX)



S-65338

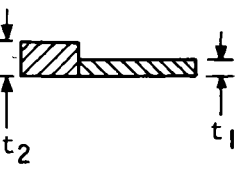
Figure 2-46. HSHX Cross Section Through No-Flow Pan.



S-65339

Figure 2-47. HSHX Cross Section Through Liquid Pan.

TABLE 2-16
HSHX ALLOWABLE ΔT 'S

Type of Analysis	Components	$(\Delta T)_{all}$ (K)
<p>a. Plate Restraint</p> 	$t_2/t_1 = 6.25$ Tie Plate - Transition pan (Figure 2-46)	222
	$t_2/t_1 = 3.12$ Tie Plate - Diverter plate (Figure 2-46)	240
	$t_2/t_1 = 2.2$ No flow pan - Flowguide (Figure 2-46)	260
	$t_2/t_1 = 2.8$ Header plate - Tie plate (Figure 2-47)	247
	$t_2/t_1 = 17.5$ Header plate - Transition pan (Figure 2-47)	217
	$t_2/t_1 = 2.52$ Header plate - Exhaust pan (Figure 2-47)	250
	$t_2/t_1 = 2.52$ Header plate - Flowguide (Figure 2-47)	250
	$t_2/t_1 = 1.75$ Header plate - Liquid pan (Figure 2-47)	270
<p>b. Tie Rod or Tube Diameter Restraint</p>	Header plate - Finned tube (Figure 2-47)	128
	Header plate - Tie Rod (Figures 2-46 and 2-47)	128
<p>c. Tie Rod Axial Restraint</p>	Tie Rod (Figures 2-46 and 2-47)	128

If the plates are exposed to the same gas but at different flow rates, a ΔT will also be developed. The interface between the no-flow pan and flowguide with a t_2/t_1 of 2.2 is such an example. The maximum operating ΔT for this case will be higher than the allowable ΔT shown in Table 2-16 since the flow rate by the no-flow pan will be practically zero. The allowable thermal strain will therefore be increased by providing a corrugated joint between the pan and the flowguide.

When adjacent plate sections are exposed to different heating rates, such as when one fluid heats one section and two fluids heat an adjacent section, a ΔT will be developed. Differences in thickness may also contribute to the effect. Such areas arise around the header plate with the following components and thickness ratios: tieplates with t_2/t_1 of 2.8, transition pan with t_2/t_1 of 17.5, exhaust pan with t_2/t_1 of 2.52, flowguide with t_2/t_1 of 2.52, and liquid pan with a t_2/t of 1.75.

The computer program EASE (Elastic Analysis for Structural Engineering) was used to analyze the model shown on Figure 2-48a. EASE is a finite element program with application of the direct stiffness method. The plate temperature distribution is shown in Figure 2-48b. Three thickness ratios, t_2/t_1 , were selected to span the range of HSHX ratios and the results are illustrated in Figure 2-48c.

(3) Tie Rod or Tube Diameter Restraint

At joints between plates and circular members the components will generally be heated at different rates and a temperature difference, ΔT , will develop between them. The difference in diametral thermal expansion due to this ΔT will be $2R\alpha\Delta T$. This leads to a strain, ϵ , of

$$\epsilon = \alpha\Delta T$$

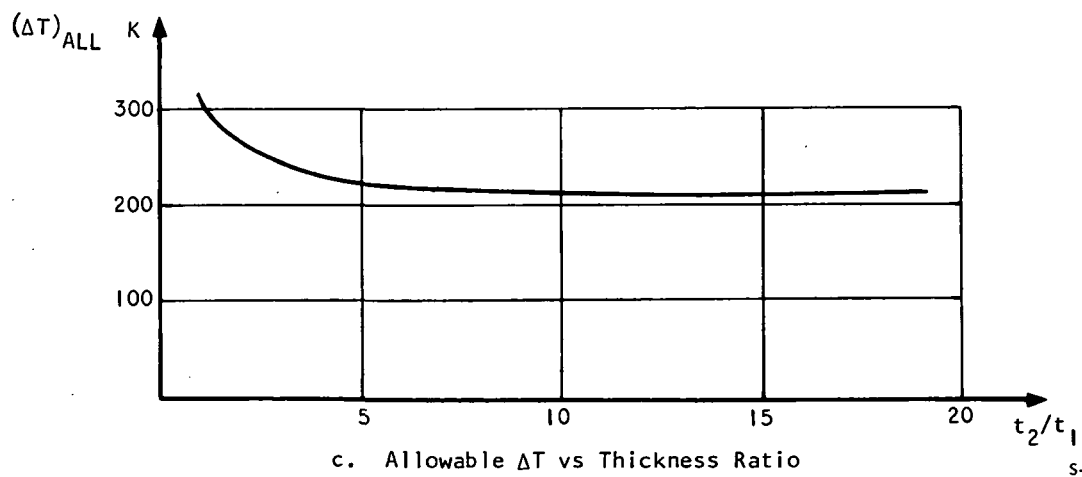
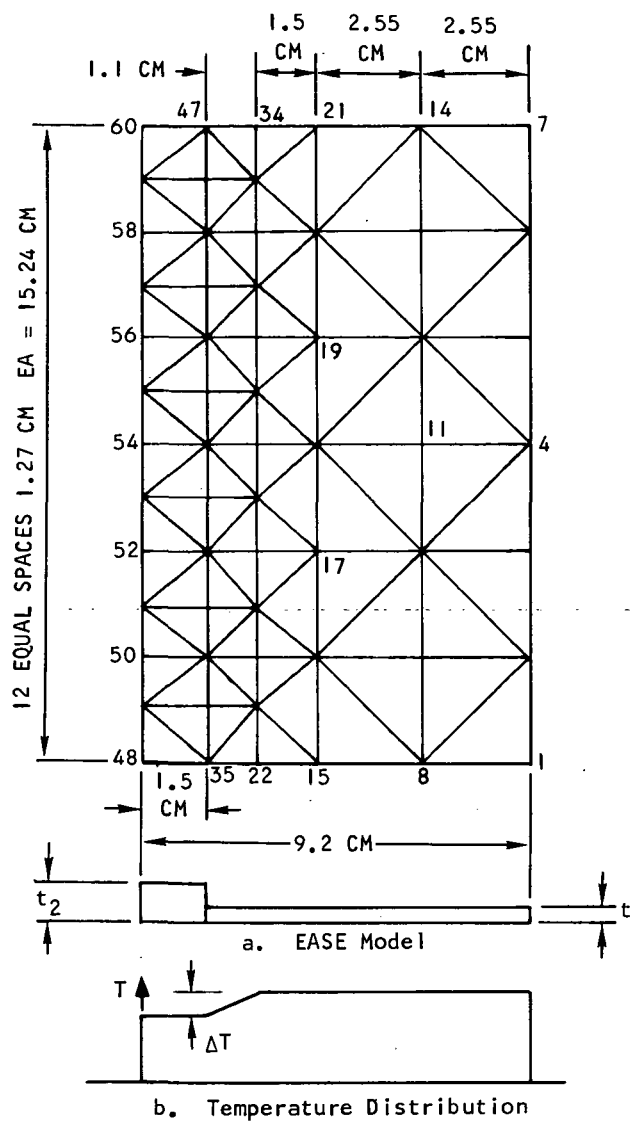
the allowable ΔT will be

$$(\Delta T)_{all} = \frac{\epsilon_{all}}{\alpha}$$

The allowable strain for Haynes 25 from Figure 2-40 is about 0.2 percent so the allowable ΔT is 128 K.

(4) Tie Rod Axial Restraint

The relatively large mass of differences between the tie rods and neighboring structure such as the header plate will lead to significantly different thermal responses. The resulting temperature differences will cause axial loads in the tie rods. Assuming rigid end restraint of the tie rod, the difference in thermal expansion due to a ΔT will be $L\alpha\Delta T$. Restraint leads to a uniform axial strain, ϵ , of



S-65340

Figure 2-48. Plate Temperature Gradient Analysis

$$\epsilon = \alpha \Delta T$$

The allowable ΔT will be

$$(\Delta T)_{all} = \frac{\epsilon_{all}}{\alpha}$$

For the allowable strain of about 0.2 percent for Haynes 25, the ΔT is 128 K.

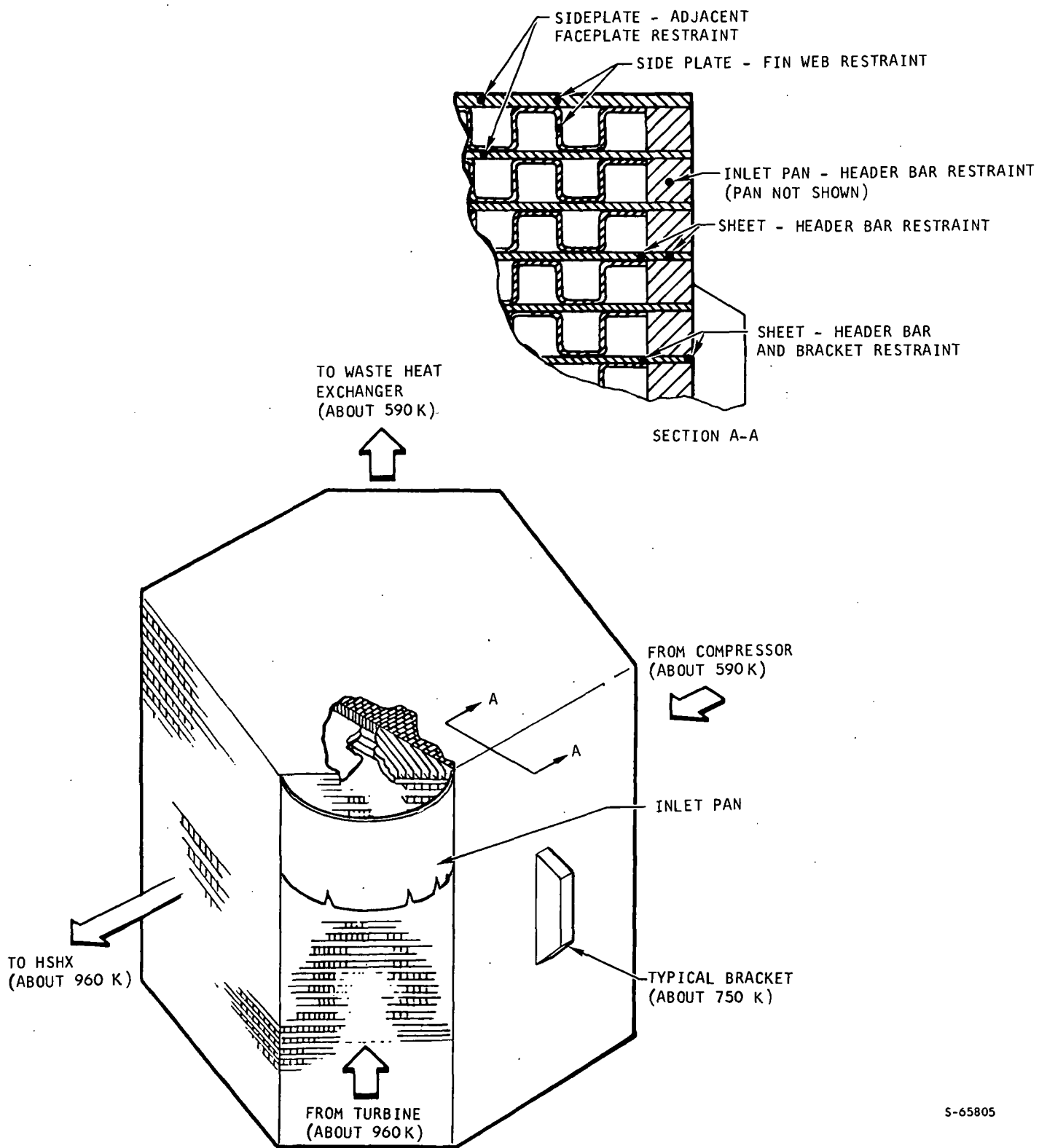
2. Recuperator Structural Design

The temperature difference capability of the Hastelloy X recuperator has been investigated following the approach used for the HSHX. Allowable temperature differences were determined for the maximum temperature regions (960 K) and the preliminary bracket location (about 750 K). Figure 2-49 shows the local recuperator geometry and the areas under consideration. Figure 2-50 shows typical time-temperature and stress-strain curves (shutdown transient state not shown) for any of the mechanical restraints shown on Section A-A, Figure 2-49. The temperature difference, ΔT , between two adjacent components reaches a maximum and then decreases to a low steady state value (see Figure 2-50a). The maximum strain on the stress strain curve occurs when the ΔT is maximum as indicated by point A. Point B indicates the beginning of steady state. Creep relaxation during steady-state conditions is also indicated.

a. Allowable Temperature Gradients

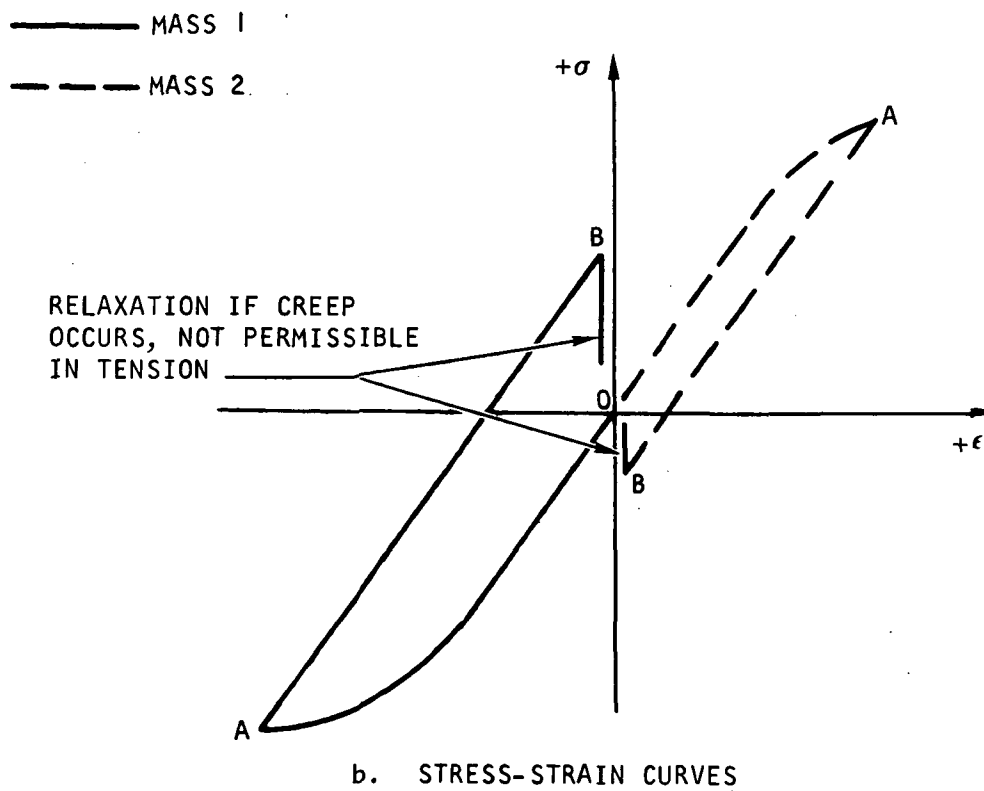
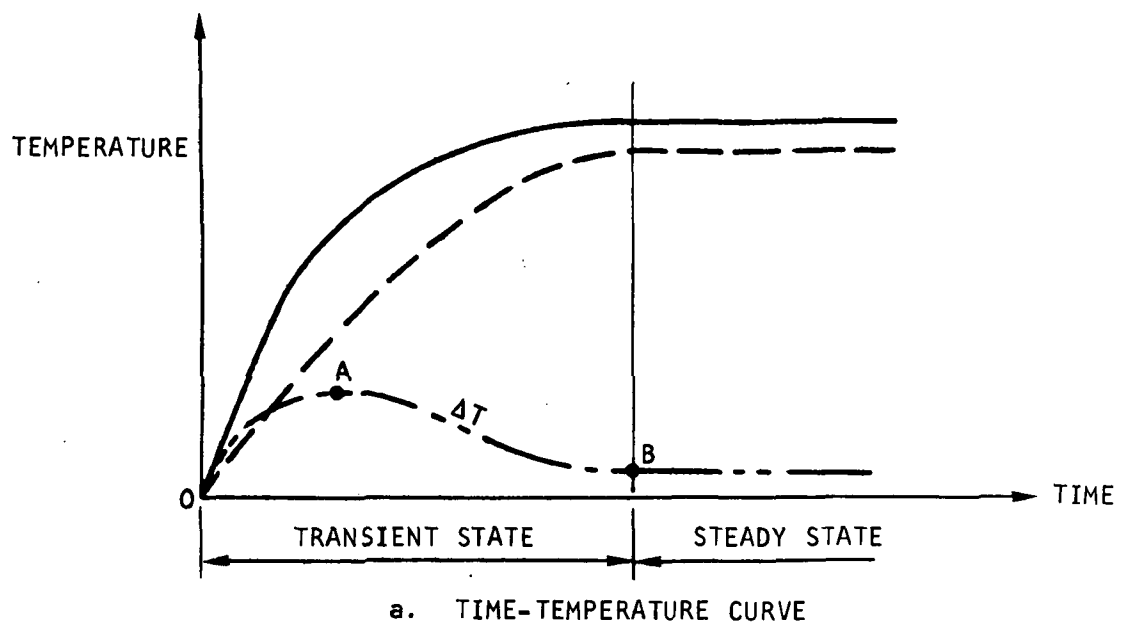
The allowable temperature differences, ΔT , between adjacent components are tabulated in the following table. Geometry details and derivations are discussed below. The advantage associated with placing the brackets away from the high temperature areas is highlighted by the fact that the ΔT capability exceeds the difference between ambient and maximum operating temperature and therefore guarantees adequate sheet life.

Type of Restraint	ϵ_{all} , percent	$(\Delta T)_{all}$, K	Operating Temperature, K
Sideplate - adjacent faceplate	0.16	66	960
Sheet - header bar	0.16	133	
Sideplate - fin web	0.16	111	
Inlet pan - header bar	0.16	180	
Sheet - header bar and bracket	0.70	710	750



S-65805

Figure 2-49. Recuperator



S-65807

Figure 2-50. Typical Component Temperature and Stress-Strain Behavior

b. Sideplate Restraint

Section A-A in Figure 2-49 shows details of the plate fin construction for a counterflow arrangement. During transient heating conditions, there can be a temperature difference, ΔT , between adjacent plates. The separating fins transmit the loads between sheets and they introduce localized strain concentrations which reduce sheet cycle life. The fabrication cycle and the presence of braze alloy also reduce life. The associated thermal strain, ϵ , may be expressed as

$$\epsilon = K\alpha\Delta T \quad (14)$$

where K is a factor which includes geometry and material conditions and α is the coefficient of thermal expansion. The factor, K, was determined from cyclic life tests of small scale specimens conducted by AiResearch and described in NASA CR-1884, October 1971. In those tests Hastelloy X parent metal and plate fin specimens were subjected to alternating strains.

Plate-fin specimens were brazed with 0.0025 mm thickness Palnir 1. The test results at 1000 K (corresponds approximately to 960 K operating temperature when overtemperature is included) were extrapolated to the desired 4000 cycle life and allowable total strain values of 0.356 and 0.55 percent were determined for sheets brazed to fins and for parent metal. The allowable strain for Hastelloy X parent metal is therefore 1.55 times that for Hastelloy X sheet brazed to fins. This factor (K value in equation 14) can be considered to be a strain concentration factor associated with the fabricating process and the material geometry. The above tests were performed at a constant cycle rate; however, tension relaxation is expected, and the allowable strain is somewhat lower. For the allowable parent metal strain of 0.16 percent and a coefficient of thermal expansion $15.67 \mu\text{m/m-K}$, the allowable ΔT for the sheet brazed to fins is

$$\Delta T_{all} = \frac{\epsilon_{all}}{1.55(\alpha)} = 66 \text{ K}$$

c. Header Bar-Sheet Type Restraint

Header bar-sheet type restraint occurs when a ΔT is developed between two different size plates which are brazed or welded together. Four different restraints of this type are shown on Figure 2-49. The thermal strain, ϵ , due to this restraint can also be expressed as

$$\epsilon = K\alpha\Delta T$$

where K, the strain concentration, is the product of a geometrical factor and a factor due to the presence of braze or weld alloys at the interfaces between components. The strain concentration due to braze or weld alloy was assumed to be 1.25, intermediate between parent metal ($K = 1$) and the 1.55 factor noted above since there is no fin notch effect. The effect of braze or weld alloys will be determined experimentally during the recuperator small scale tests.

As an example in computing allowable ΔT , a geometry factor of 0.61 was computed for the sheet-header bar interaction. This combined with the 1.25 factor for braze alloy gives an allowable ΔT for the sheet of 133 K

$$(\Delta T)_{all} = \frac{\epsilon_{all}}{K\alpha} = \frac{0.0016}{(0.61)(1.25)(15.67 \times 10^{-6})} = 133 \text{ K}$$

3. Mounting System

A preliminary heat exchanger mount system has been selected which will have a planar mounting bracket array as shown in Figure 2-51. The basic array is rectangular with a mount at each of the corners (solid brackets). Additional mounts will be added along two sides of the rectangle to reduce the x- and z- loads at individual mounts (additional mounts are shown by dotted lines). The final selection of these intermediate mounts will depend on available space for brackets and on load levels acceptable to the final bracket geometry.

Some of the desirable characteristics which this system satisfies are:

- (a) Bellows movement requirements in the x-direction are minimized by restraining x-motion on the side closest to the TAC. (Fixed point in z is not definitely determined although WHX locations appear desirable to reduce recuperator loads.)
- (b) Recuperator mounts are placed so that temperatures are less than 750 K, primarily to avoid creep damage during thermal strain cycling (see Hastelloy X allowable strain vs temperature, Figure 2-39).
- (c) Mounts are located in a single plane on one side of the recuperator and WHX to simplify thermal growth considerations and to minimize frame size (the frame can be entirely on one side of the package). This arrangement also minimizes moments arising from loads offset from the bracket bolting plate.
- (d) The HSHX is mounted on the recuperator to simplify the mount system and to avoid placing brackets in high temperature regions.

Several other bracket arrangements were considered, including a box type array which is compared to the selected planar array in Figure 2-52. The planar array provides a simpler frame design, including easier access to the heat exchangers, and reduced complexity of thermal motions (angles at mounts). These advantages outweighed the primary advantage of the box type which was that the individual mount loads were lower and more equitably distributed between four supports in each direction. The preliminary investigations also considered the following:

- (a) Bracket placement on recuperator side plates or header bar array; the latter was slightly preferable since the offset fins adjacent to the sideplates lowers thermal strain capability as compared to the plates.

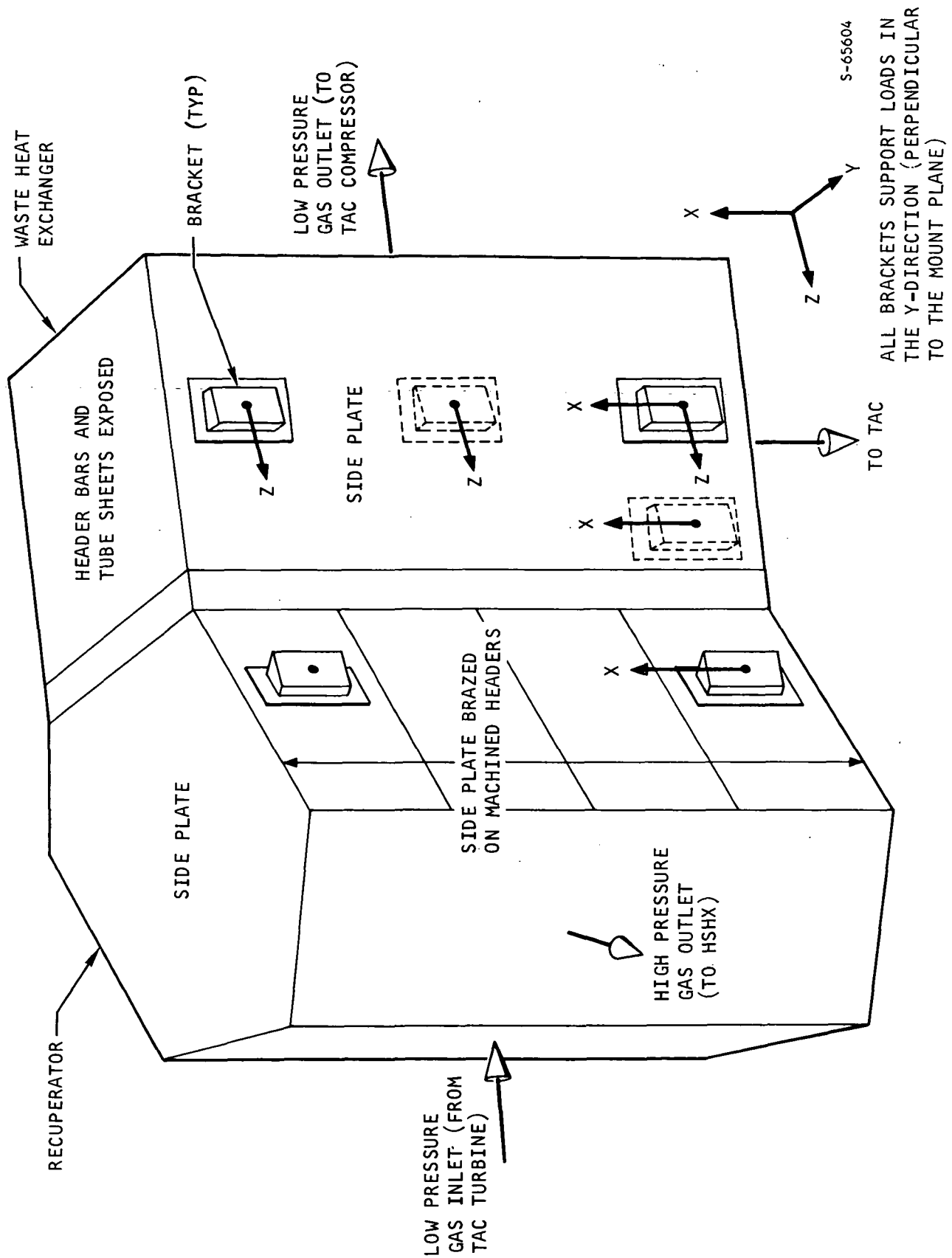
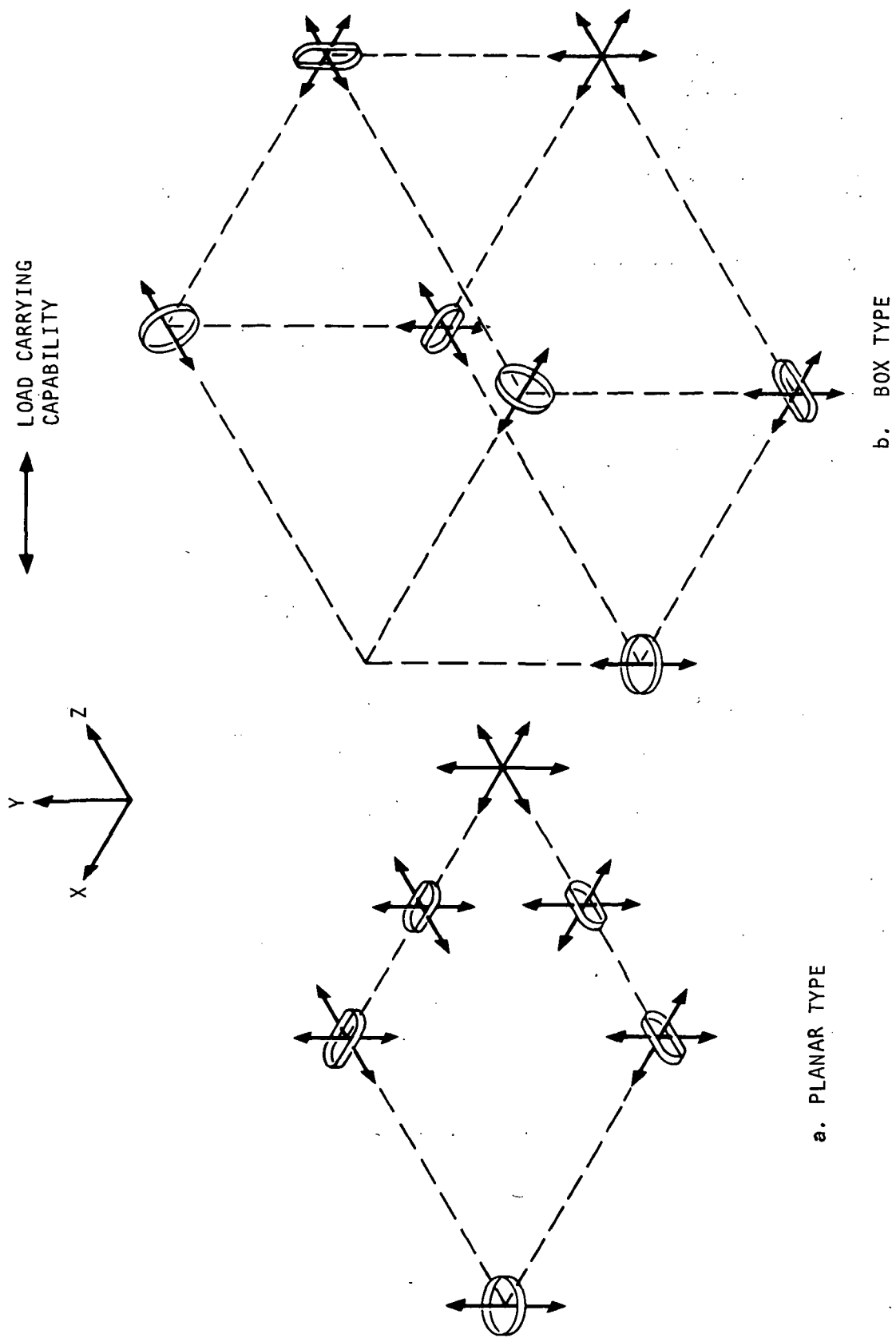


Figure 2-51. Preliminary Heat Exchanger Mounting System



S-65600

Figure 2-52. Comparison of Thermal Provisions and Directions for Load Capability of Planar and Box Type Mounting Bracket Arrays

- (b) Inertia load capabilities of the recuperator and WHX; natural frequencies above 50 Hz and satisfactory stresses at 24 g inertia loads are expected.
- (c) Frame member locations for the planar and box type; this includes achieving frame stiffness which will give satisfactory mount bracket load distribution.
- (d) Preliminary sizing of a recuperator bracket and adjacent core for the select mounting array loads.

4. Ducting

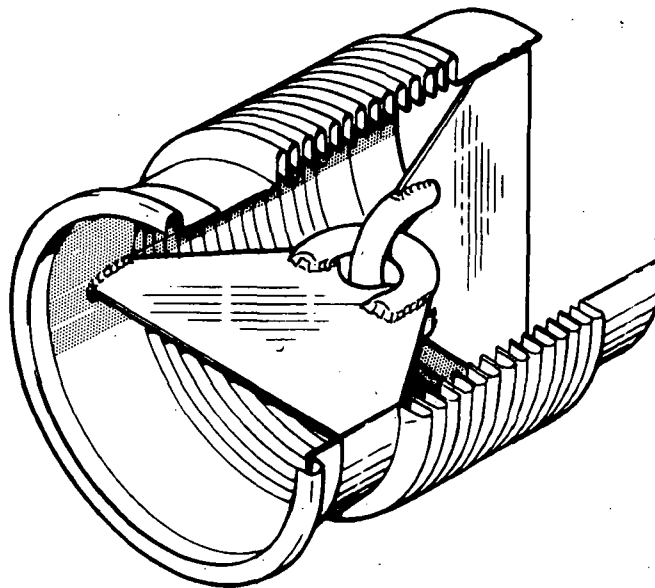
The ducts, exclusive of bellows sections, connecting the various components should be designed primarily for internal pressure loads. Duct diameters are determined by heat-transfer-fluid flow requirements and the expansion joint stiffnesses are determined by the interface load requirements. The interconnecting ducts between HXDA components will have operating temperatures of 420 K to 1140 K.

The hot-gas ducts will constitute an important design area, since the gas temperatures and pressures are substantial and differential thermal expansions are expected to be large. As an example of relative deflections that can be expected between room temperature and operating temperature, the growth of a 100 cm Hastelloy X tube raised in temperature to 1000 K is about 1.0 cm. The relatively large thermal expansions should be accommodated by using flexible joints in the duct system to minimize thermal loads.

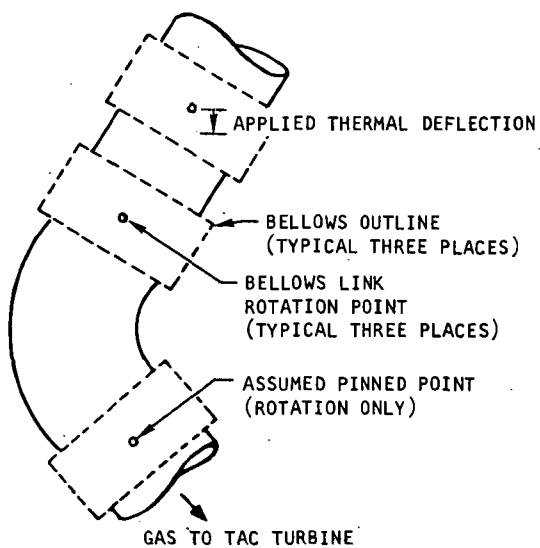
Duct strength for pressure containment and inertia loads must be considered. The duct wall thickness probably will be based primarily on cylinder hoop stress although allowance for local stress concentrations at corners and joints will be required. Inertia loads in the longer ducts may require intermediate supports and the inertia bending moments may affect duct geometry in some cases.

5. Bellows

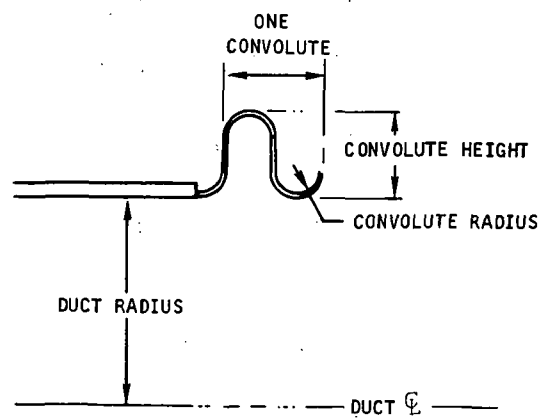
Expansion joints will be required in the ducts connecting the components in the package. The recommended approach to accommodate the thermal movement between components is to incorporate three link-type convolute bellows in each section. The use of link-type bellows, shown in Figure 2-53, provides pressure balance in the piping system; this avoids unbalance forces on the components and simplifies the package support system (the piping system may be more complicated with the link-type bellows since they must be out-of-line to provide three directional thermal expansion capability). In addition, a combination of link- or rotation-type bellows provides the desired movement capability without applying excessive forces to the heat exchanger manifolds. This is particularly important for the elevated temperature bellows in the system because pressure containment strength requirements dictate relatively small convolute heights and large wall thicknesses, which are opposite requirements for thermal stress and load alleviation.



a. LINK-TYPE CONVOLUTED BELLOWS



b. TYPICAL BELLOWS ARRANGEMENT



c. BELLOWS GEOMETRY

S-61550 -A

Figure 2-53. Bellows Design

The primary stresses in the bellows convolutes are due to pressure and thermal forces. Pressure stress design can be used to establish an acceptable convolute geometry, and bellows buckling strength establishes the maximum active length of the convolutes. Allowable segment lengths between bellows can then be determined to avoid excessive thermal stresses and flange loads for the relative thermal expansion of the components. The relative thermal movements that must be accommodated by a set of three bellows is obtained from the mount system geometry and appropriate thermal expansion of component sections. Typical high temperature bellows design parameters are listed in Table 2-17.

TABLE 2-17
TYPICAL HIGH TEMPERATURE BELLWS DESIGN

Variables		Haynes 25 at 970 K
Input	Internal pressure, kN/sq m	1380
	Duct diameter, cm	18
	Allowable pressure stress, MN/sq m	68
	Material yield stress, MN/sq m	250
	Elastic modulus, MN/sq m	170×10^3
	Thermal deflection, cm	0.51
Output	Thickness per ply, cm	0.048
	Number of ply	2
	Convolute radius, cm	0.20
	Convolute height, cm	0.76
	Number of convolutes	34
	Bellows link separations, cm	23 and 33

REFERENCES

1. Spera, D. A., "Calculation of Thermal-Fatigue Life Based on Accumulated Creep Damage," NASA TND-5489, October 1969.
2. Manson, S. S., "Fatigue: A Complex Subject-Some Simple Approximations," Experimental Mechanics, July 1965.
3. Cooper, R. A., "Creep Effects on Elevated Temperature Fatigue," Paper presented at Westec Conference, Los Angeles, California, March 8-11, 1971.
4. Halford, G. R., "Cyclic Creep-Rupture Behavior of Three High Temperature Alloys," NASA TND-6309, May 1971.
5. Spera, D. A., "The Calculation of Elevated-Temperature Cyclic Life Considering Low-Cycle Fatigue and Creep," NASA TND-5317, July 1969.
6. Richard, C. E., Duncan, J. D., Demogenes, C., and Flieder, W. C., "Low-Cyclic Fatigue Evaluation for Regeneratively Cooled Panels," To be published by NASA, performed under Contract NAS 1-5002.
7. Anon: Huntington Nickel Alloys. Bulletin 20 1-68 T-15, Huntington Alloy Products Division, The International Nickel Company, Inc. 1968.
8. Anon: Steels for Elevated Temperature Service. ADUSS-1089, United States Steel, January 1966.
9. Anon: AiResearch Test Data, 1970.
10. Anon: "Metallic Materials and Elements for Aerospace Vehicle Structures," MIL-HDBK-5A, January 5, 1970 (Change Notice).
11. Anon: "Hastelloy Alloy," Report F30, 037D, Union Carbide Corporation Stellite Division, October 1964.
12. Spera, D. A., "The Calculation of Elevated-Temperature Cyclic Life Considering Low-Cycle Fatigue and Creep," NASA TND-5317, July 1969.
13. Anon: Haynes Alloy No. 25. Report F30, 041C, Haynes Stellite Company, June 1962.

SECTION 3

BRAZING DEVELOPMENT TESTS

INTRODUCTION

The use of gold-based, Palniro 1 (AMS4784) braze alloy in foil thickness of 0.025 mm was not considered excessive in the HXDA design because of previous experience with plate-fin heat exchanger assemblies using 0.050 mm foil thicknesses. However, if the use of thinner braze foil can be shown to be acceptable in the HXDA multisandwich heat exchanger fabrications, then inherent savings of cost and weight are possible.

The objective of these small scale tests was to investigate the use of a minimum thickness Palniro braze foil that could be used in the HXDA plate fin heat exchangers. Braze foil thicknesses of 0.008 mm, 0.013 mm, and 0.019 mm were selected for evaluation because of availability. Micrographic examination of test specimens was utilized to evaluate whether acceptable fin-to-plate contact can be maintained throughout the heat exchanger core matrix. Braze alloy flow characteristics and filleting characteristics were evaluated and room temperature pressure containment capabilities determined for test specimens using braze alloy foil thicknesses selected above.

TEST SPECIMEN DESIGN

The detail design of the test specimen is shown in SK 51876. The test specimens were designed as one-third size recuperator modules with the total stack height of the modules approximately equivalent to the HXDA recuperator design.

The core modules were designed to have a maximum fin crush of 0.05 mm and a minimum fin crush of 0.013 mm. The fin density used in the pressurized side of the module was 6.3 fins/cm, fabricated from 0.10 mm thickness Hastelloy X material. A fin density of 7.9 fin/cm, with a 0.15 mm thickness Hastelloy X fin was used on the unpressurized side.

TEST SPECIMEN FABRICATION

Detail parts of the test specimens, except the pans, were fabricated from Hastelloy X material. A completed test module is shown in Figure 3-1. The cores were assembled and then brazed in a single furnace cycle. Oxidized stainless steel slip sheets were placed between the core modules to prevent diffusion bonding the core modules together while still simulating the thermal gradients that would occur during brazing of a full size recuperator.

The pressure containment capabilities and braze fin joint quality were investigated for the three test modules utilizing braze foil thicknesses of 0.008 mm, 0.013 mm, and 0.019 mm. The core modules with 0.008 mm and 0.013 mm foil also had foil with a 0.025 mm thickness to provide further photographic joint comparisons.

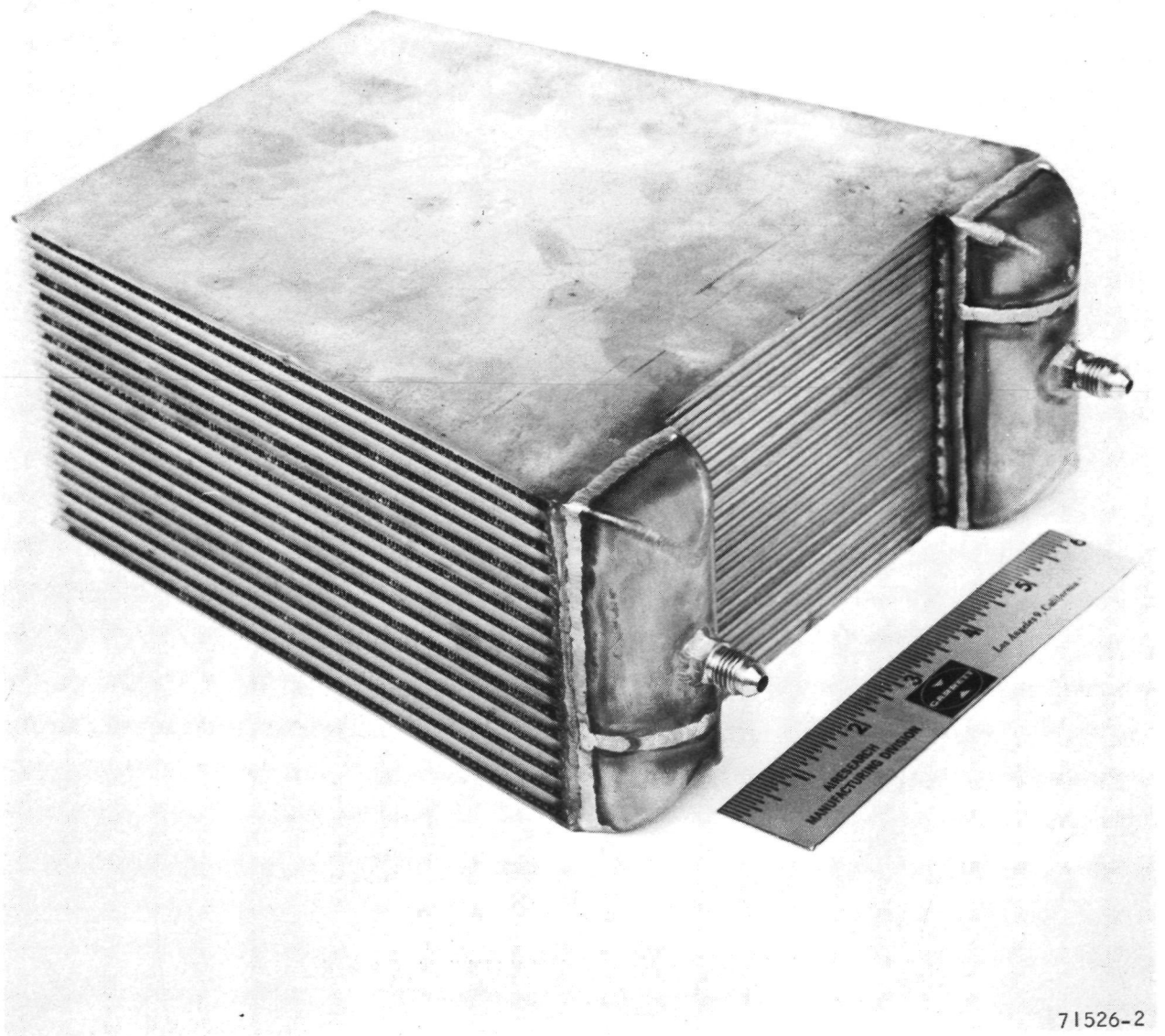
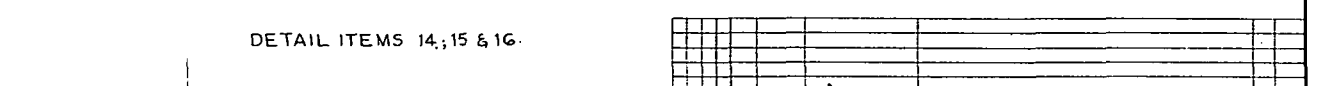
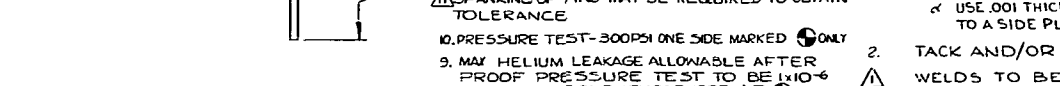
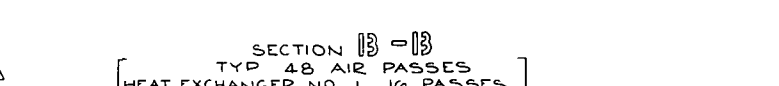


Figure 3-1. Brazing Development Test Module

--	--



QTY REQD		ITEM NO.	CODE IDENT NO.	PART OR IDENTIFYING NO.	NOMENCLATURE OR DESCRIPTION	SYN	ZONE
3		1		-5 BRATED ASSY			3
					PARTS LIST		
UNLESS OTHERWISE SPECIFIED:					 AMERICAN MANUFACTURING COMPANY		

TEST PROCEDURE

The test modules were each submerged in water and subjected to a nitrogen proof pressure test of 2080 kN/sq m and a helium leakage test (one side only). The helium leakage of all modules was less than 9×10^{-8} scc/min.

After proof pressure testing and helium leak testing was completed, the test modules were connected to a hydrostatic pressure source for destructive testing at room temperature. The test module was filled with oil and the pressure was gradually increased until rupture occurred within the test module as evidenced by a sudden decrease in pressure within the unit. Each unit was tested in this manner.

DATA REDUCTION

For the burst pressure test data to be useful, a means of correlating tests such as those conducted in this evaluation with other plate fin geometries is desired. The applied pressure is not a true measure of the severity of the loading on this structure since fin geometry and, to a lesser extent, face sheet geometry can be widely varied to improve or reduce the plate fin internal pressure strength. The simplest means of expressing the loading level is the fin tensile stress, given by the following:

$$\sigma_{fin} = \text{load/fin area}$$

The theoretical relation between fin stress and pressure, P , is therefore

$$\sigma_{fin} = P (b_{fin} - t_{fin}) / t_{fin} \quad (3-1)$$

where b_{fin} and t_{fin} are the spacing and thickness, respectively. The above relation is modified to account for actual fin strength by including the strength factor, f , as a correlating factor between pressure and fin stress at failure. Therefore

$$P_{rupture} = f \sigma \left[t_{fin} / (b_{fin} - t_{fin}) \right] \quad (3-2)$$

where σ is now the material ultimate strength capability for burst rupture.

The major factors which affect fin strength are fin geometry, plate thickness and joint quality. In these tests, fin geometry and plate thickness were held constant in an attempt to evaluate joint quality variation with changes in braze foil thickness. Fin strength or fin efficiency (f) was calculated by rearranging equation 3-2 into the following form:

$$f = P_{rupture} / \left[\sigma t_{fin} / (b_{fin} - t_{fin}) \right] \quad (3-3)$$

RESULTS AND DISCUSSION

The core modules burst at the pressure shown in Table 3-1. The fin rupture pressure correlated to a fin efficiency which is also shown in the table.

TABLE 3-1

BURST PRESSURE, TEST RESULTS FOR RECUPERATOR TEST MODULES

<u>Braze Alloy Thickness, mm</u>	<u>Burst Pressure kN/sq m</u>	<u>Fin Efficiency</u>
0.019	27,400	0.506
0.013	24,600	0.454
0.008	22,500	0.416

Available test data for 0.025 mm thickness foil performed on related programs show burst strength ratios of 0.61 and 0.83 for single layer sandwich panels. Conditions in a multiple layer heat exchanger would probably cause a degradation in strength capability. However, a direct correlation with the tests performed on this program was not feasible due to differences in fin geometry, face sheet thickness, and brazing conditions. Figures 3-2a through 3-2d show photomicrographs of the fin joint qualities for braze alloy thicknesses of 0.008 mm, 0.013 mm, 0.019 mm, and 0.025 mm, respectively. The photomicrographs show a definite improvement in filleting characteristics as braze alloy thickness was increased. It can be seen that all of the braze alloy was used to form the fin-to-tube sheet braze joint with little or no braze alloy remaining on the tube sheet between the fins.

The test results indicate that the thicker braze alloys show a better joint formation from the standpoint of fillet formation and that the large braze joint fillet resulted in higher short-term room temperature burst capabilities. No direct comparison can be made to correlate short-term burst test capabilities to creep rupture capabilities, but previous test data obtained on the Hypersonic Research Engine program show that in a limited number of samples, the thicker alloy (0.025 mm) yielded better creep rupture capabilities than a thinner alloy (0.019 mm). Therefore, since the room temperature burst test did not show a drastic difference in short term pressure containment capabilities as anticipated between the 0.019 and 0.013 mm thick Palmiro 1 braze alloys, single sandwich test panels should be subjected to creep rupture testing to obtain design data.

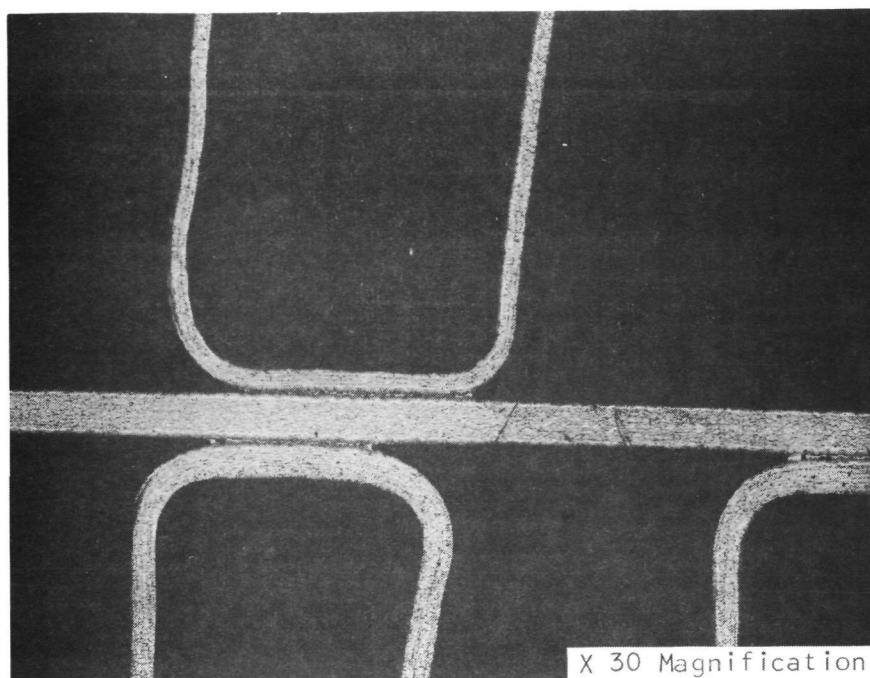


Figure 3-2a. Fillet Formation of 0.008 mm Thick Palniro I Braze Alloy (Micro 24834)

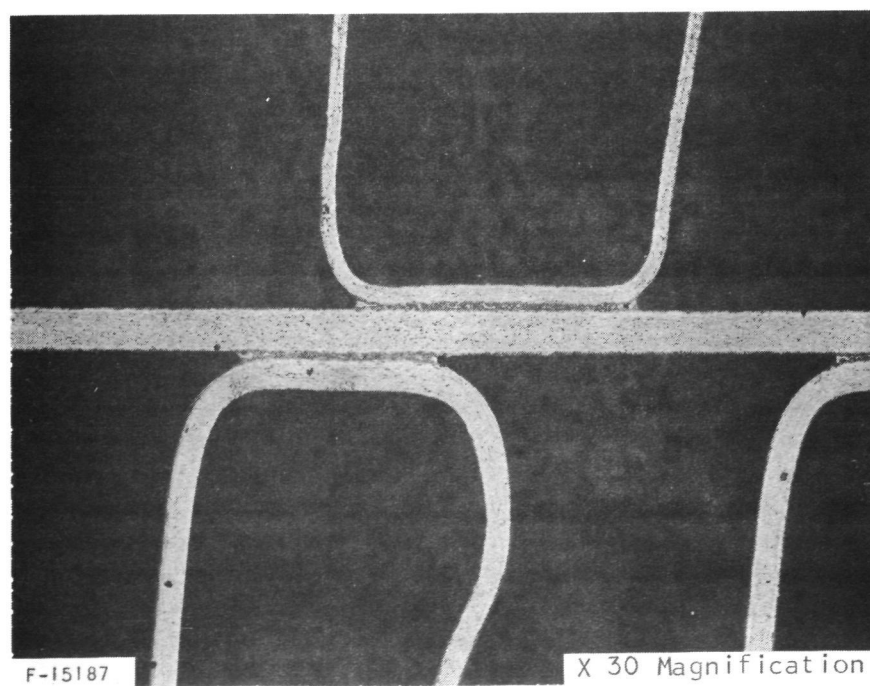


Figure 3-2b. Fillet Formation of 0.013 mm Thick Palniro I Braze Alloy (Micro 24837)

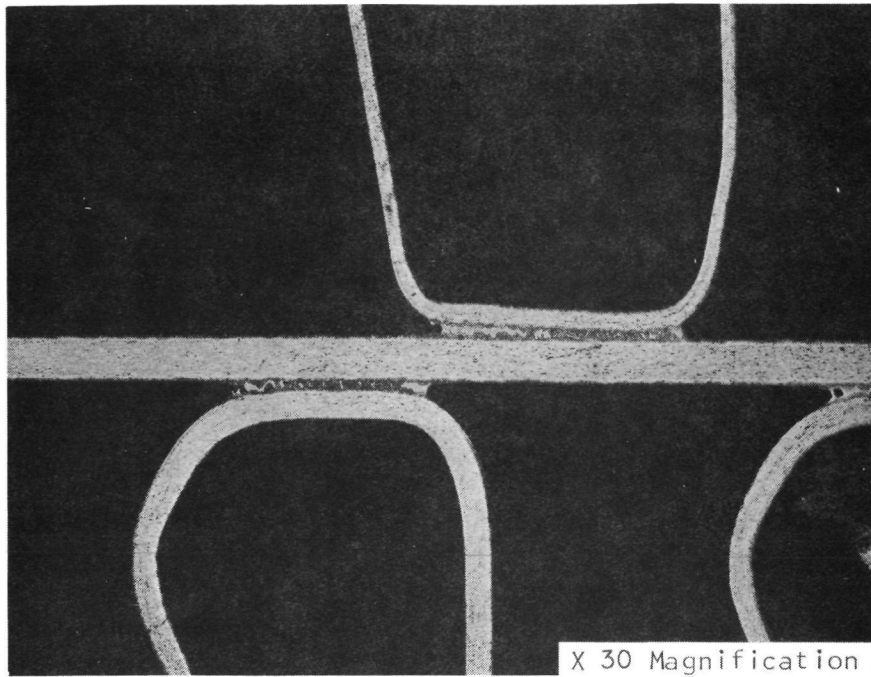


Figure 3-2c. Sample Showing Fillet Formation of 0.019 mm Thick Palniro I Braze Alloy (Micro 24838)

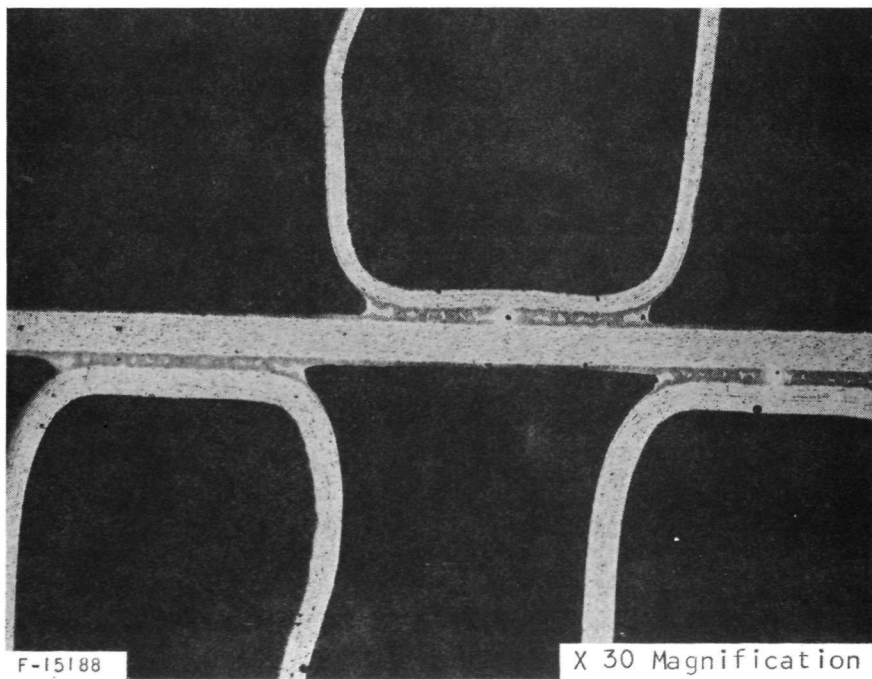


Figure 3-2d. Sample Showing Braze Joint Configuration of 0.025 mm Thick Palniro I Braze

CONCLUSIONS

Test results from the 0.019 and 0.013 mm braze foil test modules show that a 25 percent reduction of braze alloy only reduces the short time pressure containment capabilities by 10 percent with reasonable filleting characteristics. Further reduction of braze foil thickness to 0.008 mm did not show a drastic reduction of short term pressure containment capability but braze filleting was almost nonexistent. Therefore, the brazing development tests show potential for the use of braze foil thicknesses in the range of 0.013 to 0.025 mm as a cost and weight savings measure. Future testing should be performed on test modules fabricated from 0.013 mm braze foil to obtain creep rupture and low-cycle fatigue test data.

Additional fabrication precautions to insure proper braze joint fitup should be considered in the cost analyses associated with using the thinner gold based braze foils. The requirement for more stringent control of the detail parts becomes imperative to ensure that the necessary fin-header-bar fitup is maintained. Therefore, depending on the design of a particular heat exchanger, the cost savings associated with thinner braze foil may be offset by increased material handling costs.

SECTION 4

RECUPERATOR STRUCTURAL TESTS

INTRODUCTION

The objective of these tests was to establish the cyclic thermal strain capability of two critical recuperator areas: (1) the pan-to-heat exchanger core joint and (2) the sheet-to-header bar interface. These recuperator areas, shown schematically in Figure 4-1, typically experience high thermal strains due to temperature differences developed during transient heating conditions associated with each operating cycle. This is an important consideration for required operations to 955 K with the specified life requirement of 1000 cycles.

The test method consists of mechanically applying a fully reversed bending strain to beam specimens to simulate thermally induced strains. This mechanical loading approach provides a consistent, repeatable, and accurately controlled strain range during sample test life. The use of a constant test temperature avoids varying material properties and simplifies analysis of the results. The test apparatus used on this program was constructed for NASA under Contract NAS 1-5002.

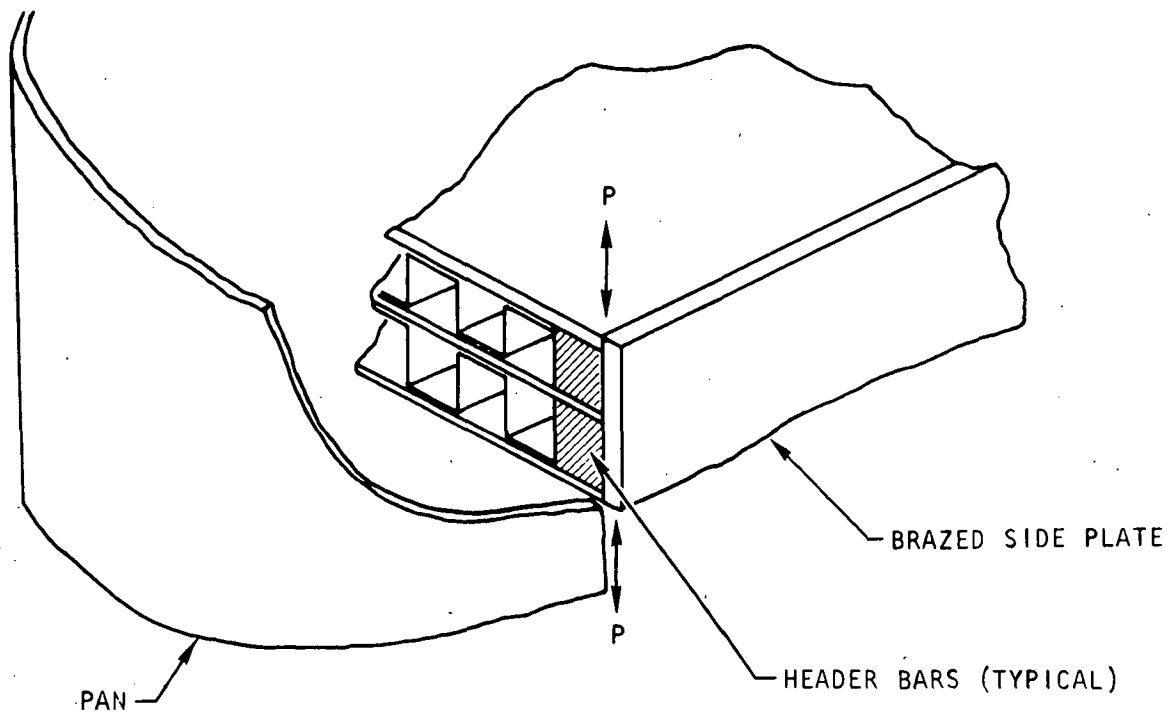
The selected test conditions are summarized in Table 4-1 for the two specimen types. Testing was completed at room temperature to obtain basic low-cycle fatigue data and repeated at an elevated temperature (1000 K) to obtain cyclic life where creep damage was predominate over basic fatigue damage. The 1000 K test temperature is approximately the maximum operating temperature plus 55 K (design criteria). This test temperature coincides with previous tests of brazed plate-fin sandwiches fabricated from Hastelloy X and Palniro I performed under NASA Contract NAS 1-5002.

TABLE 4-1

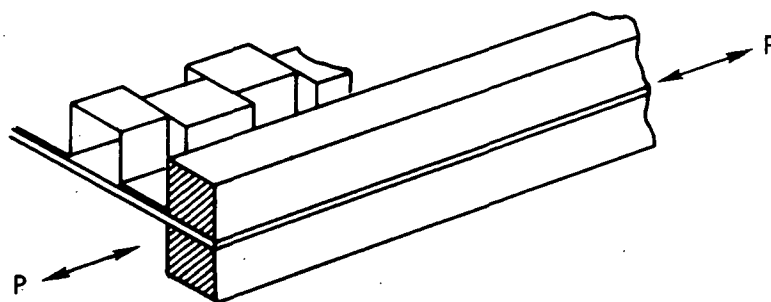
TEST CONDITIONS, RECUPERATOR STRUCTURAL EVALUATION

Specimen	Braze Alloy	Weld Alloy	Test Temperature	Number of Specimens		
				ϵ_1	ϵ_2	ϵ_3
Pan-to-heat exchanger core joint	Palniro I	None	Room temperature	3	3	3
			1000 K	3	3	3
	Palniro I	Yes	Room temperature	3	3	3
			1000 K	3	3	3
Sheet-to-header bar interface	Palniro I	None	Room temperature	3	3	3
			1000 K	3	3	3

$\epsilon \sim$ applied strain



a. PAN RESTRAINT (HEADER BAR AND BRAZED SIDE PLATE LOADING)



b. CORE RESTRAINT (PLATE LOADING)

S-64917

Figure 4-1. Plate-Fin Core Thermal Loads

Three samples were tested at each of three strain levels for a total of nine samples at each temperature. The strain levels were selected to give a range of cycles to failure from approximately 100 to 1000 cycles. This provides a reasonable minimum amount of data for constructing curves of the logarithm of plastic strain range vs the logarithm of cycles to failure. Since these curves are straight lines on a logarithmic display, interpolation to desired values of plastic strain range or life is possible.

TEST SPECIMEN DESIGN

The two test specimen designs are illustrated in Figure 4-2 to show the differences in cross-section. Detail design of the two test specimens for the recuperator structural test can be found in drawings SK 51874 and SK 51875. The first test specimen consists of a combination of sheet and bar material that was intended to simulate the sheet-to-header bar joint in the recuperator design. The absence of fins in this specimen reflects the fact that critical strains, which cause potential cracking of the sheet material and result in interpass leakage, occur only in localized regions adjacent to the header bars. The other specimen simulates the joint between the pan, header bars, and brazed side plate. The test plan calls for one-half of the samples to be tested with a weld pass over the brazed joint as identified by the SK 51875-I assembly, while the other half was to be tested with no weld pass over the brazed joint as identified by the SK 51875-II assembly.

The specimens have a uniform height of 0.573 ± 0.013 cm and surface finish (at extreme bending fibers) of $1.6 \mu\text{m}$. The method of failure detection is to measure the decrease in load required to deform the specimens around the mandrel. However, the sample simulating the sheet-to-header bar interaction provides an internal cavity that can be pressurized and measurement of pressure loss is an alternate method of failure detection. This method is desirable since a small facesheet crack between the bars will not be initially detectable by loss in an applied load.

The brazed and welded pan-to-header bar test specimen did not perform satisfactorily in room temperature tests. The test samples experienced cracks in an excess braze alloy fillet inside the specimen. Since the cracking did not occur in the weld but in an excess braze fillet, the test specimen was redesigned in an effort to eliminate the problem.

Additional weld test specimens were fabricated from available test specimens and metallographically examined. This approach led to the formulation of a recommended design for welding without changing the basic design approach. The present design requires welding on a 0.0662 cm thick land (Figure 4-3a) while the recommended design will have a 0.254 cm thick land (Figure 4-3b). Increasing the parent metal land in the test specimen reduces the heat input to the braze alloy and should eliminate the braze cracking problem.

With the existing parent metal land, the heat from the TIG welding process melts a braze alloy reservoir inside the cavity of the test specimen. Only in this regard does the test specimen differ from a brazed heat exchanger assembly. With the increased parent metal land and the weld still made over

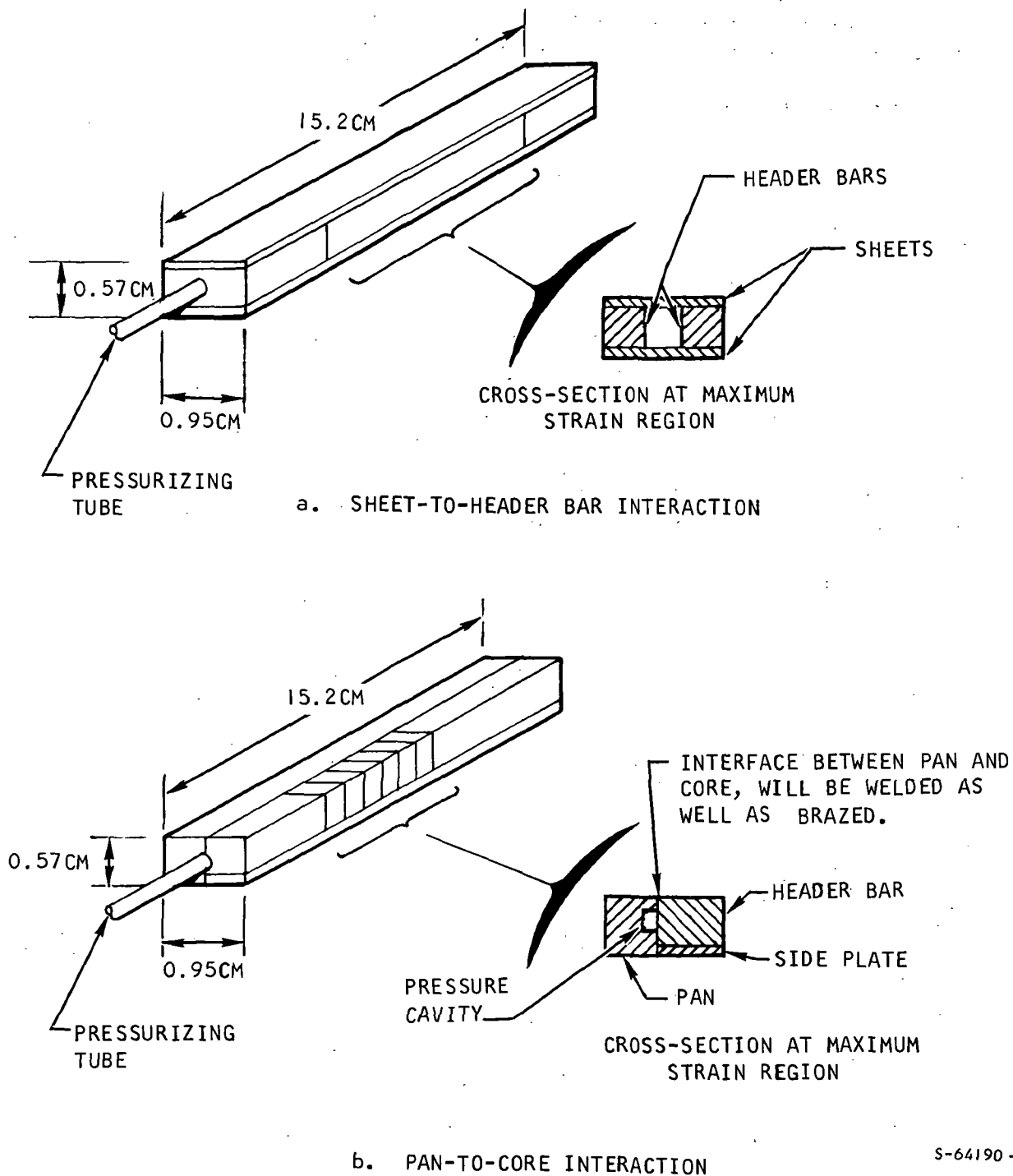
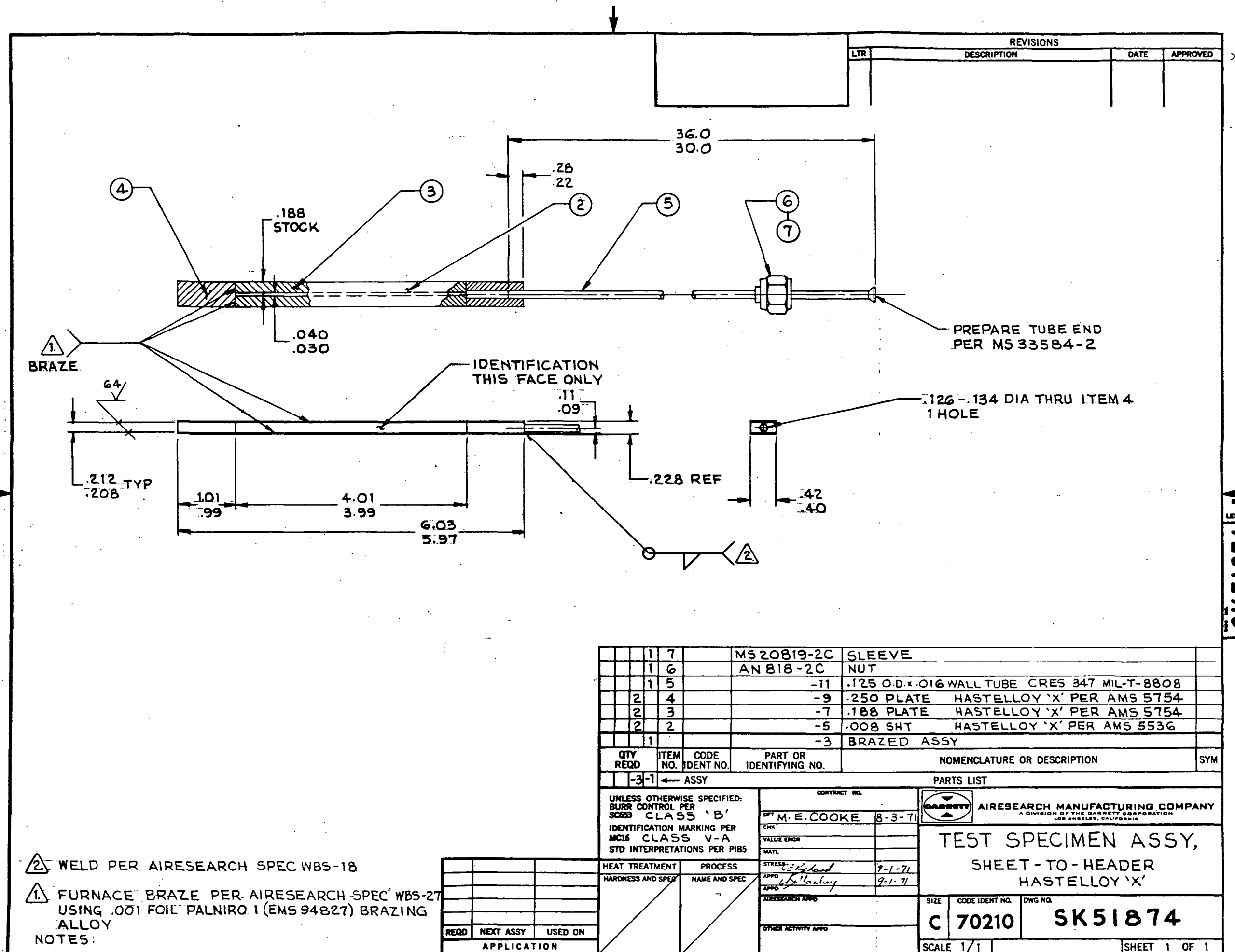
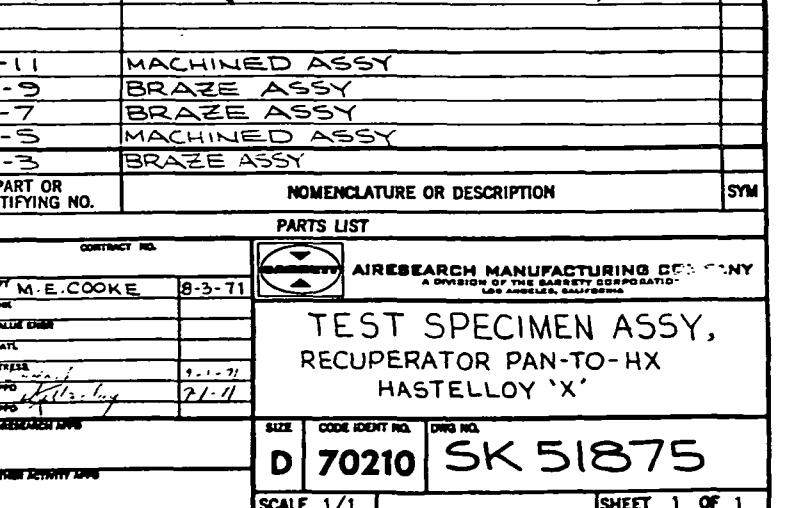
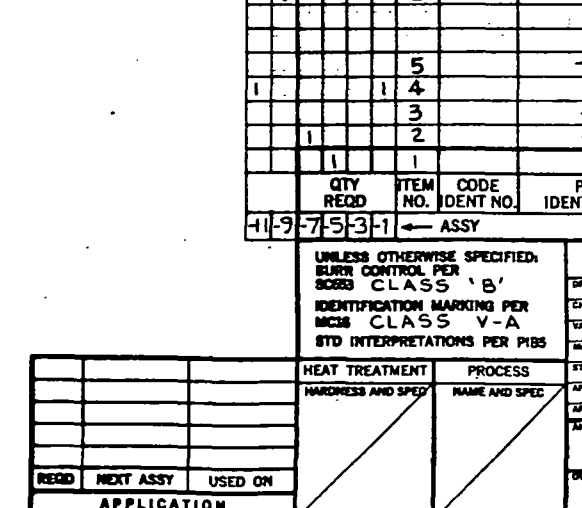
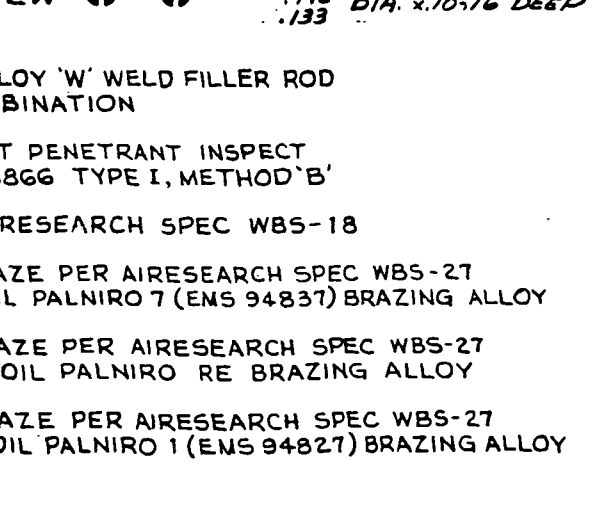
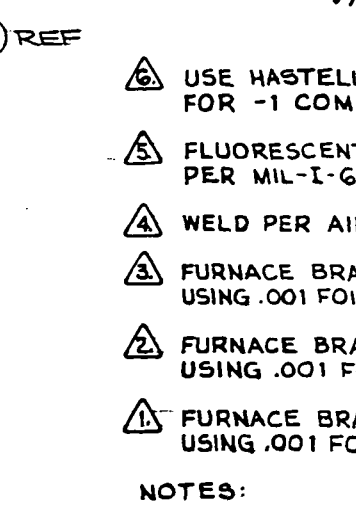
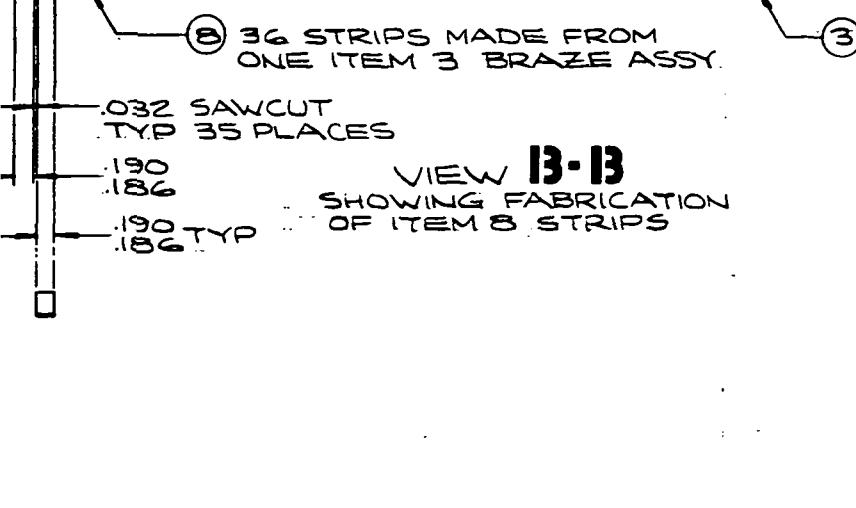
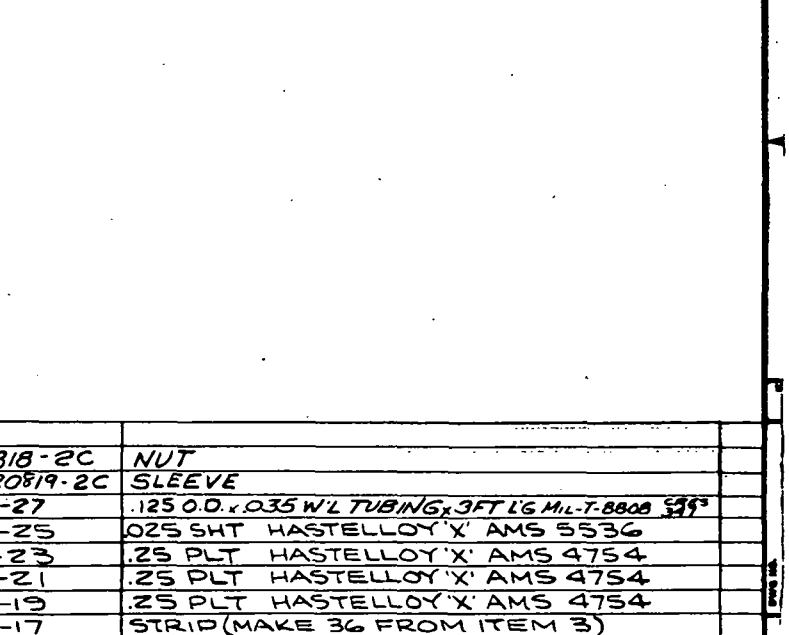
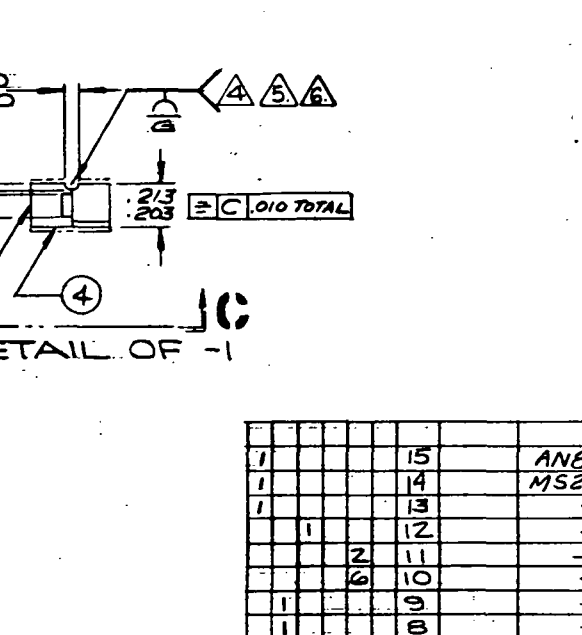
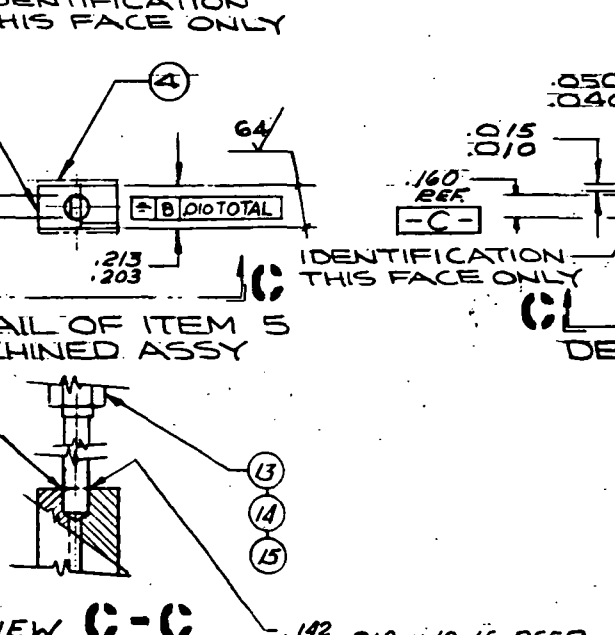
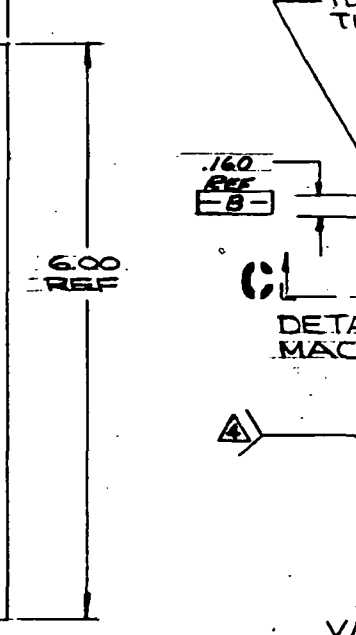
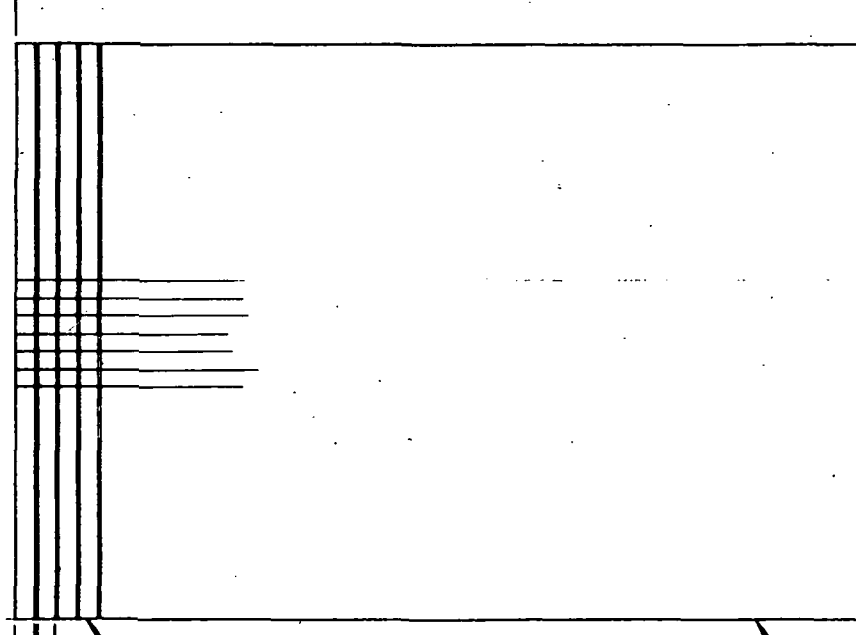
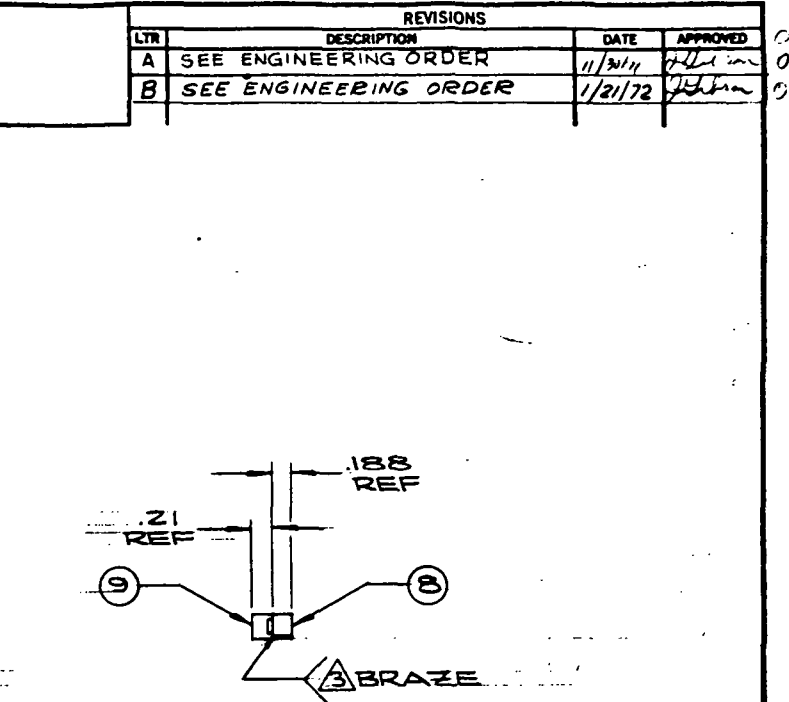
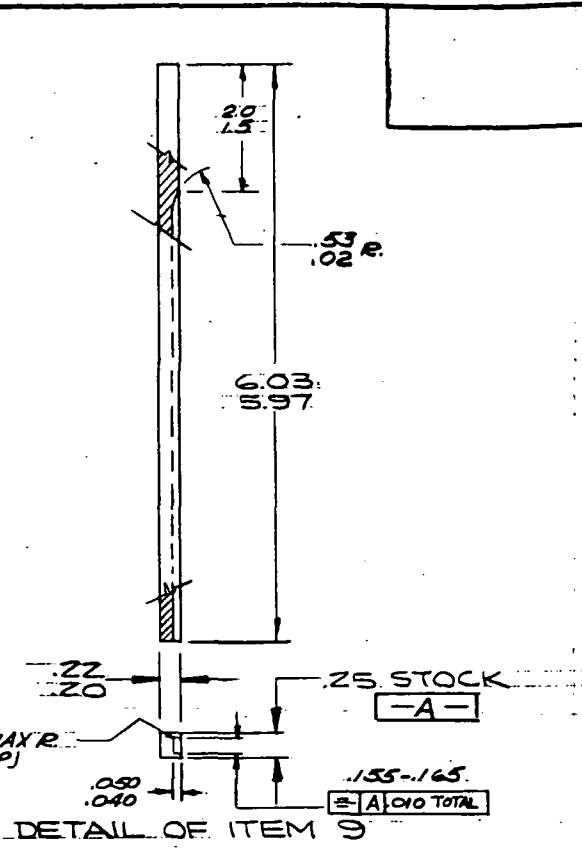
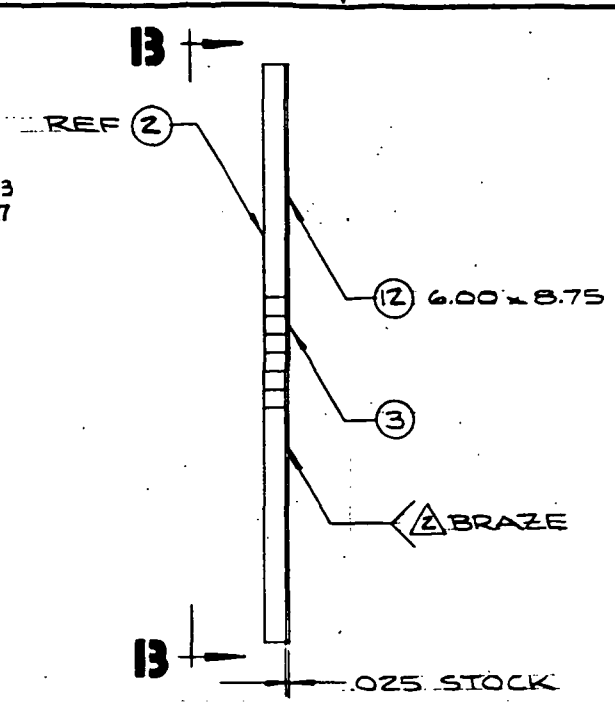
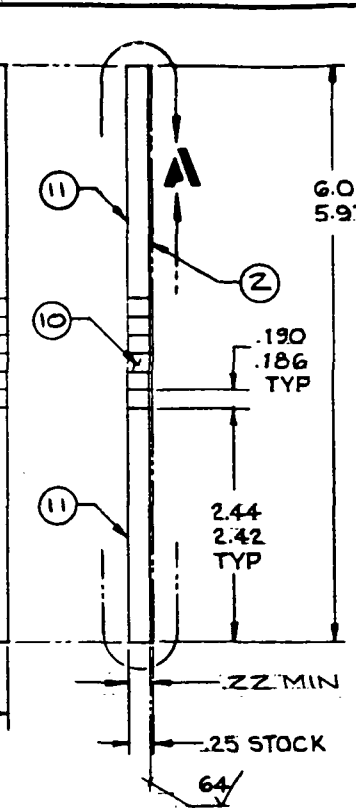
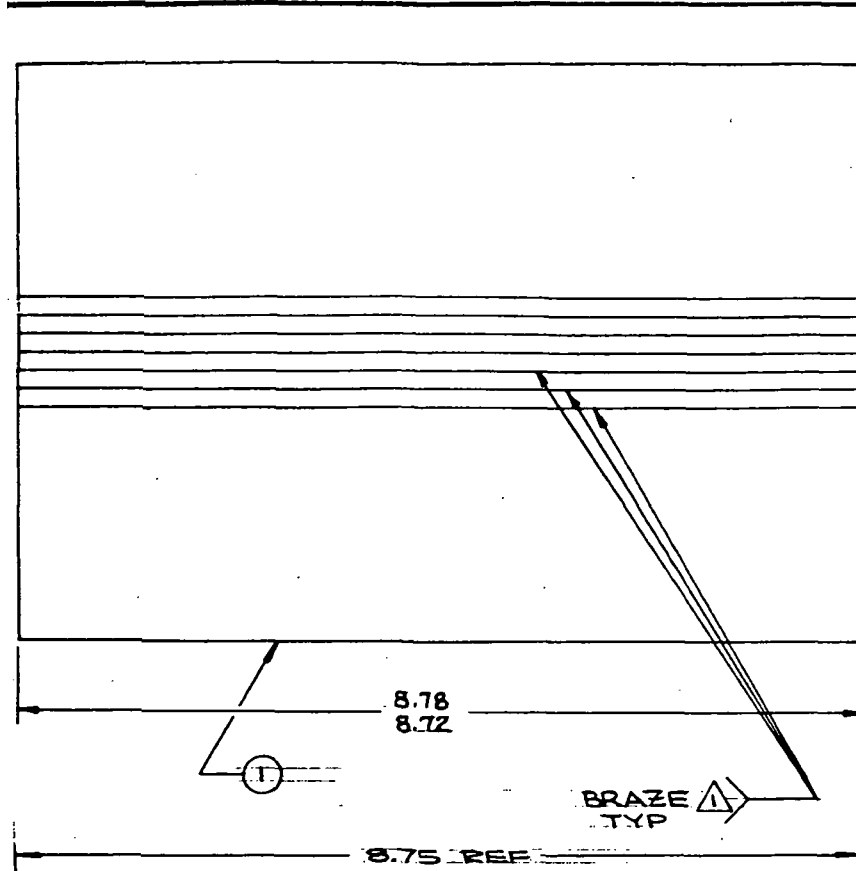


Figure 4-2. Recuperator Test Specimens



REVISIONS			
LTR	DESCRIPTION	DATE	APPROVED
A	SEE ENGINEERING ORDER	11/30/71	John
B	SEE ENGINEERING ORDER	1/21/72	John

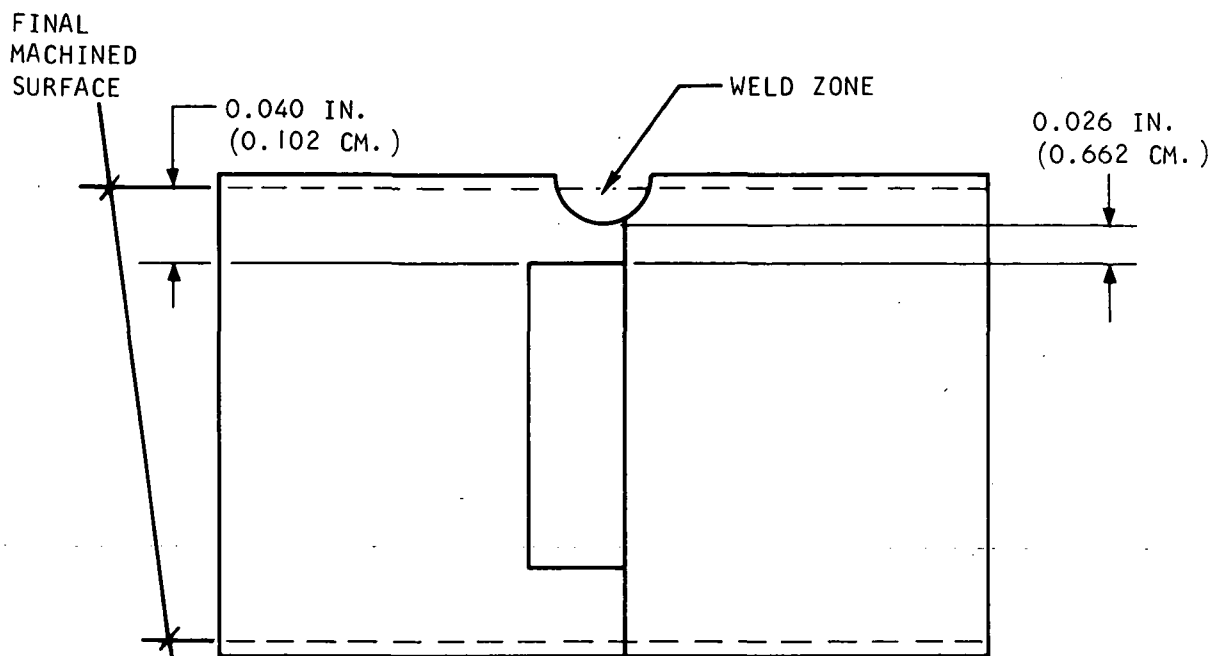


- 6. USE HASTELLOY 'W' WELD FILLER ROD FOR -1 COMBINATION
- 5. FLUORESCENT PENETRANT INSPECT PER MIL-I-6866 TYPE I, METHOD 'B'
- 4. WELD PER AIRESEARCH SPEC WBS-18
- 3. FURNACE BRAZE PER AIRESEARCH SPEC WBS-27 USING .001 FOIL PALNIRO 7 (EMS 94837) BRAZING ALLOY
- 2. FURNACE BRAZE PER AIRESEARCH SPEC WBS-27 USING .001 FOIL PALNIRO RE BRAZING ALLOY
- 1. FURNACE BRAZE PER AIRESEARCH SPEC WBS-27 USING .001 FOIL PALNIRO 1 (EMS 94827) BRAZING ALLOY

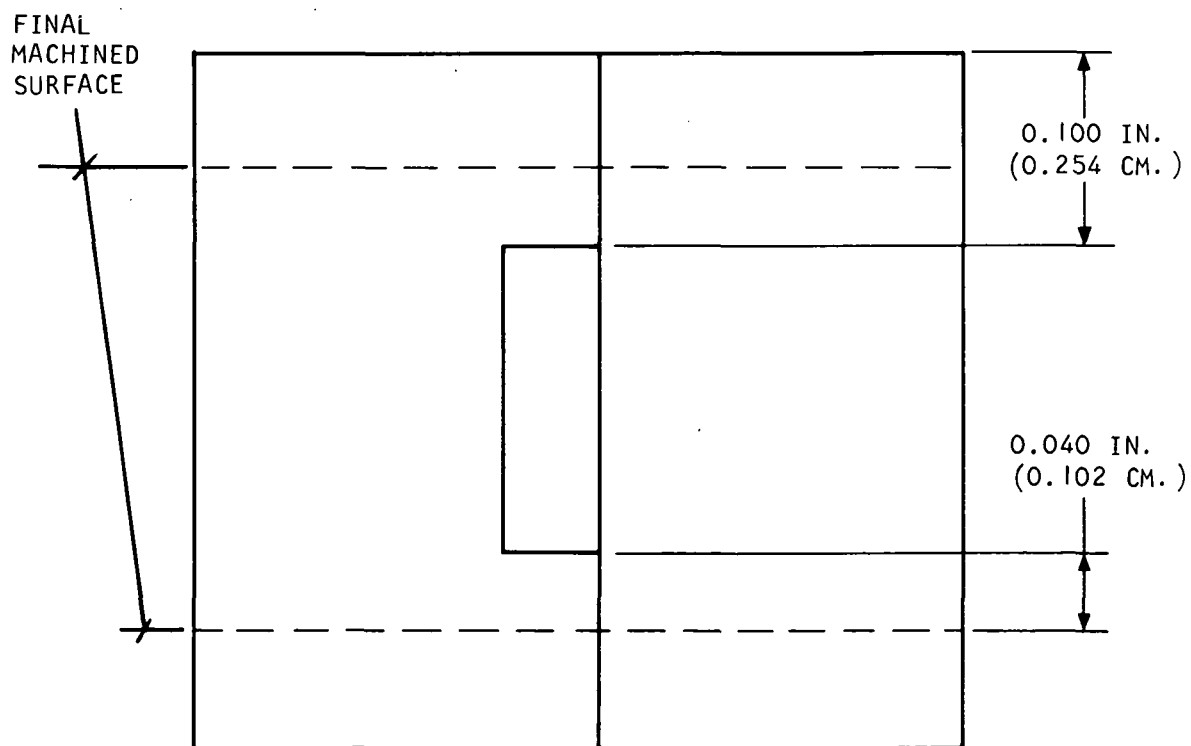
NOTES:

QTY	ITEM	CODE	PART OR	NOMENCLATURE OR DESCRIPTION	SYM
REQD	NO.	IDENT NO.	IDENTIFYING NO.		
11-9-7	5-3-1	← ASSY			
1	15		AN818-2C	NUT	
1	14		MS20519-2C	SLEEVE	
1	13		-27	.125 O.D. x .035 W/L TUBING, 3 FT LG MIL-T-8808 595	
1	12		-25	.025 SHT HASTELLOY 'X' AMS 5536	
1	11		-23	.25 PLT HASTELLOY 'X' AMS 4754	
1	10		-21	.25 PLT HASTELLOY 'X' AMS 4754	
1	9		-19	.25 PLT HASTELLOY 'X' AMS 4754	
1	8		-17	STRIP (MAKE 36 FROM ITEM 3)	
1	5		-11	MACHINED ASSY	
1	4		-9	BRAZE ASSY	
1	3		-7	BRAZE ASSY	
1	2		-5	MACHINED ASSY	
1	1		-3	BRAZE ASSY	

UNLESS OTHERWISE SPECIFIED: SURF CONTROL PER SPEC CLASS 'B' IDENTIFICATION MARKING PER MCS CLASS V-A STD INTERPRETATIONS PER PHS		CONTRACT NO. OFF M. E. COOKE 8-3-71		AIRESEARCH MANUFACTURING COMPANY A DIVISION OF THE SARGENT CORPORATION LOS ANGELES, CALIFORNIA	
HEAT TREATMENT HARDNESS AND SPEED		PROCESS NAME AND SPEC		TEST SPECIMEN ASSY, RECUPERATOR PAN-TO-HX HASTELLOY 'X'	
RECD NEXT ASSY USED ON APPLICATION		DATE 7-1-71		SIZE CODE IDENT NO. DRG NO. D 70210 SK 51875	
				SCALE 1/1 SHEET 1 OF 1	



a. PRESENT SPECIMEN DESIGN



b. REVISED SPECIMEN DESIGN

S-69180

Figure 4-3. Weld-Over-Braze Low Cycle Fatigue Specimen Design

reduced to a level that does not cause the present cracking problem. It should be emphasized that the cracking does not occur in the weld zone but only in the braze alloy reservoir which is unique to the test specimens.

TEST SPECIMEN FABRICATION

The sheet-to-header bar test specimen (SK 51874) is fabricated from Hastelloy X material and was brazed into an integral assembly using 0.025 mm thick Palniro I (AMS 4784) braze foil. The header base and end-plates (Items 3 and 4, respectively, of SK 51874) were double-disc ground to ensure that the detail parts were within the tolerance required for brazing. The assemblies were brazed in a vacuum furnace at 1400 K and subsequently leak checked at a nitrogen pressure 625 kN/sq m to ensure braze joint integrity. The pan-to-core test specimen (SK 51875) consisted of two different test specimens of the same basic design.

The basic pan-to-core specimen was fabricated from a brazed assembly consisting of two plates and simulated header bars that were brazed with 0.025 mm thick Palniro I (AMS 4784) braze alloy. A 0.635 cm thick Hastelloy X sheet was brazed to this first subassembly with 0.025 mm thick Palniro RE braze foil to complete the intermediate subassembly (Item 3 of SK 51875). The final brazed assembly (Item 4) was completed by brazing a simulated pan strip to the intermediate brazed assembly with 0.025 cm thick Palniro 7 (AMS 4786) braze foil. Final machining of the brazed assembly was completed after the final braze cycle and the surface finish of the resulting assembly was 1.6 μ m on the two critical surfaces.

The brazed-only test specimen was completed at this point by welding a pressurization tube into the end of the test specimen. A leak check was performed on the assembly at a nitrogen pressure level of 695 kN/sq m to ensure braze joint integrity. The braze-over-weld test specimen differed from the braze only test specimen in that a groove was machined down the braze alloy (on one side only) that joined the simulated pan strip to the simulated core assembly (Palniro 7 braze joint). This groove was then filled with Hastelloy W weld filler rod and ground flush with the machined surface (1.6 μ m finish). The weld-on-braze test specimen was completed by welding the pressurization tube into the end of the test specimens and leak checking at a nitrogen pressure level of 695 kN/sq m.

Additional weld-on-braze test specimens were fabricated by taking the basic brazed assembly that was not machined to the final part thickness, 0.58 cm, and placing Hastelloy W weld buildup on top of the Palniro 7 (AMS 4786) braze joint. The test specimen was then machined (1.6 μ m finish) to the final thickness of 0.57 cm and leak checked as described on the other test specimens.

TEST PROCEDURE

Specimen load-deflection behavior was established to insure the proper deflection during testing because the central region of the specimen must conform to the mandrel radius to give the known alternating strain. A limited acceptable deflection range exists because insufficient deflection leads to reduced strain levels and excessive deflections produce unacceptable strains at the edge of mandrel. The height of each test specimen was measured and recorded prior to the initiation of testing. Room temperature testing was performed at a cycle rate of 0.5 Hz and the elevated temperature testing was performed at a cycle rate of 0.33 Hz. Specimen temperature during the elevated temperature testing was monitored and controlled by a thermocouple attached to the adjacent spacer bars used to position the specimen on the mandrel. Initial and final readings were recorded and the specimen temperature was controlled to within ± 6 K during the test period.

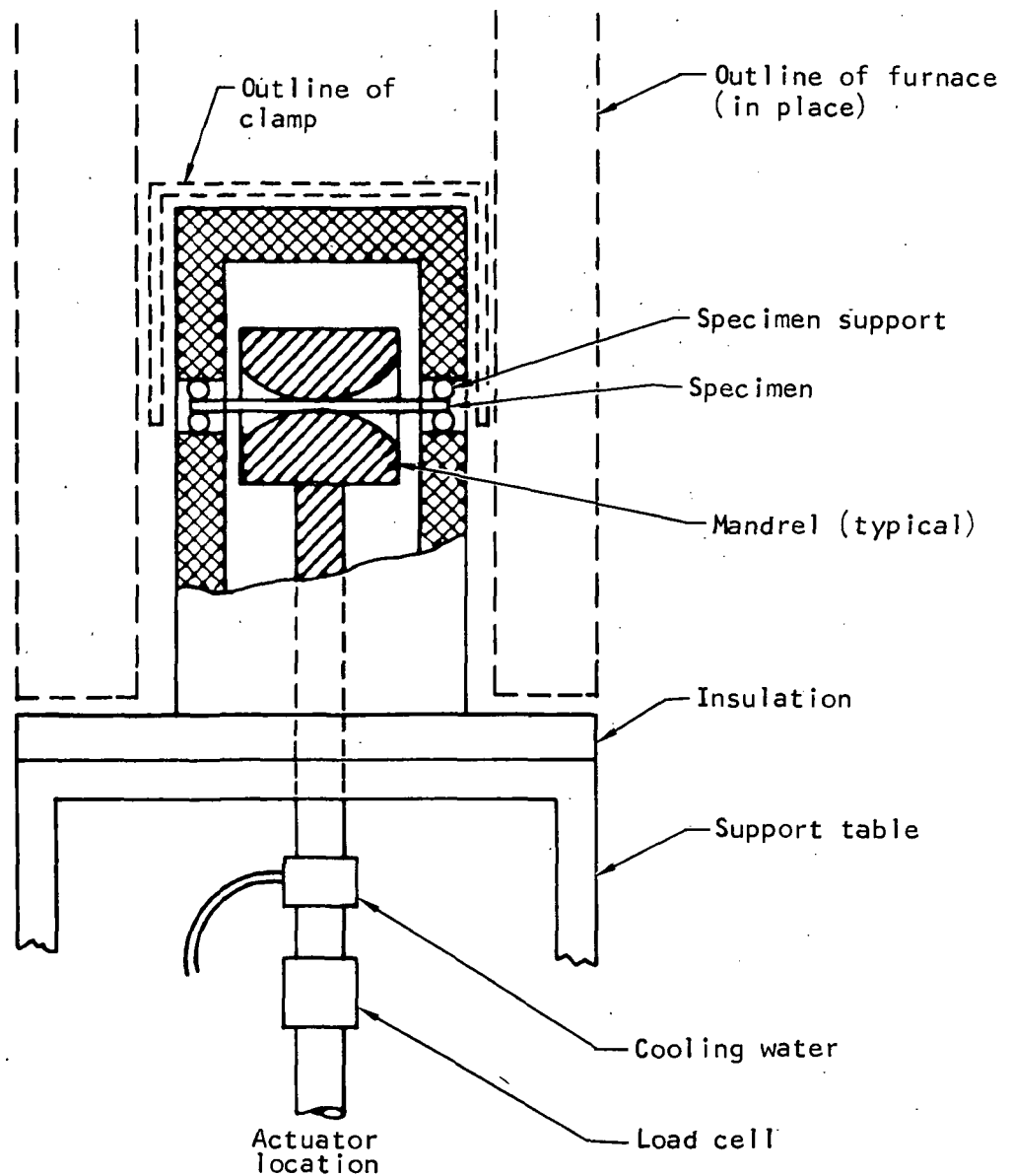
Test specimen failure was determined by a loss in test specimen cavity pressure which occurred when a crack was initiated in an external joint or surface. When the internal cavity pressure of 105 kN/sq m absolute decreased to 69.5 kN/sq m absolute, failure of the specimen was assumed and the test was complete.

The cyclic-life testing was performed on an apparatus, shown in Figure 4-4, which applies a known alternating strain by bending the specimen around opposed curved mandrel surfaces. A hydraulic ram moves the mandrels through the required stroke while the ends of the specimen are restrained from moving in the direction of ram travel.

The ram is driven by a double acting cylinder and ram force levels are monitored by an integral load cell. Stroke reversal is controlled by a four-way solenoid valve and limit switches. Adjustable contacts permit control of stroke length and stroke speed by throttling the flow of hydraulic fluid to the apparatus.

The specimen holding section was designed to fit into a 20 cm Marshall furnace for elevated temperature testing. The sample length was 15 cm and the sample support spacing was 13 cm. The furnace rests on the support table shown in Figure 4-4. The heated zone is partially insulated by packing around the base of the furnace which, together with a cooling water jacket around the ram, prevents the load cell from overheating during high temperature tests. The ram head and specimen support section are fabricated from Alloy 713C permitting operation up to about 1200 K. The ram is of two-piece construction permitting removal of the head for changing mandrels when necessary. Five pairs of mandrel blocks are available with radii from 0.6 cm to 81 cm.

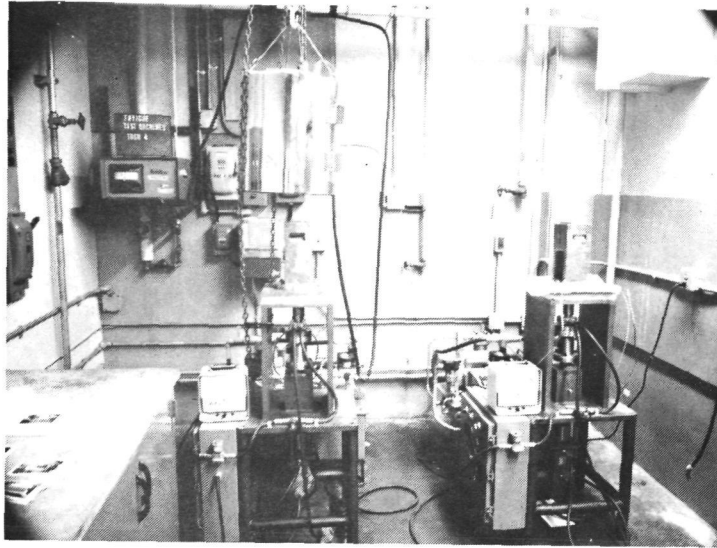
Peripheral equipment includes a pump, flow regulator, pressure control system, counter, and control panel. The control system includes switches connected in series with the pump which automatically terminates testing when reduced ram hydraulic pressure (specimen load) is sensed. Load behavior of the test specimen was recorded on a continuous reading, strip chart recorder with the recorder speed set at 10 cm/min.



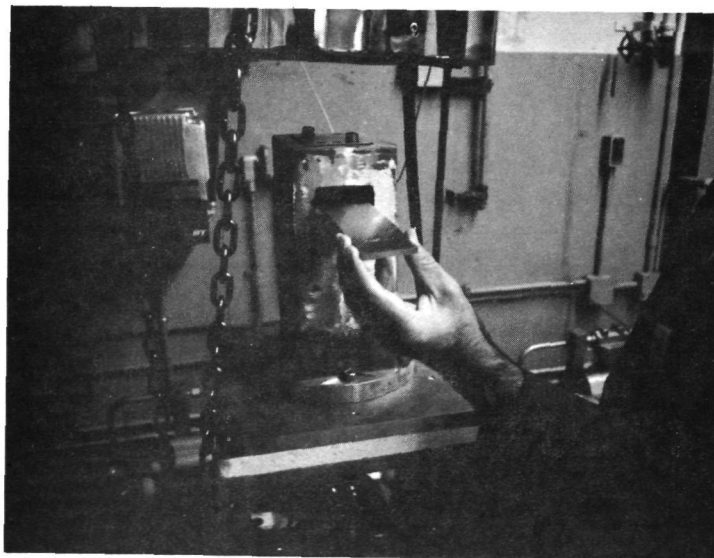
S-64916

a. Specimen loading and support

Figure 4-4. Fatigue Test Apparatus (Page 1 of 2)



Test facility



Specimen placement in test rig

F-12171

Figure 4-4. Fatigue Test Apparatus (Page 2 of 2)

DATA REDUCTION

Plastic Strain Range

When the specimen conforms to the mandrel radius, the applied total engineering strain in the specimen length dimension, ϵ'_l , is related to overall specimen height, h , and mandrel radius, R , by

$$\epsilon'_l = h/(R + 0.5h) \quad (4-1)$$

The general relation between true and engineering strains

$$\epsilon = \ln(1 + \epsilon') \quad (4-2)$$

is used to convert to the total true strain component, ϵ_l , since the desired true strains are noticeably different from engineering strains at the tested strain levels. Subsequent computation of true plastic strain ranges is determined from the total true strain for the specimens utilizing material stress-strain properties for the repeating cycle shown in Figure 4-7. The total strain range consists of twice the elastic strain plus the plastic strain so material stress-strain behavior was correlated to the loading curve from points 4 to 1. The compressive stress-strain curve is assumed to be identical to the tensile curve. The engineering properties were converted to true stress-strain values by the power law relation which accurately described uniaxial true stress-strain behavior.

$$\sigma = B \epsilon_p^m \quad (4-3)$$

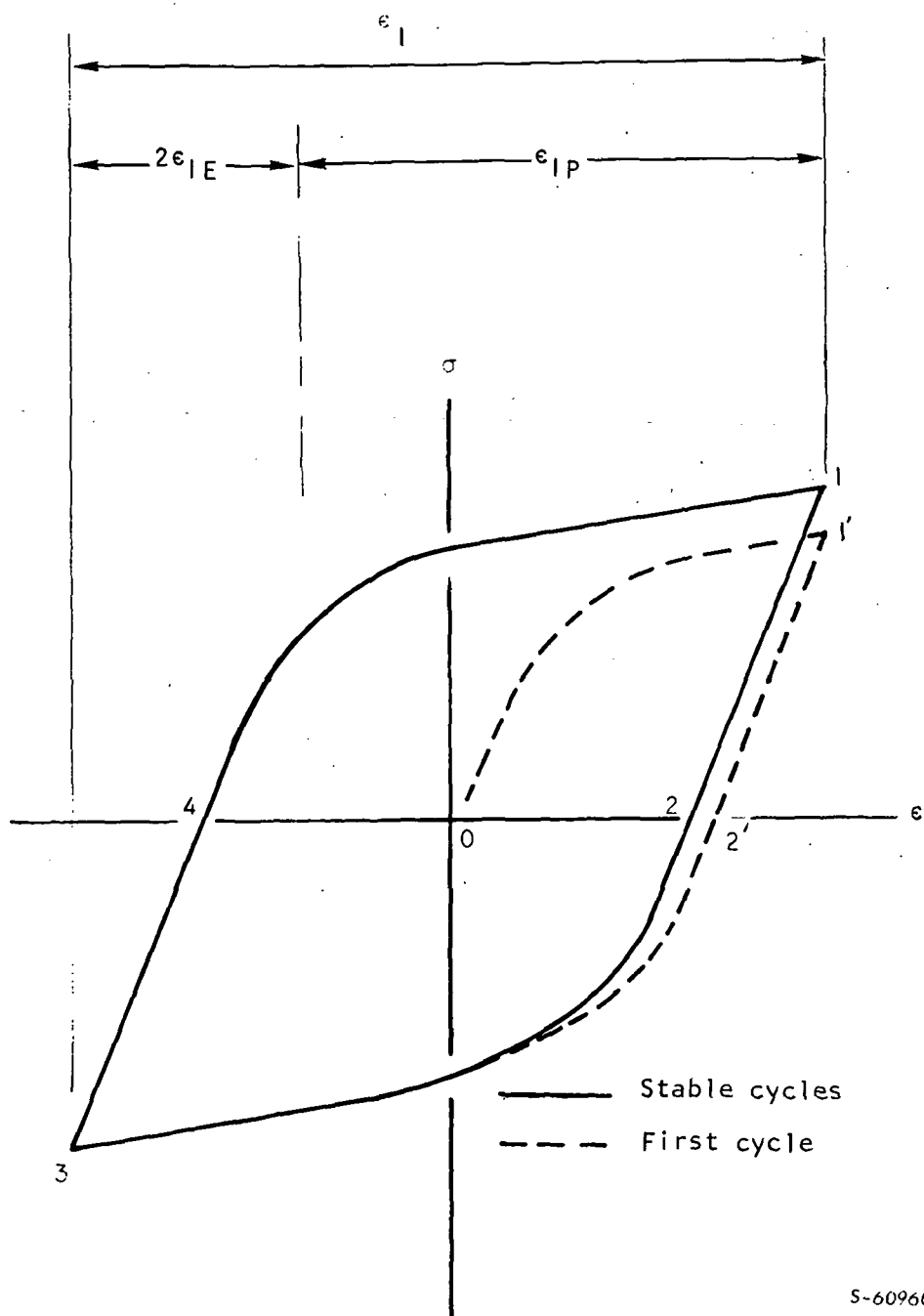
A strain hardening exponent, m , of 0.16 accounts for cyclic material behavior. Assuming that ultimate strength is not affected by cyclic hardening or softening, the constant, B , is

$$B = \sigma'_u \epsilon^m / (m)^m \quad (4-4)$$

The factor, ϵ^m , converts engineering ultimate to the equivalent true stress at the tensile instability strain, m .

The specimens perform as a beam so the cycle for the lengthwise components (Figure 4-5) is the same for uniaxial loading and the plastic strain component, ϵ_{lp} , is the desired plastic strain range ϵ_p . The total uniaxial strain is therefore related to true stress by

$$\epsilon_l = 2\epsilon_{lE} + \epsilon_p = \frac{2\sigma}{E} + \left(\frac{\sigma}{B}\right)^{1/m} \quad (4-5)$$



S-60960

Figure 4-5. Assumed True Stress-Strain Cyclic Behavior, Lengthwise Component

Equations 4-3 and 4-5 permit calculations of plastic strain ranges from the uniaxial total strain by the equation

$$\epsilon_P + \frac{2B\epsilon_P^m}{E} = \epsilon_I$$

The resulting true plastic strain ranges and the associated material properties for the test specimens are summarized in Table 4-2 for use in the recuperator test results.

Cycles to Failure

The test cycle was adjusted to give specimen life for a common reference height, h_o , of 0.572 cm. This permitted computation of plastic strains at the single specimen height. The adjusted cycle life, $N_{adjusted}$, was related to test life, N_{test} , through Equation 4-1 and an inverse one-half power relation in the Universal Slope Equation. Therefore, we have, approximately

$$N_{Adjusted} = N_{Test} (h/h_o)^2 \quad (4-6)$$

The logarithmic average of a set of data points, j , is

$$N_{average} = 10 \left(\frac{1}{j} \sum_i^j \log (N_{Adjusted}) \right) \quad (4-7)$$

Adjusted cyclic life calculations for the recuperator test specimen failures and the resulting average cyclic life for each mandrel size are summarized in Table 4-2.

TABLE 4-2

PLASTIC STRAIN RANGES AND MATERIAL PROPERTIES FOR
RECUPERATOR TEST RESULTS

a. Plastic Strain Range

Temperature	Mandrel Radius, cm	Applied Total Engineering Strain, percent (Equation 4-1)	Associated True Total Strain Range, percent (Equation 4-2)	True Plastic Strain Range, percent (Equation 4-6)
Room temperature	13	4.40	4.30	3.51
	23	2.47	2.44	1.74
	41	1.40	1.39	0.77
	81	0.70	0.70	0.20
1000 K	13	4.40	4.30	3.60
	23	2.47	2.44	1.82
	41	1.40	1.39	0.84
	81	0.70	0.70	0.25

b. Material Properties

Temperature	Elastic Modulus, MN/sq m	Ultimate Tensile Stress, MN/sq m
Room temperature	198×10^3	847
1000 K	149×10^3	556

NOTES: (1) Material Properties for Hastelloy X Brazed with Palnir 1, Tests reported in NASA CR-1884

(2) Strain Ranges from NASA CR-1884

RESULTS AND DISCUSSION

Cyclic-life test results for the sheet-to-header bar and brazed pan-to-header bar specimens are summarized in Table 4-3. The brazed and welded pan-to-header bar specimen did not perform satisfactorily due to cracks experienced in an excess braze alloy fillet and sufficient meaningful test data was not obtained.

The room temperature test (0.5 Hz cycle rate) results for the specimens are compared graphically to previous tests performed for NASA Langley (NASA CR-1884, October, 1971) in Figure 4-6. In all specimens, failure was detected by loss in gas pressure through a 0.025 to 0.075 cm fracture depth. As expected, Hastelloy X parent metal has the highest cyclic life capability. The sheet-to-header bar specimens show a reduction in cyclic life of about 70 percent compared to parent metal, probably due to the presence of the braze alloy. The brazed pan-to-header bar specimen showed significantly greater data scatter than the other specimens. The difference in data scatter between the two specimen types is attributed to the behavior of braze when subjected to tensile loading, as in the case of pan-to-header bar specimen, when compared to shear loading, as in the case of the sheet-to-header bar specimen. Plate fin specimens tested previously and reported in NASA CR-1884, show the lower cyclic life capability. This reduction in cyclic life is primarily attributed to notches associated with the offset fin geometry.

The 1000 K elevated temperature test results (continuous cycling rate of 0.4 Hz) are summarized in Figure 4-7. Overall comparisons are similar; however, the slope of the plastic strain range vs cycles to failure curves vary from specimen to specimen. This could be attributed to varying creep behavior of the different alloys because creep is the primary damage mechanism at this temperature.

TABLE 4-3

RECUPERATOR CYCLE LIFE RESULTS

Specimen Type	Test Temperature	13 cm Mandrel			23 cm Mandrel			41 cm Mandrel			81 cm Mandrel		
		h/h_o	Cycles Test	Avg	h/h_o	Cycles Test	Avg	h/h_o	Cycles Test	Avg	h/h_o	Cycles Test	Avg
Sheet-to-Header Bar	Room Temperature	1.013	53		1.018	246		1.013	1272				
		1.018	51	51	1.013	273	257	1.013	1249	1290			
		1.013	46		1.013	233		1.013	1249				
Pan-to-Header Bar, Brazed	1000 K				1.013	64		1.013	265		1.013	1467	
					1.013	76	74	1.013	164	214	1.013	1494	1510
					1.013	75		1.013	164		1.013	1462	
Pan-to-Header Bar, Brazed and Welded	Room Temperature	0.956	20		0.920	36		0.920	1886				
		0.942	43	37	0.947	119	78	0.942	1700	1700			
		0.916	91		0.942	163		0.942	1418				
Pan-to-Header Bar, Brazed and Welded	1000 K				0.938	37		0.933	128		0.929	852	
					0.938	10	16	0.933	84	74	0.938	1376	1050
					0.938	17		0.920	58		0.938	1478	
Pan-to-Header Bar, Brazed and Welded	Room Temperature							0.942	118				
								0.942	85	89			
Pan-to-Header Bar, Brazed and Welded	1000 K												

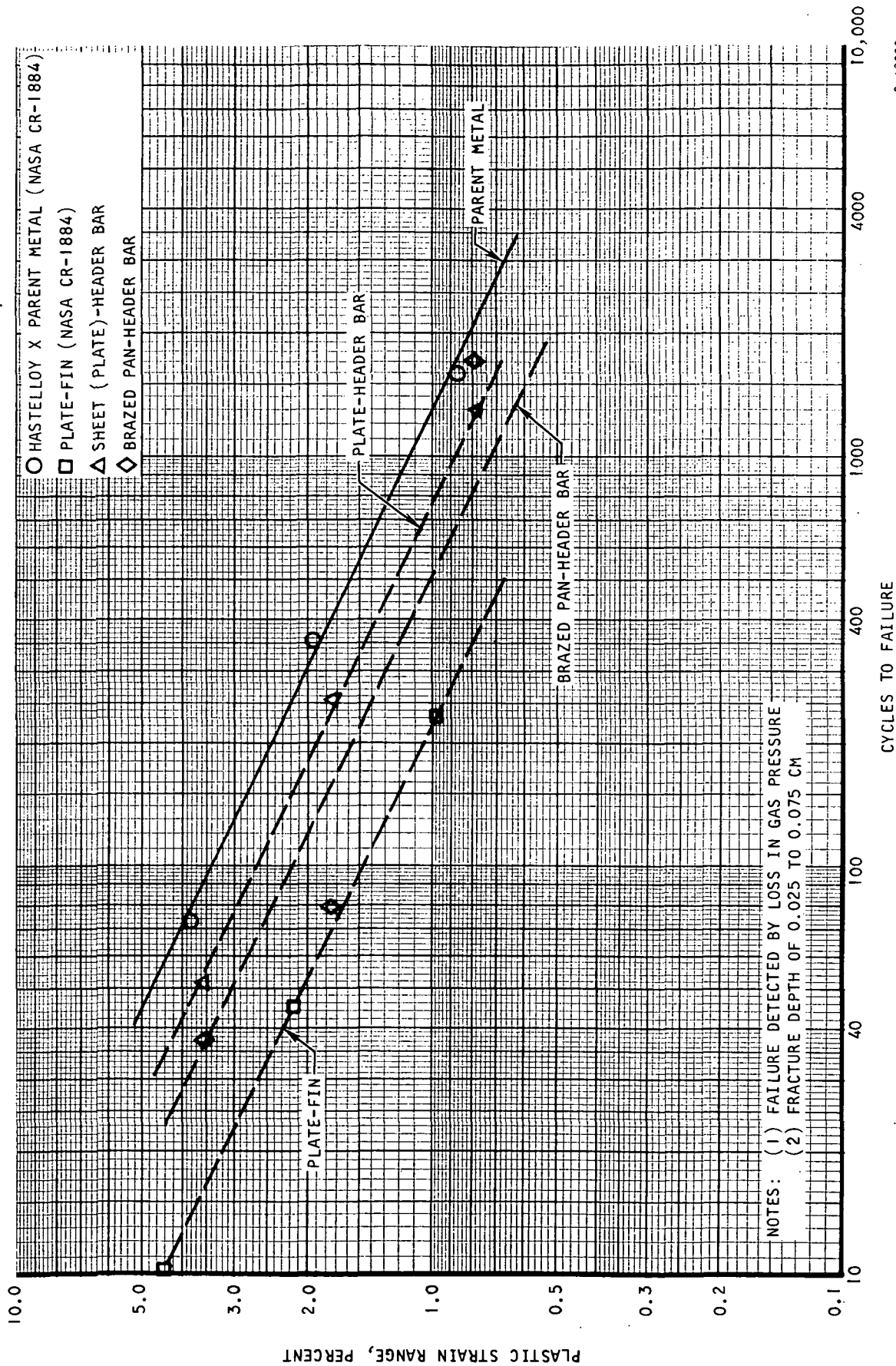
Notes: (1) Adjustment to constant height, h_o , of 0.572 cm

$$N_{\text{Adjusted}} = N_{\text{Test}} (h/h_o)^2$$

(2) Logarithmic Average from:

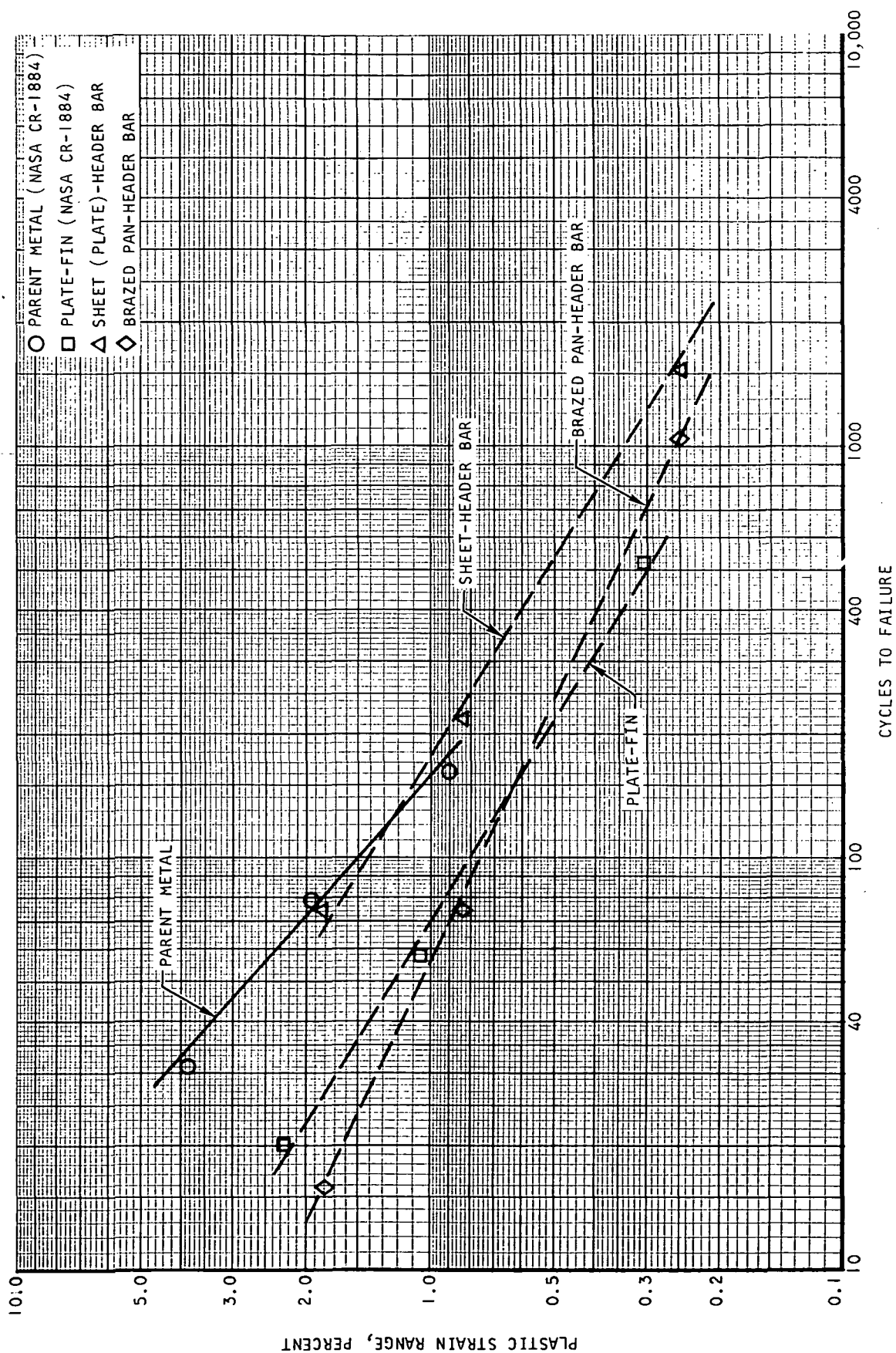
$$N_{\text{Average}} = 10^{\frac{1}{j} \sum_{i=1}^j \log (N_{\text{Adjusted}})_k}$$

(3) Room temperature rate = 0.5 H_z , 1000K rate = 0.4 H_z



S-69028

Figure 4-6. Comparison of Recuperator and Hastelloy X Parent Metal Specimens at Room Temperature



S-69027

Figure 4-7. Comparison of Recuperator and Hastelloy X Parent Metal Specimens at 1000 K

CONCLUSION

Results of the room temperature tests show that the sheet-to-header bar specimens will provide approximately 70 percent of the parent metal cyclic strain capability obtained in previous tests. This reduction in cyclic strain capability is partially attributed to the presence of braze alloy. The room temperature pan-to-header bar specimens showed a further 15 percent reduction in cyclic strain capability. The comparable plate-fin data from previous testing shows the lower cyclic strain capability. This further reduction in fatigue strength was primarily attributed to the offset-fin geometry which is unique to the plate-fin test specimens.

The elevated temperature test results compare similarly; however, the slope of the life cycle curve is different for each specimen, pointing to the need for further evaluation of cyclic creep damage accumulated at the required operating temperature.

As a result of the recuperator structural tests, it was concluded that the sheet-to-header bar joint design will provide adequate cyclic strain capability to satisfy the 1000 cycle life requirement. However, acceptability of the pan-to-heat exchanger core joint was not determined due to problems associated with the weld-over-braze test specimens. The brazed and welded pan-to-header bar specimen did not perform satisfactorily due to cracks experienced in an excess braze alloy fillet. It was concluded that heat from the weld process penetrates the existing parent metal land causing remelt of the braze alloy inside the test specimen cavity and that increasing the parent metal land thickness will eliminate the cracking problem associated with the weld-over-braze process. It should be emphasized that the cracking occurs in the braze alloy reservoir which is unique to the test specimen design and does not reflect the actual recuperator pan-to-header bar joint.

SECTION 5

HEAT SOURCE HEAT EXCHANGER STRUCTURE TESTS

INTRODUCTION

The objective of these tests was to verify the low cycle fatigue properties of the material selected for use on the heat source heat exchanger. From the preliminary structural analysis, the Haynes 188 material, which is a cobalt-based alloy, was selected as the desired structural material. However, since Haynes 188 is a new material, Haynes 25 was included in the testing as an alternate material. Initially, the specimens were subjected to a vacuum exposure at 1140 K for 100 hr. This treatment was intended to simulate operating exposure in a vacuum at a temperature of 977 K for times up to the 100,000 hr design life.

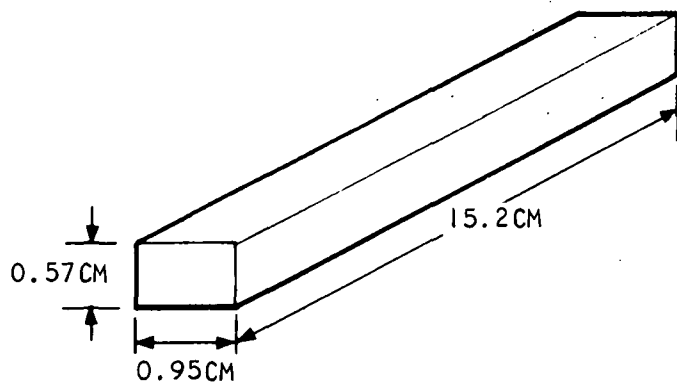
The tests were conducted at room temperature and 1030 K; the latter corresponds to the specified 977 K maximum operating temperature plus the 55 K overtemperature capability required for design. Three specimens were tested at three different strain levels giving a total of nine test points at each temperature for each test specimen configuration. In addition, a test incorporating a second load profile with a 5 minute hold time at temperature was included in the case of the parent metal specimens to provide further data on the creep damage fraction at the elevated temperature condition. The desired cyclic life range was approximately 100 to 1500 cycles. The tests provided logarithmic curves of the plastic strain range vs cycles to failure to facilitate comparison of the specimens and to provide convenient design data for interpolation and extrapolation.

TEST SPECIMEN DESIGN

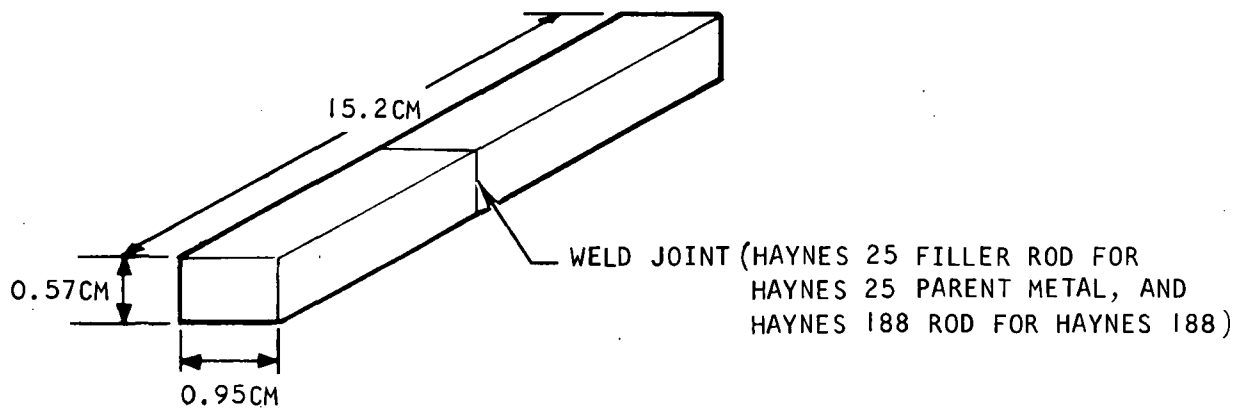
The test specimens were designed to verify the various uses of the material in fabrication of the heat source heat exchanger. The test specimens were tested to simulate the use of the material in the following conditions: parent metal, parent metal welded to parent metal, and parent metal welded to Hastelloy X material. The heat source heat exchanger test specimen designs are shown schematically in Figure 5-1 and the detail designs can be found in drawings SK 51871, SK 51872, and SK 51873.

TEST SPECIMEN FABRICATION

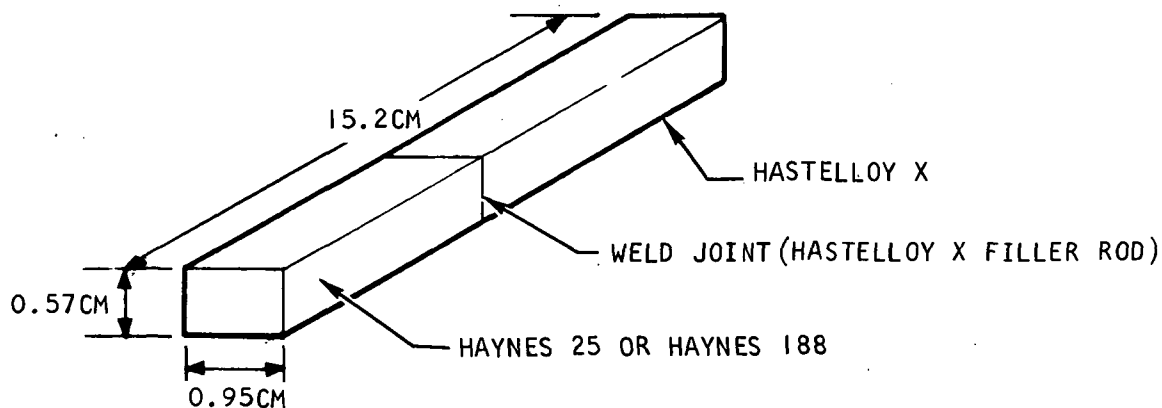
The parent metal test specimens were sectioned from 0.96 cm thick plate stock and then final machined to a 0.57 cm height, 0.95 cm width and 15.2 cm length with a 1.6 μm surface finish. The welded specimens were fabricated from 0.96 cm thick plates welded together, straightened after welding, and then final machined to a 0.57 cm height, 0.96 cm width and 15.2 cm length with a 1.6 μm surface finish. The test specimens were identified on the vertical surface of the specimen away from the edges and centers to prevent any premature failure due to part identification. Accelerated life vacuum exposure for 100 hr at 1140 K was imposed on all of the test specimens. This thermal aging cycle was intended to simulate operating exposure in a vacuum at a temperature of 977 K for times up to the 100,000 hr design life.



a. PARENT METAL, HAYNES 25 OR HAYNES 188



b. WELDED PARENT METAL, HAYNES 25 OR HAYNES 188



c. HAYNES 25 OR HAYNES 188 WELDED TO HASTELLOY X

S-64191 -8

Figure 5-1. Heat Source Heat Exchanger Test Specimens

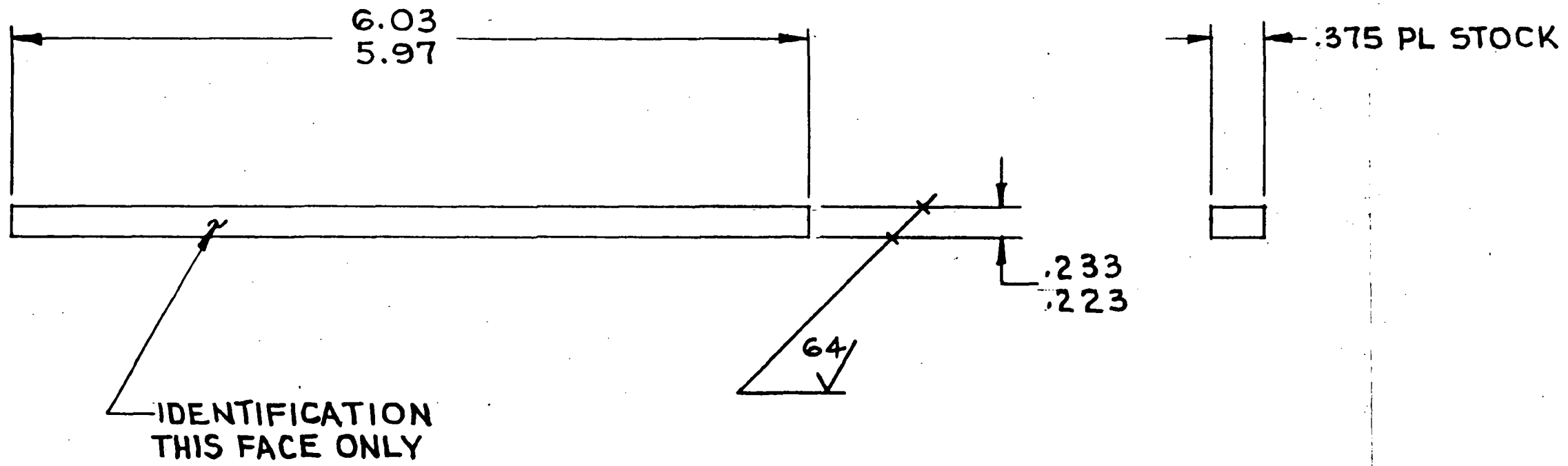


1L81SXS
ON 9MG

REV LTR

REVISIONS

LTR	DESCRIPTION	DATE	APPROVED



					-2	.375 PLATE HAYNES 188 (NO SPEC AVAILABLE)	1
					-1	.375 PLATE HAYNES 25 PER AMS 5759	1
QTY REQD	ITEM NO.	CODE IDENT NO.	PART OR IDENTIFYING NO.	NOMENCLATURE OR DESCRIPTION			SYM
			← ASSY	PARTS LIST			
			UNLESS OTHERWISE SPECIFIED: STD INTERPRETATIONS PER PIBS BURR CONTROL PER SC633 CLASS 'B' IDENTIFICATION MARKING PER MC18 CLASS V-A PROCESS	CONTRACT NO.		AIRESEARCH MANUFACTURING COMPANY A DIVISION OF THE BARRETT CORPORATION LOS ANGELES, CALIFORNIA	
			HEAT TREATMENT	DFT M.E. COOKE 8-2-71		TEST SPECIMEN, 1 PIECE HAYNES 25 OR HAYNES 188	
				CHK APPLIED MICH. 9-1-71			
				APPD Killackey		SIZE CODE IDENT NO. DWG NO.	
				AIRESEARCH APPD		B 70210 SK 51871	
REQD	NEXT ASSY	USED ON	APPLICATION	OTHER ACTIVITY APPD		SCALE 1/1 SHEET 1 OF 1	

1. MAY BE PURCHASED FROM:
HAYNES STELLITE DIVN OF CABOT
INDUSTRIES , KOKOMO , INDIANA

NOTES

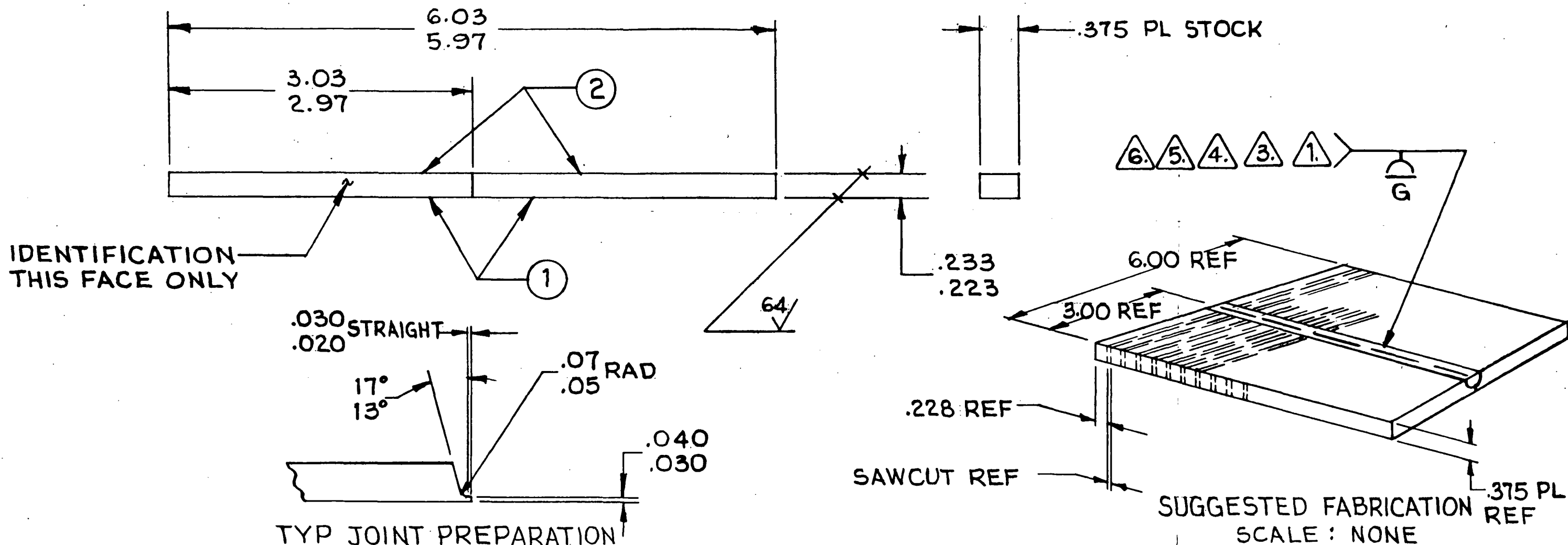


SK51872
ON DMD

REV A
LTR

REVISIONS

LTR	DESCRIPTION	DATE	APPROVED
A	SEE ENGINEERING ORDER	12/2/71	J. H. HARRIS



- 6. USE HAYNES 188 WELD FILLER ROD FOR -2 COMBINATION
- 5. USE HAYNES 25 WELD FILLER ROD FOR -1 COMBINATION
- 4. FLUORESCENT PENETRANT INSPECT PER MIL-I-6866 TYPE I, METHOD 'B'
- 3. RADIOGRAPHIC INSPECTION PER MIL-STD-453
- 2. MAY BE PURCHASED FROM:
HAYNES STELLITE DIVN OF CABOT INDUSTRIES, KOKOMO, INDIANA
- 1. WELD PER AIRESEARCH SPEC WBS-18 NOTES

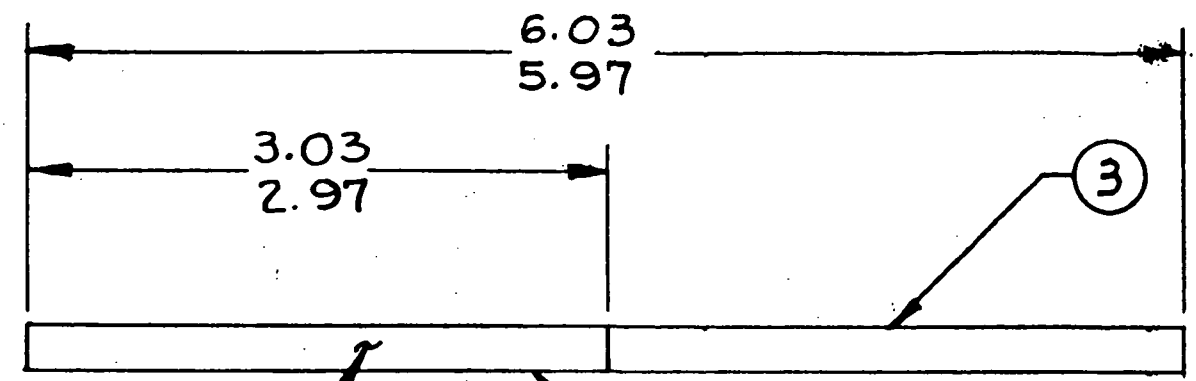
2	2	-5	.375 PLATE	HAYNES 188 (NO SPEC AVAILABLE)	2
2	1	-3	.375 PLATE	HAYNES 25 PER AMS 5759	2
QTY REQD	ITEM NO.	CODE IDENT NO.	PART OR IDENTIFYING NO.	NOMENCLATURE OR DESCRIPTION	SYM
-2	-1	← ASSY		PARTS LIST	
			UNLESS OTHERWISE SPECIFIED: STD INTERPRETATIONS PER PIBS BURR CONTROL PER SC653 CLASS 'B' IDENTIFICATION MARKING PER MC16 CLASS V-A	CONTRACT NO. OFT M.E. COOKE 8-2-71 CHK APPLIED MECH 9-1-71 VALUE ENGR APPD K. H. HARRIS 9-1-71 AIRESEARCH APPD	
			PROCESS		
			HEAT TREATMENT		
REQD	NEXT ASSY	USED ON			
			APPLICATION		
				AIRESEARCH MANUFACTURING COMPANY A DIVISION OF THE GARRETT CORPORATION LOS ANGELES, CALIFORNIA	
				TEST SPECIMEN ASSY HAYNES 25 OR HAYNES 188	
				SIZE B	
				CODE IDENT NO. 70210	
				DWG NO. SK51872	
				SCALE 1/1	
				SHEET 1 OF 1	



SK51873
ON 5MD

REV 4
LTR

REVISIONS			
LTR	DESCRIPTION	DATE	APPROVED
A	SEE ENGINEERING ORDER	12/2/71	<i>[Signature]</i>



.375 PL STOCK

IDENTIFICATION
THIS FACE ONLY

.030 STRAIGHT
.020

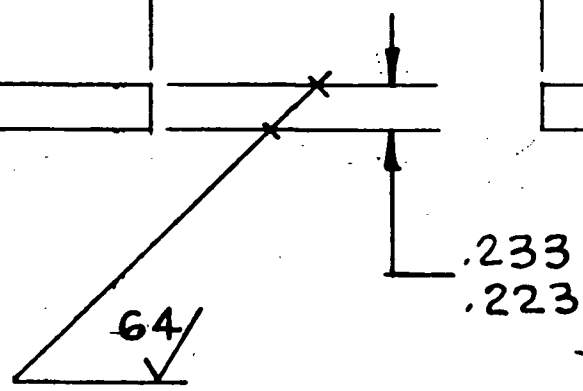
17°
13°

.07 RAD
.05

1
2

.040
.030

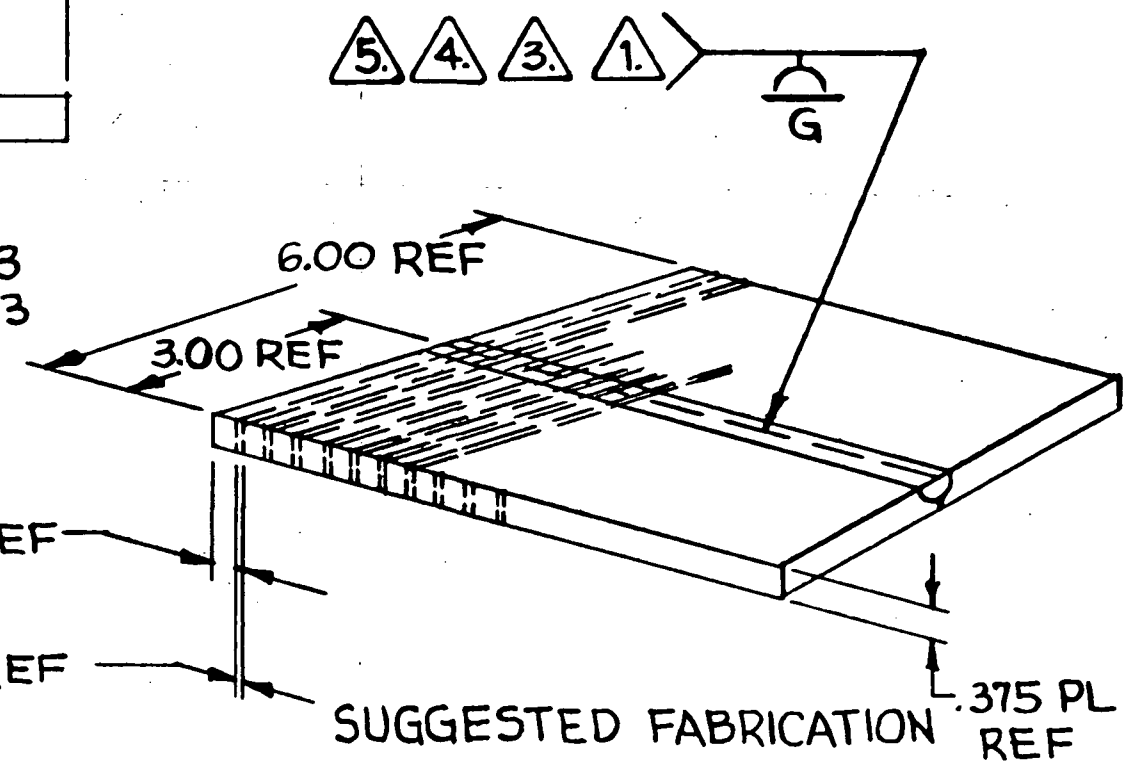
TYP JOINT PREPARATION



.233
.223

.228 REF

SAWCUT REF



SUGGESTED FABRICATION
SCALE: NONE

- 5. USE HASTELLOY 'X' WELD FILLER ROD FOR -1 & -2 COMBINATIONS
- 4. FLUORESCENT PENETRANT INSPECT PER MIL-I-6866, TYPE I, METHOD 'B'
- 3. RADIOGRAPHIC INSPECTION PER MIL-STD-453
- 2. MAY BE PURCHASED FROM:
HAYNES STELLITE DIVN OF CABOT INDUSTRIES, KOKOMO, INDIANA
- 1. WELD PER AIRESEARCH SPEC WBS-18

1	1	3		-9	.375 PLATE HASTELLOY 'X' PER AMS 5754	
1		2		-7	.375 PLATE HAYNES 188 (NO SPEC AVAILABLE)	2
	1	1		-5	.375 PLATE HAYNES 25 PER AMS 5759	2
QTY REQD	ITEM NO.	CODE IDENT NO.	PART OR IDENTIFYING NO.	NOMENCLATURE OR DESCRIPTION		SYM
	-2-1	← ASSY	PARTS LIST			
			UNLESS OTHERWISE SPECIFIED: STD INTERPRETATIONS PER PIBS BURR CONTROL PER SC653 CLASS 'B' IDENTIFICATION MARKING PER MC16 CLASS V-A	CONTRACT NO.	AIRESEARCH MANUFACTURING COMPANY A DIVISION OF THE BARRETT CORPORATION LOS ANGELES, CALIFORNIA	
			PROCESS	DFT M.E. COOKE 8-2-71 CHKD APPLIED MFCW C.E. Richard 9-1-71 VALUE ENGR		
			HEAT TREATMENT	APPD J. Mackey 9-1-71 AIRESEARCH APPD		
			OTHER ACTIVITY APPD			
REQD	NEXT ASSY	USED ON	APPLICATION			
			SIZE	CODE IDENT NO.	DWG NO.	
			B	70210	SK 51873	
			SCALE 1/1	SHEET 1 OF 1		

TEST PROCEDURE

Specimen load-deflection behavior was established to insure the proper deflection during testing. The central region of the specimen conformed to the mandrel radius to give the known alternating strain. A limited acceptable specimen deflection range exists since insufficient deflection leads to reduced strain levels and excessive deflection would have produced unacceptable strains at the edge of the mandrel.

The height of each test specimen was accurately measured and recorded prior to testing. The room temperature testing was performed at a cycle rate of 0.5 Hz and the elevated temperature testing (1030 K) was performed at a cycle rate of 0.33 Hz. The parent metal Haynes 25 and Haynes 188 test specimens were also tested at 1030 K with a 5 minute hold time at maximum strain once per cycle.

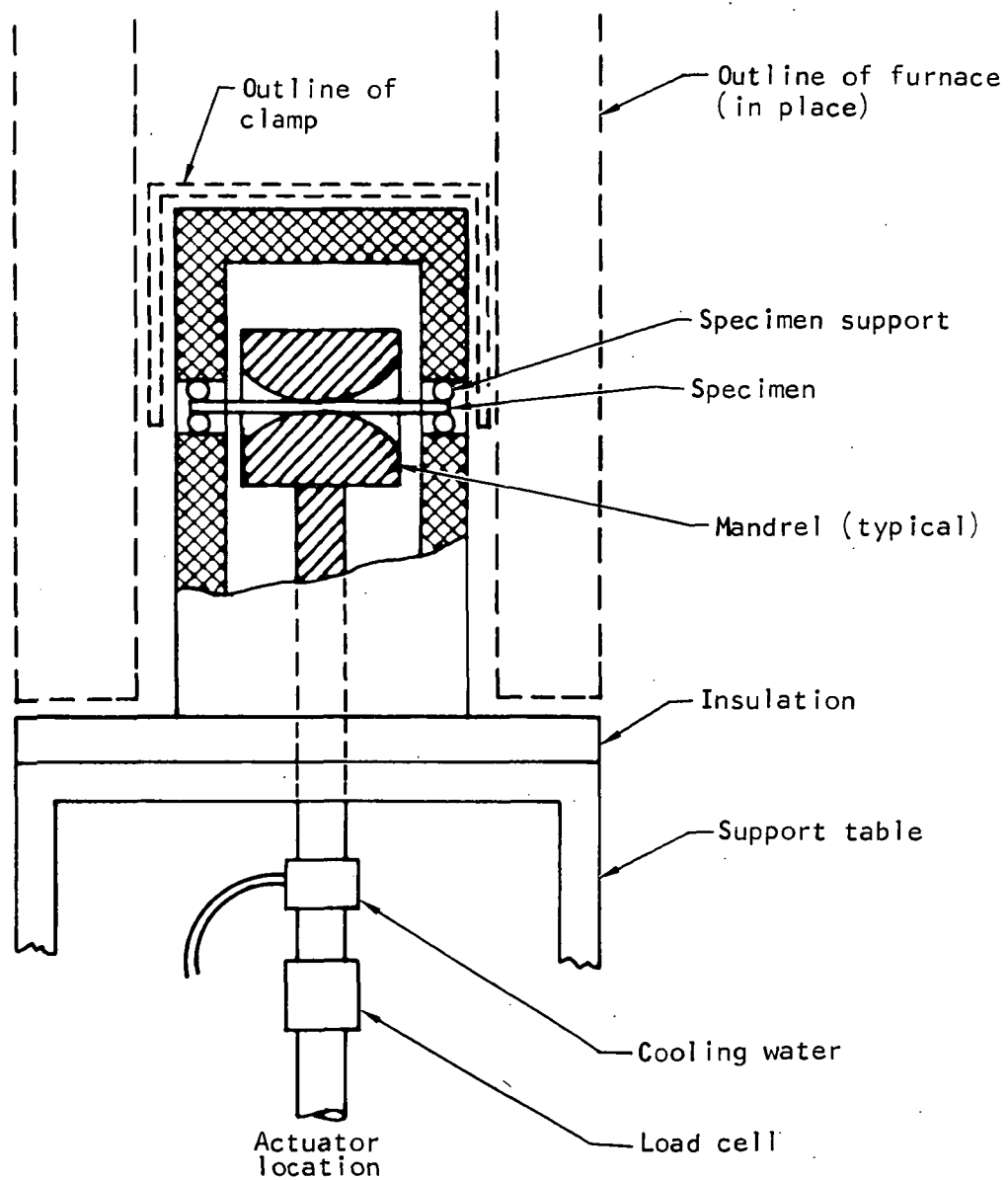
The cyclic life tests were performed on an apparatus, shown in Figure 5-2, which applied a known alternating strain by bending the specimen around opposed curved mandrel surfaces. A hydraulic ram moved the mandrels through the required stroke while the ends of the specimen were restrained from moving in the direction of ram travel.

The ram was driven by a double acting cylinder and ram force levels were monitored by an integral load cell. Stroke reversal was controlled by a four-way solenoid valve and limit switches. Adjustable contacts permitted control of stroke length, and stroke speed was controlled by throttling the flow of hydraulic fluid to the apparatus.

The specimen holding section was designed to fit into an 20 cm ID Marshall furnace for elevated temperature testing. The resulting sample length was 15.2 cm and the sample support spacing was 13 cm. The furnace rested on the support table shown in Figure 5-2a. The heated zone was partially insulated by packing around the base of the furnace which, along with a cooling water jacket around the ram, prevented the load cell from overheating during high temperature tests. The ram head and specimen support section were fabricated from Alloy 713C permitting operation up to approximately 1200 K. The ram was of two-piece construction permitting removal of the head for changing mandrels when necessary. Five pairs of mandrel blocks were available with radii from 0.6 cm to 80 cm.

Peripheral equipment included a pump, flow regulator, pressure control system, counter, and control panel. The control system includes switches connected in series with the pump which automatically terminates testing when reduced ram hydraulic pressure (specimen load) was sensed. Load behavior of each test specimen was recorded on a continuous reading, strip chart recorder with the recording speed set at 10 cm/min. This recording then becomes a graphical display of the load history for each specimen and permits verification of the cycle rate and sustained load hold time.

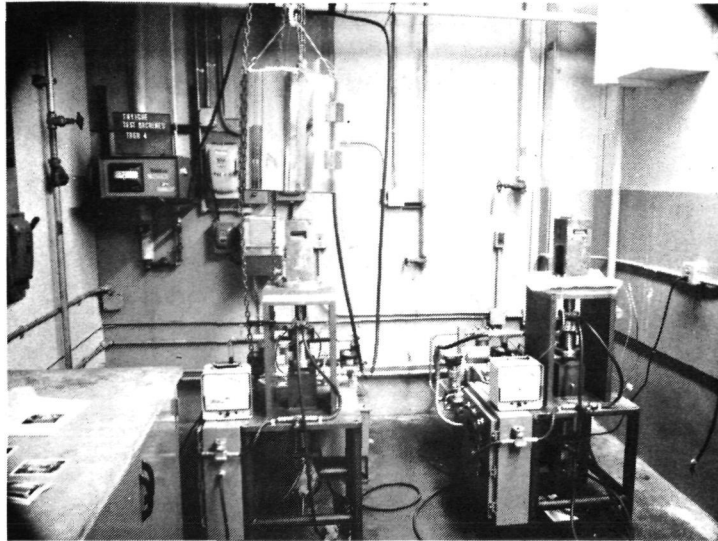
The temperature during the elevated temperature testing was monitored and controlled by a thermocouple attached to the spacer bars used to position the specimen on the mandrel. Initial and final readings were recorded and the specimen temperature was controlled to within ± 6 K during the test period.



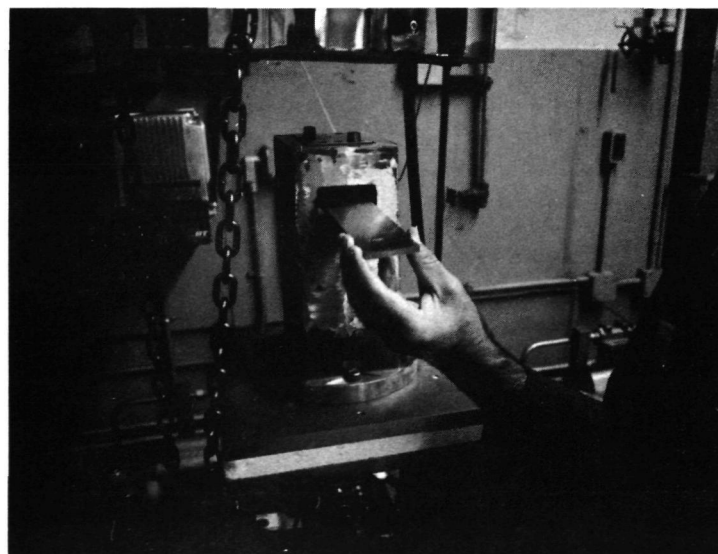
S-64916

a. Specimen loading and support

Figure 5-2. Fatigue Test Apparatus (Page 1 of 2)



Test facility



Specimen placement in test rig

F-12171

Figure 5-2. Fatigue Test Apparatus (Page 2 of 2)

Test specimen failure was determined by decrease in the actuator load used to deflect the test specimen. A 50 percent decrease in the mean actuator load was defined as the point of test specimen failure.

DATA REDUCTION

Plastic Strain Range

When the specimen conforms to the mandrel radius, the applied total engineering strain in the specimen length dimension, ϵ'_l , is related to overall specimen height, h , and mandrel radius, R , by

$$\epsilon'_l = h/(R + 0.5h) \quad (5-1)$$

The general relation between true and engineering strains

$$\epsilon = \ln(1 + \epsilon') \quad (5-2)$$

is used to convert to the total true strain component, ϵ_l , since the desired true strains are noticeably different from engineering strains at the tested strain levels. Subsequent computations of true plastic strain ranges were determined from the total true strain for the specimens utilizing material stress-strain properties for the repeating cycle shown in Figure 5-3. The total strain range shown in Figure 5-3 consists of twice the elastic strain plus the plastic strain so material stress-strain behavior was correlated to the loading curve from points 4 to 1. The compressive stress-strain curve is assumed to be identical to the tensile curve. The resulting (true) plastic strain ranges are summarized for the four specimen types in Table 5-1a, and the associated material engineering properties from published data (References 1 and 2) are presented in Table 5-1b. The engineering properties were converted to true stress-strain values by the power law relation which accurately describes uniaxial true stress-strain behavior.

$$\sigma = B \epsilon_p^m \quad (5-3)$$

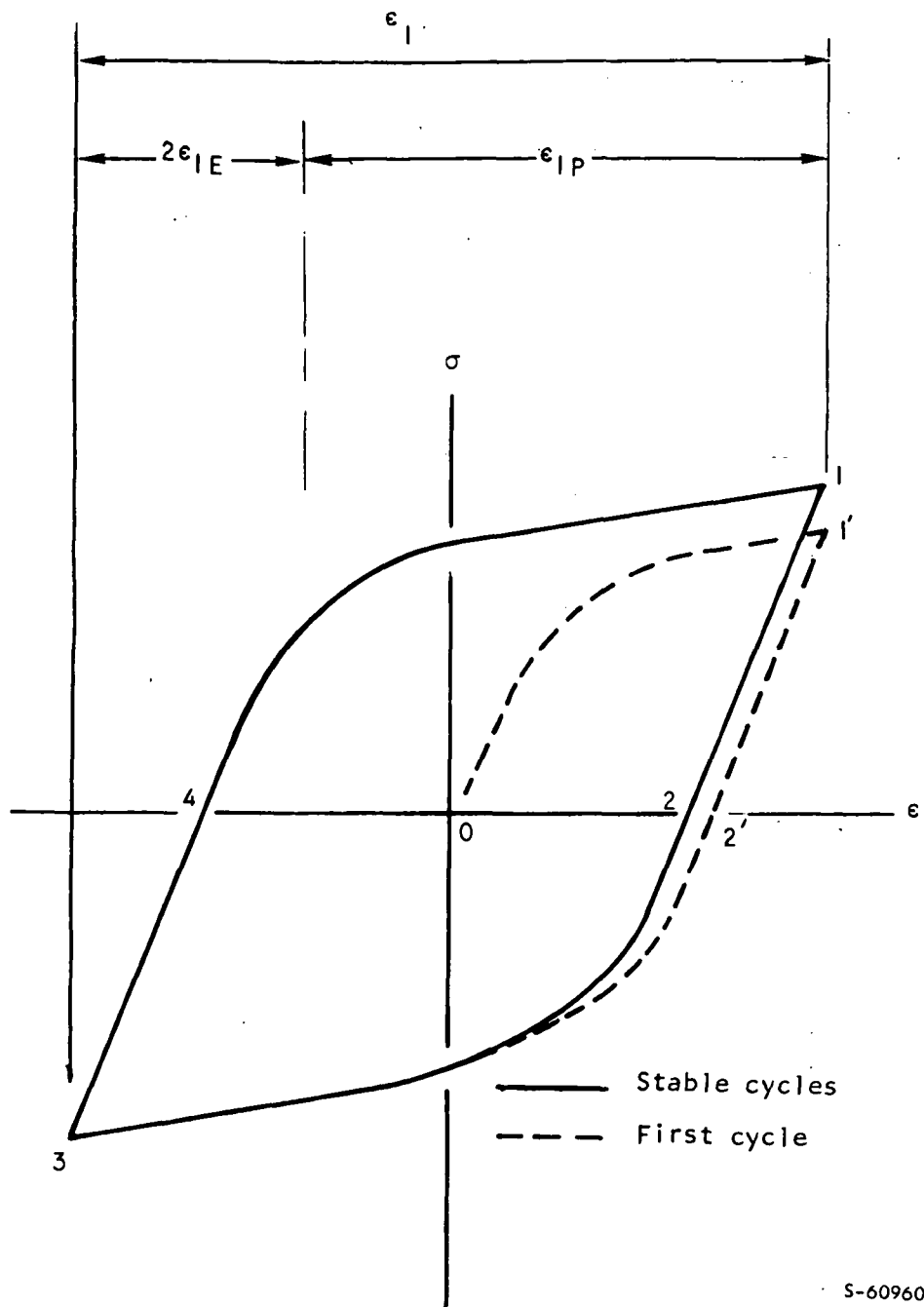
A strain hardening exponent, m , of 0.16 accounts for cyclic material behavior (References 3 and 4). Assuming that ultimate strength is not affected by cyclic hardening or softening, the constant, B , is

$$B = \sigma'_u \epsilon_u^m / (m)^m \quad (5-4)$$

The factor, ϵ_u^m , converts engineering ultimate to the equivalent true stress at the tensile instability strain, m .

The specimens perform as a beam so the cycle for the lengthwise components (Figure 5-3) is the same for uniaxial loading and the plastic strain component, ϵ_{lp} , is the desired plastic strain range ϵ_p . The total uniaxial strain is therefore related to true stress by

$$\epsilon_l = 2\epsilon_{lE} + \epsilon_p = \frac{2\sigma}{E} + \left(\frac{\sigma}{B}\right)^{1/m} \quad (5-5)$$



S-60960

Figure 5-3. Assumed True Stress-Strain Cyclic Behavior, Lengthwise Component

TABLE 5-1

PLASTIC STRAIN RANGE AND MATERIAL PROPERTIES

a. Plastic Strain Range

Material	Temperature	Mandrel Radius, cm	Applied Total Engineering Strain, Percent (Equation 5-1)	Associated True Total Strain Range, Percent (Equation 5-2)	True Plastic Strain Range Percent (Equation 5-6)
Haynes 188	Room Temperature	6	8.61	8.26	7.45
		13	4.40	4.30	3.58
		23	2.47	2.44	1.79
		41	1.40	1.39	0.82
	1030 K	13	4.40	4.30	3.69
		23	2.47	2.44	1.89
Haynes 25	Room Temperature	13	4.40	4.30	3.48
		23	2.47	2.44	1.71
		41	1.40	1.39	0.75
	1030 K	13	4.40	4.30	3.79
		23	2.47	2.44	1.98
		41	1.40	1.39	0.99

b. Material Properties

Material	Temperature	Elastic Modulus, MN/sq m (References 1 and 2)	Ultimate Tensile Stress MN/sq m (References 1 and 2)
Haynes 188	Room Temperature	230×10^3	900
	1030 K	170×10^3	630
Haynes 25	Room Temperature	220×10^3	1000
	1030 K	170×10^3	450

Equations 5-3 and 5-5 permit calculation of plastic strain ranges (Table 5-1a) from the uniaxial total strain by the equation

$$\epsilon_p + \frac{2B\epsilon_p^m}{E} = \epsilon_t$$

Cycles to Failure

The test cycle life was adjusted to give specimen life for a common reference height, h_o , of 0.572 cm. This permitted computation of plastic strains at the single specimen height. The adjusted cycle life, N_{adjusted} , was related to test life, N_{test} , through Equation 5-1 and an inverse one-half power relation in the Universal Slope Equation. Therefore, we have approximately

$$N_{\text{Adjusted}} = N_{\text{Test}}(h/h_o)^2 \quad (5-6)$$

The logarithmic average of a set of data points, j , is

$$N_{\text{average}} = 10 \left(\frac{1}{j} \sum_{i=1}^j \log (N_{\text{Adjusted}}) \right) \quad (5-7)$$

RESULTS AND DISCUSSION

The test cycle rate at room temperature was 0.5 Hz. This limited the increase in specimen temperature during testing to a maximum of approximately 28 K. The elevated temperature test rate was 0.33 Hz corresponding to the nominal rate used in previous tests with Hastelloy X and Palnir 1. The continuous cycling at 0.33 Hz provides a comparison with Haynes 25 (L-605) data obtained by Spera (Reference 5). The cycles with a 5 min hold at maximum strain illustrated the added damage effect of creep relaxation which occurs during typical high temperature heat exchanger operations. However, the duration of the hold was selected to produce a noticeable loss in life and does not correspond to expected HSHX operating conditions. The test data for all of the specimens are summarized in Table 5-2 and presented graphically in Figures 5-4 and 5-5.

The parent metal results in Figure 5-4 show a large life reduction at 1030 K as compared to room temperature, particularly for Haynes 188. The loss in life at elevated temperature was due to accumulated creep damage during each cycle. The added hold time caused further life reductions due to the additional creep damage which became more significant at the lower strain levels. These curves show that Haynes 188 parent metal is superior to Haynes 25 parent metal at room temperature. However, the difference in cyclic life is not nearly as pronounced at 1030 K as it is at room temperature. This test data supported the published data in literature which indicates approximately equal creep strengths at elevated temperatures which is not expected when considering the fact that Haynes 188 has higher ductility than Haynes 25.

The room temperature tests of the welded specimens as shown in Figure 5-5 indicate that welded Haynes 188 is somewhat stronger than welded Haynes 25, and has about 50 percent greater cycles to failure at equal plastic strain ranges. Also, the specimens with a bimetallic weld had about 50 percent less cycles to failure than the welded specimens with the same alloys. The various curves were arbitrarily drawn parallel to the Haynes 188 parent metal curve since this appears to be within the accuracy obtained with this limited number of specimens. There was considerably more scatter in the welded specimens than in the parent metal specimens. For example, the maximum ratio of maximum to minimum cyclic life in a group of three specimens of Haynes 188 parent metal, Haynes 188 welded, and Haynes 188 welded to Hastelloy X was 2.4, 8.1, and 4.4, respectively. The associated values for Haynes 25 were 1.8, 2.7, and 3.4. Thus, even though the welded specimens were machined subsequent to the welding operation (and remachined in some cases) the welding process resulted in more variation within a group of specimens.

TABLE 5-2

HSHX CYCLE LIFE RESULTS

Material	Specimen Type	Test Temperature K	6 cm Mandrel			13 cm Mandrel			23 cm Mandrel			41 cm Mandrel		
			h/h _o	Cycles		h/h _o	Cycles		h/h _o	Cycles		h/h _o	Cycles	
				Test	Avg		Test	Avg		Test	Avg		Test	Avg
Haynes 188	Parent Metal	Room Temperature	1.018	52		1.013	206		1.013	1277				
			1.022	22	40	1.000	271	228	1.018	1113	1350			
			1.013	49		0.991	211		1.013	1577				
		1030				1.022	51		1.018	168		1.000	648 ⁽³⁾	
						1.022	58	55	1.018	169	183	1.013	521	600
						1.022	50		1.022	194		1.004	620	
	Welded	Room Temperature				1.022	48		1.027	247		1.022	752	
						0.991	12	22	1.022	252	294	1.022	440	1100
						1.031	17		1.027	352		1.022	3550	
		1030				1.022	30		1.027	94		1.022	238	
						1.022	24	25	1.022	92	96	1.027	422	356
						1.022	19		1.000	93		1.013	397	
	Welded to Hastelloy X	Room Temperature				1.022	17		1.022	146		1.022	1312	
						1.018	16	12	1.027	161	168	1.027	320	881
		1030				1.009	5		1.031	172		1.022	1417	
						1.013	19		1.031	61		1.031	166	
Haynes 25	Parent Metal	Room Temperature				1.018	43		1.018	322		1.004	1627	
						1.018	24	33	1.022	308	291	1.004	1603	1680
						1.022	31		1.022	219		1.000	1769	
		1030				1.018	55		1.022	182		0.987	410	
						1.018	20	35	1.009	142	161	0.987	528	430
						1.018	21		1.027	145		1.004	384	
	Welded	Room Temperature				1.022	41		1.009	104		1.018	206	
						1.022	45	44	1.018	110	111	1.013	225	208
						1.027	40		1.018	110		1.018	177	
		1030				1.009	21		1.009	73		1.009	1373	
						1.009	21	21	1.009	200	105	1.004	1409	1150
						1.009	20		1.004	77		1.004	762	
	Welded to Hastelloy	Room Temperature				1.009	32		1.009	92		1.009	398	
						1.004	22	27	1.027	110	101	1.009	405	411
		1030				1.004	27		1.027	90		1.027	393	
						1.027	13	18	1.027	25	37	1.027	197	200

Notes: (1) Adjustment to constant height, h_o, of 0.572 cm

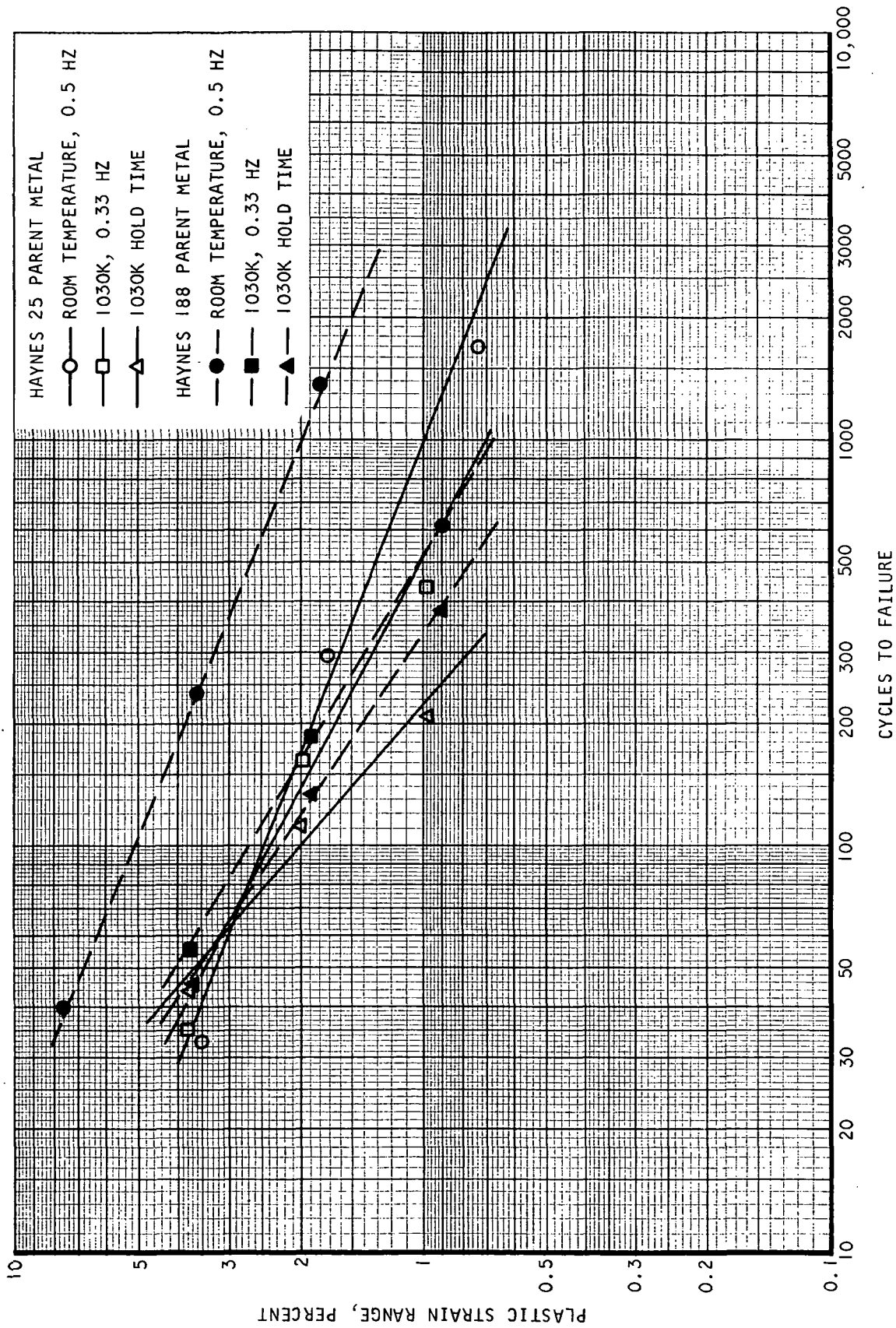
$$N_{\text{Adjusted}} = N_{\text{Test}} \left(\frac{h}{h_o} \right)^2$$

(2) Logarithmic Average from:

$$N_{\text{Average}} = 10^{\left(\frac{1}{j} \sum_{i=1}^j \log(N_{\text{Adjusted}})_k \right)}$$

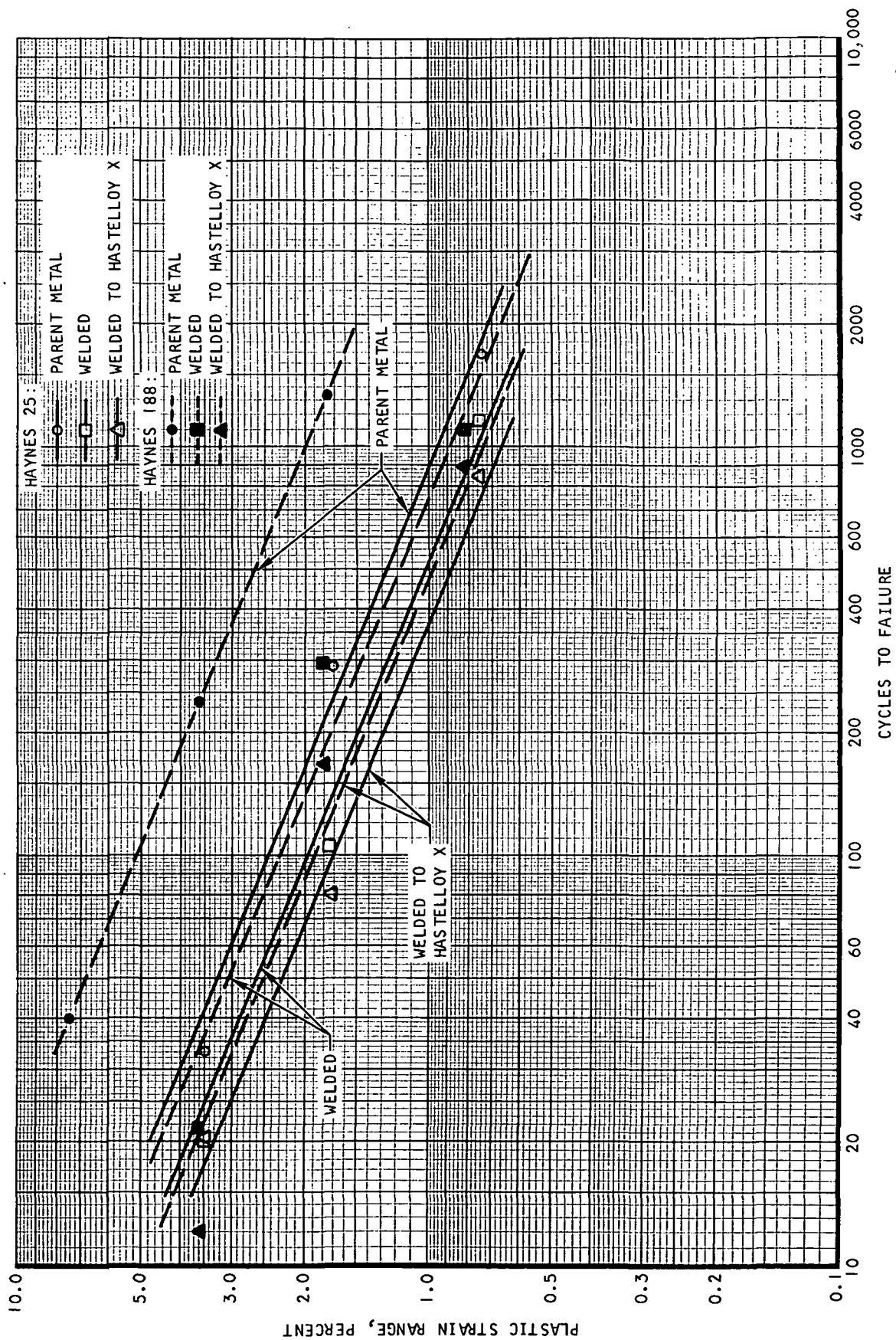
(3) Tested at 1000 K

(4) Room temperature rate = 30 cpm, 1030 K rate = 20 cpm, 5 sec holds once per cycle in 1030 K hold time tests.



S-68407

Figure 5-4. HSHX Parent Metal Cycle Life Summary



S-68724

Figure 5-5. Comparison of Parent Metal and Welded Specimens at Room Temperature.

The 1030 K tests at a continuous cycling rate of 0.33 Hz are shown graphically in Figure 5-6. As in the room temperature comparison these curves were drawn parallel to the Haynes 188 parent metal line. The general trend noted at room temperature was repeated at 1030 K in that parent metal specimens have the highest cycle life capability and Haynes alloys welded to Hastelloy X have the lowest life. However, contrary to the room temperature comparison between Haynes 25 and Haynes 188, the welded Haynes 25 specimens had about 25 percent higher cycles to failure than welded Haynes 188 at the same applied strain range. The scatter in the data generally followed the same trends at elevated temperature as was noted at room temperature. For Haynes 188 parent metal, welded, and welded to Hastelloy X, the ratio of highest to lowest life in a group of three specimens was 1.2, 1.8, and 1.7, respectively. For Haynes 25, the associated values were 2.8, 1.5, and 2.4. The scatter at 1030 K was therefore, much less than at room temperature.

The Haynes 25 parent metal specimens at 1030 K on the 13 cm mandrel gave the ratio from highest to lowest life of 2.8 and this was not only inconsistent from the general scatter range of the parent metal tests but exceeded the welded specimen scatter. Hold time tests on the same mandrel gave life values of from 41 to 45 cycles and this exceeded tests at 20 and 21 cycles when continuous cycling was employed. As a result, photomicrographs of the 20 and 55 cycle parent metal specimens were obtained. As shown in Figure 5-7, the grains of the 20 cycle specimens are half the size of those for the 55 cycle specimen. Fracture propagation was the same for both specimens, indicating that test temperatures were similar. It was assumed that the different grain sizes resulted during preparation by the material supplier, possibly from rolling above and below the transition temperature of Haynes 25 material. Similar evaluations of several pairs of specimens with large scatter did not show such a noticeable difference in grain size.

Figure 5-8 shows a comparison of cyclic life test results of the two parent metal alloys evaluated in this program with Hastelloy X and Inconel 625 parent metal specimens. The latter two alloys were tested on the same machine for NASA Langley (Reference 6). There are some differences in test temperature and testing rate as noted in the figure. The most notable aspect in the comparison is the relatively small difference in cyclic life capability of the four alloys at about 1000 K.

The Haynes 25 (L-605) parent metal data can be compared to Spera tests at room temperature and 1030 K (Figure 8c of Reference 5). These tests show a room temperature life of about 10,000 cycles at 0.9 percent total strain range, which is slightly greater than reported in Reference 5. The 1030 K value in this program was about 2000 cycles compared to about 500 cycles reported in Reference 5 for the same total strain range. It can be inferred that the 100 hr exposure in vacuum at 1140 K that preceded these tests did not cause an appreciable change in Haynes 25 ductility but there was probably a slight increase in creep strength.

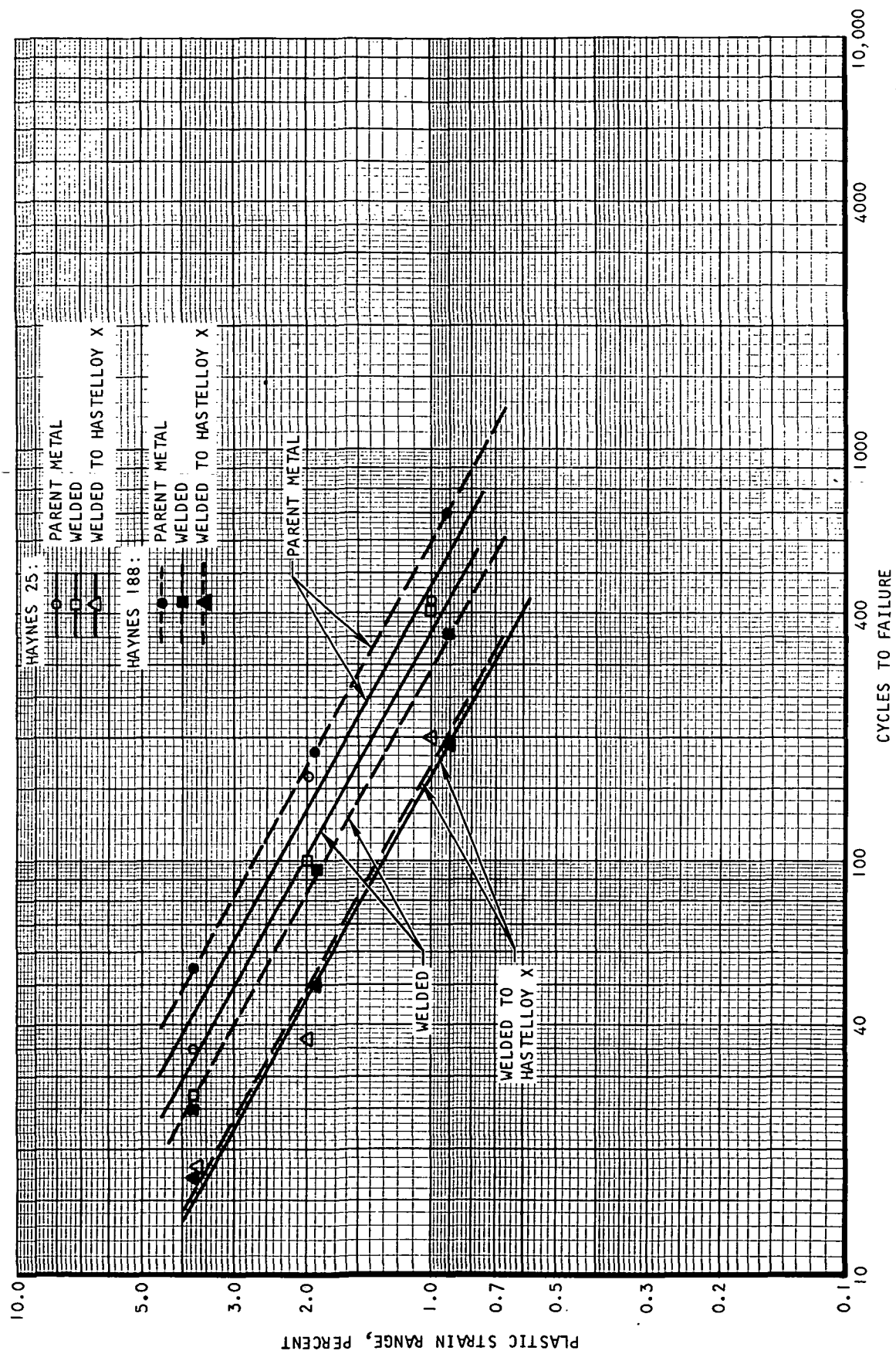


Figure 5-6. Comparison of Parent Metal and Welded Specimens at 1030 K, Continuous 0.33 Hz Cycle Rate).

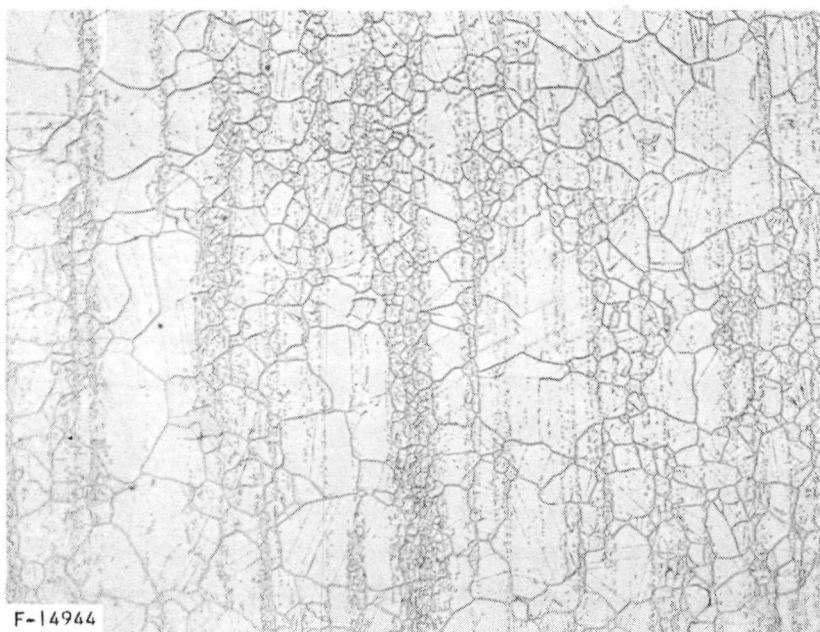
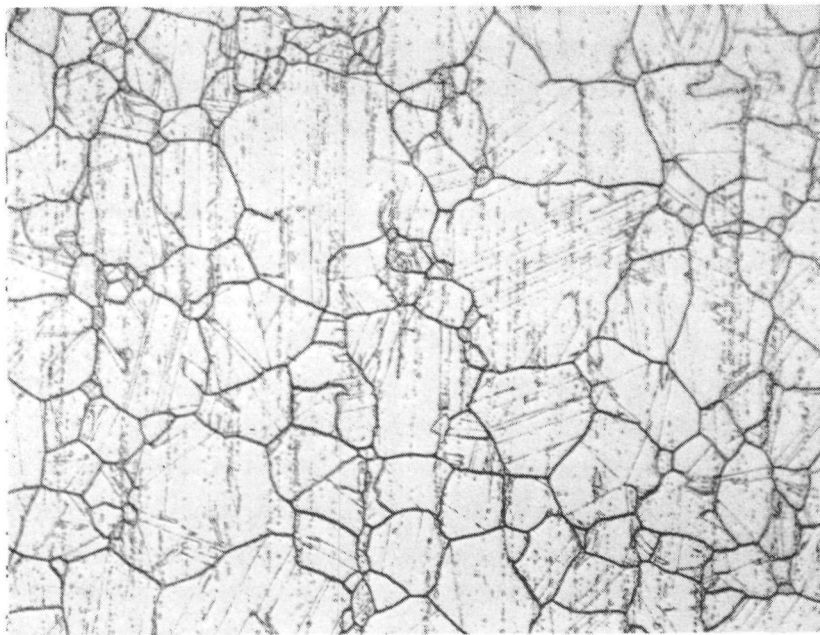


Figure 5-7. Grain Structure of Haynes 25 Parent Metal,
Tested at 1030 K on the 13 cm Mandrel

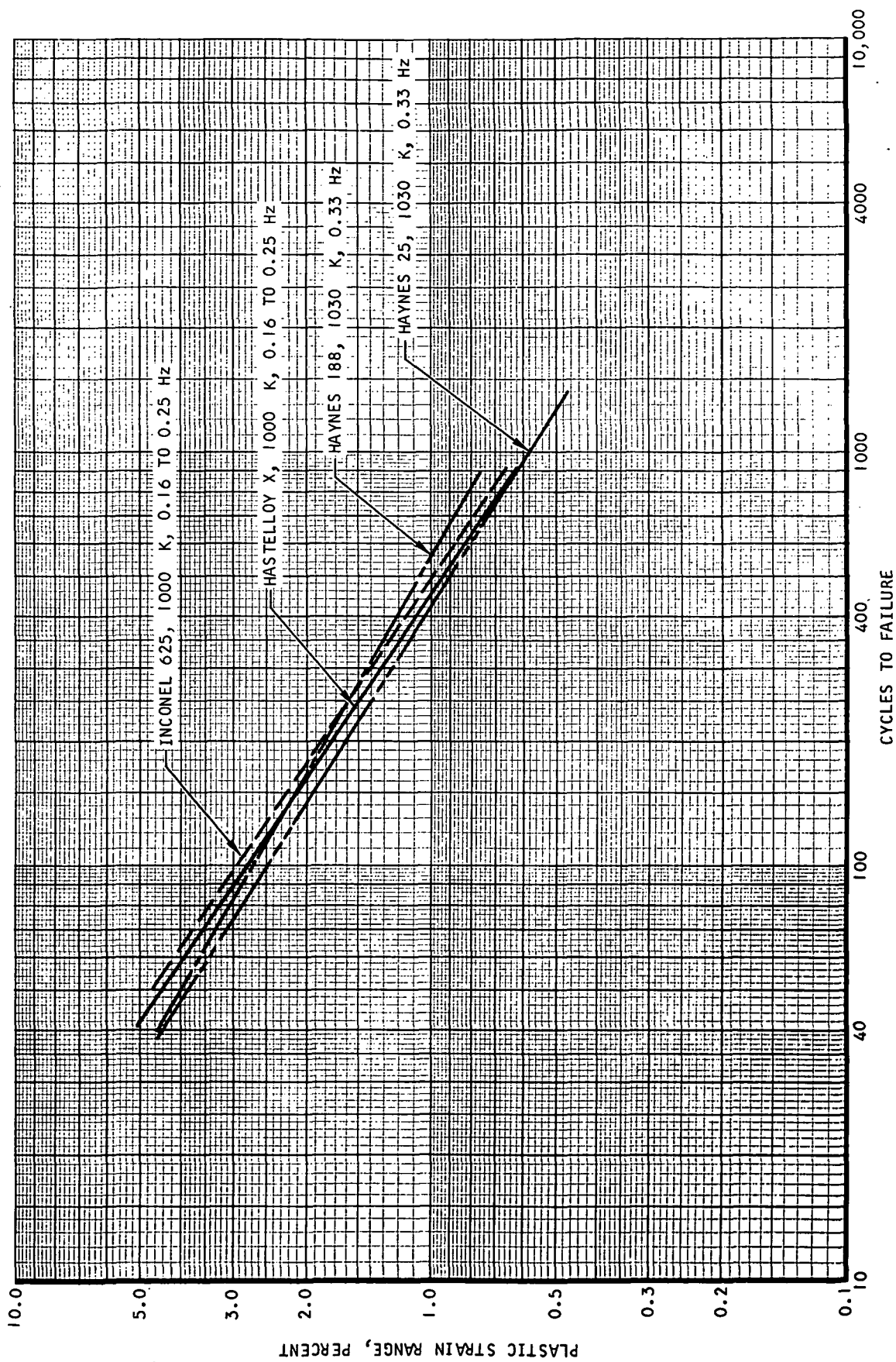


Figure 5-8. Comparison of Hastelloy X, Inconel 625, Haynes 25 (L-605) and Haynes 188 at Elevated Temperature.

S-68722

CONCLUSIONS

Results of the parent metal cyclic life testing indicates that Haynes 188 material provides superior room temperature cyclic life capability. However, elevated temperature testing shows that the cyclic fatigue capability at 1030 K is essentially equivalent for the two materials. The degradation of cyclic fatigue life in test specimens which included a 5 minute hold time during each load cycle was evident for both materials but somewhat less severe for Haynes 188. A comparison of these test results with similar tests performed on Hastelloy X and Inconel 625 materials which are documented in NASA CR-1884 shows that Haynes 188 parent metal provides slightly superior fatigue properties for the 1000 cycle life requirement at 1030 K.

Results of the welded specimen tests show a severe reduction in cyclic fatigue capability at room temperature, especially in the case of the welded Haynes 188 specimen. This is a clear indication that the weld procedure has severely impaired room temperature ductility and further welding development is necessary, especially in the use of Haynes 188. The bimetallic weld specimens showed a further reduction in low-cycle fatigue strength but not nearly as significant as the initial effect of the weld joint in the parent metal. Finally, the Haynes 188 elevated temperature test results showed a more reasonable 32 percent reduction in cyclic strain capability attributed to the parent metal weld joint with an additional 20 percent reduction attributed to the presence of a bimetallic (Haynes 188 - Hastelloy X) weld. The Haynes 25 elevated temperature test results show a smaller 14 percent reduction in cyclic strain capability due to the parent metal weld joint but a larger additional reduction of 30 percent due to the bimetallic (Haynes 25 - Hastelloy X) weld.

As a result of the HSHX structure tests, it was concluded that Haynes 188 or Haynes 25 will provide acceptable material for use in the fabricated heat source heat exchanger. The test results do, however, indicate that the weld procedure significantly impairs low-cycle fatigue capability and allowable cyclic strain must be reduced accordingly for the HSHX design.

REFERENCES

1. Anon: Haynes Developmental Alloy No. 188, Report F-30,361, Union Carbide Corporation, August 1967.
2. Anon: Haynes Alloy No. 25, Report F-30,041C, Haynes Satellite Company, June 1962.
3. Carden, A. E., and T. B. Slade, "High Temperature Low-Cycle Fatigue Experiments on Hastelloy X." ASTM STP 459, American Society for Testing and Materials, 1969.
4. Morrow, JoDean, and F. R. Tuler, "Low Cycle Fatigue Evaluation of Inconel 713 C and Waspaloy." Journal of Basic Engineering, June 1965.
5. Spera, D. A.: "The Calculation of Elevated-Temperature Cyclic Life Considering Low-Cycle Fatigue and Creep." NASA TN-D-5317, July 1969.
6. Richard, C. E., J. D. Duncan, C. Demogenes, and W. G. Flieder, "Low-Cycle Fatigue Evaluation for Regeneratively Cooled Panels," NASA CR-1884, October 1971.

SECTION 6

ALTERNATE LOW TEMPERATURE BRAZE ALLOY TESTS

INTRODUCTION

The objective of this task was to select a low cost, ductile braze alloy suitable for use in the fabrication of the waste heat exchanger. The alternate braze alloy may replace the costly Palniro I (AMS 4784) braze alloy currently identified for the waste heat exchanger design.

AiResearch suggested a possible alternate braze alloy based on the results of its preliminary I R & D evaluation of a number of copper base and ductile nickel base braze alloys. Several alloys, Nicuman 23 and AMI-716HP-C, had similar properties and brazing characteristics. Because it was more readily available in foil form, the NASA Project Manager approved the final selection of Nicuman 23 as the braze alloy to be used in the cyclic life and rupture tests. Using the alternate braze alloy selected, several small specimen sections of the waste heat exchanger plate-fin core were subjected to room temperature and 640 K burst tests. If the short term burst strength at the elevated temperature was shown to be less than predicted by comparing room temperature and 640 K yield strength, creep rupture tests were to be conducted on new samples to determine the minimum pressure containment capability based on a creep rupture design.

Tests were conducted on the waste heat exchanger and pan-to-header bar joint samples, brazed with the alternate braze alloy, to determine the cyclic thermal strain capability. These low-cycle fatigue tests were performed at room temperature and at 640 K and a life range of from 100 to 1000 cycles was investigated. The objective of these tests was to establish the cyclic thermal strain capability of the critical braze joint areas of the pan-to-heat exchanger core. This area in the heat exchanger typically experiences high thermal strains due to temperature differences developed during transient heating conditions associated with each operating cycle. This is an important consideration for required operations to 640 K for the specified life requirement of 1000 cycles.

The test method employed consists of mechanically applying a fully reversed bending strain to beam specimens to simulate thermally induced strains. This mechanical loading approach provides a consistent, repeatable, and accurately controlled strain range during sample test life. Use of a constant test temperature avoids varying material properties and simplifies the analysis of the results. The test apparatus used on this program was constructed for NASA under Contract NAS 1-5002.

The cyclic life test conditions are summarized in Table 6-1 for the pan-to-heat exchanger specimen type. Tests were conducted at room temperature to obtain basic fatigue data and at an elevated temperature of 640 K to obtain cyclic life where creep damage may predominate over fatigue damage. The 640 K test temperature is approximately the maximum operating temperature plus a 55 K overtemperature capability as established in the HXDA design criteria.

TABLE 6-1

TEST CONDITIONS, ALTERNATE BRAZE ALLOY STRUCTURAL EVALUATION

Specimen	Braze Alloy	Weld Alloy	Test Temperature	Number of Specimens		
				ϵ_1	ϵ_2	ϵ_3
Pan-to-heat exchanger core joint	Nicuman 23	None	Room temperature	3	3	3
			640 K	3	3	3
	Nicuman 23	Yes	Room temperature	3	3	3
			640 K	3	3	3

$\epsilon \sim$ applied strain

Three samples were to be tested at each of three strain levels for a total of nine samples at each temperature. The strain levels selected give a range of cycles to failure from approximately 100 to 1000. This provides a reasonable minimum amount of data for constructing curves of the logarithm of plastic strain range vs the logarithm of cycles to failure. Since the curves are straight lines on a logarithmic display, interpolation or extrapolation to desired values of plastic strain range or cyclic life is possible.

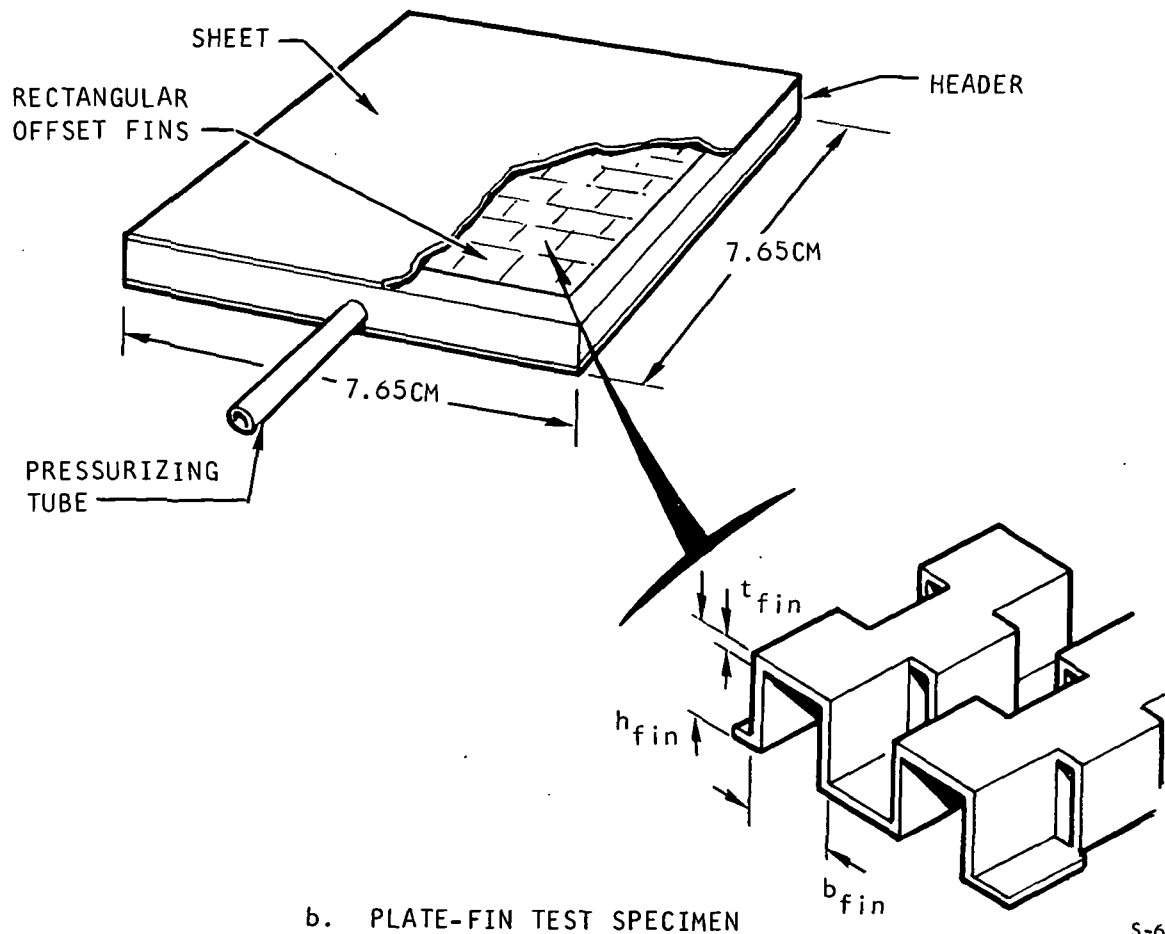
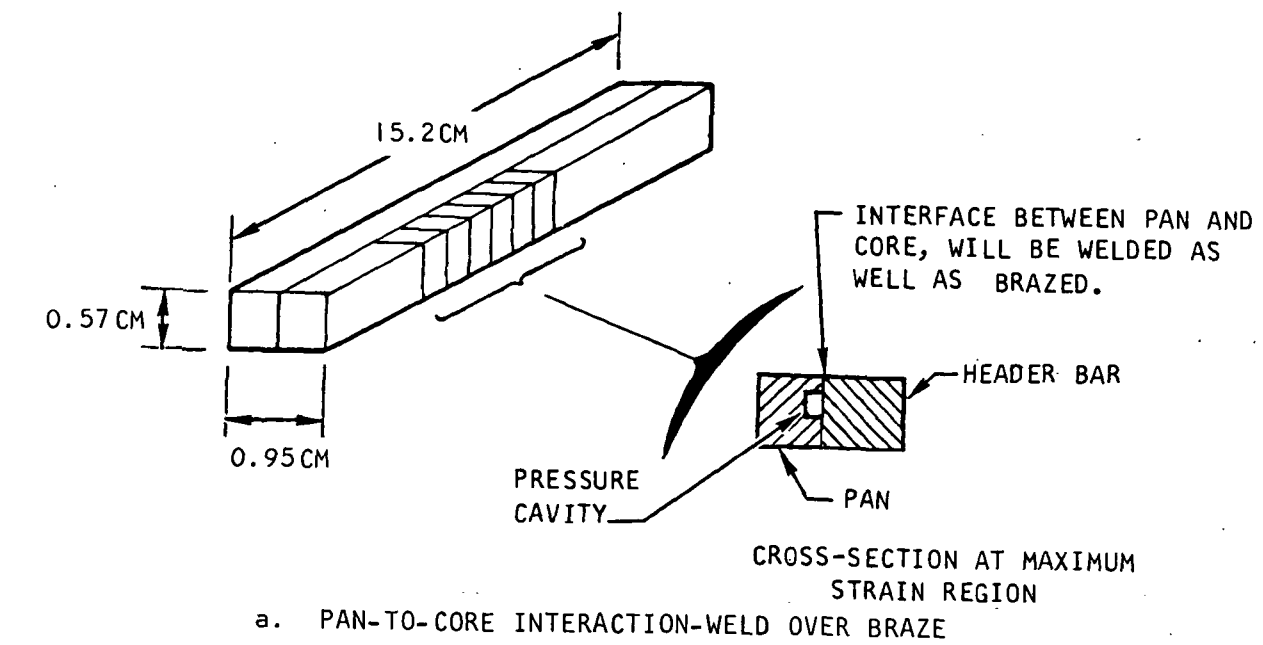
TEST SPECIMEN DESIGN

Design of the two specimen types to be brazed with the alternate braze alloy are shown in Figure 6-1. The low cycle fatigue specimen, shown in Figure 6-1a, simulates the joint between the pan, header bars and brazed side plate. This sample was fabricated with and without a weld pass over the braze joint to determine whether the cycle life of the weld-over-braze joint is acceptable or whether a special braze joint design without the superimposed weld will be required. Figure 6-1b illustrates the type of plate fin test panel that was brazed with the alternate braze alloy for burst testing.

Detail design of the low-cycle fatigue test specimen is shown in Drawing SK 51923 and detail design of the burst specimen is shown in SK 51928. The burst specimen is designed for testing at 640 K to evaluate creep and short time strength characteristics of the alternate braze alloy joints.

TEST SPECIMEN FABRICATION

The plate fin test specimen was fabricated using nickel fins of the type used for the preliminary design of the waste heat exchanger with stainless steel type 347 tube sheets and header bars. The Nicuman 23 braze alloy was placed on the tube sheets in 0.050 mm thick foil form. The test specimen was



S-69333 -A

Figure 6-1. Alternate Low Temperature Braze Alloy Test Specimens

assembled and brazed in a hydrogen atmosphere furnace at a brazing temperature of 1260 K. During the brazing operation only the header bars on the no-flow side of the fin were brazed in place to allow the hydrogen to flow through the plate fin sandwich during brazing. The other two header bars and pressurizing tube were brazed into the assembly using the low melting point alloy Silcoro 60 (1160 K) in a vacuum furnace. The header bars were previously nickel plated to insure good alloy flow and filleting. The brazed assemblies were proof pressure tested and leak checked at a nitrogen pressure of 3480 kN/sq m in a water filled tank.

The two low cycle fatigue specimens were fabricated from the same brazed assembly. The basic low cycle fatigue test specimen was fabricated from a brazed assembly consisting of two plates and simulated header bars that were brazed with 0.025 mm thick Palniro 1 (AMS 4784) braze alloy. The second and final brazed assembly consisted of a simulated pan strip brazed to the first brazed assembly with the 0.050 mm thick Nicuman 23 braze foil in a hydrogen atmosphere furnace. Final machining of the brazed assembly was completed after the final braze cycle. The surface finish of the brazed assembly was held to 1.6 μ m on the two critical surfaces. The brazed-only specimen was completed at this point by welding a pressurization tube into the end of the test specimen and leak checking the assembly at a nitrogen pressure level of 695 kN/sq m to ensure braze joint integrity.

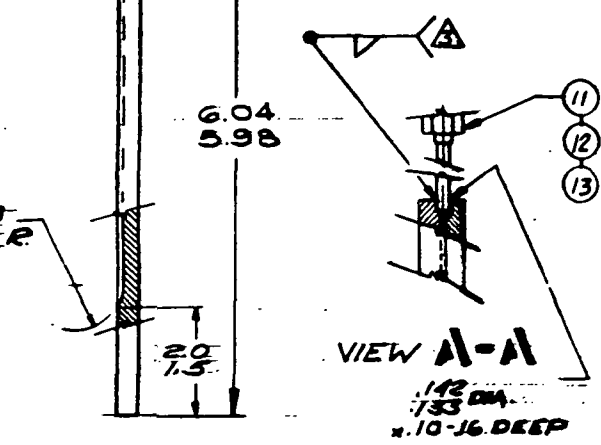
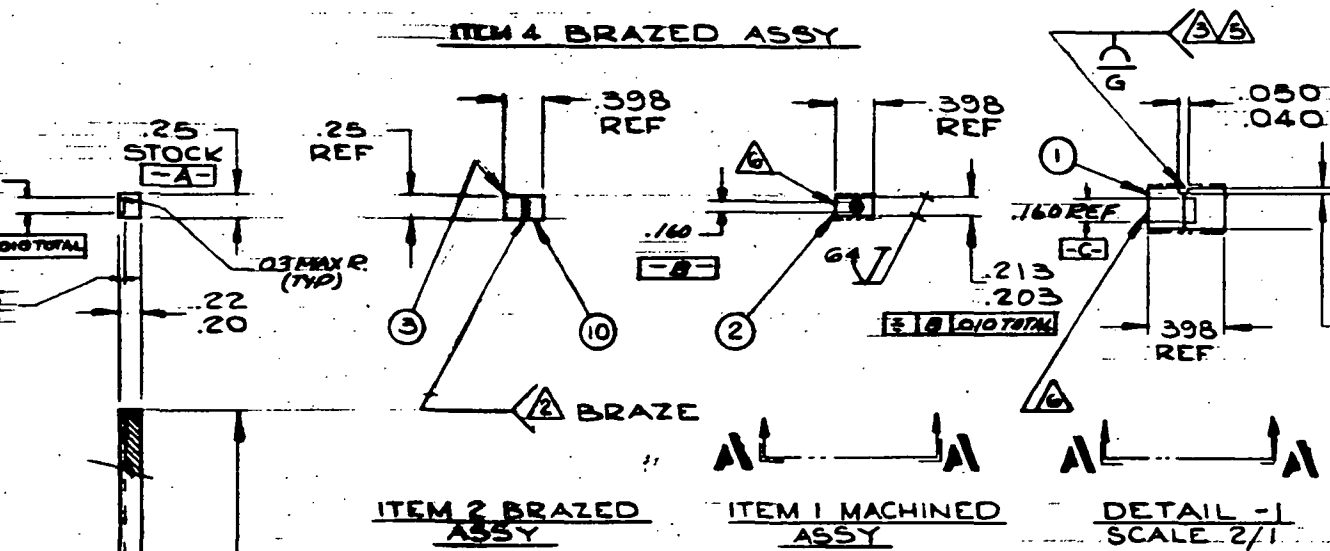
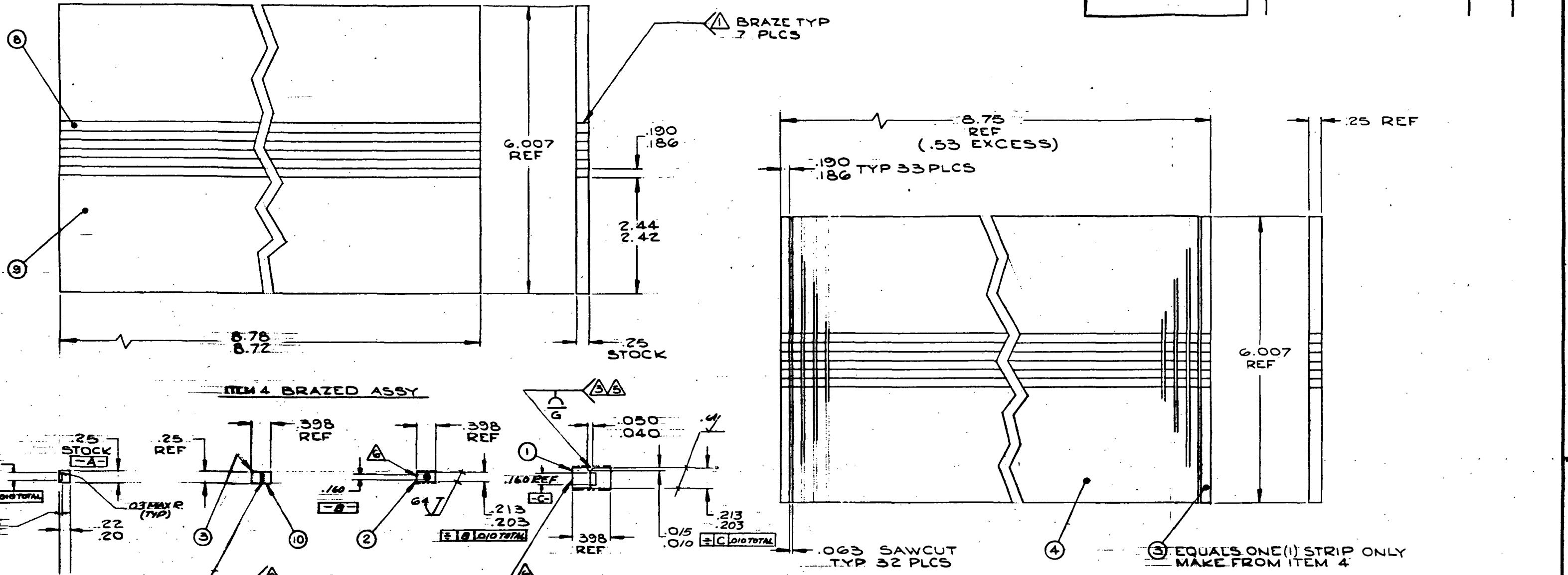
Two types of weld-over-braze low cycle fatigue test specimens were fabricated. The first method used a TIG process and the second method used a pulse arc TIC process with Nickel 61 filler wire. The Hastelloy W and Inconel 82 filler material were not used in the welding process because of problems encountered with weld bead cracking. Metallographic examination of the welded test specimens indicated that a better weld was obtained with the pulse arc welding procedure than with the normal TIG welding procedure. The random and premature failures exhibited by the test specimens regardless of the welding procedure indicated that the cause of the failures was more associated with the design of the test specimen than with the welding procedure. The effect of the braze alloy on the welding procedure was felt to be minimal because of the ability to weld the test specimens satisfactorily in the areas where there was no pressure cavity.

The welding was done prior to the final machining and consisted of a weld buildup along the Nicuman 23 braze joint. The final machining and pressure testing procedure was the same as with the brazed only test specimens.

A revised test specimen design should be incorporated into any new specimens fabricated. The present design requires welding on a 0.0662 cm thick land while the recommended design will have 0.254 cm thick land. (See Figure 6-2.) Increasing the parent metal land in the test specimen will eliminate the braze alloy cracking problem.

With the existing parent metal land, the heat from the TIG welding process melts a braze alloy reservoir inside the cavity of the test specimen. Only in this regard does the test specimen differ from a brazed heat exchanger assembly. With the increased parent metal land and the weld still made over the braze

REVISIONS			
LTR	DESCRIPTION	DATE	APPROVED
A	SEE E.O.	1-21-72	BJ

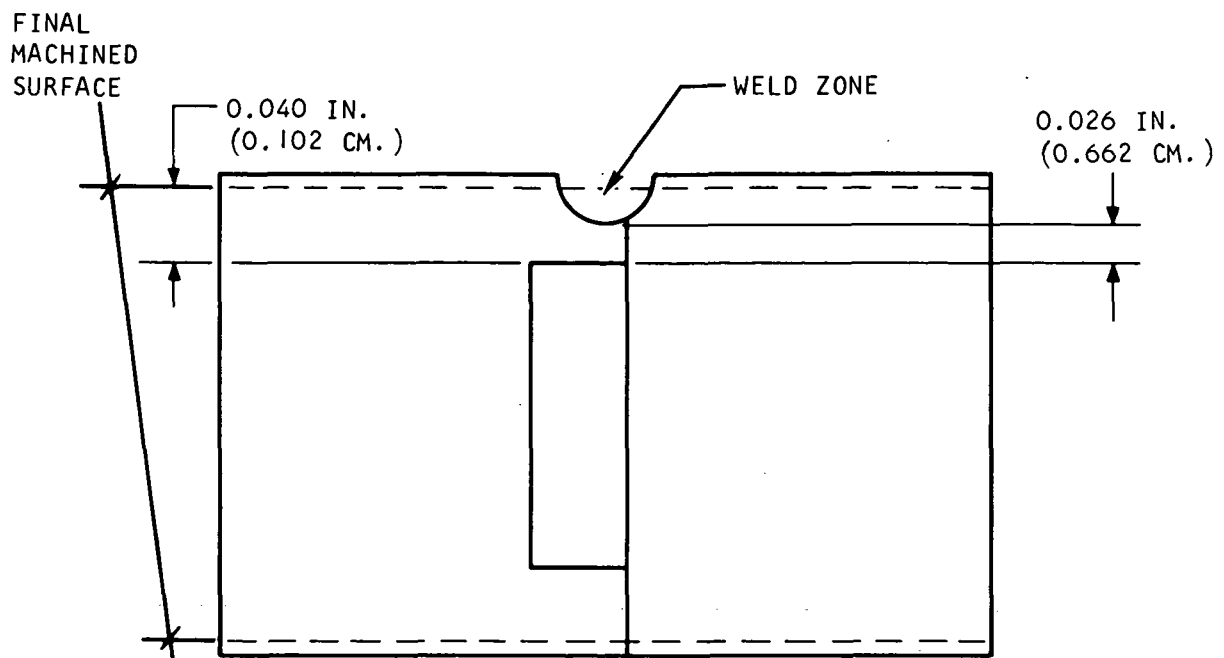


DETAIL ITEM 10

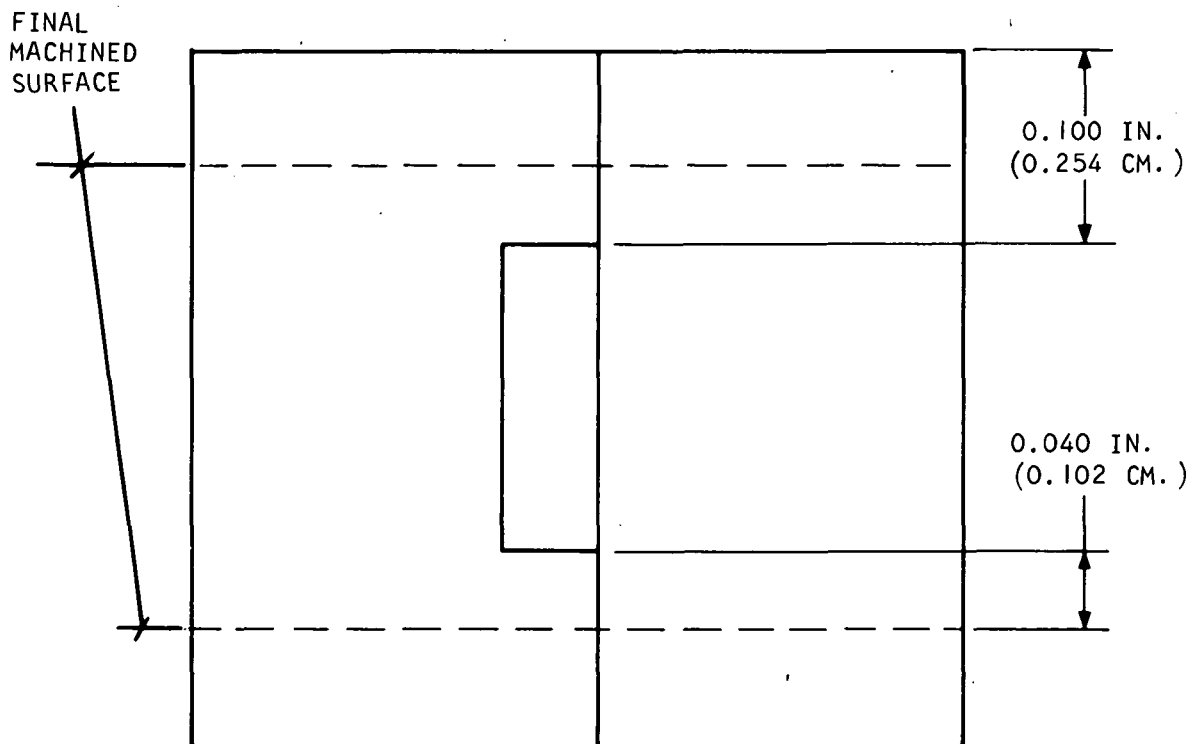
- USE HAST'W' WELD FILLER ROD FOR -1 COMBINATION.
 - IDENTIFICATION THIS FACE ONLY.
 - FLUORESCENT PENETRANT INSPECT PER MIL-I-6866, TYPE I, METHOD 'B'.
 - ALL MACHINED SURFACES 125.
 - WELD PER AIRESEARCH SPECIFICATION WBS-18.
 - FURNACE BRAZE PER AIRESEARCH SPECIFICATION WBS-27, USING NICUMAN 23, .002 FOIL BRAZING ALLOY.
 - FURNACE BRAZE PER AIRESEARCH SPECIFICATION WBS-27, USING PAL 1 EMS 94827 BRAZING ALLOY, .001 FOIL.
- NOTES: UNLESS OTHERWISE SPECIFIED

QTY	ITEM NO.	CODE IDENT NO.	PART OR IDENTIFYING NO.	NOMENCLATURE OR DESCRIPTION	SYM
1	13		AN818-20	NUT	
1	12		MS20819-20	SLEEVE	
1	11		-23	.125 O.D. x .035 W.L. TUBING x 3 FT LG MIL-T-8808 CRES 347	
2	10		-21	.25 PLT CRES 347 MIL-S-6721 COMP Cb	
6	9		-19	.25 PLT CRES 347 MIL-S-6721 COMP Cb	
	8		-17	.25 PLT CRES 347 MIL-S-6721 COMP Cb	
			-9	BRAZED ASSY	
			-7	MACHINED ASSY	
			-5	BRAZED ASSY	
			-3	MACHINED ASSY	

UNLESS OTHERWISE SPECIFIED: BLUR CONTROL PER SCHE		CONTRACT NO. 12-8-71		AIRESEARCH MANUFACTURING COMPANY A DIVISION OF THE BARRETT CORPORATION LOS ANGELES, CALIFORNIA
IDENTIFICATION MARKING PER MCS CL V-A STD INTERPRETATIONS PER PHS		DATE 12-7-71		
HEAT TREATMENT HARDNESS AND SPEC		PROCESS NAME AND SPEC		TEST SPECIMEN ASSY. WASTE HX, PAN TO HX. CRES 347
RECD NEXT ASSY USED ON APPLICATION		DATE 12-11-71		
SIZE D 70210		DWG NO. SK 51923		SCALE 1/1
				SHEET 1 OF 1



a. PRESENT SPECIMEN DESIGN



b. REVISED SPECIMEN DESIGN

S-69180

Figure 6-2. Weld-Over-Braze Low Cycle Fatigue Specimen Design

joint, the local temperature at the braze alloy reservoir will be reduced to a level that does not cause the present cracking problem associated with the weld-over braze process. It should be emphasized that the cracking does not occur in the weld zone but only in the braze alloy reservoir unique to the test specimens.

TEST PROCEDURE

Plate-Fin Burst Testing

The plate fin test specimen was connected to a hydrostatic pressure source for room temperature burst testing. The pressure was incrementally increased until rupture of the test specimen occurred as evidenced by a sudden decrease in the internal pressure of the test specimen. Figure 6-3 shows a plate fin test specimen before and after burst testing.

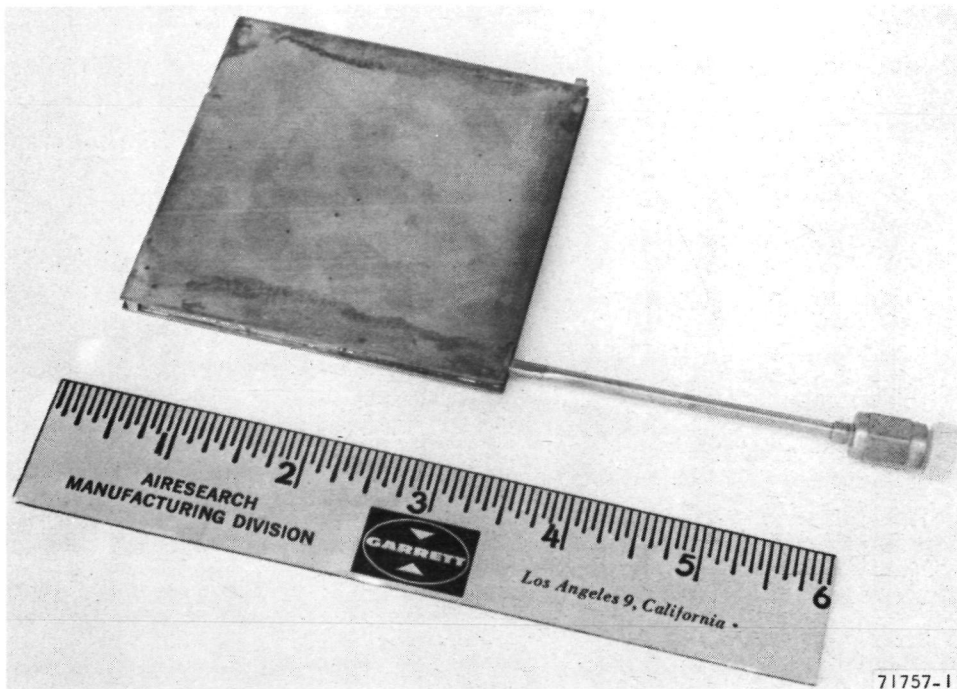
The elevated temperature (640 K) testing of the plate fin test specimens was performed in an atmosphere furnace. The temperature of the test specimen was monitored by a thermocouple attached to the face sheet of the test specimen. The test specimens were connected to a nitrogen pressurization source, placed in the furnace and the temperature was allowed to stabilize at 640 K. The pressure inside the test specimen was incrementally increased until rupture of the test specimen occurred as evidenced by a sudden decrease in the internal pressure of the test specimen.

Low Cycle Fatigue Testing

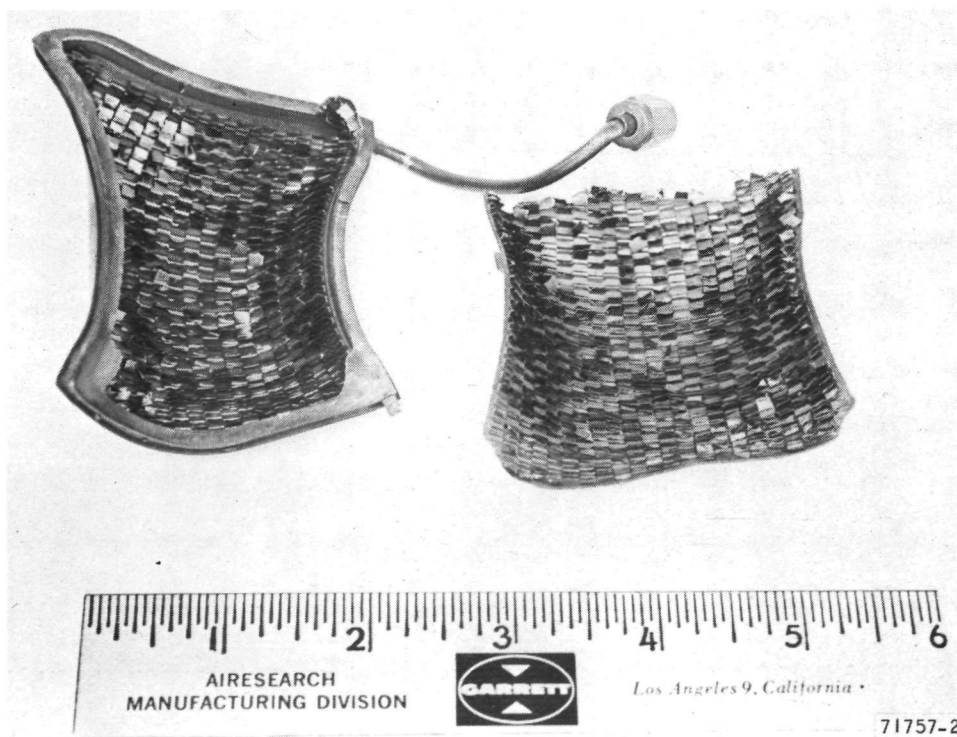
The cyclic-life testing was performed on an apparatus, shown in Figure 6-4, which applies a known alternating strain by bending the specimen around opposed curved mandrel surfaces. A hydraulic ram moves the mandrels through the required stroke while the ends of the specimen are restrained from moving in the direction of ram travel.

The ram is driven by a double acting cylinder and ram force levels are monitored by an integral load cell. Stroke reversal is controlled by a four-way solenoid valve and limit switches. Adjustable contacts permit control of stroke length and stroke speed by throttling the flow of hydraulic fluid to the apparatus.

The specimen holding section was designed to fit into a 20 cm Marshall furnace for elevated temperature testing. The sample length is 15 cm and the sample support spacing was 13 cm. The heated zone is partially insulated by packing around the base of the furnace which, together with a cooling water jacket around the ram, prevents the load cell from overheating during high temperature tests. The ram head and specimen support section are fabricated from Alloy 713C permitting operation up to about 1200 K. The ram is of two-piece construction permitting removal of the head for changing mandrels when necessary. Five pairs of mandrel blocks are available with radii from 0.6 cm to 81 cm.



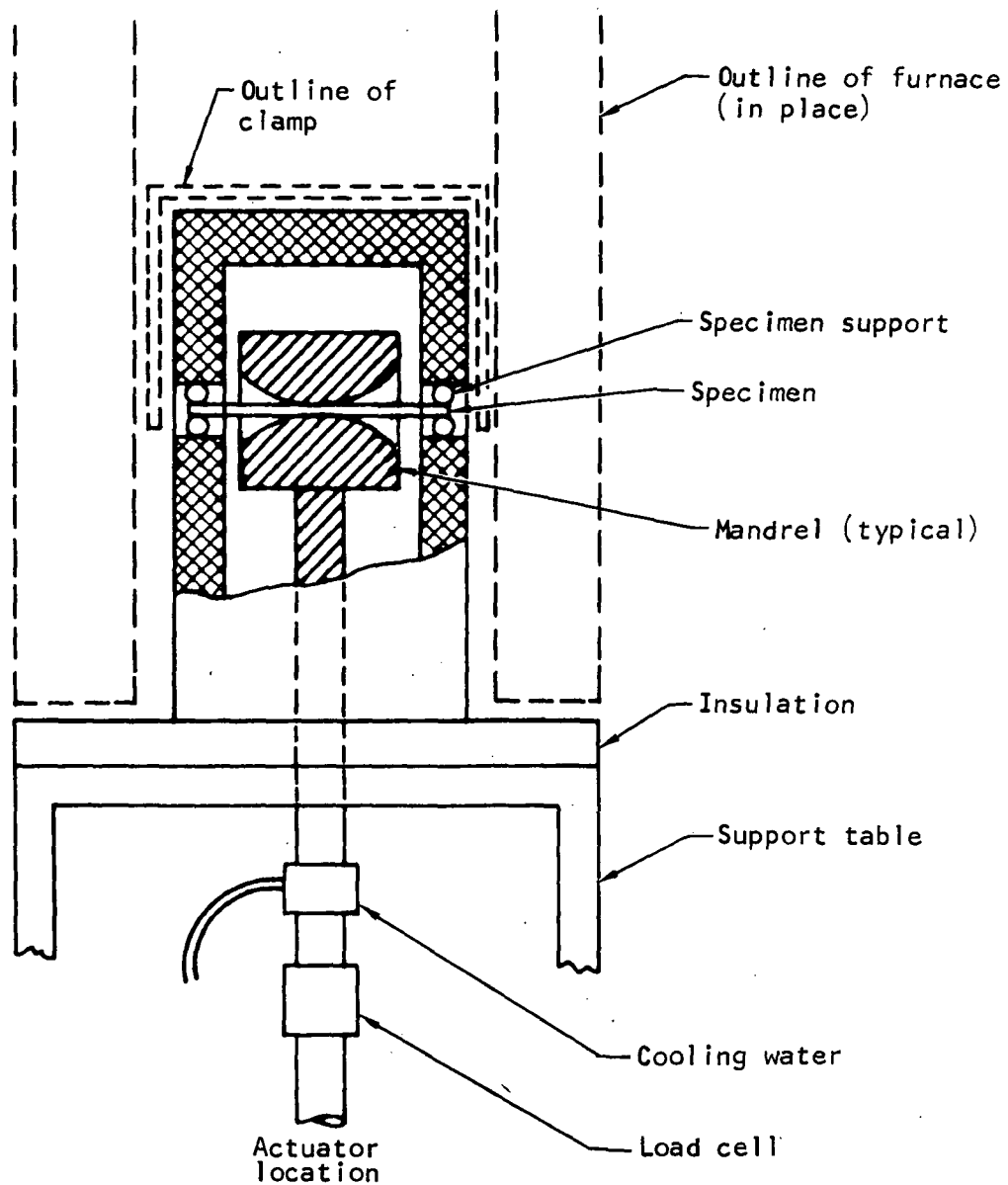
a. COMPLETED TEST SPECIMEN PRIOR TO TESTING



b. TEST SPECIMEN AFTER ROOM TEMPERATURE BURST TEST

F-15706

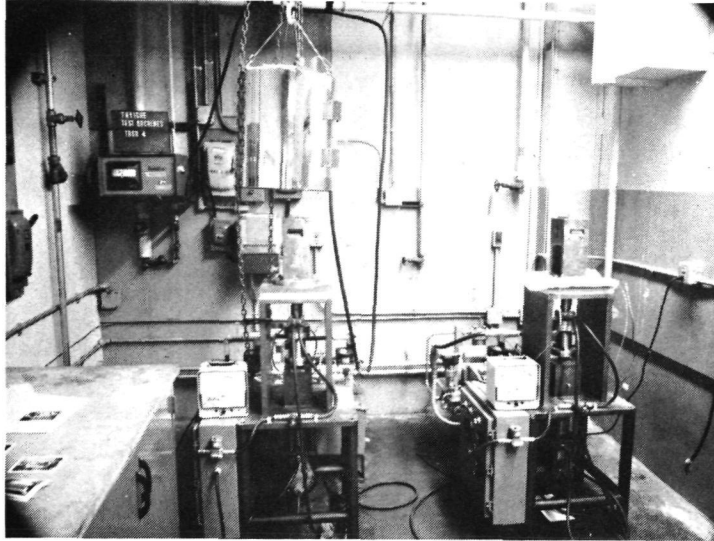
Figure 6-3. Plate Fin Test Specimen



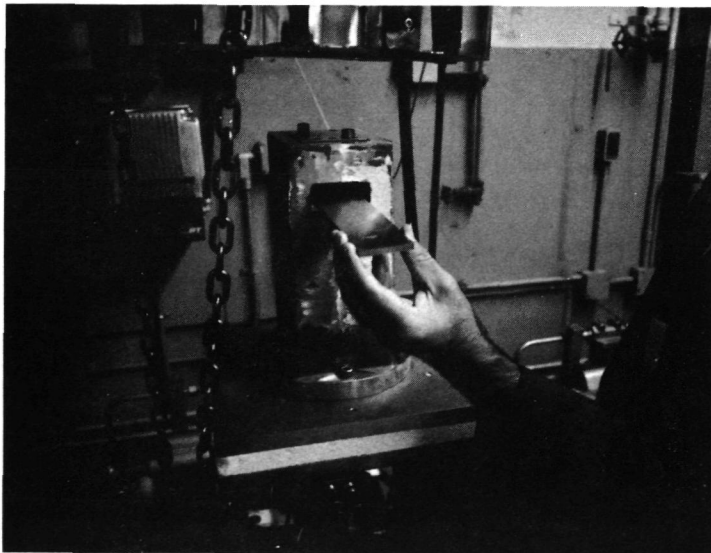
S-64916

a. Specimen loading and support

Figure 6-4. Fatigue Test Apparatus (Page 1 of 2)



Test facility



Specimen placement in test rig

F-12171

Figure 6-4. Fatigue Test Apparatus (Page 2 of 2)

Peripheral equipment includes a pump, flow regulator, pressure control system, counter, and control panel. The control system included switches connected in series with the pump which automatically terminate testing when reduced ram hydraulic pressure (specimen load) is sensed. Load behavior of the test specimen was recorded on a continuous reading, strip chart recorder with the recorder speed set at 110 cm/min.

Specimen load-deflection behavior was first established to insure the proper deflection during testing. A limited acceptable deflection range exists because insufficient deflection leads to reduced strain levels and excessive deflections produce unacceptable strains at the edge of the mandrel. The height of each test specimen was measured and recorded prior to the initiation of testing. Room temperature testing was performed at a cycle rate of 0.5 Hz and the elevated temperature testing was performed at a cycle rate of 0.33 Hz. Specimen temperature during the elevated temperature testing was monitored and controlled by a thermocouple attached to the adjacent spacer bars used to position the specimen on the mandrel. Initial and final readings were recorded and the specimen temperature was controlled to within ± 6 K during the test period.

Test specimen failure was determined by a loss in test specimen cavity pressure which occurred when a crack is initiated in an external joint or surface. When the internal cavity pressure of 105 kN/sq m (absolute) decreased to 69.5 kN/sq m (absolute), failure of the specimen was assumed and the test was complete.

DATA REDUCTION

Plastic Strain Range

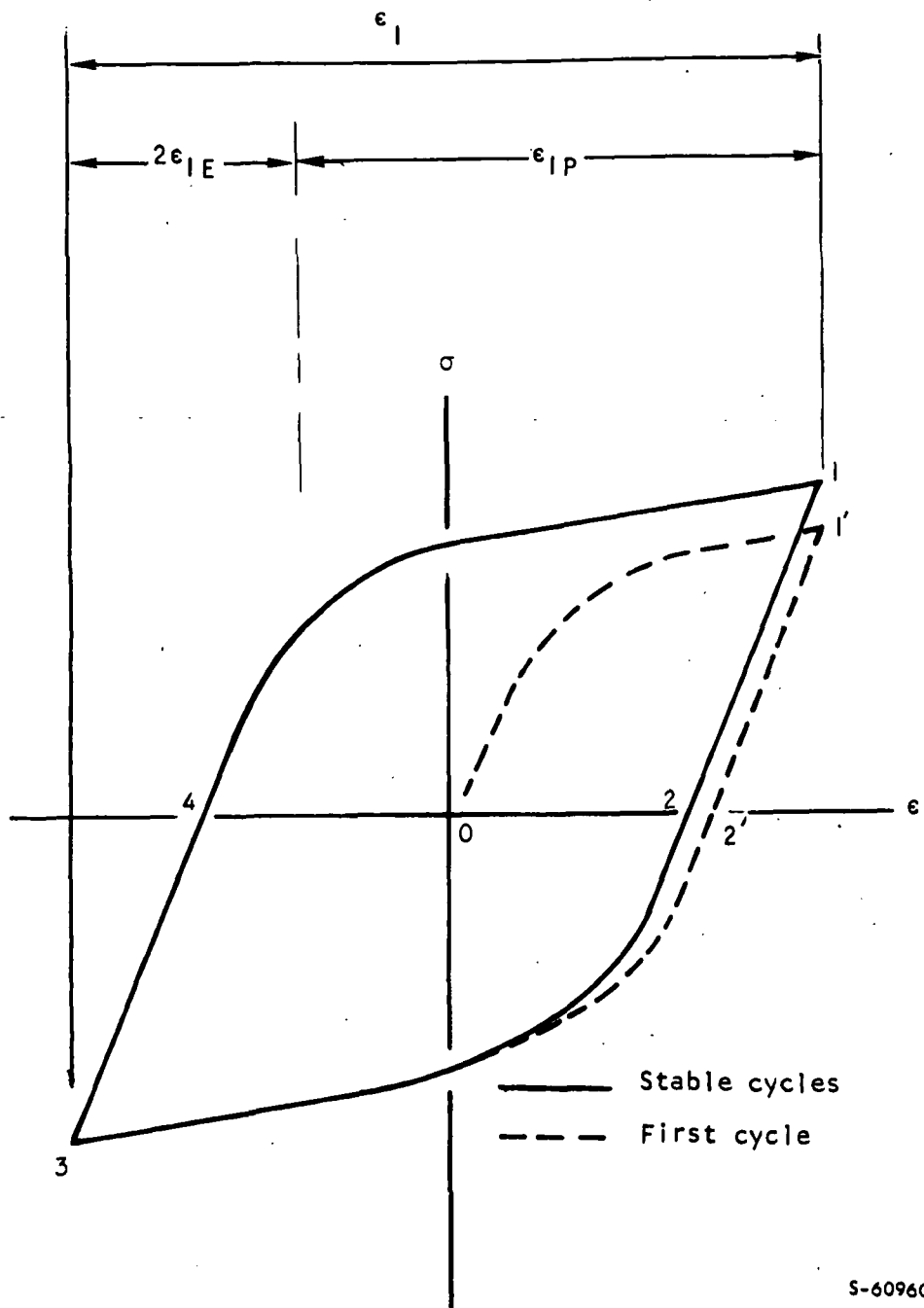
When the specimen conforms to the mandrel radius, the applied total engineering strain in the specimen length dimension, ϵ'_l , is related to overall specimen height, h , and mandrel radius, R , by

$$\epsilon'_l = h/(R + 0.5h) \quad (6-1)$$

The general relation between true and engineering strains

$$\epsilon = \ln(1 + \epsilon') \quad (6-2)$$

is used to convert to the total true strain component, ϵ_l , since the desired true strains are noticeably different from engineering strains at the tested strain levels. Subsequent computations of true plastic strain ranges were determined from the total true strain for the specimens utilizing material stress-strain properties for the repeating cycle shown in Figure 6-5. The total strain range shown in Figure 6-5 consists of twice the elastic strain plus the plastic strain so material stress-strain behavior was correlated to the loading curve from points 4 to 1. The compressive stress-strain curve is assumed to be identical to the tensile curve. The resulting (true) plastic strain ranges are summarized for the test specimens in Table 6-2a, and the associated material engineering properties from published data are presented



S-60960

Figure 6-5. Assumed True Stress-Strain Cyclic Behavior, Lengthwise Component

TABLE 6-2

PLASTIC STRAIN RANGE AND MATERIAL PROPERTIES FOR
ALTERNATE BRAZE ALLOY TEST RESULTS

a. Plastic Strain Range				
Test Temperature	Mandrel Radius, cm	Applied Total Engineering Strain, percent (Equation 6-1)	True Total Strain Range, percent (Equation 6-2)	True Plastic Strain Range, percent (Equation 6-6)
Room temperature	13	4.40	4.30	3.70
	23	2.47	2.44	1.91
	41	1.40	1.39	0.92
640 K	13	4.40	4.30	3.79
	23	2.47	2.44	1.99
	41	1.40	1.39	0.98

b. Material Properties

Temperature	Elastic Modulus, MN/sq m	Ultimate Tensile Stress, MN/sq m
Room temperature	191×10^3	625
640 K	170×10^3	465

NOTES: (1) Specimen height (h) is 0.572 cm

(2) Material properties and strain ranges are for Type 347 stainless steel

in Table 6-2b. The engineering properties were converted to true stress-strain values by the power law relation which accurately describes uniaxial true stress-strain behavior.

$$\sigma = B \epsilon_p^m \quad (6-3)$$

A strain hardening exponent, m , of 0.16 accounts for cyclic material behavior. Assuming that ultimate strength is not affected by cyclic hardening or softening, the constant, B , is

$$B = \sigma'_u e^m / (m)^m \quad (6-4)$$

The factor, e^m , converts engineering ultimate to the equivalent true stress at the tensile instability strain, m .

The specimens perform as a beam so the cycle for the lengthwise components (Figure 6-5) is the same for uniaxial loading and the plastic strain component, ϵ_{lp} , is the desired plastic strain range ϵ_p . The total uniaxial strain is therefore related to true stress by

$$\epsilon_l = 2\epsilon_{lE} + \epsilon_p = \frac{2\sigma}{E} + \left(\frac{\sigma}{B}\right)^{1/m} \quad (6-5)$$

Equations 3 and 5 permit calculation of plastic strain ranges (Table 6-2) from the uniaxial total strain by the equation

$$\epsilon_p + \frac{2B\epsilon_p^m}{E} = \epsilon_l$$

Cycles to Failure

The test cycle life was adjusted to give specimen life for a common reference height, h_o , of 0.572 cm. This permitted computation of plastic strains at the single specimen height. The adjusted cycle life, $N_{adjusted}$, was related to test life, N_{test} , through Equation 1 and an inverse one-half power relation in the Universal Slope Equation. Therefore, we have, approximately

$$N_{Adjusted} = N_{Test} (h/h_o)^2 \quad (6-6)$$

The logarithmic average of a set of data points, j , is

$$N_{average} = 10 \left(\frac{1}{j} \sum_{i=1}^j \log (N_{Adjusted}) \right) \quad (6-7)$$

The adjusted cyclic life calculations for the alternate braze alloy specimens and the resulting average cyclic life for each mandrel size are summarized in Table 6-3.

TABLE 6-3

WASTE HEAT EXCHANGER ALTERNATE BRAZE ALLOY EVALUATION,
CYCLE LIFE TESTS

Type	Test Temperature	13 cm Mandrel			23 cm Mandrel			41 cm Mandrel		
		h/h _o	Cycles		h/h _o	Cycles		h/h _o	Cycles	
			Test	Average		Test	Average		Test	Average
Braze	Room temperature	0.924	92		0.920	203		0.929	877	
		0.916	84	76	0.924	304	221	0.920	736	643
		0.916	96		0.920	286		0.916	673	
	640 K	0.920	102		0.920	123		0.924	966	
		0.929	67	73	0.924	253	173	0.916	632	621
		0.924	88		0.929	284		0.911	662	
								0.920	103 ⁽⁴⁾	
Braze and Welded	Room temperature								6 26 72 804	76

NOTES: (1) Adjustment to constant height, h_o, of 0.572 cm

$$N_{\text{Adjusted}} = N_{\text{Test}} (h/h_o)^2$$

(2) Logarithmic Average from:

$$N_{\text{Average}} = 10^{\left(\frac{1}{j} \sum_{k=1}^j \log (N_{\text{Adjusted}})_k \right)}$$

(3) Room temperature rate = 0.5 H_z, 640 K rate = 0.4 H_z

(4) Test result not included in Figure 6-5 because resulting cycle life discrepancy is much greater than for the other data points.

RESULTS AND DISCUSSION

The room temperature and elevated temperature short term burst test results are shown in Table 6-4.

TABLE 6-4
PLATE FIN, ALTERNATE BRAZE ALLOY, BURST TEST RESULTS

<u>Number</u>	<u>Temperature, K</u>	<u>Rupture Pressure, kN/sq m</u>	<u>Fin Effectiveness</u>
1	294	23,600	0.773
2	294	21,600	0.709
3	294	21,500	0.704
4	640	15,300	0.623
5	640	15,100	0.617
6	640	15,700	0.642

Cycle life testing of the brazed 347 stainless steel specimen results are summarized in Table 6-3 and Figure 6-6. The tests show no significant loss in cyclic life at 640 K, as compared to room temperature. The pressure containment evaluation can therefore be based on short-time burst tests rather than creep rupture tests.

When compared to a Hastelloy X Palnbro braze specimen the alternate braze alloy showed higher cyclic life in the specimens with a plastic strain range less than 1 percent. Test results indicate that the alternate braze alloy is structurally (equal or slightly) superior for applications where the life requirement is greater than 400 cycles and the temperature is not greater than 640 K.

The brazed and welded test specimens gave indications of braze joint cracking. The weld-on-braze specimens failed on the 41 cm mandrel in as little as 6 cycles indicating a braze joint cracking problem associated with the test specimen design.

Experience gained on welding the low cycle fatigue bars indicates that additional handling procedures would be required in welding a large core that was brazed with the Nicuman 23 braze alloy. In addition to using the nickel weld filler wire to weld over the Nicuman 23 alloy, the welding must be accomplished in an inert (argon) atmosphere to minimize the oxidation associated with using a high manganese-containing braze alloy.

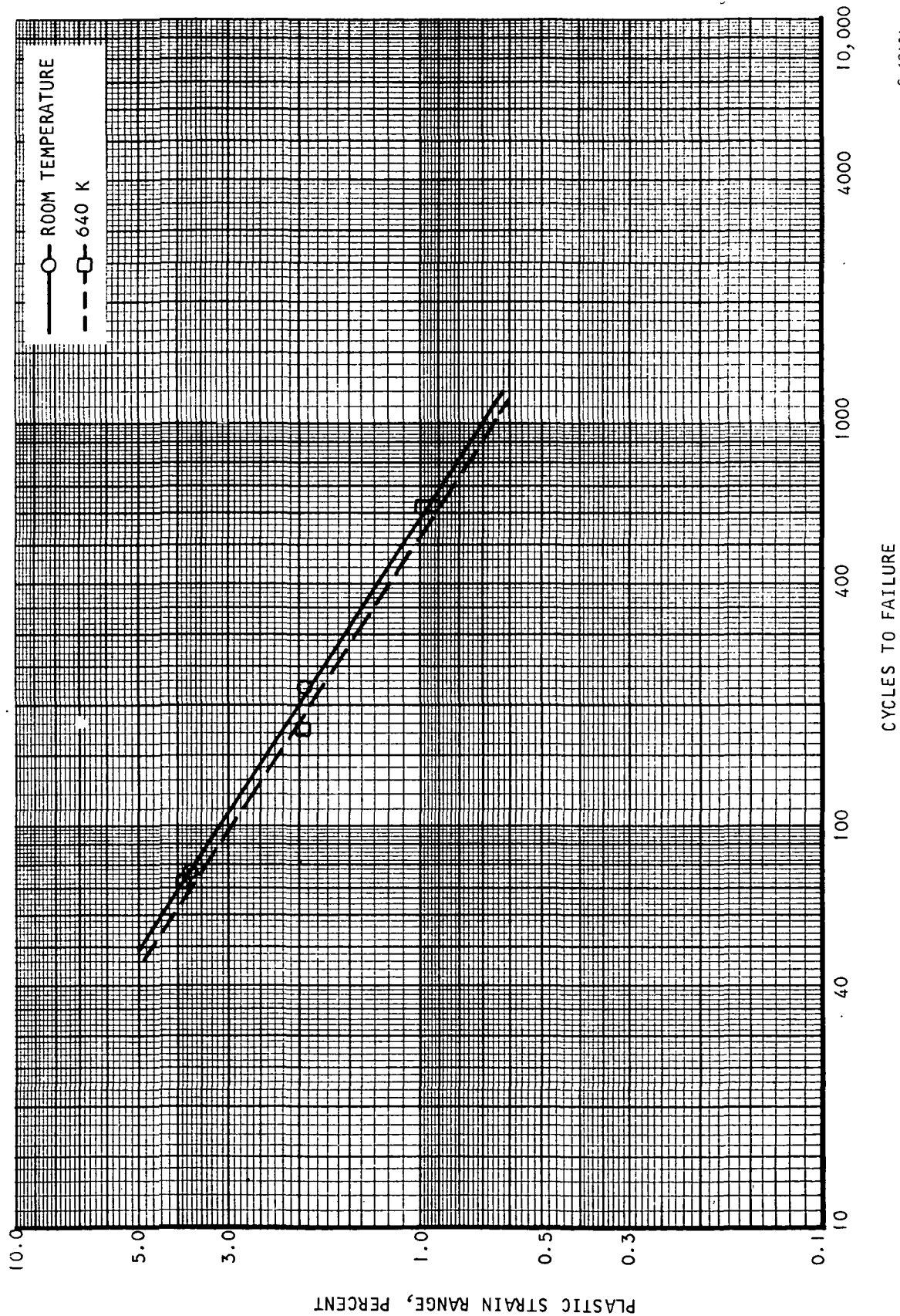


Figure 6-6. Cycles to Failure vs Plastic Strain Range for 347 Stainless Steel Brazed With
Palniro 1 and Nicuman 23 (Pan-to-Header Bar Type)

S-69181

CONCLUSIONS

As a result of the alternate braze alloy tests it was concluded that Nicuman 23 step brazing will provide adequate cyclic life and no significant degradation need be associated with elevated temperatures less than 640 K. Fabrication of the brazed and welded test specimens gave indications of weld bead cracking. Metallographic examination of various weld specimens indicated that a better weld resulted from the pulse-arc welding procedure than from the normal TIG welding procedure. However, random failures exhibited by the test specimens, regardless of the weld procedure, indicated that the problem was associated with the test specimen design. A revised test specimen design was accomplished to eliminate the cracking problem but fabrication and testing was not included in the scope of this problem.

Nicuman 23 is structurally adequate as an alternate braze alloy for use in the waste heat exchanger environment. However, acceptability of the weld-over-braze joint design was not determined and testing of the redesigned specimen design is required to verify the use of the superimposed weld.